

# **Finite Deformations of Fiber-Reinforced Rubberlike Solids, and of Adhesively Bonded T-peel Joints**

Qian Li

Dissertation submitted to the faculty of the Virginia Polytechnic Institute and State University in partial fulfillment of the requirements for the degree of Doctor of Philosophy in Engineering Mechanics

Doctor of Philosophy  
In  
Engineering Mechanics

Romesh C. Batra, Co-Chair

David A. Dillard, Co-Chair

Mark S. Cramer

Shane D. Ross

Robert L. West

September 27, 2017

Blacksburg, VA

Keywords: fiber-reinforced rubberlike material, user-defined subroutine, finite deformations, transversely isotropic material, T-peel specimens, finite element analysis

Copyright 2017, Qian Li

# Finite Deformations of Fiber-Reinforced Rubberlike Solids, and of Adhesively Bonded T-peel Joints

Qian Li

## Abstract

Fiber-reinforced rubberlike materials (FRRM) commonly used in tires undergo large deformations, and exhibit different response in tension and compression along the fiber direction. Assuming that the response of a fiber-reinforced rubberlike material can be modeled as transversely isotropic with the fiber direction as the axis of transverse isotropy, we express the stored energy function,  $W$ , in terms of the five invariants of the right Cauchy-Green strain tensor and the fiber direction, and account for different response in tension and compression along the fiber direction. It has been shown in the literature that in shear-dominated deformations, the 5<sup>th</sup> invariant,  $I_5$ , significantly contribution to the stress-strain curve. We have implemented the constitutive relation in the commercial software, LS-DYNA. The numerical solutions of several boundary value problems studied here agree with their analytical solutions derived by using Ericksen's inverse approach, in which a part of the solution is assumed and unknowns in the presumed solution are then found by analyzing the pertinent boundary value problem. However, computed results have not been compared with experimental findings.

For  $W$  of the FRRMs an expression that is a complete quadratic function of the five invariants is also examined. Homogeneous deformations such as simple extension, simple shear, and biaxial loading problems are studied to delineate the mechanical behaviors of FRRMs. Consistency with the infinitesimal deformation theory requires that linear terms in the 4<sup>th</sup> and 5<sup>th</sup> invariants,  $I_4$  and  $I_5$ , be included in the expression for  $W$ . Stability analysis of deformations reveals the qualitative changes triggered by the second order terms of the quadratic function. Analytical solutions for inflation, extension and twist deformations caused by internal pressure, end torque, and axial force for a pressurized cylindrical laminate are derived using Ericksen's inverse method. Effects of fiber orientations on the mechanical behaviors of a  $\pm\alpha$  angle-ply cylindrical tube are investigated using the derived analytical solutions.

The T-peel test, widely used for characterizing adhesion across a plethora of adhesives, adherends, and geometries, results in a range of responses that may complicate meaningful interpretation of the test data. This research effort, involving several specific specimen types, was undertaken to investigate concerns that commonly used configurations may not always result in plateaus in the force-displacement response. We experimentally and numerically study debonding of T-peel specimens having 75 mm bond length and 0.81 mm thick adherends made of either 6061 aluminum (Al) or one of the three steels (G70 70U hot dip galvanized, E60 electrogalvanized (EGZ), 1010 cold-rolled steel (CRS) bonded with either LORD® 406 or Maxlok™ acrylic adhesive. For the EGZ and the Al adherends, specimens with a bond length of 250 mm and adherend thickness of 1.60 mm are also examined. Effects of adherend materials and thicknesses, bond lengths, and adhesives on test results are examined using three metrics to interpret the T-peel bond performance. We find a limited correlation between the commonly used “T-peel strength” and the energy dissipated per unit debond area. For those two metrics, the relative performances of the CRS and the Al specimens are quite different. Quasi-static plane strain deformations of the test specimens are analyzed by the finite element method (FEM) and a cohesive zone model using the commercial software, ABAQUS, to help interpret the test data. Numerical results provided energies required to elastically and plastically deform the adherends, and help determine the transition from non-self-similar to self-similar debonding. The FE simulations also facilitate determination of the fraction of the crosshead displacement at which self-similar debonding occurs. Results reported herein should help practitioners select appropriate specimen dimensions for extracting meaningful data for adhesive performance.

# **Finite Deformations of Fiber-Reinforced Rubberlike Solids, and of Adhesively Bonded T-peel Joints**

Qian Li

## **General Audience Abstract**

Tire belts, seals, and impact absorbing cushions are usually made of fiber-reinforced rubberlike materials (FRRMs), but are difficult to analyze because their response to complex loading situations is strongly dependent on a variety of material properties. Many biological soft tissues, such as tendons, ligaments and arteries are also typically modeled as FRRMs. We assume that a fiber-reinforced rubberlike material can be modeled as nonlinear, incompressible and directionally dependent, with different response in tension and compression along the fiber direction. For such a material, the stored energy functions,  $W$ , depends upon five invariant metrics of the imposed strain state and the fiber direction. Explicit expressions for the stresses are derived for two polynomial functions of the five invariants for  $W$ . Homogeneous deformations such as simple extension, simple shear, and biaxial loading problems, nonhomogeneous deformations such as plane strain bending of a rectangle beam into a circular one, and inflation, twist and extension of a pressurized cylindrical laminate, are analyzed to reveal the mechanical behaviors described by the developed material models. To enable the numerical solutions, the developed material models are incorporated in the commercial software, LS-DYNA, as user-defined subroutines. The implementations have been verified by ensuring that the computed solutions of several boundary value problems agree well with the derived analytical solutions or those available in the literature. The work provides theoretical guidelines for using quadratic polynomial functions for material models of FRRM, and delivers the software (user-defined material subroutines) capable of numerically analyzing large deformations of FRRM with different responses in tension and compressions.

Large elasto-plastic deformations of T-peel joints have been analyzed using the commercial software, ABAQUS, to delineate conditions that result in self-similar debonding, enabling one to appropriately partition the energy involved in bending the adherends and propagating a debond. Using experimentally measured fracture energies from separate double cantilever beam (DCB)

tests, implemented in a traction-separation law, accurate estimates of required peel force, crosshead displacements at break, and plastically deformed peel arm shapes are made. The demonstrated success of predicting load-displacement curves, deformed shape, and various energy metrics by using the traction-separation law in ABAQUS provides us with a framework to use in the future assessment of T-peel configurations being addressed in this study.

## Acknowledgement

I sincerely and humbly thank my advisors, Professors Romesh Batra and David Dillard for the knowledge in mechanics and problem-solving skills they have taught me. It has been a challenging, rewarding, and fun ride for me since I joined the group. They not only have offered me high-quality training in research, but also have inspired my career interests in being an engineer who has the most satisfaction in having problems solved and enjoys sharing the knowledge and experience with others. Moreover, they are honest, reasonable, and care about the students. They are the best advisors I can imagine having.

I sincerely thank Professors Shane Ross, Mark Cramer, and Robert West for their valuable time on serving on committee. I also want to sincerely thank Professors James Hanna and Shima Shahab for the valuable suggestions for my future career. I want to especially thank Anoop Varghese at Bridgestone Americas, Youliang Guan at the Technology Research Institute for Heavy Machinery (China), and Shantanu Ranade at 3M (US) for the valuable comments and suggestions on my work and communication skills. Special thanks also go to Arka Chattopadhyay, Lisha Yuan, and Yuqing Zhao from the Computational Mechanics Laboratory and Drew Snelling from Design, Research, and Education for Additive Manufacturing Systems Laboratory for the kind help in research. In addition, I want to thank my teammates, Ahmad Mojdehi, Kayla Howes, Doug Hartley, Bikramjit Mukherjee, and Ivan Vu in Adhesion Mechanics Laboratory, Weili Wu, Unchalisa Taetragool, Balachandar Guduri, Priyal Shah, Guillaume Antoine, and Jian Xiao in the Computational Mechanics Laboratory for helpful discussions on the research. I would also like to express my great appreciation to Jessica Grimes, Tim Tomlin and Cristina Rosa Castaner for their prompt and kind help with administrative and technical issues during my graduate study.

At last I want to take this opportunity to express my greatest gratitude to my family: my parents, my wife and daughter, and my sisters for everything I have. Family is the most important thing in my life.

## Table of Contents

<b>Chapter 1: Introduction .....</b>	<b>1</b>
1.1 Transversely isotropic solids and structures.....	1
1.1.1 Literature review on material modeling of FRRM .....	1
1.1.2 Literature review on finite deformation of cylindrical composite tubes .....	9
1.1.3 Objectives of this work .....	11
1.2 Adhesively Bonded T-peel Joints .....	12
1.2.1 Brief review on previous analytical and numerical work on peel tests.....	12
1.2.2 Objectives of this work .....	16
1.3 Organization of the dissertation .....	16
References .....	18
<b>Chapter 2: Constitutive Relation for Large Deformations of Fiber-reinforced Rubberlike Materials with Different Response in Tension and Compression .....</b>	<b>23</b>
Abstract .....	23
2.1 Introduction .....	23
2.2 Constitutive relations for fiber-reinforced rubberlike materials .....	26
2.3 Implementation of the material model in LS-DYNA.....	30
2.4 Verification of the implementation of the user-defined subroutine .....	31
2.4.1 Simple extension of a cube .....	32
2.4.2 Simple shear deformations of a cube .....	36
2.4.3 Plane strain bending of fiber-reinforced rectangular beam.....	40
2.5 Conclusions .....	50
Acknowledgements: .....	50
Appendix A: Source code for the user-defined material subroutines .....	51
Appendix B: Example LS-DYNA input file .....	72
References .....	85
<b>Chapter 3: Strain Energy Density Function Quadratic in Components of Cauchy-Green Strain Tensor for Finite Deformations of Incompressible Transversely Isotropic Solids ...</b>	<b>87</b>
Abstract .....	87
3.1 Introduction .....	88
3.2 Material model for FRRM.....	91
3.2.1 Expression for the strain energy density, $W$ .....	92

3.2.2 Constitutive relation for infinitesimal deformations .....	93
3.2.3 Response of the matrix material.....	95
3.2.4 Response of the fiber-reinforced rubberlike material (FRRM).....	106
3.3 Implementation of the material model in LS-DYNA.....	134
3.4 Conclusions .....	137
Acknowledgements .....	138
Appendix C: Source code for the user-defined material subroutines.....	138
Appendix D: Example LS-DYNA input file.....	151
References .....	165
<b>Chapter 4: Experimental and Numerical Explorations of Transitions to Self-Similar Debonding in Steel and Aluminum T-peel Tests.....</b>	<b>167</b>
Abstract .....	167
4.1 Introduction .....	168
4.2 Experimental results .....	171
4.2.1 Specimen description .....	171
4.2.2 Uniaxial tests on adherends.....	172
4.2.3 Deformations of the adhesively bonded joints.....	173
4.3 Numerical simulations.....	181
4.3.1 Simulation details.....	181
4.3.2 Maxlok™ adhesive .....	187
4.3.3 LORD® 406 adhesive.....	191
4.3.4 Debonding metrics from results of numerical simulations .....	193
4.3.5 Adherend thickness and the bond length needed for the aluminum specimens to exhibit self- similar debonding.....	195
3.6 Discussion on the limitations of the numerical modeling in this work.....	196
4.4 Conclusions .....	197
Acknowledgements .....	198
Appendix E: Failure surfaces and failure modes of Al specimens bonded with LORD® 406	198
Appendix F: Influence of the CZM parameter $T_{max}$ on numerical results.....	202
Appendix G: Remarks on CRS specimens.....	203
References .....	205
<b>Chapter 5: Conclusions and Contributions.....</b>	<b>208</b>

5.1 Fiber-reinforced rubberlike materials (FRRM)..... 208  
5.1.1 Major accomplishments: ..... 208  
5.1.2. Practical implications and future work ..... 209  
5.2 Adhesively bonded T-peel joints..... 210  
5.2.1 Major accomplishments: ..... 210  
5.2.2 Practical implications and future work ..... 210  
References ..... 211

## List of Figures

**Figure 1.1.** (a) 8-node solid (matrix) element with a 4-node membrane (rebar) element (b) 8-node solid element made of a homogenized material.....2

**Figure 1.2.** Configurations of FRRMs in which fibers are denoted in red and purple colors and the matrix in green color; (a) the material can be modeled as transversely isotropic with the fiber direction as the axis of transverse isotropy; (b) the material can be modeled as orthotropic with the  $X_1$  -, the  $X_2$  - and the  $X_3$  - axes as normal to the three planes of symmetry; and (c) the two layers have different material symmetries.....6

**Figure 1.3.** Illustration of the four categories of T-peel specimens, showing shapes before, during, and after debonding.....14

**Figure 1.4.** Four quadrants for the four categories; from left to right: inelastic to elastic, from bottom to top: non self-similar to self-similar debonding.....14

**Figure 2.1.** Schematic sketch of the simple extension of a cube made of a fiber-reinforced rubberlike material with fibers inclined at angle  $\alpha$  to the  $X_1X_3$  - plane; (left) fiber-reinforced body, (right) equivalent homogenized transversely isotropic body.....34

**Figure 2.2.** Normalized Cauchy stress component vs. the axial stretch for  $\alpha = 0^\circ, 30^\circ$  and  $90^\circ$  .....36

**Figure 2.3.** Schematic sketch of the simple shearing of a cube made of a fiber-reinforced rubberlike material with fibers inclined at angle  $\alpha$  to the  $X_1X_3$  - plane .....37

**Figure 2.4.** For  $\alpha = 0^\circ, 30^\circ$  and  $90^\circ$ , normalized Cauchy stress components vs. the shear strain  $k$  .....40

**Figure 2.5.** Schematic sketch of the bending of a straight rectangular beam into a circular beam; (1) reference configuration, (2) deformed configuration .....41

**Figure 2.6.** For  $\alpha = 0^\circ$  and  $90^\circ$ , the through-the-thickness variation of the hoop stress and the Almansi-Hamel hoop strain.....48

**Figure 2.7.** For  $\alpha = 0^\circ$ , the through-the-thickness variation of the hydrostatic pressure.....49

**Figure 3.1.** Mooney-Rivlin plot for the test data of Sasso et al. [26].....99

**Figure 3.2.** Comparison of predicted and experimental [26] engineering stress vs. axial stretch curves.....100

**Figure 3.3.** Stretches  $\lambda_1$  and  $\lambda_2$  for equal biaxial dead loading of a membrane represented by the material model (3.13) with  $h_2/h_1=0.1$  and  $h_{11}/h_1=0.0, 0.005, 0.01, 0.03$ .....103

<b>Figure 3.4.</b> Schematic sketch of the simple extension of a rectangular block made of an incompressible fiber-reinforced rubberlike material with fibers in the $X_1X_3$ - plane inclined at angle $\alpha$ to the $X_1$ -axis.....	107
<b>Figure 3.5.</b> Plots of $\lambda_2$ versus $\lambda_1$ for symmetric and unsymmetrical solutions of Eq. (3.39); $h_{11}/h_1 = 0.001, 0.01, 0.1, 1$ ; (a) $h_{14}/h_1 = 2$ (b) $h_{14}/h_1 = 4$ (c) $h_{14}/h_1 = 6$ (d) $h_{14}/h_1 = 8$ .....	112
<b>Figure 3.6.</b> Plots of $\lambda_2$ versus $\lambda_1$ for symmetric and unsymmetrical solutions of Eq. (3.39); $h_{11}/h_1 = 0.001, 0.01, 0.1, 1$ ; (a) $h_{14}/h_1 = -2$ (b) $h_{14}/h_1 = -4$ (c) $h_{14}/h_1 = -6$ (d) $h_{14}/h_1 = -8$ .....	114
<b>Figure 3.7.</b> Uniaxial stress-stretch relations and free energy densities associated with “symmetric” and “unsymmetrical” solutions for $h_{11}/h_1 = 1$ ; $h_{14}/h_1 = 4, 6, 8$ .....	116
<b>Figure 3.8.</b> Uniaxial stress-stretch relations and free energy densities associated with “symmetric” and “unsymmetrical” solutions for $h_{11}/h_1 = 1$ ; $h_{14}/h_1 = -4, -6, -8$ .....	118
<b>Figure 3.9.</b> Schematic of deformations of the middle portion of a long cylindrical tube; (a) reference configuration, (b) deformed configuration.....	122
<b>Figure 3.10.</b> Plots of the dimensionless inner pressure, end moment and reduced axial load versus $(r_1/R_1)$ for $\alpha = 0^\circ, 30^\circ, 45^\circ, 60^\circ$ and $90^\circ$ for Eq. (3.74) .....	130
<b>Figure 3.11.</b> Plots of the dimensionless inner pressure, end moment and reduced axial load versus $(r_1/R_1)$ for $\alpha = 0^\circ, 30^\circ, 45^\circ, 60^\circ$ and $90^\circ$ for Eq. (3.77) .....	133
<b>Figure 3.12.</b> For $\alpha_1 = \alpha_2 = \phi = 30^\circ$ the through-the-thickness variation of the Cauchy stresses and the Almansi-Hamel strains.....	137
<b>Figure 4.1.</b> Geometric configuration of T-peel specimens (not to scale).....	172
<b>Figure 4.2.</b> Experimental true axial stress-true axial strain curves for the four adherend materials.....	173
<b>Figure 4.3.</b> Representative images of the failed T-peel specimens for the two acrylic adhesives and the four adherend materials.....	174
<b>Figure 4.4.</b> Axial force vs. the cross-head displacement curves (initial portion not shown) for six replicates of each specimen bonded with either LORD <sup>®</sup> 406 or Maxlok <sup>™</sup> adhesive .....	175
<b>Figure 4.5.</b> Three T-peel metrics normalized by their values for the HDG adherend for the two adhesives and the four adherends with 0.81 mm thickness.....	178
<b>Figure 4.6.</b> Effect of the Al adherend thickness on the deformed shapes (after failure) and the force-displacement curves. Bond length = 75 mm.....	179

<b>Figure 4.7.</b> Force-displacement curves for the 0.81 mm thick Al adherends with 75 and 250 mm bond lengths.....	181
<b>Figure 4.8.</b> True axial stress-true axial plastic strain curves for the HDG, the EGZ, the Al and the CRS used in the FEAs. Solid curves are fits to the test data; symbols indicate data points input into ABAQUS.....	182
<b>Figure 4.9.</b> Mode-I traction-separation relation showing input to (solid lines) and output (triangles) from ABAQUS; $G_{IC} = 2 \text{ kJ/m}^2$ , $T_{\max} = 100 \text{ MPa}$ , $K_e = 1 \text{ TPa/mm}$ .....	185
<b>Figure 4.10.</b> FE mesh in a small portion of T-peel specimen (during peeling) .....	186
<b>Figure 4.11.</b> Comparison of the experimental and the computed force-displacement curves for the 0.81 mm thick EGZ and the Al specimens bonded with Maxlok™ and having 75 mm bond length.....	188
<b>Figure 4.12.</b> Qualitative comparison of the experimental and the computed deformed shapes for the 0.81 mm thick EGZ and the Al specimens bonded with Maxlok™ and having 75 mm bond length.....	188
<b>Figure 4.13.</b> Peel force and projected crack length normalized by their plateau values versus the crosshead displacement for the EGZ and the Al specimens; Adhesive: Maxlok™; Bond length: 75 mm; Adherend thickness: 0.81 mm.....	191
<b>Figure 4.14.</b> Comparison of experimental and computed force-displacement traces for 0.81 mm thick specimens bonded with the LORD® 406 adhesive.....	193
<b>Figure 4.15.</b> Normalized peel strength - displacement traces for the four Al specimens of different adherend thicknesses. ( $l = 75\text{mm}$ , bond length; $t_b = 0.4, 0.8, 1.2$ and $1.6 \text{ mm}$ , adherend thickness).....	196
<b>Figure E-1.</b> Failure surfaces of the six Al specimens bonded with LORD® 406.....	199
<b>Figure E-2.</b> Experimental force-displacement curves of the six replicates for Al specimens bonded with LORD® 406.....	200
<b>Figure E-3.</b> Comparison of deformed Al specimens 3 and specimen 4 bonded with LORD® 406.....	201
<b>Figure E-4.</b> Numerical force-displacement curves of the six replicates for Al specimens bonded with LORD® 406 and having bond length of 75 mm. $K_e = 1 \text{ TPa/mm}$ , $T_{\max} = 10 \text{ MPa}$ . $G_{IC} = 200 \text{ J/m}^2 \sim 600 \text{ J/m}^2$ .....	202
<b>Figure F-1.</b> Effect of $T_{\max}$ value on the force - crosshead displacement curves for the EGZ specimens bonded with the Maxlok™ adhesive and having bond length of 75 mm.....	203

**Figure G-1.** Comparison of experimental and computed force-displacement curves for the CRS specimens using three sets of values of the CZM parameters. Pictures of the failed surfaces are included in the inset (oxide formation is present as photo taken long after testing).....204

**Figure G-2.** Comparison of experimental force-displacement curves for 75 mm bond length CRS specimens with the computed force-displacement curves for 250 mm bond length CRS specimen using guessed CZM parameters.....205

## List of Tables

<b>Table 3.1.</b> Material parameters found by the Mooney-Rivlin plot (denoted by *) and the least squares fit to the experimental data.....	99
<b>Table 3.2.</b> Stretch $\lambda_2$ versus stretch $\lambda_1$ for biaxially loaded membrane with equal dead loads. Free energies of solutions corresponding to points B <sub>2</sub> , C <sub>2</sub> and D <sub>2</sub> are less than those for B <sub>1</sub> , C <sub>1</sub> and D <sub>1</sub> , respectively.....	103
<b>Table 3.3</b> Values of parameters for the tube geometry and material constants.....	131
<b>Table 4.1.</b> Debonding characterization from testing results.....	177
<b>Table 4.2.</b> Energy metrics from the experimental and the computed results; bond length = 75 mm; thickness = 0.81 mm.....	194

# Chapter 1: Introduction

This dissertation addresses finite deformation analysis of two distinct problems. The first problem, studied in Chapters 2 and 3, deals with material modeling and finite deformations of incompressible, transversely isotropic solids. The second problem, studied in Chapters 4, involves analysis of fracture of the adhesively bonded T-peel joints. We have briefly reviewed below the two topics.

## 1.1 Transversely isotropic solids and structures

Tire belts, seals, and impact absorbing cushions are usually made of fiber-reinforced rubberlike materials (FRRMs) that can be modeled as anisotropic, inhomogeneous, nearly incompressible, and nonlinear elastic. Many biological soft tissues, such as tendons, ligaments and arteries are also typically modeled as FRRMs [1]. FRRMs exhibit high specific strength and stiffness in the fiber direction, properties that can be exploited to reduce weight and cost, and potentially increase the durability of components made of these materials. The rubberlike matrix, often with relatively low strength and stiffness but large values of failure strain, maintains fibers in their relative positions, thereby providing desirable mechanical properties and function. In addition, due to the fact that fibers can easily buckle and have negligible stiffness in axial compression, FRRMs usually exhibit different responses in tension and compression. Finding distributions of stresses and strains is important in structural design since many failure criteria are based on either stresses or strains at a point. Stresses cannot be measured directly and must be predicted from analyses using engineering mechanics principles. Furthermore, the optimal design of fiber-reinforced composites (e.g., fiber volume fraction, fiber orientation, fiber/matrix bonding, matrix material) requires the development of efficient, robust and reliable techniques to accurately predict the structural response to applied loads, since experimentally designing them is time consuming and very expensive.

### *1.1.1 Literature review on material modeling of FRRM*

The available techniques for predicting stresses includes analytical methods, providing closed-form solutions but often limited to simple geometries and boundary conditions, and numerical methods providing only approximate solutions, including for complex structures and loading



membrane that is assumed to resist loads in the fiber direction only. For example, one constitutive relation for the rebar material [4] can be described by Eq. (1.1).

$$\boldsymbol{\sigma}_f = E_f \ln(\lambda_r) \mathbf{a}_0 \otimes \mathbf{a}_0 \quad (1.1)$$

where  $\boldsymbol{\sigma}_f$  is the Cauchy stress tensor in the rebar layer in the global coordinates, and  $E_f$  is the extensional modulus of fibers. The stretch in the fiber direction,  $\lambda_r$ , is given by

$$\lambda_r \mathbf{a}_0 = \mathbf{F} \mathbf{A}_0 \quad (1.2)$$

Here  $\mathbf{A}_0$  is a unit vector along the fiber direction in the reference configuration,  $\mathbf{a}_0$  denotes the unit vector along the fiber direction in the current or the deformed configuration,  $\mathbf{F} = \partial \mathbf{x} / \partial \mathbf{X} = \mathbf{I} + \partial \mathbf{u} / \partial \mathbf{X}$  is the deformation gradient for the host element evaluated at a point in the membrane,  $\mathbf{u}$  is the displacement vector,  $\mathbf{x}$  is the position vector in the current or the deformed configuration of a material point that occupied the place  $\mathbf{X}$  in the undeformed or the reference configuration, and  $\mathbf{a}_0 \otimes \mathbf{b}_0$  is the tensor product between vectors  $\mathbf{a}_0$  and  $\mathbf{b}_0$ . We introduce a local Cartesian coordinate system  $(r-l_1-l_2)$  in which the  $r$ -direction is always along the fiber and the transverse directions  $l_1$  and  $l_2$  are perpendicular to the fiber. The local Cartesian coordinate system  $(r-l_1-l_2)$  is herein referred to as the material principal coordinate system.

Typically, the volume of the membrane element equals the volume of fibers in the composite, and the location where the membrane element is placed in the host element is determined by the fibers' physical location in the composite. The displacements of the membrane nodes are constrained to the interpolated values of the displacements of the solid element nodes; e.g. see Eq. (1.3).

$$\mathbf{x} = \sum_{\alpha=1}^8 N_{\alpha} \mathbf{x}_{\alpha}, \quad \mathbf{u} = \sum_{\alpha=1}^8 N_{\alpha} \mathbf{u}_{\alpha} \quad (1.3)$$

Here  $N_{\alpha}$ ,  $\mathbf{x}_{\alpha}$  are, respectively, the Lagrange shape function and the position vector for Node  $\alpha$  of the 8-node brick element, and  $\mathbf{u}_{\alpha}$  is the displacement vector for Node  $\alpha$  of the 8-node brick element. Thus, basic unknowns are the nodal displacements of the 8-node brick element, and

the computational cost of such formulations is reasonable. The stiffness of the composite element is found by simply adding the stiffness of the embedded membrane element to that of the host 8-node brick element made of an isotropic matrix material.

An alternative to the rebar element approach involves representing the inhomogeneous material by an equivalent anisotropic, homogeneous one whose mechanical properties depend upon the volume fractions and the mechanical properties of the constituents and the fiber orientations. As depicted in Figure 1.1 (b), the composite can be modeled using one 8-node brick element consisting of the homogenized material. However, the success of this approach relies on finding constitutive relations for the equivalent homogenized material so that under the same applied surface tractions (loads) or surface displacements or their linearly-independent combination, the composite and the homogenized structure have identical structure level responses. For infinitesimal deformations homogenization techniques include the rule of mixtures, the equivalent energy principle, and the Mori-Tanaka scheme [6]. Batra et al. [7], amongst others, have compared results of different homogenization techniques for a fiber-reinforced epoxy. Several empirical equations that are widely used for fiber-reinforced elastomers such as cord-rubber composites are summarized in [7].

The Voigt and Reuss bounds for the overall material properties have been derived by Ogden [8] and Ponte Castaneda [9]. In general, it is difficult to obtain closed-form expressions for the effective properties of FRRMs due to both material and geometric nonlinearities, and the different responses in axial tension and compression. The use of homogenized material properties can provide useful information at a reasonable computational cost, especially during the early stages of design. However, results obtained using the equivalent homogeneous material should be compared with those from experiments to validate the mathematical model. Of course, the use of a homogenized material model precludes consideration of detailed stresses/strains at the fiber/matrix interface, and near fiber ends. Thus the local stress distribution in the homogenized material is quite different from that in the actual inhomogeneous FRRM at fine details, especially when discontinuities are present, including broken fibers, free edges, interfaces, etc.

Numerous phenomenological constitutive models for simulating the macroscopic response of structures composed of nonlinear and anisotropic hyperelastic materials have been proposed [1].

For a hyperelastic material, there exists a stored or strain energy density function (per unit reference volume),  $W$ , of the deformation gradient,  $\mathbf{F}$ . For simplicity we use rectangular Cartesian coordinates both in the undeformed and the deformed configurations. For a homogeneous material,  $W$  does not explicitly depend upon the material particle,  $\mathbf{X}$ . The requirement that  $W$  be invariant under rigid body motions superimposed upon the deformed body implies that  $W$  be a function of  $\mathbf{U}$  or  $\mathbf{C}$  where  $\mathbf{F} = \mathbf{R}\mathbf{U}$  is the polar decomposition of  $\mathbf{F}$  into an orthogonal matrix  $\mathbf{R}$  and a symmetric positive-definite matrix  $\mathbf{U}$ , and  $\mathbf{C} = \mathbf{U}^2$  is the right Cauchy-Green strain tensor.

The functional form  $W = W(\mathbf{C})$  can be further simplified by exploiting material symmetry. For example, for an isotropic material,  $W$  must be invariant under all rotations of the reference configuration before it is loaded. This implies that  $W = W(\mathbf{C})$  be a function of the three invariants,  $I_1 = \text{tr}\mathbf{C}$ ,  $I_2 = 1/2[(\text{tr}\mathbf{C})^2 - \text{tr}\mathbf{C}^2]$ ,  $I_3 = \det\mathbf{C}$ . A general requirement is that  $W > 0$  for every  $\mathbf{F} \neq \mathbf{R}$  that satisfies  $I_3 > 0$ . In terms of the components of  $\mathbf{C}$  with respect to a rectangular Cartesian coordinate system,  $I_1$  and  $I_2$  have the following expressions.

$$\begin{aligned} I_1 &= C_{11} + C_{22} + C_{33} \\ I_2 &= C_{11}C_{22} + C_{22}C_{33} + C_{11}C_{33} - (C_{12})^2 - (C_{23})^2 - (C_{13})^2 \end{aligned} \tag{1.4}$$

We note that  $C_{ii}$  equals the square of the stretch of a line element parallel to the  $X_i$ -axis in the reference configuration. Thus  $I_1$  equals the sum of squares of stretches along the  $X_1$ -,  $X_2$ -, and  $X_3$ -axes. The invariant  $I_3$  equals the product of the squares of these three stretches and hence is  $\geq 1$ . It can be shown that for an incompressible material for which admissible deformations are volume-preserving and hence satisfy  $I_3 = 1$ ,  $I_1 \geq 3$ , and  $I_2 \geq 3$ , the minimum values of  $I_1$  and  $I_2$  occur in the reference configuration [1, 29].

Fung et al. [10], and Chuong and Fung [11] expressed  $W$  in terms of components of the Green-St Venant strain tensor. Ericksen and Rivlin [12] showed that  $W$  for a transversely isotropic material is at most a function of five invariants of the strain tensor, and obtained closed-form analytical solutions for a few boundary value problems (BVP). Pipkin [13] analytically solved several BVPs for incompressible fiber-reinforced materials by assuming that the fibers are inextensible. For plies

of different fiber orientation bonded together, Spencer [14], among others, has shown that  $W$  can be expressed as a function of several invariants of  $C$  that involve the fiber direction in the reference configuration.

Weiss et al. [15] presented a constitutive relation for a biological soft tissue modeled as a transversely isotropic and incompressible nonlinear elastic material. A comprehensive review of constitutive relations for arteries is given by Holzapfel and Ogden [16].

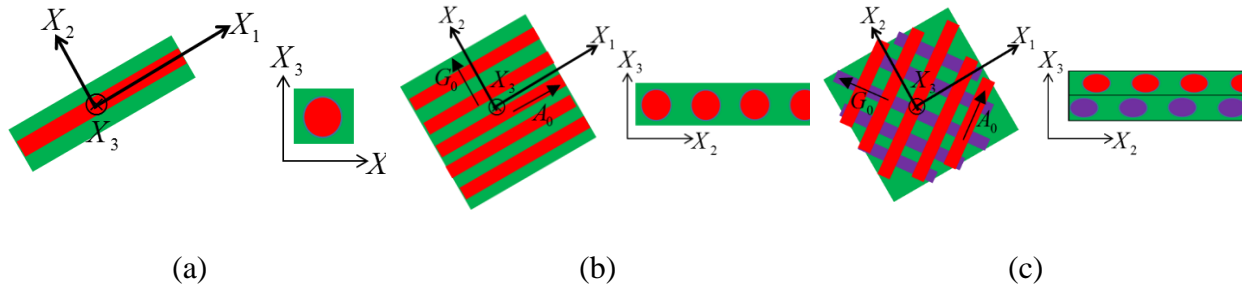


Figure 1.2. Configurations of FRRMs in which fibers are denoted in red and purple colors and the matrix in green color; (a) the material can be modeled as transversely isotropic with the fiber direction as the axis of transverse isotropy; (b) the material can be modeled as orthotropic with the  $X_1$ -, the  $X_2$ - and the  $X_3$ - axes as normal to the three planes of symmetry; and (c) the two layers have different material symmetries.

The FRRM shown in Figure 1.2 (a) is usually modeled as transversely isotropic with the unit vector  $\mathbf{A}_0$  along the fiber in the reference configuration as the axis of transverse isotropy. Ericksen and Rivlin [12] showed that  $W$  for a transversely isotropic material is a function of the five invariants,  $I_1, I_2, I_3, I_4, I_5$ , of the strain tensor  $C$ , where  $I_4 = \mathbf{A}_0 \cdot C \mathbf{A}_0, I_5 = \mathbf{A}_0 \cdot C^2 \mathbf{A}_0$ . For a transversely isotropic material, rotations do not affect  $W$ . Material properties in every direction in the  $X_2X_3$  – plane are the same for a transversely isotropic material. Batra [17] has derived universal relations for these materials that provide necessary conditions for the material being studied to be transversely isotropic. In addition to  $I_1, I_2, I_3$ , either  $I_4$  or  $I_5$  is commonly used to characterize transversely isotropic FRRMs [15, 18-23]. Murphy [24] has recently pointed out that both  $I_4$  and  $I_5$  should be considered if the shear modulus of the material for infinitesimal shear deformations

in the planes parallel to and normal to the fiber direction are to match those found from the test data.

The FRRM representation shown in Figure 1.1 (b) is usually modeled as an orthotropic material that has three planes of symmetry. The normals to these planes are aligned along the fiber direction, the thickness direction, and the direction perpendicular to -- but in the plane of -- the fibers. These three directions are called the material principal directions. For an orthotropic material [14],  $W$  is a function of the seven invariants,  $I_1, I_2, I_3, I_4, I_5, I_6$  and  $I_7$ , where

$$I_6 = \mathbf{G}_0 \cdot \mathbf{C} \mathbf{G}_0, I_7 = \mathbf{G}_0 \cdot \mathbf{C}^2 \mathbf{G}_0 \quad (1.5)$$

Here, the unit vector  $\mathbf{A}_0$  is aligned along the  $X_1$  - axis (the fiber direction) and the unit vector  $\mathbf{G}_0$  along the  $X_2$  - axis (perpendicular to the fiber and in the plane of the FRRM layer). The invariants  $I_4(C_{11})$  and  $I_6(C_{22})$  equal, respectively, squares of stretches along the unit vectors  $\mathbf{A}_0$  and  $\mathbf{G}_0$ . Invariants  $I_5(C_{11}^2 + C_{12}^2 + C_{13}^2)$  and  $I_7(C_{12}^2 + C_{22}^2 + C_{23}^2)$  account for both shearing and stretching deformations, since the off-diagonal components of  $\mathbf{C}$  represent changes in angles between two line elements parallel to the coordinate axes in the reference configuration.

For a rubberlike material reinforced with two families of fibers, as illustrated in Figure 1.1(c), and characterized by two unit vectors  $\mathbf{A}_0$  and  $\mathbf{G}_0$  in the reference configuration, Spencer [14] proposed that  $W$  can be expressed as a function of 8 invariants  $I_1, I_2, I_3, I_4, I_5, I_6, I_7$  and  $I_8$ , where

$$I_8 = \cos \theta \mathbf{A}_0 \cdot \mathbf{C} \mathbf{G}_0, \quad \cos \theta = \mathbf{A}_0 \cdot \mathbf{G}_0 \quad (1.6)$$

and  $\theta$  is the angle between the two families of fibers in the reference configuration. If the two families of fibers are initially orthogonal, then  $\cos \theta = 0$  and the material can be modeled as orthotropic, and  $W$  reduces to a function the 7 invariants as mentioned above. Furthermore, orthotropic symmetry also occurs even if the two families of fibers are not orthogonal, but are mechanically equivalent, in which case, the material is said to be locally orthotropic in the reference configuration with respect to the mutually orthogonal planes that bisect the two fiber families (or directions  $\mathbf{A}_0$  and  $\mathbf{G}_0$ ) and the surface in which the fibers lie [14]. For a locally

orthotropic material, Spencer [14] proposed that  $W$  can be expressed as a function of the seven invariants  $I_1, I_2, I_3, I_8, I_9, I_{10}$  and  $I_{11}$  where

$$I_9 = I_4 + I_6, I_{10} = I_4 I_6, I_{11} = I_5 + I_7 \quad (1.7)$$

For various material symmetries Zheng [25] has given the invariants to use in the expression for  $W$ .

For a general anisotropic hyperelastic material, there are no planes of symmetry and  $W$  is a function of the six components of  $C$ . All six components of  $C$  always determine the material response, however, they appear in specific forms when the material point exhibits material symmetry.

For an incompressible hyperelastic material,  $I_3 = 1$ , and  $W$  is determined by the remaining invariants. However, expressions for stresses can be derived from  $W$  only to within a hydrostatic pressure that cannot be determined from the deformation gradient but is found as a part of the solution of the boundary value problems.

It is very challenging to find the specific form of  $W$  for a given FRRM since tests to cover a large range of variation in one of the invariants while keeping the other invariants constant are needed. Rivlin [26, 27] accomplished this for soft rubbers and showed that the test data can be reproduced by assuming the rubber to be incompressible and setting  $W = 2(C_1 + C_2)$ , where  $C_1$  and  $C_2$  are material constants. Rivlin has shown that these two constants can be determined from a simple tension test. Furthermore,  $2(C_1 + C_2)$  equals the shear modulus of the material for infinitesimal strains.

The nonlinear elastic behavior of FRRMs is generally described by assuming  $W$  to be either a polynomial, an exponential, or a logarithmic function of the invariants. The mathematical expression and the number of invariants to include in the expression for  $W$  are usually guided by the experimental data. For example, a strong stiffening effect of each layer observed at high stresses has motivated researchers to use an exponential function for the description of the strain energy stored in the collagen fibers [1]. If the experimental results suggest that the effect of shearing deformations on the material response is insignificant, then constitutive relations without

$I_5$  or  $I_7$  may capture well the material response. There is currently no one phenomenological constitutive relation that can reasonably well predict the response of FRRMs under different loadings [1].

### ***1.1.2 Literature review on finite deformation of cylindrical composite tubes***

Structures made of fiber-reinforced rubberlike materials often involve multiple layers of material stacked to form laminates. Each layer may have a different fiber orientation and, in some cases, be composed of a different material. Among such laminated composites, the two-layer  $+/-\alpha$  angle-ply tube is one of the most popular units seen in both engineering structures and biological tissues. Examples include tire belts and rubber hoses [28], widely used in transportation and industry, provide appropriate combinations of strength, stiffness, and flexibility for the intended application. The function of fiber-reinforced rubberlike materials such as these plays a very important role in the safety of many engineering structures. In [19], the media and adventitia of the artery are modeled as thick-walled cylindrical tubes composed of two families of collagen fibers wound in a helical configuration. It is agreed that assessment of the mechanical responses of the structures is crucial to understanding many cardiovascular diseases [1]. Analytical solutions are highly desirable for characterization of the material responses and structural design. In the context of nonlinear elasticity for rubberlike materials, finite deformations of cylindrical tubes made of rubberlike materials have been extensively studied. For isotropic rubberlike materials, Batra [29] studied the finite radial expansion and torsion deformations of cylindrical tubes under pressure and end torque loadings. Batra and Bahrami [30] studied finite axisymmetric radial deformations of a circular cylinder composed of an inhomogeneous Mooney–Rivlin material with the two material parameters varying continuously through the cylinder thickness either by a power law or an affine relation. Under the restriction of inextensible fibers, Spencer et al. [31] studied the infinitesimal inflation and axial compression of circular cylindrical tube reinforced with two families of helical fibers. For studying the response of an artery under the combined axial extension, inflation, and torsion, each material layer is modeled as orthotropic with different material principal axes. Hamdaoui et al. [32] analyzed combined finite extension, radial expansion, and torsion of a circular cylindrical tube made of a transversely isotropic material. They have shown that the extension, inflation, and torsion of the thick-walled circular cylindrical tubes are only controllable for certain directions: the radial direction and an arbitrary direction in planes normal locally to the radial

direction. Instabilities for cylindrical tubes made of rubberlike materials under finite deformations have also been of interest to researchers, especially in the area of biomechanics, due to its possible connection to the development of non-physiological states such as an arterial aneurysm [33]. There are numerous studies on the non-monotonic behaviors of the pressure-stretch relations for thin tubes made of rubberlike materials, we refer to Kanner and Horgan [34], and Gent [35] for an extensive discussion on different isotropic material models using strain-energy densities that depend on the principal strain invariants and the principal stretches. In the case of isotropic rubberlike materials, a popularly studied instability phenomenon is called limit point instability, that is, the pressure–stretch (or internal volume) curve quickly reaches a maximum in pressure and then begins to decrease [36]. In addition, the constitutive relations reflecting strain-stiffening [35] typically can exhibit a local maximum followed by a local minimum, after which the pressure increases again until the tube bursts. This is referred to as an inflation-jump instability. Muller [37] has studied the instabilities in the thin cylindrical tubes made of Mooney-Rivlin materials. Such limit point instability that occurs in inflation of long tubes is manifested by the appearance a non-uniform deformation at a critical pressure where one portion of the tube undergoes a bulge or an aneurysm while the remainder remains slightly inflated. Considering that biological tissues such as arterial walls are highly anisotropic due to the organized arrangement of the load carrying (collagen) components, anisotropic material models should be used to describe such structures. Horny [33] et al. use anisotropic material models to demonstrate that whether the pressure-stretch relations are monotonic or not strongly depends on the fiber angles and the ratio of weights by which fibers and matrix contribute to the strain energy density function. In their work, the fiber’s contribution to the strain energy density is described by a so-called standard reinforcing model based only on the invariants reflecting axial deformation in the fiber direction.

Given complex geometries of components made of FRRMs, however, it is often very difficult, if not impossible, to find analytical solutions to initial boundary value problems (IBVPs). Therefore, numerical methods, such as the finite element method (FEM), that can account for geometric irregularities, material heterogeneities, realistic boundary conditions, and large deformations, are used to analyze such problems. The FEM is a technique to numerically find an approximate solution of a given IBVP that is a mathematical representation of a physical problem. Several commercial software packages (e.g., ABAQUS, ANSYS, and LS-DYNA) use the FEM to solve

IBVPs numerically, and are regularly used in many industries. These packages are user-friendly and serve as investigative tools for engineers. Many well-developed material models, such as isotropic linear elastic, isotropic elastic-plastic, and orthotropic linear elastic, are built into these commercial codes, allowing engineers to predict deformations in real structures made of these materials. However, reliable, thermodynamically consistent, and experimentally validated material models for FRRMs have not been implemented in these codes. The user-defined features in many commercial codes like ABAQUS and LS-DYNA allow users to add in-house developed constitutive relations and avoid the development and maintenance of the complete software.

### ***1.1.3 Objectives of this work***

The objectives for Chapter 2 are

- (1) Develop material models for FRRMs with different response in tension and compression
- (2) Implement user-defined subroutines for these materials in LS-DYNA
- (3) Verify the implementation by comparing predictions with analytical solutions of simple IBVPs including both homogeneous and nonhomogeneous deformations

The objectives for Chapter 3 are:

- (1) Study homogeneous deformations such as simple extension, simple shear, and biaxial loading problems to delineate the mechanical behaviors of FRRMs described by a complete quadratic function of the five invariants for the stored energy function,  $W$
- (2) Derive analytical solutions for the inflation-extension-twist finite deformations of a  $\pm\alpha$  angle-ply cylindrical tube using Ericksen's inverse method, and study the effects of fiber orientations on the mechanical behaviors of the tubes
- (3) Implement and verify the developed user-defined subroutine in LS-DYNA by using comparing numerical results to the analytical ones

## 1.2 Adhesively Bonded T-peel Joints

In Chapter 4 we use both experimental and numerical techniques to study one common test method for adhesion testing: The T-peel test. The background and the brief literature review are given as follows.

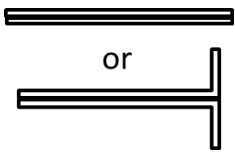
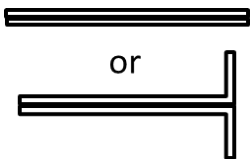
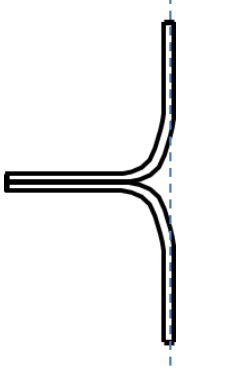
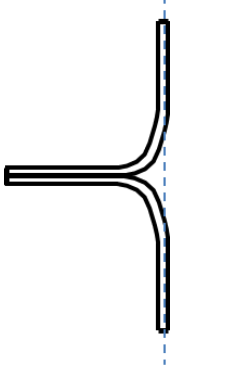
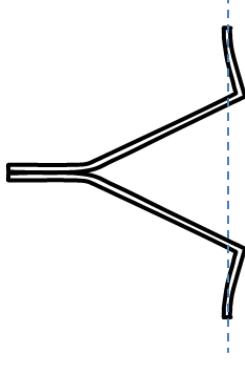
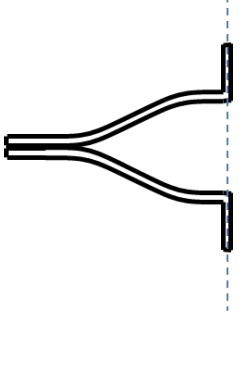
The T-peel test, like other peel tests, often involves large adherend deflections and strains. Compared to other adhesion test methods, the T-peel test is often used when both adherends are sufficiently flexible to allow the unbonded portions to be bent perpendicular to the bonded portion of the joint for mounting in a universal test frame. Furthermore, since specimen fabrication is inexpensive and testing using realistic adherend thicknesses is easy, this method is frequently used in the automotive industry and many others. Its widespread use, however, involves a large range of specimen configurations and resulting deformation modes that complicate the analysis and interpretation of results. The T-peel specimen deformations and test results strongly depend on the specific configuration and material properties, which influence the force required for debonding as well as the resulting shape the specimen assumes during testing. Furthermore, it is recognized that many T-peel specimens involve considerable plastic energy dissipation in the deforming adherends. For such cases, the fracture energy associated with breaking the adhesive layer is significantly less than the apparent peel energy or the work done by the applied load during the debonding process. Thus, without proper analysis and interpretation, typical results obtained from the T-peel tests, such as the “T-peel strength,” may only be useful for qualitative comparisons.

### *1.2.1 Brief review on previous analytical and numerical work on peel tests*

Several techniques for analyzing T-peel specimen test results have been proposed [38-52]. Kim et al. [39, 40] derived the moment-curvature relations for pure bending of elastic-plastic beams to calculate the plastic dissipation in the adherend, and related the experimentally measured peel force to the specific fracture energy using an energy balance. They showed that the measured peel strength could be two orders of magnitude higher than the actual fracture energy due to plastic energy dissipated for peeling thin ( $\sim 10 \mu\text{m}$  thick) Cu films. Kinloch et al. [41] proposed an energy balance approach to estimate the fracture toughness of an adhesive for fixed-arm and T-peel tests. They calculated the plastic bending energy by finding the work done by moments acting on the

peeling arms. The rotation at the root and the maximum curvature of the adherend were calculated based on the assumption of a beam on an elastic foundation. They developed a freely downloadable spreadsheet, ICPEEL [38], that assumes self-similar debonding defined below. However, this assumption does not apply to all T-peel tests as used by some institutions. It requires additional classifications such as the four categories of the pre- and post-test T-peel specimen configurations defined in Figure 1.3 and delineated in [53, 54]. These depend on whether or not self-similar debonding and plastic deformations occur in the adherends.

Figure 1.3 and Figure 1.4 schematically depict the specimen configurations prior to, during, and after testing for the four categories.

	Category I: Adherends deform elastically; self-similar debonding occurs	Category II: Adherends deform plastically; self-similar debonding occurs	Category III: Adherends deform plastically; self-similar debonding does not occur	Category IV: Adherends deform elastically; self-similar debonding does not occur
Before debonding				
During debonding				

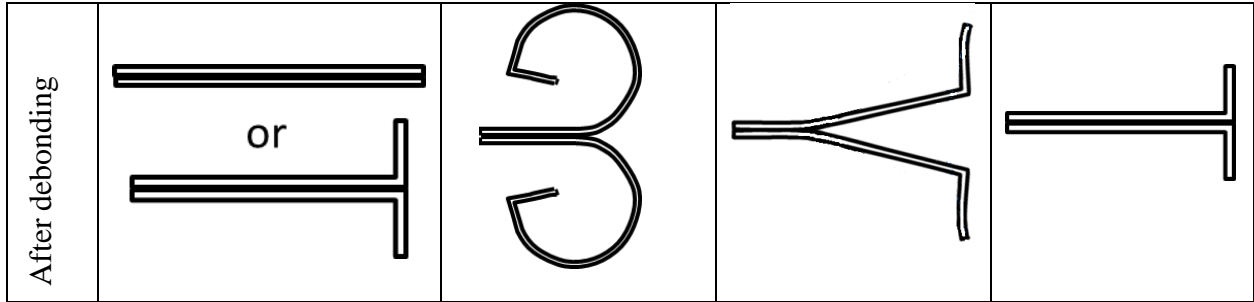


Figure 1.3. Illustration of the four categories of T-peel specimens, showing shapes before, during, and after debonding.

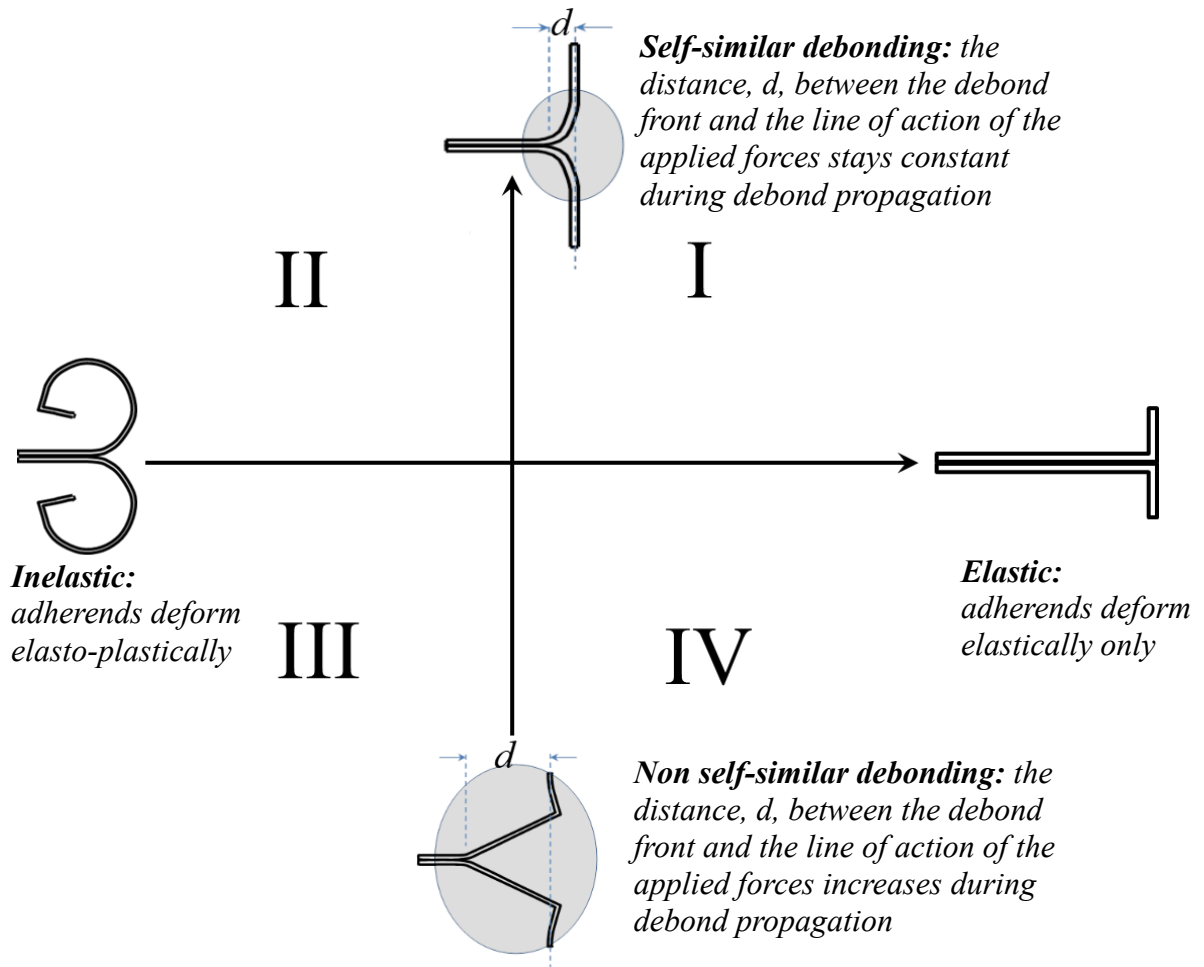


Figure 1.4. Four quadrants for the four categories; from left to right: inelastic to elastic, from bottom to top: non self-similar to self-similar debonding

There are several analytical approaches [39-41, 45, 46] available to extract the fracture energy from peel tests data involving adherends' plastic deformations. In this dissertation, we determine

the actual fracture energy associated with deforming and breaking the adhesive layer by using the finite element analysis (FEA) and the cohesive zone model (CZM), mainly because it involves fewer simplifying assumptions than the analytical methods, e.g., see [55-60]. Since steady state fracture propagation is not *a priori* assumed in the FEA, the response from initiation to non-self-similar debonding and the transition to self-similar debonding can be studied. Grant et al. [61] used the FEA to study stress and strain distributions for T-peel joints with short bond length by varying geometric parameters such as the bondline thickness and the adherend radius. They found the bending moment at failure to be constant for different geometries considered, and suggested using the maximum uniaxial stress as a failure criterion for T-peel joints with flush spew fillet. Yang et al. [60] and Alfano et al. [55] have employed the CZM to simulate fracture of T-peel specimens with short bond lengths and a relatively long pre-crack. Their computed peel force versus displacement curves compared well with experimental findings. They neither extracted the energy involved in deforming the adherends nor observed self-similar debonding, possibly because of the short bond length employed. Besides the CZM, other methods such as node release [62] and element deletion [63] have been employed to simulate crack initiation and propagation for T-peel specimens. Hadavinia et al. [62] modeled crack initiation in the adhesive layer by using a “critical plastic strain fracture criterion” in their FEA of elastic-plastic peel tests and crack propagation by the node release technique. They found good agreement between the computed adhesive fracture energy and that determined by previously reported analytical and direct-measurement methods for tests involving self-similar debonding.

We recall the two standards used in industries to characterize strengths of the T-peel specimens. The ASTM D1876 [64] standard defines “T-peel strength” as the average force per unit bond width needed to propagate the debond over 127 mm length after the initial peak and at least 10 load readings taken at fixed increments of the crosshead motion. The ISO11339 [65] recommends disregarding the first 25 mm and the last 25 mm of the bond length, and find the average force for at least 100 mm of peeling by finding the best fit flat line to the data. Thus the minimum bond length needed for these standards is approximately 150 mm. However, specimens with a 75 mm bond length have been adopted by automotive companies as being generally equivalent [66, 67] to the long bond length ( $\geq 150$  mm). Here we explore concerns that using this shorter specimen may pose, despite industry preference for faster tests using less material.

### ***1.2.2 Objectives of this work***

The objectives of this work are:

- (1) Conduct the T-peel tests for the specimens with different adherend materials, bond lengths, and adherend thicknesses, all bonded with structural acrylic adhesives, and analyze the resulting configurations
- (2) Evaluate the T-peel tests results using several different metrics for reporting T-peel results
- (3) Develop finite element analysis models for simulating the process of T-peel testing to help interpret the experimental results, and validate the numerical results by comparing the computed permanently deformed shapes and reaction force versus displacement curves with the corresponding experimental ones
- (4) Numerically study the transition from non-self-similar debonding to self-similar debonding during the T-peel testing, extract the energy involved in deforming the adherend plastically from the total energy, and find the non-self-similar/self-similar ratio in the load-displacement curves for several bond length/adherend thickness ratios for aluminum specimens

### **1.3 Organization of the dissertation**

In Chapter 2, we develop the material subroutine for the fiber-reinforced rubberlike materials showing different responses in tension and compression. By assuming that a fiber-reinforced rubberlike material can be modeled as a homogeneous and transversely isotropic hyperelastic material with the fiber direction as the axis of transverse isotropy, we have proposed an expression for the strain energy density in terms of the five invariants of the right Cauchy-Green strain tensor. For compressible and incompressible materials, it involves five and four material constants, respectively. However, the hydrostatic pressure for incompressible materials is found from the solution of the boundary value problem, and is thus an independent variable along with the three displacement components. The material model represents different response for axial compression and axial tension along the fiber direction. The constitutive relation has been implemented in the commercial software, LS-DYNA as a user-defined subroutine. For three static boundary value

problems, results computed by using the subroutine have been found to agree well with those computed analytically. Full verification of the implementation of the subroutine requires similar comparisons for numerous boundary value problems. Also, predictions from the material model need to be compared with the test data to validate it and establish its range of applicability. When test data for different modes of deformation becomes available, the form of the strain energy density assumed here may need to be modified. However, the new form of the strain energy density can be similarly implemented in LS-DYNA.

In Chapter 3, for  $W$  of the FRRMs an expression that is a complete quadratic function of the five invariants is examined. Homogeneous deformations such as simple extension, simple shear, and biaxial loading are studied to delineate the mechanical behaviors of the FRRMs. Consistency with the infinitesimal theory requires terms linear in both the 4<sup>th</sup> and the 5<sup>th</sup> invariants,  $I_4$  and  $I_5$ , be included in the expression for  $W$ . A stability analysis of simple tensile/compressive deformations with the load along the fiber reveals the possibility of unequal lateral stretches triggered by the considering the  $(I_4 - 1)(I_1 - 3)$  term in  $W$ . Analytical solutions for inflation, extension and twist deformations caused by internal pressure, end torque, and axial force for a pressurized cylindrical laminate are derived using Ericksen's inverse method. Effects of fiber orientations on the mechanical deformations of a  $\pm\alpha$  angle-ply cylindrical tube are investigated. To numerically solve boundary-value problems, this material model is incorporated in the commercial software, LS-DYNA, as a user-defined subroutine. The implementation has been verified by ensuring that the computed solutions of a few boundary value problems agree well with either their analytical solutions or those available in the literature.

In Chapter 4, we discuss the experimental and numerical analysis for several T-peel testing configurations. In this study, the usefulness of this designation procedure is demonstrated for a series of tests on T-peel specimens prepared using several common steels and an aluminum alloy adherends bonded with two acrylic adhesives. Different adherend thicknesses and bond lengths were also included, and all specimens were tested using standard test procedures. Finite element analyses were used to aid in interpreting the results. The simulations qualitatively capture the permanent deformations of the adherends and quantitatively predict the main features of the load-displacement curves. In view of experimental results, the significant effects that properties such as adherend thickness, bond lengths, yield behavior, and adhesion levels have on the resulting

configurations T-peel indicate the need for caution in interpreting the T-peel results across various systems. Each category would require its own analysis and interpretation. Several metrics were evaluated based on the experimental test results, and comparisons revealed some concerns with current practices, e.g. for specimens that do not reach self-similar state during debonding, the energy metric rather than the T-peel strength more realistically describes the adhesion integrity. Correlations between the computed force plateau and the constant projected crack length are demonstrated from the FEA results, implying the force plateau can be used as the indicator for self-similar debonding. From the FEA results, the partitioning of the computed total energy into different components for several T-peel configurations (HDG, EGZ, and AI) indicate that most of the total energy supplied goes to permanently deforming the adherends rather than fracturing the debond. For specimens with the aluminum adherends, the FE simulations enable finding the non-self-similar/self-similar ratio in the load-displacement curves for several bond length/adherend thickness ratios, which providing insightful information for engineers in selecting appropriate specimen dimensions for extracting meaningful data. Conclusions and contributions of the dissertation are summarized in Chapter 5.

## References

1. Humphrey, J.D., *Cardiovascular Solid Mechanics*. 2002, New York: Springer.
2. Helnwein, P., Liu, C.H., Meschke, G. and Mang, H.A., *A New 3-D Finite Element Model for Fiber-Reinforced Rubber Composites—Application to Analysis of Automobile Tires*. *Finite Element Analysis and Design*, 1993. **14**: p. 1-16.
3. Mang, H.A. and Meschke, G., *Nonlinear Finite-Element Analysis of Reinforced and Prestressed Concrete Structures*. *Engineering Structures*, 1991. **13**(2): p. 211-226.
4. Meschke, G. and Helnwein, P., *Large-Strain 3d-Analysis of Fiber-Reinforced Composites Using Rebar Elements - Hyperelastic Formulations for Cords*. *Computational Mechanics*, 1994. **13**(4): p. 241-254.
5. ABAQUS, *ABAQUS Version 6.11 Documentation*. 2011.
6. Mori, T. and Tanaka, K., *Average Stress in Matrix and Average Elastic Energy of Materials with Misfitting Inclusions*. *Acta Metallurgica*, 1973. **21**(5): p. 571-574.
7. R. C. Batra, G. Gopinath and J. Q. Zheng, *Damage and Failure in Low Energy Impact of Fiber-Reinforced Polymeric Composite Laminates*, *Composite Structures*, 2012. 94: p.540-547
8. Ogden, R.W., *Extremum Principles in Nonlinear Elasticity and Their Application to Composites .1. Theory*. *International Journal of Solids and Structures*, 1978. **14**(4): p. 265-282.

9. Castaneda, P.P., *The Overall Constitutive Behavior of Nonlinearly Elastic Composites*. Proceedings of the Royal Society of London Series a-Mathematical and Physical Sciences, 1989. **422**(1862): p. 147-171.
10. Fung, Y.C., Fronek, K. and Patitucci, P., *Pseudoelasticity of Arteries and the Choice of Its Mathematical Expression*. American Journal of Physiology, 1979. **237**(5): p. H620-H631.
11. Chuong, C.J. and Fung, Y.C., *3-Dimensional Stress-Distribution in Arteries*. Journal of Biomechanical Engineering-Transactions of the Asme, 1983. **105**(3): p. 268-274.
12. Ericksen, J.L. and Rivlin, R.S., *Large Elastic Deformations of Homogeneous Anisotropic Materials*. Journal of Rational Mechanics and Analysis, 1954. **3**(3): p. 281-301.
13. Pipkin, A.C., *Stress Analysis for Fiber-Reinforced Materials*. Advances in Applied Mechanics, 1979. **19**.
14. Spencer, A.J.M., *Constitutive Theory of Strongly Anisotropic Solids*. Continuum Theory of the Mechanics of Fiber-Reinforced Composites, ed. Spencer A.J.M. 1984, Vienna: Springer.
15. Weiss, J.A., Maker, B.N. and Govindjee, S., *Finite Element Implementation of Incompressible, Transversely Isotropic Hyperelasticity*. Computer Methods in Applied Mechanics and Engineering, 1996. **135**(1-2): p. 107-128.
16. Holzapfel, G.A. and Ogden, R.W., *Constitutive Modelling of Arteries*. Proceedings of the Royal Society a-Mathematical Physical and Engineering Sciences, 2010. **466**(2118): p. 1551-1596.
17. Batra, R.C., *Universal Relations for Transversely Isotropic Elastic Materials*. Mathematics and Mechanics of Solids, 2002. **7**(4): p. 421-437.
18. deBotton, G., Hariton, I. and Socolsky, E.A., *Neo-Hookean Fiber-Reinforced Composites in Finite Elasticity*. Journal of the Mechanics and Physics of Solids, 2006. **54**(3): p. 533-559.
19. Gasser, T.C., Ogden, R.W. and Holzapfel, G.A., *Hyperelastic Modelling of Arterial Layers with Distributed Collagen Fibre Orientations*. Journal of the Royal Society Interface, 2006. **3**(6): p. 15-35.
20. Guo, Z.Y., Peng, X.Q. and Moran, B., *A Composites-Based Hyperelastic Constitutive Model for Soft Tissue with Application to the Human Annulus Fibrosus*. Journal of the Mechanics and Physics of Solids, 2006. **54**(9): p. 1952-1971.
21. HOLZAPFEL, G.A., GASSER, T.C. and Ogden, R.W., *A New Constitutive Framework for Arterial Wall Mechanics and a Comparative Study of Material Models*. Journal of Elasticity, 2000. **61**: p. 1-48.
22. Merodio, J. and Ogden, R.W., *Mechanical Response of Fiber-Reinforced Incompressible Non-Linearly Elastic Solids*. International Journal of Non-Linear Mechanics, 2005. **40**(2-3): p. 213-227.
23. Peng, X.Q., Guo, Z.Y. and Moran, B., *An Anisotropic Hyperelastic Constitutive Model with Fiber-Matrix Shear Interaction for the Human Annulus Fibrosus*. Journal of Applied Mechanics-Transactions of the Asme, 2006. **73**(5): p. 815-824.
24. Murphy, J.G., *Transversely Isotropic Biological, Soft Tissue Must Be Modelled Using Both Anisotropic Invariants*. European Journal of Mechanics a-Solids, 2013. **42**: p. 90-96.
25. Zheng, Q.S., *On Transversely Isotropic, Orthotropic and Relative Isotropic Functions of Symmetrical Tensors, Skew-Symmetrical Tensors and Vectors .2. The Representations for*

- 3-Dimensional Transversely Isotropic Functions (Vol 31, Pg 1411, 1993)*. International Journal of Engineering Science, 1994. **32**(4): p. 719-719.
26. Rivlin, R.S., *Large Elastic Deformations of Isotropic Materials .4. Further Developments of the General Theory*. Philosophical Transactions of the Royal Society of London Series a-Mathematical and Physical Sciences, 1948. **241**(835): p. 379-397.
  27. Rivlin, R.S., *Large Elastic Deformations of Isotropic Materials .1. Fundamental Concepts*. Philosophical Transactions of the Royal Society of London Series a-Mathematical and Physical Sciences, 1948. **240**(822): p. 459-508.
  28. Demirkoparan, H. and Pence, T.J., *Magic Angles for Fiber Reinforcement in Rubber-Elastic Tubes Subject to Pressure and Swelling*. International Journal of Non-Linear Mechanics, 2015. **68**: p. 87-95.
  29. Batra, R.C., *Elements of Continuum Mechanics*. 2006: AIAA Publishers.
  30. Batra, R.C. and Bahrami, A., *Inflation and Eversion of Functionally Graded Non-Linear elastic Incompressible Circular Cylinders* International Journal of Non-Linear Mechanics, 2009. **44**: p. 311-323.
  31. Spencer, A.J.M., Rogers, T.G. and Moss, R.L., *An Optimal Angle of Winding for Pressurized Fibre-Reinforced Cylinders* Mechanics Research Communications, 1974. **1**: p. 27-32.
  32. Hamdaoui, M.E., Merodio, J., Ogden, R.W. and Rodríguez, J., *Finite Elastic Deformations of Transversely Isotropic Circular Cylindrical Tubes*. International Journal of Solids and Structures, 2014. **51**(5): p. 1188-1196.
  33. Horny, L., Netušil, M. and Horak, Z., *Limit Point Instability in Pressurization of Anisotropic Finitely Extensible Hyperelastic Thin-Walled Tube*. International Journal of Non-Linear Mechanics, 2015. **77**: p. 107-114.
  34. Kanner, L.M. and Horgan, C.O., *Elastic Instabilities for Strain-Stiffening Rubber-Like Spherical and Cylindrical Thin Shells under Inflation*. International Journal of Non-Linear Mechanics, 2007. **42**(2): p. 204-215.
  35. Gent, A.N., *Elastic Instabilities in Rubber*. International Journal of Non-Linear Mechanics, 2005. **40**(2-3): p. 165-175.
  36. Mangan, R. and Destrade, M., *Gent Models for the Inflation of Spherical Balloons*. International Journal of Non-Linear Mechanics, 2015. **68**: p. 52-58.
  37. Müller, I. and Strehlow, P., *Rubber and Rubber Balloons*. Lecture Notes in Physics. Vol. 637. 2004: Springer.
  38. Georgiou, I., Hadavinia, H., Ivankovic, A., Kinloch, A.J., Tropsa, V. and Williams, J.G., *Cohesive Zone Models and the Plastically Deforming Peel Test*. Journal of Adhesion, 2003. **79**(3): p. 239-265.
  39. Kim, K.S. and Aravas, N., *Elastoplastic Analysis of the Peel Test*. International Journal of Solids and Structures, 1988. **24**(4): p. 417-435.
  40. Kim, K.S. and Kim, J., *Elasto-Plastic Analysis of the Peel Test for Thin-Film Adhesion*. Journal of Engineering Materials and Technology-Transactions of the Asme, 1988. **110**(3): p. 266-273.
  41. Kinloch, A.J., Lau, C.C. and Williams, J.G., *The Peeling of Flexible Laminates*. International Journal of Fracture, 1994. **66**(1): p. 45-70.
  42. Kinloch, A.J. and Williams, J.G., *The Mechanics of Peel Tests*. The Mechanics of Adhesion, ed. Pocius A.V. and D.A. Dillard. 2002: Elsevier: Amsterdam.

43. Kinloch, A.J. and Williams, J.G., *The Mechanics of Peel Tests*, in *The Mechanics of Adhesion*, Dillard D.A. and A.V. Pocius, Editors. 2002, Elsevier: Amsterdam. p. 273-302.
44. Lindley, P.B., *Ozone Attack at a Rubber- Metal Bond*. Journal of the Institution of the Rubber Industry, 1971. **5**(6): p. 243-248.
45. Moidu, A.K., Sinclair, A.N. and Spelt, J.K., *Analysis of the Peel Test - Prediction of Adherend Plastic Dissipation and Extraction of Fracture Energy in Metal-to-Metal Adhesive Joints*. Journal of Testing and Evaluation, 1995. **23**(4): p. 241-253.
46. Moidu, A.K., Sinclair, A.N. and Spelt, J.K., *On the Determination of Fracture Energy Using the Peel Test*. Journal of Testing and Evaluation, 1998. **26**(3): p. 247-254.
47. Spies, G.J., *The Peeling Test on Redux - Bonded Joints*. Aircraft Engineering and Aerospace Technology, 1953. **25**(3): p. 64-70.
48. Spies, G.J., *The Peeling Test on Redux-Bonded Joints: A Theoretical Analysis of the Test Devised by Aero Research Limited*. Aircraft Engineering and Aerospace Technology, 1953. **25**(3): p. 64 - 70.
49. Thouless, M.D., Adams, J.L., Kafkalidis, M.S., Ward, S.M., Dickie, R.A. and Westerbeek, G.L., *Determining the Toughness of Plastically Deforming Joints*. Journal of Materials Science, 1998. **33**(1): p. 189-197.
50. Thouless, M.D. and Jensen, H.M., *Elastic Fracture-Mechanics of the Peel-Test Geometry*. Journal of Adhesion, 1992. **38**(3-4): p. 185-197.
51. Williams, J.G., *Root Rotation and Plastic Work Effects in the Peel Test*. Journal of Adhesion, 1993. **41**(1-4): p. 225-239.
52. Williams, J.G., *Energy Release Rates for the Peeling of Flexible Membranes and the Analysis of Blister Tests*. International Journal of Fracture, 1997. **87**(Copyright 1998, IEE): p. 265-88.
53. Dillard, D.A., *The T-Peel Test*. Testing Adhesive Joints: Best Practices,, ed. al. L.F.M.d.S.e. 2012: Wiley-VCH: Weinheim.
54. Dillard, D.A., Li, Q., Batra, R.C. and Graham, I. *Interpreting T-Peel Test Results in Light of Four Different Specimen Configuration Categories*. in *36th Annual Meeting of the Adhesion Society*. 2013. Daytona Beach.
55. Alfano, M., Furguele, F., Lubineau, G. and Paulino, G.H., *Simulation of Debonding in Al/Epoxy T-Peel Joints Using a Potential-Based Cohesive Zone Model*. Procedia Engineering, 2011. **10**: p. 1760-1765.
56. Needleman, A., *A Continuum Model for Void Nucleation by Inclusion Debonding*. Journal of Applied Mechanics-Transactions of the Asme, 1987. **54**(3): p. 525-531.
57. Needleman, A., *Numerical Modeling of Crack Growth under Dynamic Loading Conditions*. Computational Mechanics, 1997. **19**(6): p. 463-469.
58. Tvergaard, V. and Hutchinson, J.W., *The Relation between Crack-Growth Resistance and Fracture Process Parameters in Elastic Plastic Solids*. Journal of the Mechanics and Physics of Solids, 1992. **40**(6): p. 1377-1397.
59. Wei, Y. and Hutchinson, J.W., *Interface Strength, Work of Adhesion and Plasticity in the Peel Test*. International Journal of Fracture, 1998. **93**(1-4): p. 315-333.
60. Yang, Q.D., Thouless, M.D. and Ward, S.M., *Numerical Simulations of Adhesively-Bonded Beams Failing with Extensive Plastic Deformation*. Journal of the Mechanics and Physics of Solids, 1999. **47**(6): p. 1337-1353.

61. Grant, L.D.R., Adams, R.D. and da Silva, L.F.M., *Experimental and Numerical Analysis of T-Peel Joints for the Automotive Industry*. Journal of Adhesion Science and Technology, 2009. **23**(2): p. 317-338.
62. Hadavinia, H., Kawashita, L., Kinloch, A.J., Moore, D.R. and Williams, J.G., *A Numerical Analysis of the Elastic-Plastic Peel Test*. Engineering Fracture Mechanics, 2006. **73**(16): p. 2324-2335.
63. Yang, X., Xia, Y., Zhou, Q., Wang, P.C. and Wang, K., *Modeling of High Strength Steel Joints Bonded with Toughened Adhesive for Vehicle Crash Simulations*. International Journal of Adhesion and Adhesives, 2012. **39**: p. 21-32.
64. ASTM-D1876, *Peel Resistance for Adhesives, T-Peel Test* American Society for Testing and Materials: West Conshohocken, PA.
65. ISO-11339, *T-Peel Test Flexible to Flexible Bonded Assemblies*.
66. Chrysler, *Ms-Cd507: Structural Adhesive – Two Component – Room Temperature Cure – Metal Bonding Applications*.
67. Technologies, F.G., *Wss-M2g410-A2: Aftermarket Adhesive, Weldable, Rivetable, Air Dry, Structural, Aluminum*. 2002.

## Chapter 2: Constitutive Relation for Large Deformations of Fiber-reinforced Rubberlike Materials with Different Response in Tension and Compression

The contents of this chapter have appeared in *Tire Science and Technology*, 44, 51-72, 2016.

### Abstract

Fiber-reinforced rubberlike materials commonly used in tires undergo large deformations, and exhibit different response in tension and compression along the fiber direction. Assuming that the response of a fiber-reinforced rubberlike material can be modeled as transversely isotropic with the fiber direction as the axis of transverse isotropy, we express the stored energy function in terms of the five invariants of the right Cauchy-Green strain tensor and account for different response in tension and compression along the fiber direction. The constitutive relation accounts for both material and geometric nonlinearities, and incorporates effects of the 5<sup>th</sup> strain invariant,  $I_5$ . It has been shown by Merodio and Ogden that in shear dominated deformations,  $I_5$  makes a significant contribution to the stress-strain curve. We have implemented the proposed constitutive relation in the commercial software, LS-DYNA. The numerical solutions of a few boundary value problems studied here agree with their analytical solutions derived by using Ericksen's inverse approach in which part of the solution is assumed and unknowns in the presumed solution are found by analyzing the pertinent boundary value problem. However, computed results have not been compared with experimental findings. When test data becomes available, one can modify the form of the strain energy density and replace the proposed constitutive relation by the new one in LS-DYNA.

**Key words:** fiber-reinforced rubberlike material model, user-defined subroutine, finite plane strain bending, different response in tension and compression

### 2.1 Introduction

Fiber-reinforced rubberlike materials exhibit high specific strength and stiffness in the fiber direction that can be exploited to reduce weight and cost, and simultaneously increase durability of components (e.g., tires, belts, seals, and impact absorbing cushions) made of such materials. The rubberlike matrix, with low strength and stiffness but large values of failure strain, maintains

fibers in their relative positions, thereby providing desirable mechanical properties. Optimal design of these composites (e.g., fiber volume fraction, fiber orientation, fiber/matrix bonding, matrix material) requires the development of efficient, robust and reliable numerical techniques to accurately predict the system level response of structures made of these materials to applied loads, since experimentally designing and characterizing them is time consuming and very expensive.

The often used numerical technique to analyze large deformations of engineering structures is the finite element method (FEM). For example, Batra [1] modeled rubber as a Mooney-Rivlin material and used the FEM to analyze finite plane strain deformations of a rubber-covered roll contacting a rigid roll. This work was subsequently generalized to large deformations of viscoelastic roll covers by Bapat and Batra [2].

Several commercial software packages (e.g., ABAQUS, ANSYS, and LS-DYNA) based on FE technology are regularly used in the tire industry. However, simulating large deformations of anisotropic materials that exhibit different response in tension and compression along the fiber direction is quite challenging and FE algorithms for large deformations of these materials have not been implemented in many commercial codes. Experimentally validated and thermodynamically consistent constitutive relations are needed for accurately modeling the response of such systems.

Tires for transportation vehicles such as cars, trucks, buses and tractors are usually made of fiber-reinforced rubberlike materials that are anisotropic, inhomogeneous, viscoelastic, and nearly incompressible. As is well known, modeling separately each constituent of the composite in a real size structure is computationally quite expensive since the ratio of the moduli of the fiber to that of the matrix is very large, necessitating an extremely fine FE mesh near the fiber/matrix interface. A rebar element method developed and successfully applied to study infinitesimal deformations of reinforced concrete structures has been extended to study finite deformations of fiber-reinforced rubberlike materials [3, 4]. In this method, either one or several planar fiber layers are embedded in a host 3-dimensional, 8-node element made of a rubberlike material. The fiber layer is usually modeled as a 4-node membrane. The displacements of the four nodes are derived from the displacements of the eight nodes of the parent element. Thus no additional degrees of freedom are introduced, and the computational cost is kept reasonable. However, the rebar element has had limited success for moderately large strains [5]. In the rebar layer model implemented in ABAQUS

[6], the fiber is assumed to be loaded in the axial direction, and the fiber material is assumed to be incompressible and hyperelastic.

The current state of the art is to replace the inhomogeneous material by an equivalent homogeneous material whose mechanical properties depend upon the volume fractions and the mechanical properties of the constituents, and analyze the same system level problem with the homogenized material. This approach provides useful information at a reasonable computational cost, especially during the early stages of design. Results derived from the use of the equivalent homogeneous material should be compared with those from experiments to validate the mathematical model. Of course, the use of a homogenized material precludes consideration of stress singularities at the fiber/matrix interface, and near fiber ends. Thus the stress distribution in the homogenized material may be quite different from that in the inhomogeneous fiber-reinforced material.

For small deformations homogenization techniques include the rule of mixtures, the equivalent energy principle, and the Mori-Tanaka scheme. Batra et al. [7], among others, have compared results of different homogenization techniques. However, for large deformations of hyperelastic materials such as fiber-reinforced rubberlike materials, it is difficult to obtain closed form expressions for the effective properties of the composites due to both material and geometric nonlinearities.

Numerous phenomenological constitutive models have been proposed for fiber-reinforced rubberlike materials that describe well some aspects of experimentally measured material response [8-17]. Pipkin [8] analytically solved several boundary value problems for incompressible fiber-reinforced materials by assuming that the fibers are inextensible. As has been postulated in [9-17], we assume that a fiber-reinforced rubberlike material can be modeled as transversely isotropic and hyperelastic with the fiber direction as the axis of transverse isotropy. Using the concepts of material objectivity and material symmetry, Ericksen and Rivlin [18] showed that the strain energy density for these materials is at most a function of five invariants of the strain tensor. Batra [19] derived universal relations for these materials that enable one to check if the material being studied is transversely isotropic.

A challenge is to find an explicit expression for the strain energy density in terms of the five invariants. We recall that the reinforcing fibers generally exhibit different response in tension and compression. Motivated by the success of the Mooney-Rivlin form of the strain energy density for isotropic incompressible rubberlike materials and the works of Pipkin [8], Qiu and Pence [10], and Merodio and Ogden [11], we postulate an expression for the strain energy density in terms of the five invariants of the strain tensor that exhibits different response in tension and compression. For incompressible fiber-reinforced materials, we analytically analyze two homogeneous deformations, namely, the uniaxial tension/compression and simple shear. These illustrate different responses in tension and compression, and the effect of including the 5<sup>th</sup> strain invariant in the constitutive relation. We then study the finite plane strain bending deformations of a rectangular beam into a circular arc for which deformations are inhomogeneous. This problem is a member of Ericksen's family of controllable deformations that can be produced in every isotropic, homogeneous and incompressible body by only applying surface tractions to the bounding surfaces. Since the beam material is transversely isotropic, Ericksen's theorem is not applicable to this problem. It is shown that the problem can be analytically solved only when fibers are either along the beam axis or along the beam thickness direction. These analytical solutions are compared with the numerical results computed by using LS-DYNA in which this material model has been implemented as a user-defined subroutine. The two sets of results are found to agree well with each other, thereby lending credibility to the implementation of the material model in the subroutine. In order to fully verify the implementation of the subroutine, several initial-boundary-value problems need to be analyzed and their numerical solutions compared with the analytical solutions. One could potentially use the method of manufactured solutions (e.g., see the material just preceding and immediately following Eq. (20) of Batra and Liang [20] ; details of the method are better described in Section 3.2 of Love and Batra [21]) to verify the implementation of the material model in the software. The identification of material parameters in the proposed constitutive relation and their evaluation from test data will be addressed in a future work.

## **2.2 Constitutive relations for fiber-reinforced rubberlike materials**

We assume that a fiber-reinforced rubberlike material can be modeled as a homogeneous, transversely isotropic and hyperelastic with the fiber direction as the axis of transverse isotropy. We use the theory of mixtures (e.g., see Bowen [22] ) in which it is assumed that a spatial point is

simultaneously occupied by all constituents of a body and they experience the same deformation gradient. The strain energy density at a point equals the sum of the strain energy densities of the constituents occupying that point weighted by their volume fractions. Following the work of Ericksen and Rivlin [18], we express the stored energy density per unit volume in the reference configuration,  $W$ , in term of the five invariants of the right Cauchy-Green strain tensor  $\mathbf{C}$ . That is

$$W = W(I_1, I_2, I_3, I_4, I_5) \quad (2.1)$$

where

$$I_1 = \text{tr}\mathbf{C}, I_2 = \frac{1}{2} \left[ (\text{tr}\mathbf{C})^2 - \text{tr}\mathbf{C}^2 \right], I_3 = \det \mathbf{C}$$

$$I_4 = \mathbf{A}_0 \cdot \mathbf{C} \mathbf{A}_0, I_5 = \mathbf{A}_0 \cdot \mathbf{C}^2 \mathbf{A}_0 \quad (2.2)$$

In equations (2.1) and (2.2),  $\mathbf{C} = \mathbf{F}^T \mathbf{F}$ ,  $\mathbf{F} = \partial \mathbf{x} / \partial \mathbf{X}$  is the deformation gradient, and  $\mathbf{x}$  the position vector in the current or the deformed configuration, with respect to rectangular Cartesian coordinates, of a material point that occupied the place  $\mathbf{X}$  in the undeformed or the reference configuration. Furthermore,  $\mathbf{A}_0$  is a unit vector along the fiber in the reference configuration,  $I_1, I_2, I_3, I_4$  and  $I_5$  are invariants of the right Cauchy-Green strain tensor for a transversely isotropic material with  $\mathbf{A}_0$  as the axis of transverse isotropy. The invariants  $I_4$  and  $I_5$  are related to the stretch along the fiber, and  $I_5$  also accounts for shearing deformations of the material [11].

For nearly incompressible materials,  $W$  is usually expressed as the sum of two terms, one for the volumetric and the other for the distortional deformations. That is,

$$W = U(J) + W(\bar{I}_1, \bar{I}_2, \bar{I}_4, \bar{I}_5) \quad (2.3)$$

where  $J = \det[\mathbf{F}] = I_3^{1/2}$  is the ratio of the volume of a material element in the current configuration to that in the reference configuration, and

$$\bar{I}_1 = J^{-2/3} I_1, \bar{I}_2 = J^{-4/3} I_2, \bar{I}_4 = J^{-2/3} I_4, \bar{I}_5 = J^{-4/3} I_5 \quad (2.4)$$

The deformation gradient  $\mathbf{F}$  can be written as the product of two matrices [23]

$$\mathbf{F} = \mathbf{F}_{vol} \bar{\mathbf{F}}, \mathbf{F}_{vol} = J^{1/3} \mathbf{I}, \bar{\mathbf{F}} = J^{-1/3} \mathbf{F} \quad (2.5)$$

where  $\mathbf{I}$  is the identity matrix. We note that

$$\det[\mathbf{F}_{vol}] = J, \det[\bar{\mathbf{F}}] = 1 \quad (2.6)$$

Thus  $\mathbf{F}_{vol}$  measures changes in volume, and  $\bar{\mathbf{F}}$  measures distortional deformations. Similarly, the right and the left Cauchy-Green tensor  $\mathbf{C}$  and  $\mathbf{B}$ , respectively, can be written as

$$\mathbf{C} = \mathbf{F}^T \mathbf{F} = J^{2/3} \bar{\mathbf{C}}, \mathbf{B} = \mathbf{F} \mathbf{F}^T = J^{2/3} \bar{\mathbf{B}} \quad (2.7)$$

For an incompressible material,  $J = 1$ , and  $\bar{I}_1, \bar{I}_2, \bar{I}_4$  and  $\bar{I}_5$  equal, respectively,  $I_1, I_2, I_4$  and  $I_5$ .

In order to find the explicit form of  $W$  for the material of interest, one needs test data from numerous experiments in which one of the invariants is varied and the remaining invariants are kept constant. In the absence of such data, one either expands  $W$  in terms of a finite Taylor series or postulates an expression for it that has a few material parameters. The Mooney and the Mooney-Rivlin material models can be regarded as examples of  $W$  expanded in finite Taylor series with one and two material constants, respectively. We note that Mooney derived the expression for  $W$  by using the kinetic theory of rubber [24]. Here we assume a simple expression for  $W$  with the understanding that if predictions from it do not agree well with the test data then the expression can be modified.

For incompressible and nearly incompressible fiber-reinforced rubberlike materials we postulate, respectively, equations (2.8) and (2.9) for  $W$ .

$$W = \begin{cases} (1-V_f)[C_1(I_1-3)+C_2(I_2-3)], & I_4 < 1 \\ (1-V_f)[C_1(I_1-3)+C_2(I_2-3)]+V_f[\gamma_4(I_4-1)^2+\gamma_5(I_5-1)^2], & I_4 \geq 1 \end{cases} \quad (2.8)$$

$$W = \begin{cases} \frac{K}{2} \left( \frac{J^2 - 1}{2} - \ln J \right) + (1 - V_f) [C_1 (\bar{I}_1 - 3) + C_2 (\bar{I}_2 - 3)], & \bar{I}_4 < 1 \\ \frac{K}{2} \left( \frac{J^2 - 1}{2} - \ln J \right) + (1 - V_f) [C_1 (\bar{I}_1 - 3) + C_2 (\bar{I}_2 - 3)] + V_f [\gamma_4 (\bar{I}_4 - 1)^2 + \gamma_5 (\bar{I}_5 - 1)^2], & \bar{I}_4 \geq 1 \end{cases} \quad (2.9)$$

Here  $V_f$  equals the volume fraction of fibers and  $C_1$ ,  $C_2$ ,  $K$ ,  $\gamma_4$  and  $\gamma_5$  are material constants whose values are to be determined from test data. Expressions (2.8) and (2.9) imply that the axial compression of fibers does not contribute to the strain energy density. Thus the problem of finding  $W$  has been reduced to that of ascertaining values of material constants. The material parameter  $K$  is usually called the bulk modulus, and is assigned a value much larger than that of the other four material parameters.

Recalling (e.g., see Batra [23] and Truesdell and Noll [25]) that the 2<sup>nd</sup> Piola-Kirchhoff stress tensor  $\mathbf{S}$  is related to the strain energy density function  $W$  by

$$\mathbf{S} = 2 \frac{\partial W}{\partial \mathbf{C}} \quad (2.10)$$

and the Cauchy stress tensor  $\boldsymbol{\sigma}$  to  $\mathbf{S}$  by

$$\boldsymbol{\sigma} = J^{-1} \mathbf{F} \mathbf{S} \mathbf{F}^T \quad (2.11)$$

we get expressions (2.12) and (2.13), respectively, for incompressible and nearly incompressible materials.

$$\begin{aligned} \boldsymbol{\sigma} = & -p \mathbf{I} + 2(1 - V_f) [C_1 \mathbf{B} + C_2 (I_1 \mathbf{B} - \mathbf{B}^2)] \\ & + 4V_f H (I_4 - 1) [\gamma_4 (I_4 - 1) \mathbf{a} \otimes \mathbf{a} + \gamma_5 (I_5 - 1) (\mathbf{a} \otimes \mathbf{B} \cdot \mathbf{a} + \mathbf{B} \cdot \mathbf{a} \otimes \mathbf{a})] \end{aligned} \quad (2.12)$$

$$\begin{aligned} J \boldsymbol{\sigma} = & \frac{K}{2} (J^2 - 1) \mathbf{I} + 2(1 - V_f) \left[ C_1 \left( \bar{\mathbf{B}} - \frac{1}{3} \bar{I}_1 \mathbf{I} \right) + C_2 \left( \bar{I}_1 \bar{\mathbf{B}} - \bar{\mathbf{B}}^2 - \frac{2}{3} \bar{I}_2 \mathbf{I} \right) \right] \\ & + 4V_f H (\bar{I}_4 - 1) \left[ \gamma_4 (\bar{I}_4 - 1) \left( \bar{\mathbf{a}} \otimes \bar{\mathbf{a}} - \frac{1}{3} \bar{I}_4 \mathbf{I} \right) + \gamma_5 (\bar{I}_5 - 1) \left( \bar{\mathbf{a}} \otimes \bar{\mathbf{B}} \cdot \bar{\mathbf{a}} + \bar{\mathbf{B}} \cdot \bar{\mathbf{a}} \otimes \bar{\mathbf{a}} - \frac{2}{3} \bar{I}_5 \mathbf{I} \right) \right] \end{aligned} \quad (2.13)$$

Here  $H$  is the Heaviside function,  $\mathbf{a} \otimes \mathbf{b}$  denotes the tensor product between vectors  $\mathbf{a}$  and  $\mathbf{b}$ ,  $\mathbf{a}$  and  $\bar{\mathbf{a}}$  are unit vectors along the vector  $\mathbf{FA}_0$ , and the hydrostatic pressure  $p$  is not determined from the deformation gradient but is found by solving the pertinent initial boundary value problem, provided that normal tractions are prescribed on a part of the boundary. Thus for an incompressible material one needs to find three components of displacement and the hydrostatic pressure whereas for a compressible material only three displacement components need to be determined. For axial compression along the fibers, the term multiplying  $V_f$  does not contribute to the Cauchy stress, resulting in a discontinuous slope at zero strain of the axial stress – axial strain curve for uniaxial deformations along the fiber. Thus the speed of longitudinal waves along the fiber direction will depend upon whether fibers are being compressed or stretched. Modifications of the constitutive relation to overcome this are being considered.

We note that most FE-based commercial solvers do not regard the hydrostatic pressure in incompressible materials as an independent variable, assume the material to be nearly incompressible, and approximate incompressibility by assigning a very large value to the bulk modulus that serves as a penalty parameter. Batra [1], amongst others, used a mixed formulation in which the pressure field is taken as an independent variable.

### **2.3 Implementation of the material model in LS-DYNA**

The commercial software LS-DYNA [26] is based on the FE technology for analyzing transient deformations of structures made of different materials. We have implemented the material model described in Section 2.2 above as a user-defined subroutine, written in FORTRAN, that employs 8-node brick elements and the constitutive relations (2.12) and (2.13) to analyze finite deformations of fiber-reinforced rubberlike materials. In order to use the subroutine, one needs, besides the regular input parameters required to analyze a problem by the FEM, values of the volume fraction of fibers,  $V_f$ , components of the unit vector  $\mathbf{A}_0$  defining the fiber orientation in the reference configuration, and values of the material parameters appearing in the constitutive relation (2.13). The source code and user's guide are given in Appendix A, and the input file for uniaxial tensile loading of a cube along the fiber direction is given in Appendix B.

## 2.4 Verification of the implementation of the user-defined subroutine

We analytically and numerically study a few boundary value problems for fiber-reinforced materials and compare the two solutions to verify the subroutine developed and implemented in LS-DYNA. For the first two problems analyzed, namely, simple extension/compression and simple shear, deformations are homogeneous. Thus the deformation gradient  $\mathbf{F}$  and hence stresses are constants in a homogeneous body, and the balance of linear momentum with zero body and null inertia forces is trivially satisfied. This implies that a FE mesh with only one element should suffice to numerically analyze the problem. The third problem involves bending of a straight beam into a circular arc in which the deformation gradient  $\mathbf{F}$  varies throughout the body. This problem has been numerically studied with LS-DYNA using mass scaling, i.e., artificially reducing the mass density to increase the wave speed. The element matrices have been computed by using 1-point integration rule and Belytschko-Bindeman hourglass control [27]. While checking the energy balance, the kinetic energy and the hourglass mode energies have been found to be negligible ensuring that static problems have been studied and the total energy is conserved.

While analytically analyzing a boundary value problem, the material of the body is assumed to be incompressible. However, during the numerical solution of the same boundary value problem, the material is taken to be nearly incompressible since the FE technology implemented in LS-DYNA does not allow the assumption of perfect incompressibility. For sufficiently large values of  $K$ , the solution of the boundary value problem for nearly incompressible materials is very close to that for incompressible materials. We note that values of material parameters are not critical for verifying the implementation of the subroutine. Thus we have set  $\gamma_4 = \gamma_5 = 1000(C_1 + C_2)V_f$ ,  $C_1V_f = C_2V_f = 1 \text{ MPa}$  where the volume fraction of fibers  $V_f = 0.3$ . The bulk modulus,  $K$ , is assigned a very large value (e.g.,  $250,000 \gamma_4$ ) to mimic the nearly incompressible response of the homogenized material for simple extension/compression and simple shear deformations. However, for the plane strain bending problem analyzed the bulk modulus is set equal to  $150 \gamma_4$  since a larger value of  $K$  required more than 65 CPU hours on 12 processors. Thus the incompressibility condition for the bending problem is not well satisfied.

### 2.4.1 Simple extension of a cube

We study simple extensional deformations of a cube of edge length  $L$  with equal and opposite axial surface tractions applied on the surfaces  $x_1 = X_1 = 0$  and  $L$ , and fibers oriented along the vector  $A_0 = (\cos \alpha, \sin \alpha, 0)$ . That is, fibers are in the  $X_1 X_2$  - plane and are inclined at an angle  $\alpha$  to the  $X_1$  - axis, as depicted in Fig. 2.1. While numerically solving the problem, the body is deformed by setting  $u_1 = x_1 - X_1 = 0$  for nodes on the surface  $X_1 = 0$ ,  $u_2 = x_2 - X_2 = 0$  for nodes on the surface  $X_2 = 0$ ,  $u_3 = 0$  at one node on the surface  $X_1 = 0$ , and simultaneously prescribing uniform values of  $u_1$  and  $u_2$  on the surfaces  $X_1 = L$  and  $X_2 = L$ . The rigid body translation is eliminated by setting  $u_3 = 0$  at a node on the surface  $X_1 = 0$ . The nonlinear problem is solved by dividing all displacements into 100 equal parts and simultaneously incrementing every displacement component by 1%. The surfaces  $X_3 = \text{constant}$  are kept traction free.

Assuming that deformations are homogeneous, we can write the deformation field as

$$x_1 = \lambda_1 X_1; \quad x_2 = \lambda_2 X_2; \quad x_3 = \lambda_3 X_3 \quad (2.14)$$

where  $\lambda_1$ ,  $\lambda_2$  and  $\lambda_3$  are stretches along the  $X_1$ ,  $X_2$  and  $X_3$  coordinate axes, respectively. For the deformation (2.14) to be admissible in an incompressible material,  $\lambda_3 = \lambda_1^{-1} \lambda_2^{-1}$ . For the deformation field (2.14), the strain invariants have the following expressions:

$$\begin{aligned} I_1 &= \lambda_1^2 + \lambda_2^2 + \lambda_1^{-2} \lambda_2^{-2} \\ I_2 &= \lambda_1^{-2} + \lambda_2^{-2} + \lambda_1^2 \lambda_2^2 \\ I_3 &= 1 \\ I_4 &= (\cos \alpha)^2 \lambda_1^2 + (\sin \alpha)^2 \lambda_2^2 \\ I_5 &= (\cos \alpha)^2 \lambda_1^4 + (\sin \alpha)^2 \lambda_2^4 \end{aligned} \quad (2.15)$$

Substituting for  $I_1$ ,  $I_2$ ,  $I_4$  and  $I_5$  from Eqs. (2.14) - (2.15) into Eq. (2.12), we get the following expressions for components of the Cauchy stress tensor.

$$\begin{aligned}
\sigma_{11} &= -p + 2\lambda_1^2(1-V_f)\left[C_1 + C_2(\lambda_2^2 + \lambda_3^2)\right] \\
&+ 4\lambda_1^2V_fH(I_4-1)(\cos\alpha)^2\left[\gamma_4(I_4-1) + 2\gamma_5(I_5-1)\lambda_1^2\right] \\
\sigma_{22} &= -p + 2\lambda_2^2(1-V_f)\left[C_1 + C_2(\lambda_1^2 + \lambda_3^2)\right] \\
&+ 4\lambda_2^2V_fH(I_4-1)(\sin\alpha)^2\left[\gamma_4(I_4-1) + 2\gamma_5(I_5-1)\lambda_2^2\right] \\
\sigma_{33} &= -p + 2\lambda_3^2(1-V_f)\left[C_1 + C_2(\lambda_1^2 + \lambda_2^2)\right] \\
\sigma_{12} &= 2\lambda_1\lambda_2V_fH(I_4-1)\sin 2\alpha\left[\gamma_4(I_4-1) + \gamma_5(I_5-1)(\lambda_1^2 + \lambda_2^2)\right] \\
\sigma_{23} &= \sigma_{32} = \sigma_{31} = \sigma_{13} = 0
\end{aligned} \tag{2.16}$$

Equilibrium equations require that the hydrostatic pressure  $p$  be a constant. We assume that the normal traction on the lateral surfaces  $X_3 = 0$ ,  $L$  vanishes. Thus  $\sigma_{33} = 0$ , and

$$p = 2\lambda_3^2(1-V_f)\left[C_1 + C_2(\lambda_1^2 + \lambda_2^2)\right] \tag{2.17}$$

Substituting for  $p$  from Eq. (2.17) into Eq. (2.16)<sub>2</sub> and using the boundary condition  $\sigma_{22} = 0$  gives

$$\begin{aligned}
&2(1-V_f)(\lambda_2^2 - \lambda_1^{-2}\lambda_2^{-2})(C_1 + C_2\lambda_1^2) \\
&+ 4\lambda_2^2V_fH(I_4-1)(\sin\alpha)^2\left[\gamma_4(I_4-1) + 2\gamma_5(I_5-1)\lambda_2^2\right] = 0
\end{aligned} \tag{2.18}$$

Thus the non-zero components of the Cauchy stress are given by

$$\begin{aligned}
\sigma_{11} &= 2(1-V_f)(\lambda_1^2 - \lambda_1^{-2}\lambda_2^{-2})\left[C_1 + C_2\lambda_2^2\right] \\
&+ 4\lambda_1^2V_fH(I_4-1)(\cos\alpha)^2\left[\gamma_4(I_4-1) + 2\gamma_5(I_5-1)\lambda_1^2\right] \\
\sigma_{12} &= 2\lambda_1\lambda_2V_fH(I_4-1)\sin 2\alpha\left[\gamma_4(I_4-1) + \gamma_5(I_5-1)(\lambda_1^2 + \lambda_2^2)\right]
\end{aligned} \tag{2.19}$$

with the value of  $\lambda_2$  expressed as a function of  $\lambda_1$  by solving Eq. (2.18).

Except for  $\alpha = 0^\circ$  and  $\alpha = 90^\circ$ , besides the axial stress  $\sigma_{11}$  one must also apply tangential tractions  $\sigma_{12}$  on the bounding surfaces  $x_1 = \text{constant}$  and  $x_2 = \text{constant}$  to produce simple extensional deformations in a fiber-reinforced rubberlike material. The magnitude of surface tractions also depends upon  $I_4$  and  $I_5$ .

Because of the difficulty in applying deformation dependent surface tractions in LS-DYNA, while numerically solving the problem we gradually increased the above mentioned applied displacements on surfaces  $X_1 = L$  and  $X_2 = L$  of the block while keeping surfaces  $X_3 = 0, L$  traction free.

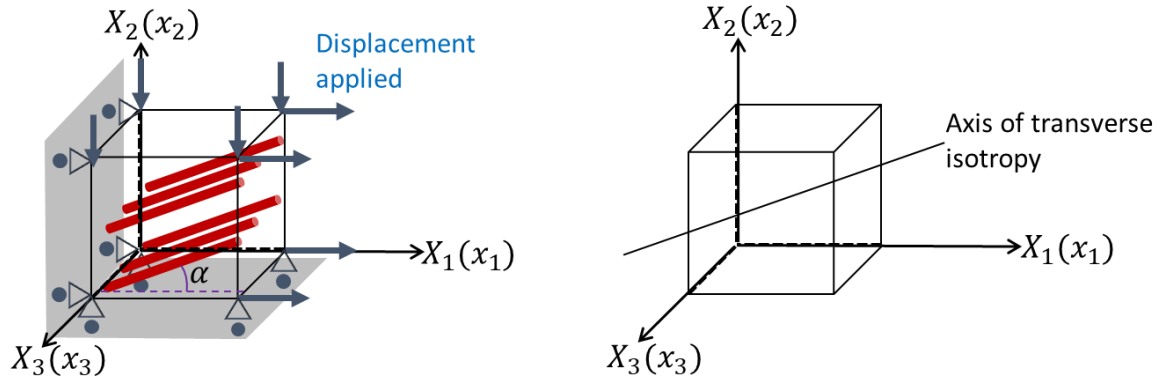
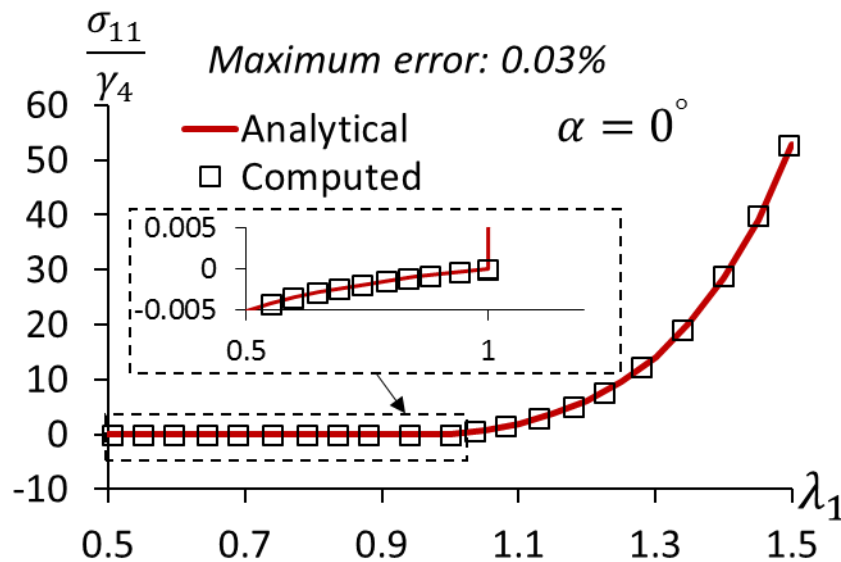
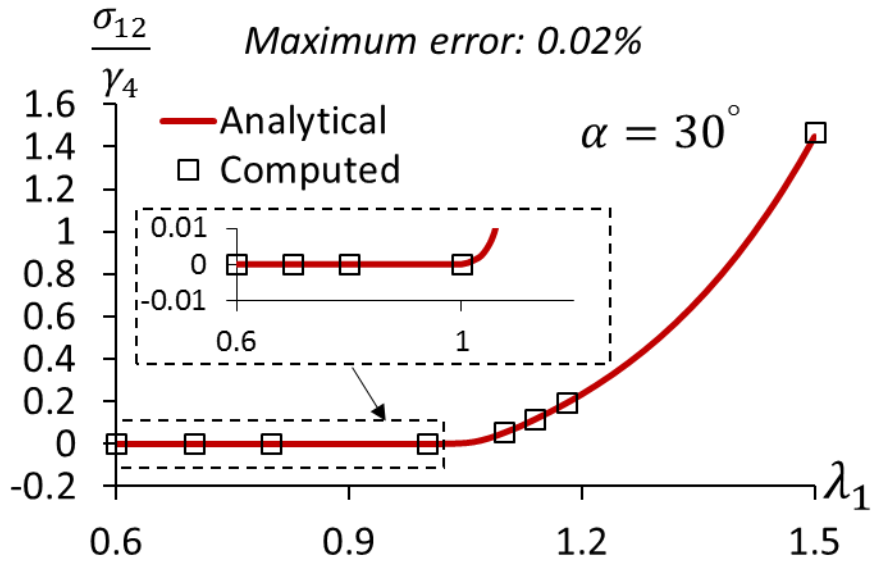
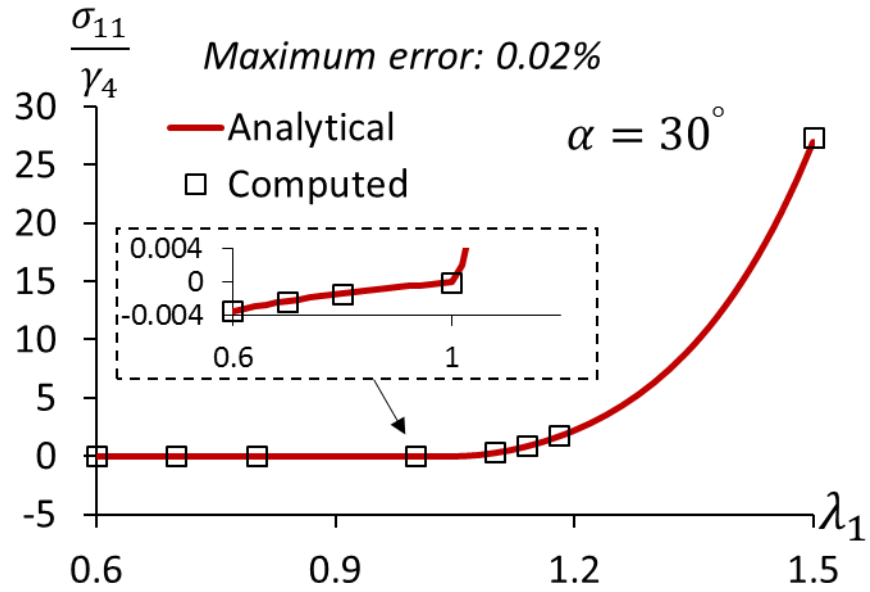


Figure 2.1. Schematic sketch of the simple extension of a cube made of a fiber-reinforced rubberlike material with fibers inclined at angle  $\alpha$  to the  $X_1X_3$ -plane; (left) fiber-reinforced body, (right) equivalent homogenized transversely isotropic body

For  $\alpha = 0^\circ, 30^\circ$  and  $90^\circ$ , the computed axial stress-axial stretch curves are compared in Fig. 2.2 with the corresponding analytical ones. We note that for  $\alpha = 0^\circ$ ,  $\lambda_1 < 1$  for axial compression and  $\lambda_1 > 1$  for axial tension along the fibers. For  $\lambda_1$  varying from 0.5 to 2, stresses computed from the user-defined subroutine agree very well with their corresponding analytical values, with the maximum difference between the two being 0.03%. For each case, one can clearly see the





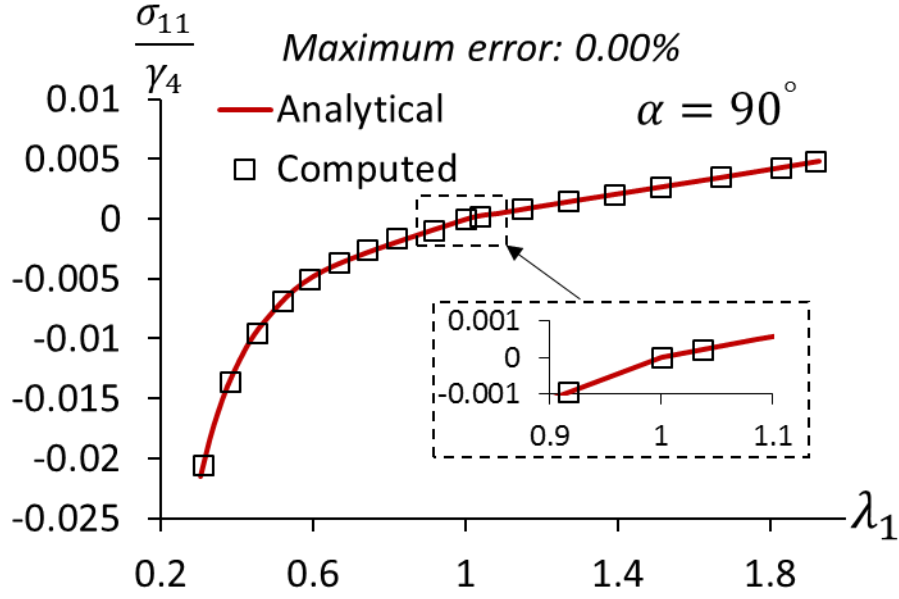


Figure 2.2. Normalized Cauchy stress component vs. the axial stretch for  $\alpha = 0^\circ$ ,  $30^\circ$  and  $90^\circ$  the change in the slope of the axial stress vs. the axial strain curve at  $\lambda_1 = 1$  due to the different response in axial tension and axial compression along the fibers. For  $\alpha = 30^\circ$  tangential tractions are also needed on the planes  $X_1 = \text{constant}$  and  $X_2 = \text{constant}$  to produce the deformation field given by Eq. (2.14). For  $\alpha = 90^\circ$  the axial traction required on the planes  $X_1 = \text{constant}$  is negligible as compared to that for  $\alpha = 0^\circ$  since in the former case essentially the matrix (rubber) is being deformed and fibers are in axial compression due to Poisson's effect.

### 2.4.2 Simple shear deformations of a cube

A simple shear deformation of a cube made of a fiber-reinforced material with fibers making an angle  $\alpha$  to the  $X_1X_3$ - plane is schematically depicted in Fig. 2.3. It can be represented as

$$x_1 = X_1 + kX_2; \quad x_2 = X_2; \quad x_3 = X_3 \tag{2.20}$$

where  $k$  can be interpreted as the shear strain. This deformation is isochoric or volume preserving and thus is admissible in a body made of an incompressible material.

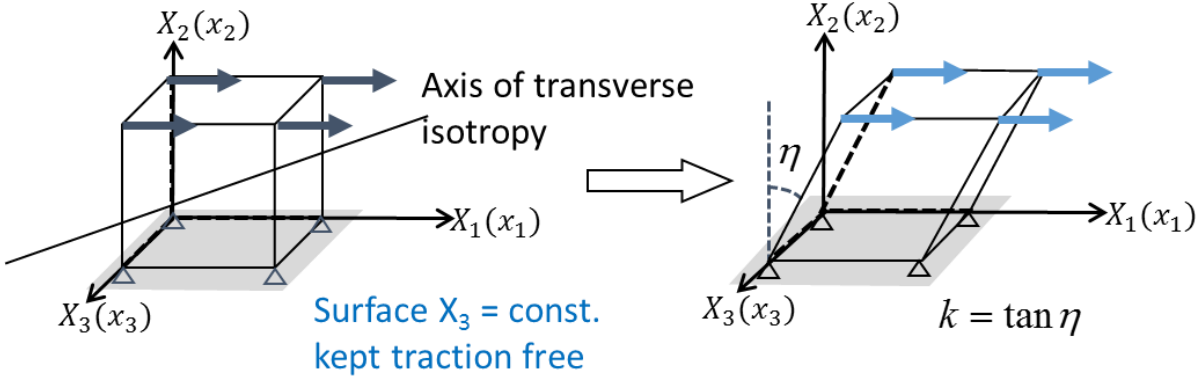


Figure 2.3. Schematic sketch of the simple shearing of a cube made of a fiber-reinforced rubberlike material with fibers inclined at angle  $\alpha$  to the  $X_1X_3$ -plane

For the deformation given by (2.20)

$$\mathbf{B} = \begin{bmatrix} 1+k^2 & k & 0 \\ k & 1 & 0 \\ 0 & 0 & 1 \end{bmatrix}, \quad \mathbf{C} = \begin{bmatrix} 1 & k & 0 \\ k & 1+k^2 & 0 \\ 0 & 0 & 1 \end{bmatrix}$$

$$I_1 = 3+k^2, I_2 = 3+k^2, I_3 = 1, I_4 = (\sin \alpha)^2 k^2 + (\sin 2\alpha)k + 1$$

$$I_5 = (\cos \alpha)^2 (1+k^2) + (\sin \alpha)^2 (k^4 + 3k^2 + 1) + (\sin 2\alpha)k(2+k^2) \quad (2.21)$$

We note that  $I_4$  depends upon  $k$  only when  $\alpha \neq 0^\circ$ . However,  $I_5$  depends upon  $k$  for all values of  $\alpha$ . Substituting for  $I_1$ ,  $I_2$ ,  $I_4$  and  $I_5$  from Eq. (2.21) into Eq. (2.12), we arrive at the following expressions for the components of the Cauchy stress tensor.

$$\begin{aligned}
\sigma_{11} &= -p + 2(1-V_f) \left[ C_1(k^2 + 1) + C_2(k^2 + 2) \right] \\
&+ 4V_f H(I_4 - 1) \left\{ \begin{aligned} &\gamma_4(I_4 - 1)(\cos \alpha + k \sin \alpha)^2 \\ &+ 2\gamma_5(I_5 - 1) \left[ (\sin \alpha)^2(k^4 + 2k^2) + (\cos \alpha)^2(1 + k^2) + \cos \alpha \sin \alpha(3k + 2k^3) \right] \end{aligned} \right\} \\
\sigma_{22} &= -p + 2(1-V_f)(C_1 + 2C_2) \\
&+ 4V_f H(I_4 - 1) \left\{ \begin{aligned} &\gamma_4(I_4 - 1)(\sin \alpha)^2 \\ &+ 2\gamma_5(I_5 - 1) \left[ (\sin \alpha)^2 + (\sin \alpha)^2 k^2 + k \cos \alpha \sin \alpha \right] \end{aligned} \right\} \\
\sigma_{33} &= -p + 2(1-V_f)(C_1 + 2C_2 + C_2 k^2) \\
\sigma_{12} &= 2(1-V_f)(C_1 + C_2)k \\
&+ 4V_f H(I_4 - 1) \left\{ \begin{aligned} &\gamma_4(I_4 - 1) \left[ \cos \alpha \sin \alpha + (\sin \alpha)^2 k \right] \\ &+ \gamma_5(I_5 - 1) \left[ 2(\sin \alpha)^2(k^3 + k) + k + \cos \alpha \sin \alpha(3k^2 + 2) \right] \end{aligned} \right\} \\
\sigma_{23} = \sigma_{32} = \sigma_{31} = \sigma_{13} &= 0
\end{aligned} \tag{2.22}$$

We assume that surfaces  $x_3 = X_3 = \text{constant}$  are traction free. Thus  $\sigma_{13} = \sigma_{33} = \sigma_{23} = 0$  and we get

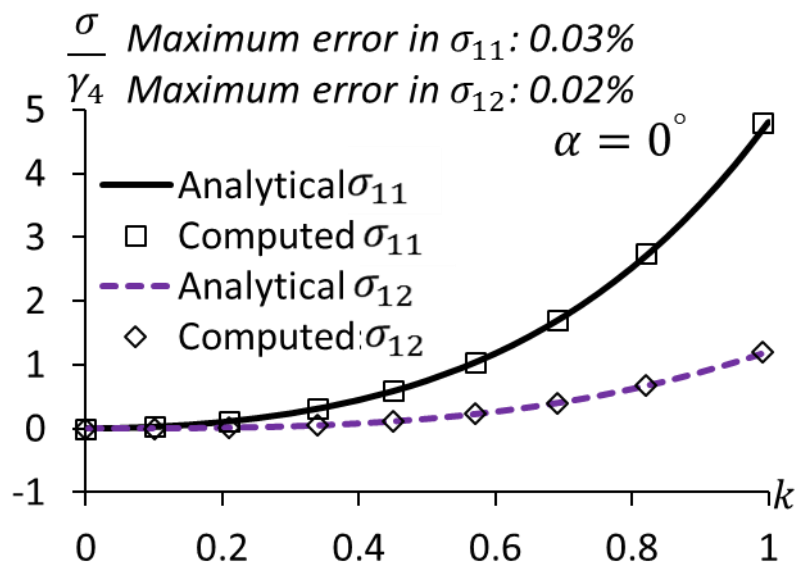
$$p = 2(1-V_f)(C_1 + 2C_2 + C_2 k^2) \tag{2.23}$$

and all components of the Cauchy stress tensor can be evaluated from the known values of the shear strain  $k$ , and the material parameters.

For  $V_f = 0$ , the shear stress  $\sigma_{12}$  is proportional to the shear strain  $k$  with  $2(C_1 + C_2)$  equaling the shear modulus. The difference between the infinitesimal and the finite deformation problems is that in the former case no normal tractions on the flat bounding surfaces act while for the latter normal tractions  $\sigma_{11}$  and  $\sigma_{22}$  given by Eq. (2.22) are needed to keep the bounding surfaces flat. This is usually referred to as the Poynting effect; e.g. see Truesdell and Noll [25]. Note that  $\sigma_{11}$  and  $\sigma_{22}$  are not equal to each other in general implying thereby that different normal surface tractions are needed on the faces  $X_1 = 0, L$  and  $X_2 = 0, L$  to maintain simple shearing deformations of the block.

For  $V_f \neq 0$ , the three stress components  $\sigma_{11}$ ,  $\sigma_{12}$  and  $\sigma_{22}$  depend upon the shear strain  $k$  and the angle  $\alpha$ .

While numerically analyzing simple shearing deformations of a cube of the fiber-reinforced material, we keep faces  $x_3 = X_3 = \text{constant}$  traction free, and apply incremental displacements  $u_1$  and  $u_2$  given by Eq. (2.20) to the remaining four faces by following the same procedure as that for the simple tension/compression problem. For  $\alpha = 0^\circ$ ,  $30^\circ$  and  $90^\circ$ , the computed and the analytical values of normalized stress components for values of the shear strain  $k$  between 0 and 1 are compared in Fig. 2.4. For the range  $[0, 1]$  of values of  $k$  considered, the Cauchy stresses are monotonically increasing functions of the shear strain  $k$ . The computed and the analytical solutions differ from each other by at most 0.0292% thereby verifying the subroutine for simple shearing deformations. For  $\alpha = 0^\circ$ , i.e., fibers along the  $X_1$  - axis in the reference configuration,  $I_4 = 1$  but  $I_5 = 1 + k^2$ . Thus for  $\alpha = 0^\circ$  the presence of fibers affects shear stresses only if  $W$  depends upon  $I_5$ . For  $\alpha = 30^\circ$ , as depicted in Figure 2.4, the slope of  $\sigma_{12}$  versus  $k$  curve at  $k = 0$  is different for  $k > 0$  and  $k < 0$  because of the assumed form of the strain energy density function. For  $\alpha = 90^\circ$ , both  $I_4$  and  $I_5$  contribute to  $W$ ,  $\sigma_{11}$ ,  $\sigma_{12}$  and  $\sigma_{22}$ .



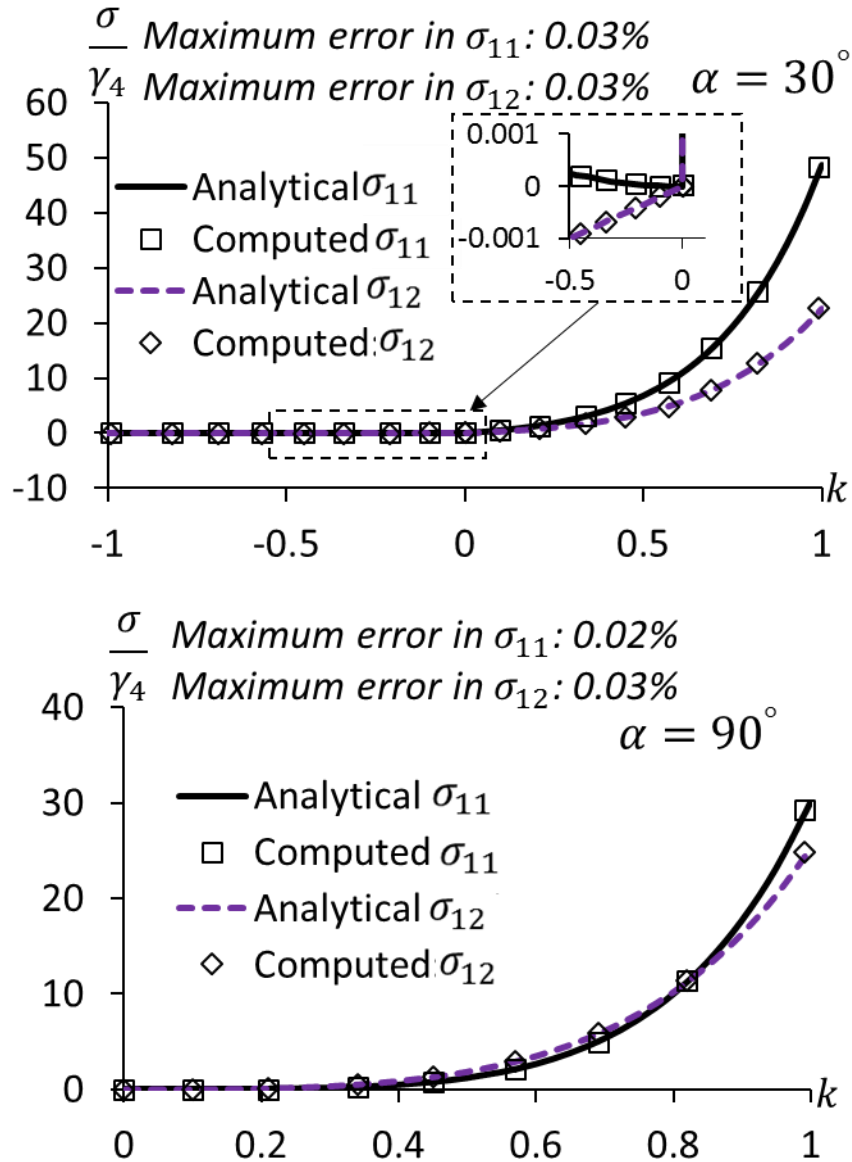


Figure 2.4. For  $\alpha = 0^\circ$ ,  $30^\circ$  and  $90^\circ$ , normalized Cauchy stress components vs. the shear strain  $k$

### 2.4.3 Plane strain bending of fiber-reinforced rectangular beam

For a rectangular beam made of a homogeneous, isotropic and incompressible hyperelastic material, Ericksen [28] showed that a straight beam can be bent into a circular arc by applying the needed surface tractions to its bounding surfaces. Here we consider these deformations and find the surface tractions required to bend a rectangular straight beam made of the fiber-reinforced hyperelastic material. By applying these surface tractions in the numerical solution of the problem

with the developed subroutine, we will find stresses and deformations induced in the beam interior and compare the computed and the analytical solutions. We note that for this problem, deformations are inhomogeneous.

A schematic sketch of the problem studied is exhibited in Figure 2.5, wherein both the rectangular and the cylindrical coordinate axes are shown. The finite plane strain bending of a rectangular beam is described by the deformation field

$$r = \sqrt{2AX_1 + \beta}, \quad \theta = DX_2, \quad z = X_3 \quad (2.24)$$

where  $A$  and  $D$  are nonzero constants,  $D = 1/A$  for deformations to be volume preserving, and the constant  $\beta$  to be determined is related to the curvature of the deformed beam. The rectangular beam bounded by planes  $X_1 = \pm h$  and  $X_2 = \pm L$  in the reference configuration is deformed into the annular wedge bounded by the cylindrical surfaces  $r = r_1$  and  $r = r_2$ , and the planes  $\theta = \pm \theta_0$  in the current configuration. Planes  $X_2 = \text{constant}$  are deformed into planes  $\theta = \text{constant}$ , and the planes  $X_1 = \text{constant}$  into radial surfaces  $r = \text{constant}$ .

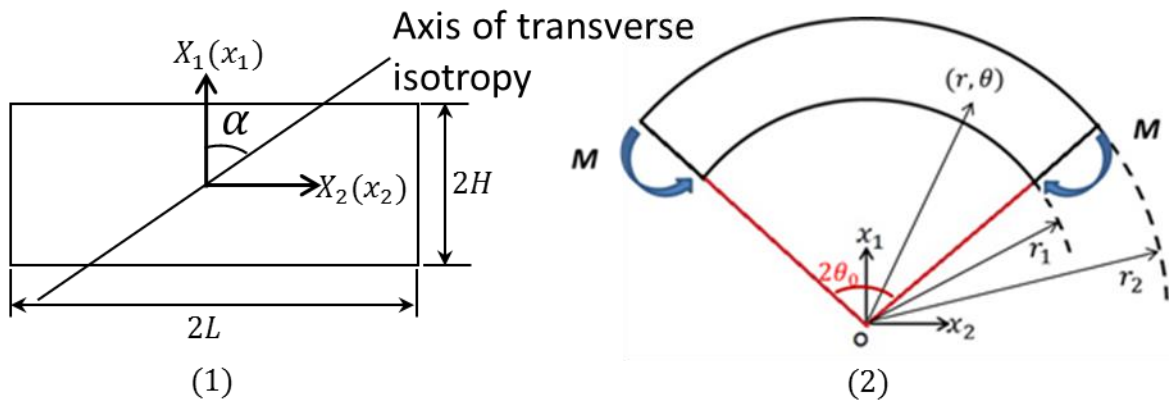


Figure 2.5. Schematic sketch of the bending of a straight rectangular beam into a circular beam; (1) reference configuration, (2) deformed configuration.

In rectangular Cartesian coordinates, the deformation (2.24) is given by

$$x_1 = \sqrt{2AX_1 + \beta} \cos(DX_2), \quad x_2 = \sqrt{2AX_1 + \beta} \sin(DX_2), \quad x_3 = X_3 \quad (2.25)$$

Referring the reader to Batra [23] and Lai et al. [29] for details, we have the following expressions for the physical components of tensors  $\mathbf{B}$  and  $\mathbf{C}$  in the cylindrical coordinate system.

$$\mathbf{B} = \mathbf{C} = \begin{bmatrix} A^2/r^2 & 0 & 0 \\ 0 & D^2 r^2 & 0 \\ 0 & 0 & 1 \end{bmatrix} \quad (2.26)$$

The strain invariants  $I_1, I_2, I_3, I_4,$  and  $I_5$  are given by

$$\begin{aligned} I_1 = I_2 &= \frac{A^2}{r^2} + D^2 r^2 + 1, \quad I_3 = 1 \\ I_4 &= \frac{A^2}{r^2} (\cos \alpha)^2 + D^2 r^2 (\sin \alpha)^2 \\ I_5 &= \frac{A^4}{r^4} (\cos \alpha)^2 + D^4 r^4 (\sin \alpha)^2 \end{aligned} \quad (2.27)$$

Substituting for  $I_1, I_2, I_4,$  and  $I_5$  from Eqs. (2.25) - (2.27) into Eqs. (2.12), we get the following expressions for the physical components of the Cauchy stress tensor in the cylindrical coordinate system.

$$\begin{aligned}
\sigma_{rr} &= -p + 2(1-V_f) \left[ C_1 \frac{A^2}{r^2} + C_2 \left( 1 + \frac{A^2}{r^2} \right) \right] \\
&+ 4V_f H(I_4 - 1) \left[ \gamma_4 (I_4 - 1) \frac{A^2}{r^2} (\cos \alpha)^2 + 2\gamma_5 (I_5 - 1) \frac{A^4}{r^4} (\cos \alpha)^2 \right] \\
\sigma_{\theta\theta} &= -p + 2(1-V_f) \left[ C_1 \frac{r^2}{A^2} + C_2 \left( 1 + \frac{r^2}{A^2} \right) \right] \\
&+ 4V_f H(I_4 - 1) \left[ \gamma_4 (I_4 - 1) \frac{r^2}{A^2} (\sin \alpha)^2 + 2\gamma_5 (I_5 - 1) \frac{r^4}{A^4} (\sin \alpha)^2 \right] \\
\sigma_{zz} &= -p + 2(1-V_f) \left[ C_1 + C_2 \left( \frac{A^2}{r^2} + \frac{r^2}{A^2} \right) \right] \\
\sigma_{r\theta} &= 2V_f H(I_4 - 1) \sin 2\alpha \left[ \gamma_4 (I_4 - 1) + \gamma_5 (I_5 - 1) \left( \frac{A^2}{r^2} + \frac{r^2}{A^2} \right) \right] \\
\sigma_{rz} &= \sigma_{rz} = \sigma_{z\theta} = \sigma_{\theta z} = 0
\end{aligned} \tag{2.28}$$

For null body forces, equations expressing the balance of linear momentum in cylindrical coordinates are (see Lai et al. [29]):

$$\begin{aligned}
\frac{\partial \sigma_{rr}}{\partial r} + \frac{1}{r} \frac{\partial \sigma_{r\theta}}{\partial \theta} + \frac{\partial \sigma_{rz}}{\partial z} + \frac{\sigma_{rr} - \sigma_{\theta\theta}}{r} &= 0 \\
\frac{\partial \sigma_{\theta r}}{\partial r} + \frac{1}{r} \frac{\partial \sigma_{\theta\theta}}{\partial \theta} + \frac{\partial \sigma_{\theta z}}{\partial z} + \frac{2\sigma_{\theta r}}{r} &= 0 \\
\frac{\partial \sigma_{zr}}{\partial r} + \frac{1}{r} \frac{\partial \sigma_{z\theta}}{\partial \theta} + \frac{\partial \sigma_{zz}}{\partial z} + \frac{\sigma_{zr}}{r} &= 0
\end{aligned} \tag{2.29}$$

For  $\alpha = 0^\circ$  and  $90^\circ$ ,  $\sigma_{r\theta} = 0$ , and the analysis of the problem is simplified. For  $\alpha = 0^\circ$  the presence of fibers only influences  $\sigma_{rr}$ , and for  $\alpha = 90^\circ$  only  $\sigma_{\theta\theta}$ . We first study the problem for

$\alpha = 0^\circ$  and  $90^\circ$ . Substitution for stress components from Eq. (2.28) into Eq. (2.29) gives  $\frac{\partial p}{\partial \theta} = 0$ ,

and  $\frac{\partial p}{\partial z} = 0$ . Thus the hydrostatic pressure  $p$  and hence all components of the stress tensor depend

only upon the radial coordinate  $r$ . The integration with respect to  $r$  of the only non-trivial equilibrium equation, (2.29)<sub>1</sub>, gives

$$\sigma_{rr} = \int_{r_1}^r \frac{\sigma_{\theta\theta} - \sigma_{rr}}{r} dr \quad (2.30)$$

where we have used the boundary condition  $\sigma_{rr}(r_1) = 0$ . The boundary condition  $\sigma_{rr}(r_2) = 0$  provides an equation for the determination of  $p$  in terms of  $A$  and  $\beta$ . The requirement that the resultant force on surfaces  $\theta = \pm \theta_0$  vanishes gives

$$\int_{r_1}^{r_2} \sigma_{\theta\theta} dr = 0 \quad (2.31)$$

As mentioned above the cylindrical surfaces  $r = r_1$  and  $r = r_2$  are also traction free. The moment,  $M$ , per unit length in the  $X_3$  - direction, applied at the end faces  $\theta = \pm \theta_0$  required to bend the beam is given by

$$\begin{aligned} M &= \int_{r_1}^{r_2} r \sigma_{\theta\theta} dr \\ &= \int_{r_1}^{r_2} [r(\sigma_{\theta\theta} - \sigma_{rr}) + r\sigma_{rr}] dr \\ &= \int_{r_1}^{r_2} [r(\sigma_{\theta\theta} - \sigma_{rr})] dr + \frac{1}{2} (r^2 \sigma_{rr}) \Big|_{r_1}^{r_2} - \frac{1}{2} \int_{r_1}^{r_2} r^2 \frac{d\sigma_{rr}}{dr} dr \\ &= \int_{r_1}^{r_2} [r(\sigma_{\theta\theta} - \sigma_{rr})] dr - \frac{1}{2} \int_{r_1}^{r_2} r^2 \frac{d\sigma_{rr}}{dr} dr \\ &= \int_{r_1}^{r_2} [r(\sigma_{\theta\theta} - \sigma_{rr})] dr - \frac{1}{2} \int_{r_1}^{r_2} r^2 \frac{\sigma_{\theta\theta} - \sigma_{rr}}{r} dr \\ &= \int_{r_1}^{r_2} \frac{1}{2} r (\sigma_{\theta\theta} - \sigma_{rr}) dr \end{aligned} \quad (2.32)$$

where we have used the boundary conditions  $\sigma_{rr}(r_1) = 0$ ,  $\sigma_{rr}(r_2) = 0$ , and Eq. (2.29)<sub>1</sub>. This simplification is also given in Truesdell and Noll [25]. Equations (2.31) and (2.32) relate  $A$  and  $\beta$  to the moment  $M$  applied at the end faces.

For  $\alpha$  other than  $0^\circ$  and  $90^\circ$ , the hydrostatic pressure  $p$  depends upon  $\theta$ , and equilibrium Eqs.

(2.29) require that  $\partial p / \partial \theta$  and  $\partial p / \partial r$  are functions of  $r$  only. Thus the condition,  $\frac{\partial^2 p}{\partial \theta \partial r} = \frac{\partial^2 p}{\partial r \partial \theta}$ ,

for finding the pressure cannot be satisfied, and there is no solution of the problem of the type given by Eq. (2.25). However, the problem may have solutions of other than those given by Eq.

(2.25). Recall that Ericksen's theorem applies only to isotropic hyperelastic materials and here we have a transversely isotropic material.

For infinitesimal deformations one defines the neutral surface by using Eq. (2.31) and it passes through the centroid of the beam cross-section. Both the hoop strain and the hoop stress vanish at points on the neutral surface. However, for the nonlinear theory, it need not pass through the beam centroid. Furthermore, points where  $\sigma_{\theta\theta} = 0$  and  $\varepsilon_{\theta\theta} = 0$  need not coincide with each other. Here

$\varepsilon_{\theta\theta}$  is a component of the Almansi-Hamel strain,  $\boldsymbol{\varepsilon} = \frac{1}{2}(\mathbf{I} - \mathbf{B}^{-1})$ , in the  $\theta$  - direction.

While numerically analyzing the plane strain boundary value problem for  $\alpha = 0^\circ$  and  $90^\circ$ , we study deformations of only the right half of the beam since the beam geometry and its deformations are symmetric about the plane  $X_2 = 0$ . However, for other values of  $\alpha$  deformations may not be symmetric because the material of the beam is transversely isotropic. Boundary conditions used are

$$\text{Surface } X_1 = -h: u_1 = x_1 - X_1, u_2 = x_2 - X_2$$

$$\text{Surface } X_1 = h: \sigma_{rr} = \sigma_{r\theta} = 0$$

$$\text{Surface } X_2 = 0: u_1 = x_1 - X_1, u_2 = 0$$

$$\text{Surface } X_2 = L: u_1 = x_1 - X_1, u_2 = x_2 - X_2 \tag{2.33}$$

We set the  $X_3$  - displacement of all nodes equal to zero to simulate plane strain deformations. The displacements given by Eq. (2.33) are incrementally applied on the faces  $X_1 = -h$ ,  $X_2 = 0$  and  $L$  are simultaneously incremented by the same percentage till their final values. We note that  $x_1$  and  $x_2$  are calculated from Eq. (2.25) after finding values of constants  $A$  and  $\beta$  from the applied moment,  $M$ . For the example problems studied below we have used values of material parameters listed just before the subsection 2.4.1, and have set  $L = 2h = 100$  mm. For  $\alpha = 0^\circ$ , values of other parameters are  $A = 0.2018$  m,  $\beta = 0.0602$  m<sup>2</sup> that correspond to  $M = 11.94$  kN-m, and  $\theta_0 = 28.4^\circ$ ,

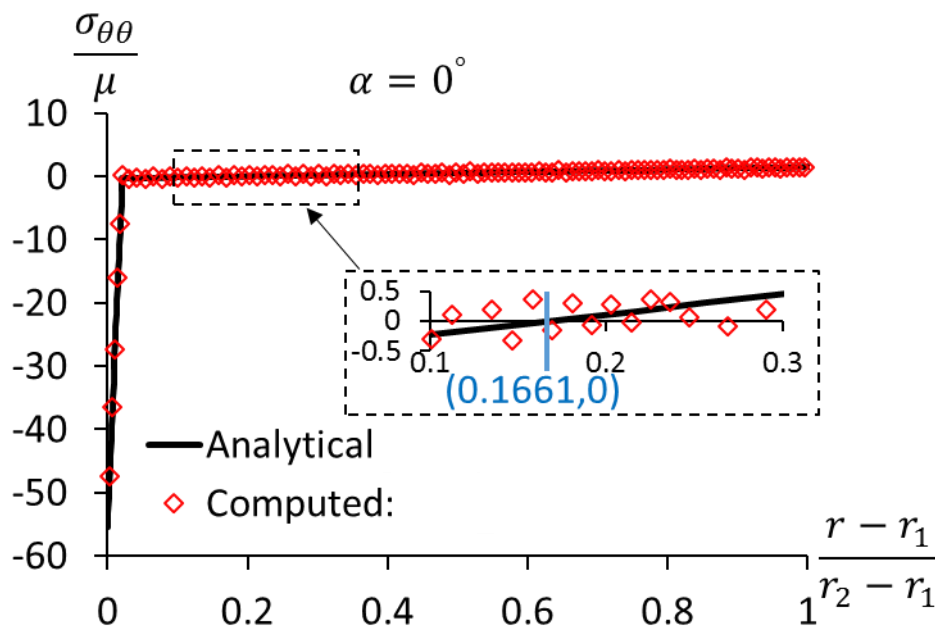
and for  $\alpha = 90^\circ$  we have  $A = 0.318$  m,  $\beta = 0.0718$  m<sup>2</sup> that correspond to  $M = 43.78$  kN-m, and  $\theta_0 = 18.02^\circ$ .

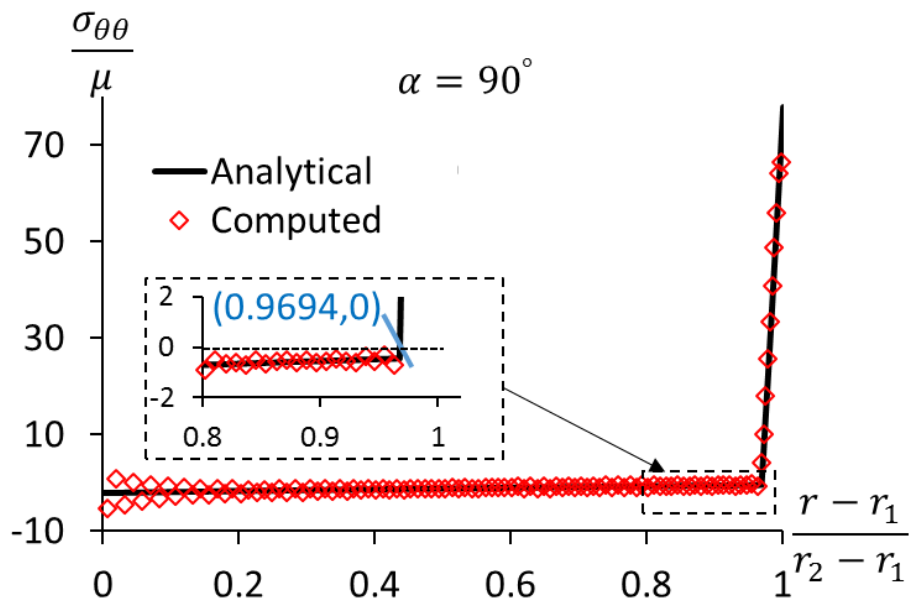
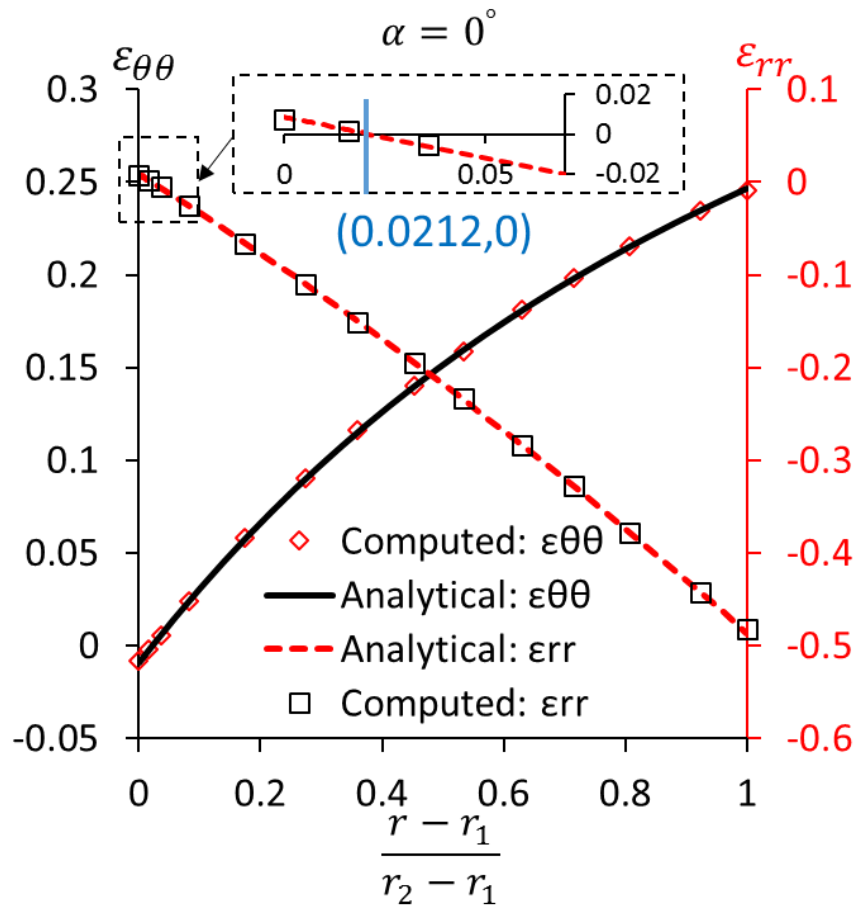
We discretize the  $100$  mm  $\times$   $100$  mm  $\times$   $1$  mm region in the reference configuration occupied by the right half of the beam into  $110 \times 150 \times 1$  FE mesh of 8-node brick elements. As mentioned above, we have set  $K = 150 \gamma_4$  in order to save on computational resources. Thus the incompressibility condition is not well satisfied and the computed hydrostatic pressure exhibits oscillations whose amplitude depends upon the value of  $K$  and the FE mesh used. For  $\alpha = 0^\circ$  and  $90^\circ$  the distribution of the computed Cauchy hoop stress normalized by the shear modulus,  $\mu = 2(C_1 + C_2)V_f$ , and the Almansi-Hamel hoop strain are compared with their values from the analytical solution in Figure 2.6. The two sets of results differ by at most 4.9%. When the FE mesh was refined to  $205 \times 150 \times 1$  elements the maximum difference between the computed and the analytical solutions was reduced to 3.8% mainly because of the improvement in the computed values of the hydrostatic pressure. However, the CPU time required to solve the problem increased by a factor of 10. The effect of different response of fibers when they are deformed in tension and compression should be clear from the plots of Fig. 2.6. In the region where fibers are stretched, stresses induced are much larger than those in the region where fibers are compressed because of the huge difference (a factor of 1000) in the axial modulus of the fibers in tension and compression. In order for the resultant axial force on a cross-section to be zero, a much larger portion of the material in the radial direction is experiencing compressive hoop stress than that for which the hoop stress is tensile. The radial locations of points where  $\sigma_{\theta\theta} = 0$  and  $\varepsilon_{\theta\theta} = 0$  are different because the hydrostatic pressure makes a significant contribution to the radial and the hoop stresses. For  $\alpha = 0^\circ$ ,  $\sigma_{\theta\theta} = 0$  and  $\varepsilon_{\theta\theta} = 0$  at points situated, respectively, at non-dimensional radii of 0.1661 and 0.0212 from the inner surface. However, the hoop stress at points for which the non-dimensional radius exceeds 0.0212 is miniscule as compared to its maximum magnitude of 55. We note that at points for which the non-dimensional radius is less than 0.0212,  $\sigma_{\theta\theta} < 0$  even though  $\varepsilon_{\theta\theta} > 0$  because of  $\varepsilon_{rr} < 0$  and the significant contribution from the hydrostatic pressure.

The hydrostatic pressure distribution exhibited in Fig. 2.7 for  $\alpha = 0^\circ$  is oscillatory due to a small value assigned to the bulk modulus  $K$ . Oscillations in the hydrostatic pressure cause oscillations

in the Cauchy stresses even though strains vary smoothly in the radial direction. As mentioned above, a larger value of  $K$  could not be used because of the excessive CPU time required to compute results. The oscillations in the hydrostatic pressure for  $\alpha = 90^\circ$  are of larger amplitude than those for  $\alpha = 0^\circ$ . However, the amplitude of oscillations is less than 5% of the maximum values of stresses induced in the deformed beam. Ideally, one should compute results with successively refined FE meshes and several values of the bulk modulus to obtain converged results. Unfortunately, this could not be accomplished due to constraints of time and the computational resources. Oscillations in the hydrostatic pressure can be smoothed out by using a pressure smoothing technique (e.g., see Hughes [30]) such as averaging the pressure in two consecutive elements but it has not been implemented in the subroutine.

Results for values of  $\alpha$  other than  $0^\circ$  and  $90^\circ$  have not been computed because there is no analytical solution available with which computed results could be compared. If we were to deform such a rectangular beam by applying only moments on the faces  $X_2 = \pm L$ , the beam will not be bent into a circular arc and the faces into which surfaces  $X_1 = \pm h$  are deformed may not be smooth. A difficulty in applying pure moments at the end faces is determining the distribution of normal surface tractions on them.





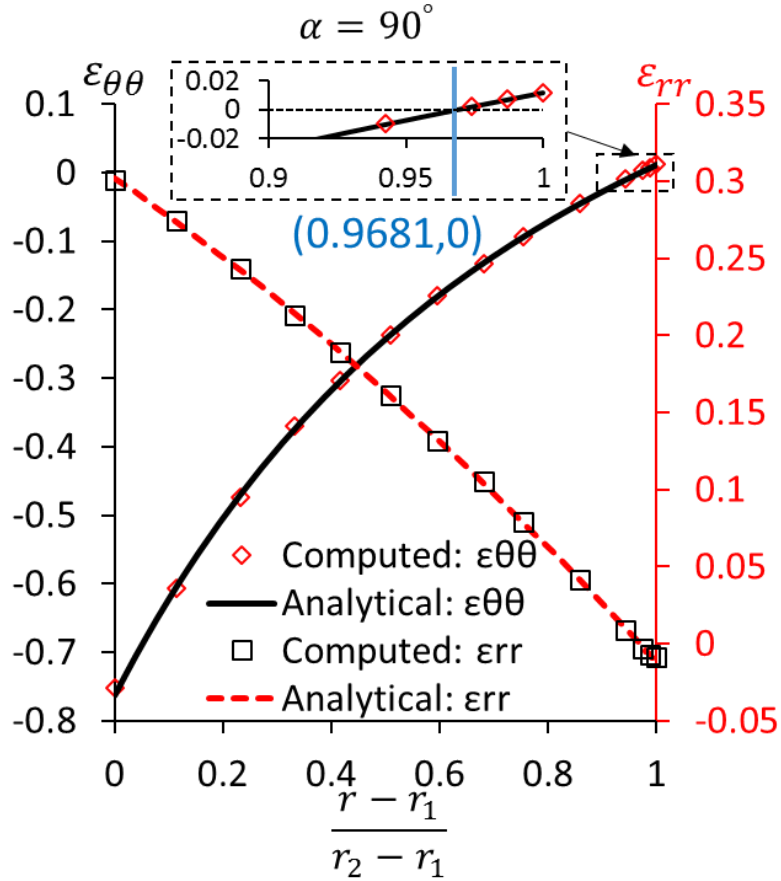


Figure 2.6. For  $\alpha = 0^\circ$  and  $90^\circ$ , the through-the-thickness variation of the hoop stress and the Almansi-Hamel hoop strain

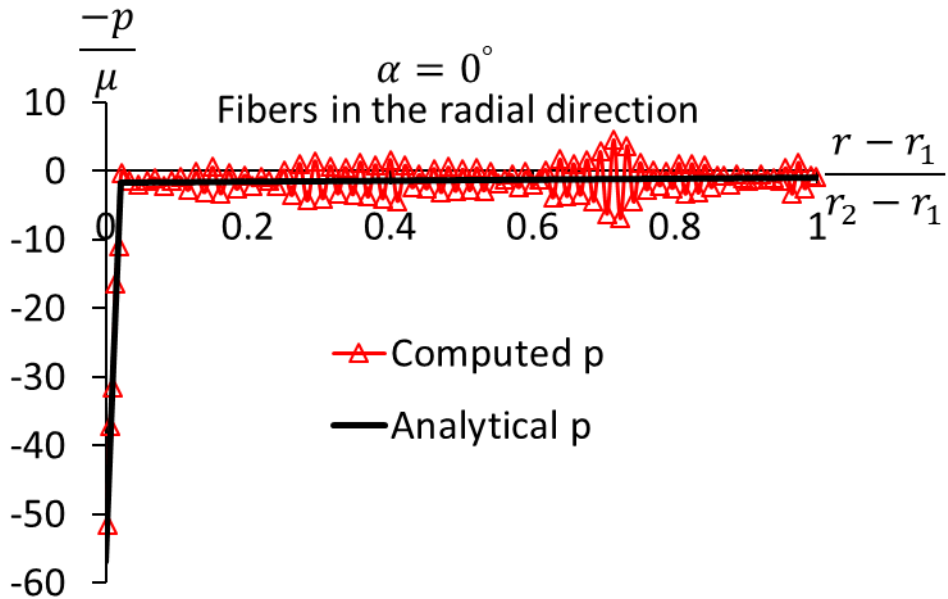


Figure 2.7. For  $\alpha = 0^\circ$ , the through-the-thickness variation of the hydrostatic pressure

## 2.5 Conclusions

By assuming that a fiber-reinforced rubberlike material can be modeled as a homogeneous and transversely isotropic hyperelastic material with the fiber direction as the axis of transverse isotropy, we have proposed an expression for the strain energy density in terms of the five invariants of the right Cauchy-Green strain tensor. For compressible and incompressible materials it involves five and four material constants, respectively. However, the hydrostatic pressure for incompressible materials is found from the solution of the boundary value problem, and is thus an independent variable along with the three displacement components. The material model represents different response for axial compression and axial tension along the fiber direction. The constitutive relation has been implemented in the commercial software, LS-DYNA as a user-defined subroutine. For three static boundary value problems, results computed by using the subroutine have been found to agree well with those computed analytically. Full verification of the implementation of the subroutine requires similar comparisons for numerous boundary value problems. Also, predictions from the material model need to be compared with the test data to validate it and establish its range of applicability. When test data for different modes of deformation becomes available, the form of the strain energy density assumed here may need to be modified. However, the new form of the strain energy density can be similarly implemented in LS-DYNA.

### **Acknowledgements:**

This work was supported by a grant from the Center for Tire Research (an NSF Industry/University Cooperative Research Center). We are indebted to the industry mentors for providing suggestions to improve upon the work.

## Appendix A: Source code for the user-defined material subroutines

```
subroutine umat45 (cm,eps,sig,epsp,hsv,dt1,capa,  
. etype,time,temp,failel,crv,cma,qmat,elsiz,idele)  
  
c  
c*****  
c| Livermore Software Technology Corporation (LSTC) |  
c| ----- |  
c| Copyright 1987-2008 Livermore Software Tech. Corp |  
c| All rights reserved |  
c*****  
c  
c*****  
c| This subroutine is developed by Qian Li and Romesh Batra |  
c| Computational Mechanics Laboratory, Virginia Tech |  
c| All rights reserved |  
c*****  
c  
c*****  
c| !!!!!!!!!!!!!!!!!!!!!!!!!!!!!!!!!!!!!!!!!!!!!!!  
c| Change this file's name to "Li_Batra-rebar.f" before use  
c  
c*****  
c  
c*****  
c| How to use the developed subroutine?  
c| 1. Bulid the new executables with the developed UMAT  
c| The required Object files can be downloaded from LS-DYNA website.  
c| Main program calls subroutine usrmat in dyn21.f,which is provided by LS-DYNA,
```

- c the developed material subroutine: "li\_batra-rebar.f" is called from there
- c Use the "make" command for the Linux version to compile the code
- c If compiling is successful, an executable will be created that you can use with your input file to run LS-DYNA.

c 2. To call the code in the LS-DYNA input file use this in keyword file:

c \*MAT\_USER\_DEFINED\_MATERIAL\_MODELS

c This defines the input for the user material interface

c Eexample input deck is provided for the example of inflation of a 2-Ply cylindrical tube

c\*\*\*\*\*

c

c\*\*\*\*\*

c| Verison of LS-DYNA: smp d R7.0.0 |

c| Verison of ABAQUS: 6.13 |

c\*\*\*\*\*

c

c Transversely isotropic material

c

c Variables

c

c cm(1)=first material constant, C1

c cm(2)=second material constant, C2

c cm(3)=second material constant, Bulk

c cm(4)=shear modulus, G

c cm(5)=volume fraction of the fibers, VF

c cm(6)=components of the fiber direction wrt local x,LAX,only for solid elements

c cm(7)=components of the fiber direction wrt local y,LAY,only for solid elements

c cm(8)=components of the fiber direction wrt local z,LAZ,only for solid elements

c cm(9)=fiber-reinforced paramter,gamma4

c cm(10)=fiber-reinforced paramter,gamma5

c cm(11)=fiber angle in the reference configuration, only for shell (membrane) elements  
c  
c eps(1)=local x strain increment  
c eps(2)=local y strain increment  
c eps(3)=local z strain increment  
c eps(4)=local xy strain increment  
c eps(5)=local yz strain increment  
c eps(6)=local zx strain increment  
c  
c sig(1)=local x stress  
c sig(2)=local y stress  
c sig(3)=local z stress  
c sig(4)=local xy stress  
c sig(5)=local yz stress  
c sig(6)=local zx stress  
c  
c hsv(10)=1st history variable  
c hsv(11)=2nd history variable  
c .  
c .  
c .  
c .  
c hsv(18)=9th history variable  
c  
c dt1=current time step size  
c capa=reduction factor for transverse shear  
c etype:  
c eq."solid" for solid elements

c eq."sld2d" for shell forms 13, 14, and 15 (2D solids)  
c eq."shl\_t" for shell forms 25, 26, and 27 (shells with thickness stretch)  
c eq."shell" for all other shell elements plus thick shell forms 1 and 2  
c eq."tshel" for thick shell forms 3 and 5  
c eq."hbeam" for beam element forms 1 and 11  
c eq."tbeam" for beam element form 3 (truss)  
c eq."dbeam" for beam element form 6 (discrete)  
c eq."beam " for all other beam elements  
c  
c time=current problem time.  
c temp=current temperature  
c  
c cma=additional memory for material data defined by LMCA at  
c 6th field of 2nd crad of \*DATA\_USER\_DEFINED  
c  
c All transformations into the element local system are  
c performed prior to entering this subroutine. Transformations  
c back to the global system are performed after exiting this  
c routine.  
c  
c All history variables are initialized to zero in the input  
c phase. Initialization of history variables to nonzero values  
c may be done during the first call to this subroutine for each  
c element.  
c  
c Energy calculations for the dyna3d energy balance are done  
c outside this subroutine.  
c

```

include 'nlqparm'
include 'iounits.inc'
include 'bk06.inc'
character*5 etype
dimension cm(*),eps(*),sig(*),hsv(*),crv(lq1,2,*),cma(*),qmat(3,3)
logical faillel
real invar1,invar2,invar4,invar5,epsp
1  ,b1,b2,b3,b4,b5,b6,bb1,bb2,bb3,bb4,bb5,bb6
2  ,c1,c2,c3,c4,c5,c6,cc1,cc2,cc3,cc4,cc5,cc6
4  ,aa1,aa2,aa3
5  ,aaaa1,aaaa2,aaaa3,aaaa4,aaaa5,aaaa6
6  ,baa1,baa2,baa3
7  ,aabaa1,aabaa2,aabaa3,aabaa4,aabaa5,aabaa6
9  ,detf,detfinv,T_vol
A  ,lambda_f,lambda_1,lnlambda_f,lnlambda_1,cons,Trr,m2,n2
B  ,cosin_theta,angle,PI,m_aa1,n_aa2,T_fiber
real F11,F21,F31,F12,F22,F32,F13,F23,F33
1  ,FF11,FF21,FF31,FF12,FF22,FF32,FF13,FF23,FF33
c
c  if (ncycle.eq.1) then
c    call usermsg('mat45')
c  endif
c
c  if (etype.eq.'solid'.or.etype.eq.'shl_t'.or.
1  etype.eq.'sld2d'.or.etype.eq.'tshel'.or.
2  etype.eq.'tet13') then
c  if (time.eq.0.0) then
c    hsv(1)=1.0

```

```

c   hsv(2)=0.0
c   hsv(3)=0.0
c   hsv(4)=0.0
c   hsv(5)=1.0
c   hsv(6)=0.0
c   hsv(7)=0.0
c   hsv(8)=0.0
c   hsv(9)=1.0
c   endif
c*****
c   deformation gradient stored in hsv(1),...,hsv(9)
c
c   compute jacobian
c*****
      def=hsv(1)*(hsv(5)*hsv(9)-hsv(6)*hsv(8))
1     -hsv(2)*(hsv(4)*hsv(9)-hsv(6)*hsv(7))
2     +hsv(3)*(hsv(4)*hsv(8)-hsv(5)*hsv(7))
c
c   compute left cauchy-green tensor
c
      b1=hsv(1)*hsv(1)+hsv(4)*hsv(4)+hsv(7)*hsv(7)
      b2=hsv(2)*hsv(2)+hsv(5)*hsv(5)+hsv(8)*hsv(8)
      b3=hsv(3)*hsv(3)+hsv(6)*hsv(6)+hsv(9)*hsv(9)
      b4=hsv(1)*hsv(2)+hsv(4)*hsv(5)+hsv(7)*hsv(8)
      b5=hsv(2)*hsv(3)+hsv(5)*hsv(6)+hsv(8)*hsv(9)
      b6=hsv(1)*hsv(3)+hsv(4)*hsv(6)+hsv(7)*hsv(9)
!     b(1,1)=b1
!     b(2,2)=b2

```

```

!   b(3,3)=b3
!   b(1,2)=b4
!   b(2,1)=b4
!   b(2,3)=b5
!   b(3,2)=b5
!   b(1,3)=b6
!   b(3,1)=b6

```

```

c*****

```

```

c   compute square of left cauchy-green tensor FF_T

```

```

c*****

```

```

bb1=b1*b1+b4*b4+b6*b6
bb2=b4*b4+b2*b2+b5*b5
bb3=b6*b6+b5*b5+b3*b3
bb4=b1*b4+b2*b4+b5*b6
bb5=b6*b4+b5*b2*b3*b5
bb6=b6*b1+b5*b4+b3*b6

```

```

!   bb(1,1)=bb1
!   bb(2,2)=bb2
!   bb(3,3)=bb3
!   bb(1,2)=bb4
!   bb(2,1)=bb4
!   bb(2,3)=bb5
!   bb(3,2)=bb5
!   bb(1,3)=bb6
!   bb(3,1)=bb6

```

```

c*****

```

```

c   compute right cauchy-green tensor F_TF

```

```

c*****

```

```

c1=hsv(1)*hsv(1)+hsv(2)*hsv(2)+hsv(3)*hsv(3)
c2=hsv(4)*hsv(4)+hsv(5)*hsv(5)+hsv(6)*hsv(6)
c3=hsv(7)*hsv(7)+hsv(8)*hsv(8)+hsv(9)*hsv(9)
c4=hsv(1)*hsv(4)+hsv(2)*hsv(5)+hsv(3)*hsv(6)
c5=hsv(4)*hsv(7)+hsv(5)*hsv(8)+hsv(6)*hsv(9)
c6=hsv(1)*hsv(7)+hsv(2)*hsv(8)+hsv(3)*hsv(9)
!   c(1,1)=c1
!   c(2,2)=c2
!   c(3,3)=c3
!   c(1,2)=c4
!   c(2,1)=c4
!   c(2,3)=c5
!   c(3,2)=c5
!   c(1,3)=c6
!   c(3,1)=c6
c*****
c   compute square of right cauchy-green tensor F_TF
c*****
cc1=c1*c1+c4*c4+c6*c6
cc2=c4*c4+c2*c2+c5*c5
cc3=c6*c6+c5*c5+c3*c3
cc4=c1*c4+c2*c4+c5*c6
cc5=c6*c4+c5*c2*c3*c5
cc6=c6*c1+c5*c4+c3*c6
!   cc(1,1)=cc1
!   cc(2,2)=cc2
!   cc(3,3)=cc3
!   cc(1,2)=cc4

```

```

!   cc(2,1)=cc4
!   cc(2,3)=cc5
!   cc(3,2)=cc5
!   cc(1,3)=cc6
!   cc(3,1)=cc6
c*****
c   deformed fiber orientations aa in current local configuration
c*****
aa1=HSV(1)*CM(6)+HSV(4)*CM(7)+HSV(7)*CM(8)
aa2=HSV(2)*CM(6)+HSV(5)*CM(7)+HSV(8)*CM(8)
aa3=HSV(3)*CM(6)+HSV(6)*CM(7)+HSV(9)*CM(8)
c
c   compute aa tensor product aa
c
aaaa1=aa1*aa1
aaaa2=aa2*aa2
aaaa3=aa3*aa3
aaaa4=aa1*aa2
aaaa5=aa2*aa3
aaaa6=aa3*aa1
!   do i=1,3
!       do j=1,3
!           aaaa(i,j)=aa(i)*aa(j)
!       end do
!   end do
c
c   compute b dot aa == baa
c

```

```

    baa1=b1*aa1+b4*aa2+b6*aa3
    baa2=b4*aa1+b2*aa2+b5*aa3
    baa3=b6*aa1+b5*aa2+b3*aa3
c
c   compute aa tensor product baa
c
    aabaa1=aa1*baa1+baa1*aa1
    aabaa2=aa2*baa2+baa2*aa2
    aabaa3=aa3*baa3+baa3*aa3
    aabaa4=aa1*baa2+baa1*aa2
    aabaa5=aa2*baa3+baa2*aa3
    aabaa6=aa3*baa1+baa3*aa1
c*****
c   compute strain invariants invar1 (I1) invar2 (I2) invar4 (I4) invar5 (I5)
c*****
    invar1=c1+c2+c3
    invar2=0.5*(c1+c2+c3)**2-0.5*(cc1+cc2+cc3)
    invar4=c1*cm(6)**2+c2*cm(7)**2+c3*cm(8)**2
1  +2*c4*cm(6)*cm(7)+2*c5*cm(7)*cm(8)+2*c6*cm(8)*cm(6)
    invar5=cc1*cm(6)**2+cc2*cm(7)**2+cc3*cm(8)**2
1  +2*cc4*cm(6)*cm(7)+2*cc5*cm(7)*cm(8)+2*cc6*cm(8)*cm(6)
    lambda_f=sqrt(invar4)
c   lambda_f: fiber stretch
c
c*****
c   compute cauchy stress
c*****
    detf=max(detf,1.e-8)

```

detfinv=1./detf

c when the fiber under compression, anisotropic term have no contribution

c isotropic: 1,2,3...; I4 related: A B...; I5 related: a b ...

if (lambda\_f .GT. 1.) then

c T\_vol: hydrostatic pressure

T\_vol=cm(3)/2.\*(detf-detfinv)+detfinv\*(

p -2./3.\*cm(1)\*detf\*\*(-2./3.)\*invar1

p -4./3.\*cm(2)\*detf\*\*(-4./3.)\*invar2

p -(4./3.)\*cm(5)\*cm(9)\*(detf\*\*(-2./3.)\*invar4-1.)

p \*detf\*\*(-2./3.)\*invar4

e -(8./3.)\*cm(5)\*cm(10)\*(detf\*\*(-4./3.)\*invar5-1.)

p \*detf\*\*(-4./3.)\*invar5)

sig(1)=T\_vol+detfinv\*(

1 +2.\*cm(1)\*detf\*\*(-2./3.)\*b1

3 +2.\*cm(2)\*detf\*\*(-4./3.)\*invar1\*b1

4 -2.\*cm(2)\*detf\*\*(-4./3.)\*bb1

A +4.\*cm(5)\*cm(9)\*(detf\*\*(-2./3.)\*invar4-1.)

B \*detf\*\*(-2./3.)\*aaaa1

a +4.\*cm(5)\*cm(10)\*(detf\*\*(-4./3.)\*invar5-1.)

b \*detf\*\*(-4./3.)\*aabaa1)

sig(2)=T\_vol+detfinv\*(

1 +2.\*cm(1)\*detf\*\*(-2./3.)\*b2

3 +2.\*cm(2)\*detf\*\*(-4./3.)\*invar1\*b2

4 -2.\*cm(2)\*detf\*\*(-4./3.)\*bb2

A +4.\*cm(5)\*cm(9)\*(detf\*\*(-2./3.)\*invar4-1.)

B \*detf\*\*(-2./3.)\*aaaa2

a +4.\*cm(5)\*cm(10)\*(detf\*\*(-4./3.)\*invar5-1.)

b \*detf\*\*(-4./3.)\*aabaa2)

$\text{sig}(3) = T\_vol + \text{detfinv} * ($   
 1 +2.\*cm(1)\*detf\*\*(-2./3.)\*b3  
 3 +2.\*cm(2)\*detf\*\*(-4./3.)\*invar1\*b3  
 4 -2.\*cm(2)\*detf\*\*(-4./3.)\*bb3  
 A +4.\*cm(5)\*cm(9)\*(detf\*\*(-2./3.)\*invar4-1)  
 B \*detf\*\*(-2./3.)\*aaaa3  
 a +4.\*cm(5)\*cm(10)\*(detf\*\*(-4./3.)\*invar5-1.)  
 b \*detf\*\*(-4./3.)\*aabaa3)

$\text{sig}(4) = \text{detfinv} * ($   
 1 +2.\*cm(1)\*detf\*\*(-2./3.)\*b4  
 2 +2.\*cm(2)\*detf\*\*(-4./3.)\*invar1\*b4  
 3 -2.\*cm(2)\*detf\*\*(-4./3.)\*bb4  
 A +4.\*cm(5)\*cm(9)\*(detf\*\*(-2./3.)\*invar4-1)  
 B \*detf\*\*(-2./3.)\*aaaa4  
 a +4.\*cm(5)\*cm(10)\*(detf\*\*(-4./3.)\*invar5-1.)  
 b \*detf\*\*(-4./3.)\*aabaa4)

$\text{sig}(5) = \text{detfinv} * ($   
 1 +2.\*cm(1)\*detf\*\*(-2./3.)\*b5  
 2 +2.\*cm(2)\*detf\*\*(-4./3.)\*invar1\*b5  
 3 -2.\*cm(2)\*detf\*\*(-4./3.)\*bb5  
 A +4.\*cm(5)\*cm(9)\*(detf\*\*(-2./3.)\*invar4-1)  
 B \*detf\*\*(-2./3.)\*aaaa5  
 a +4.\*cm(5)\*cm(10)\*(detf\*\*(-4./3.)\*invar5-1.)  
 b \*detf\*\*(-4./3.)\*aabaa5)

$\text{sig}(6) = \text{detfinv} * ($   
 1 +2.\*cm(1)\*detf\*\*(-2./3.)\*b6  
 2 +2.\*cm(2)\*detf\*\*(-4./3.)\*invar1\*b6  
 3 -2.\*cm(2)\*detf\*\*(-4./3.)\*bb6

$A + 4 \cdot \text{cm}(5) \cdot \text{cm}(9) \cdot (\text{detf}^{**}(-2./3.) \cdot \text{invar4} - 1)$   
 $B \cdot \text{detf}^{**}(-2./3.) \cdot \text{aaaa6}$   
 $a + 4 \cdot \text{cm}(5) \cdot \text{cm}(10) \cdot (\text{detf}^{**}(-4./3.) \cdot \text{invar5} - 1.)$   
 $b \cdot \text{detf}^{**}(-4./3.) \cdot \text{aabaa6}$   
 else  
 $T\_vol = \text{cm}(3)/2 \cdot (\text{detf} - \text{detfinv}) + \text{detfinv} \cdot$   
 $p \ -2./3 \cdot \text{cm}(1) \cdot \text{detf}^{**}(-2./3.) \cdot \text{invar1}$   
 $p \ -4./3 \cdot \text{cm}(2) \cdot \text{detf}^{**}(-4./3.) \cdot \text{invar2}$   
 $\text{sig}(1) = T\_vol + \text{detfinv} \cdot$   
 $1 \ +2 \cdot \text{cm}(1) \cdot \text{detf}^{**}(-2./3.) \cdot b1$   
 $3 \ +2 \cdot \text{cm}(2) \cdot \text{detf}^{**}(-4./3.) \cdot \text{invar1} \cdot b1$   
 $4 \ -2 \cdot \text{cm}(2) \cdot \text{detf}^{**}(-4./3.) \cdot bb1)$   
 $\text{sig}(2) = T\_vol + \text{detfinv} \cdot$   
 $1 \ +2 \cdot \text{cm}(1) \cdot \text{detf}^{**}(-2./3.) \cdot b2$   
 $3 \ +2 \cdot \text{cm}(2) \cdot \text{detf}^{**}(-4./3.) \cdot \text{invar1} \cdot b2$   
 $4 \ -2 \cdot \text{cm}(2) \cdot \text{detf}^{**}(-4./3.) \cdot bb2)$   
 $\text{sig}(3) = T\_vol + \text{detfinv} \cdot$   
 $1 \ +2 \cdot \text{cm}(1) \cdot \text{detf}^{**}(-2./3.) \cdot b3$   
 $3 \ +2 \cdot \text{cm}(2) \cdot \text{detf}^{**}(-4./3.) \cdot \text{invar1} \cdot b3$   
 $4 \ -2 \cdot \text{cm}(2) \cdot \text{detf}^{**}(-4./3.) \cdot bb3)$   
 $\text{sig}(4) = \text{detfinv} \cdot$   
 $1 \ +2 \cdot \text{cm}(1) \cdot \text{detf}^{**}(-2./3.) \cdot b4$   
 $2 \ +2 \cdot \text{cm}(2) \cdot \text{detf}^{**}(-4./3.) \cdot \text{invar1} \cdot b4$   
 $3 \ -2 \cdot \text{cm}(2) \cdot \text{detf}^{**}(-4./3.) \cdot bb4)$   
 $\text{sig}(5) = \text{detfinv} \cdot$   
 $1 \ +2 \cdot \text{cm}(1) \cdot \text{detf}^{**}(-2./3.) \cdot b5$   
 $2 \ +2 \cdot \text{cm}(2) \cdot \text{detf}^{**}(-4./3.) \cdot \text{invar1} \cdot b5$   
 $3 \ -2 \cdot \text{cm}(2) \cdot \text{detf}^{**}(-4./3.) \cdot bb5)$

```

sig(6)=detfinv*(
1 +2.*cm(1)*detf**(-2./3.)*b6
2 +2.*cm(2)*detf**(-4./3.)*invar1*b6
3 -2.*cm(2)*detf**(-4./3.)*bb6)
endif
c
c*****
c In the following is for the rebar element (membrane)
c Noting for the membrane element, cm(6),cm(7),cm(8) here are assigned with new values
(meanings) that
c different with those defined in the input deck
c Fiber angle input is defined as cm(11) for shell (membrane) elements
c Only "IHYPER=3" which will make the deformation gradient computed from the nodal
coordinates
c and in the global coordinate system should be used
c*****
c
else if (etype.eq.'shell') then
PI=4.D0*DATAN(1.D0)
cm(6)=cos(cm(11)/180.0*PI)
cm(7)=sin(cm(11)/180.0*PI)
cm(8)=0.0
c*****
c Histories variabls hsv(1) to hsv(9) used to store
c transformation matrix "qmat" between the global and local system in the reference
configuration
c Histories variabls hsv(10) to hsv(18): deformation gradient components: Global current to
Global reference
c given by LS-DYNA main program
c*****

```

```

if (ncycle.eq.0) then
hsv(1)=qmat(1,1)
hsv(2)=qmat(2,1)
hsv(3)=qmat(3,1)
hsv(4)=qmat(1,2)
hsv(5)=qmat(2,2)
hsv(6)=qmat(3,2)
hsv(7)=qmat(1,3)
hsv(8)=qmat(2,3)
hsv(9)=qmat(3,3)
endif

```

```
c
```

```
c*****
```

```
c Deformation gradient: Local current to Global reference
```

```
c*****
```

```

FF11=qmat(1,1)*hsv(10)+qmat(2,1)*hsv(11)+qmat(3,1)*hsv(12)
FF12=qmat(1,1)*hsv(13)+qmat(2,1)*hsv(14)+qmat(3,1)*hsv(15)
FF13=qmat(1,1)*hsv(16)+qmat(2,1)*hsv(17)+qmat(3,1)*hsv(18)
FF21=qmat(1,2)*hsv(10)+qmat(2,2)*hsv(11)+qmat(3,2)*hsv(12)
FF22=qmat(1,2)*hsv(13)+qmat(2,2)*hsv(14)+qmat(3,2)*hsv(15)
FF23=qmat(1,2)*hsv(16)+qmat(2,2)*hsv(17)+qmat(3,2)*hsv(18)
FF31=qmat(1,3)*hsv(10)+qmat(2,3)*hsv(11)+qmat(3,3)*hsv(12)
FF32=qmat(1,3)*hsv(13)+qmat(2,3)*hsv(14)+qmat(3,3)*hsv(15)
FF33=qmat(1,3)*hsv(16)+qmat(2,3)*hsv(17)+qmat(3,3)*hsv(18)

```

```
c*****
```

```
c Deformation gradient: Local current to Local reference
```

```
c*****
```

```
F11=FF11*hsv(1)+FF12*hsv(2)+FF13*hsv(3)
```

$$F21=FF21 *hsv(1)+FF22*hsv(2)+FF23*hsv(3)$$

$$F31=FF31 *hsv(1)+FF32*hsv(2)+FF33*hsv(3)$$

$$F12=FF11 *hsv(4)+FF12*hsv(5)+FF13*hsv(6)$$

$$F22=FF21 *hsv(4)+FF22*hsv(5)+FF23*hsv(6)$$

$$F32=FF31 *hsv(4)+FF32*hsv(5)+FF33*hsv(6)$$

$$F13=FF11 *hsv(7)+FF12*hsv(8)+FF13*hsv(9)$$

$$F23=FF21 *hsv(7)+FF22*hsv(8)+FF23*hsv(9)$$

$$F33=FF31 *hsv(7)+FF32*hsv(8)+FF33*hsv(9)$$

$$F13=0.0$$

$$F23=0.0$$

$$F31=0.0$$

$$F32=0.0$$

$$F33=1./(F11*F22-F12*F21)$$

$$hsv(10)=F11$$

$$hsv(11)=F21$$

$$hsv(12)=F31$$

$$hsv(13)=F12$$

$$hsv(14)=F22$$

$$hsv(15)=F32$$

$$hsv(16)=F13$$

$$hsv(17)=F23$$

$$hsv(18)=F33$$

c\*\*\*\*\*

c Noting at this step, hsv(10) to hsv(18) become Deformation gradient: Local current to Local reference

c\*\*\*\*\*

c

c computed volume ratio

c

```

    detf=hsv(10)*(hsv(14)*hsv(18)-hsv(15)*hsv(17))
1   -hsv(11)*(hsv(13)*hsv(18)-hsv(15)*hsv(16))
2   +hsv(12)*(hsv(13)*hsv(17)-hsv(14)*hsv(16))
c
c   compute left cauchy-green tensor
c
b1=hsv(10)*hsv(10)+hsv(13)*hsv(13)+hsv(16)*hsv(16)
b2=hsv(11)*hsv(11)+hsv(14)*hsv(14)+hsv(17)*hsv(17)
b3=hsv(12)*hsv(12)+hsv(15)*hsv(15)+hsv(18)*hsv(18)
b4=hsv(10)*hsv(11)+hsv(13)*hsv(14)+hsv(16)*hsv(17)
b5=hsv(11)*hsv(12)+hsv(14)*hsv(15)+hsv(17)*hsv(18)
b6=hsv(10)*hsv(12)+hsv(13)*hsv(15)+hsv(16)*hsv(18)
c
c   compute square of left cauchy-green tensor FF_T
c
bb1=b1*b1+b4*b4+b6*b6
bb2=b4*b4+b2*b2+b5*b5
bb3=b6*b6+b5*b5+b3*b3
bb4=b1*b4+b2*b4+b5*b6
bb5=b6*b4+b5*b2+b3*b5
bb6=b6*b1+b5*b4+b3*b6
c
c   compute right cauchy-green tensor F_TF
c
c1=hsv(10)*hsv(10)+hsv(11)*hsv(11)+hsv(12)*hsv(12)
c2=hsv(13)*hsv(13)+hsv(14)*hsv(14)+hsv(15)*hsv(15)
c3=hsv(16)*hsv(16)+hsv(17)*hsv(17)+hsv(18)*hsv(18)
c4=hsv(10)*hsv(13)+hsv(11)*hsv(14)+hsv(12)*hsv(15)

```

$$c5=hsv(13)*hsv(16)+hsv(14)*hsv(17)+hsv(15)*hsv(18)$$

$$c6=hsv(10)*hsv(16)+hsv(11)*hsv(17)+hsv(12)*hsv(18)$$

c

c compute square of right cauchy-green tensor F\_TF

c

$$cc1=c1*c1+c4*c4+c6*c6$$

$$cc2=c4*c4+c2*c2+c5*c5$$

$$cc3=c6*c6+c5*c5+c3*c3$$

$$cc4=c1*c4+c2*c4+c5*c6$$

$$cc5=c6*c4+c5*c2*c3*c5$$

$$cc6=c6*c1+c5*c4+c3*c6$$

c

c deformed fiber orientations aa in current local configuration

c

$$aa1=hsv(10)*cm(6)+hsv(13)*cm(7)+hsv(16)*cm(8)$$

$$aa2=hsv(11)*cm(6)+hsv(14)*cm(7)+hsv(17)*cm(8)$$

$$aa3=hsv(12)*cm(6)+hsv(15)*cm(7)+hsv(18)*cm(8)$$

c

c compute aa tensor product aa

c

$$aaaa1=aa1*aa1$$

$$aaaa2=aa2*aa2$$

$$aaaa3=aa3*aa3$$

$$aaaa4=aa1*aa2$$

$$aaaa5=aa2*aa3$$

$$aaaa6=aa3*aa1$$

c

c compute b dot aa == baa

c

$$\text{baa1} = \text{b1} * \text{aa1} + \text{b4} * \text{aa2} + \text{b6} * \text{aa3}$$

$$\text{baa2} = \text{b4} * \text{aa1} + \text{b2} * \text{aa2} + \text{b5} * \text{aa3}$$

$$\text{baa3} = \text{b6} * \text{aa1} + \text{b5} * \text{aa2} + \text{b3} * \text{aa3}$$

c

c compute aa tensor product baa

c

$$\text{aabaa1} = \text{aa1} * \text{baa1} + \text{baa1} * \text{aa1}$$

$$\text{aabaa2} = \text{aa2} * \text{baa2} + \text{baa2} * \text{aa2}$$

$$\text{aabaa3} = \text{aa3} * \text{baa3} + \text{baa3} * \text{aa3}$$

$$\text{aabaa4} = \text{aa1} * \text{baa2} + \text{baa1} * \text{aa2}$$

$$\text{aabaa5} = \text{aa2} * \text{baa3} + \text{baa2} * \text{aa3}$$

$$\text{aabaa6} = \text{aa3} * \text{baa1} + \text{baa3} * \text{aa1}$$

c

c compute strain invariants invar1 (I1) invar2 (I2) invar4 (I4) invar5 (I5)

c

$$\text{invar1} = \text{c1} + \text{c2} + \text{c3}$$

$$\text{invar2} = 0.5 * (\text{c1} + \text{c2} + \text{c3}) ** 2 - 0.5 * (\text{cc1} + \text{cc2} + \text{cc3})$$

$$\text{invar4} = \text{c1} * \text{cm}(6) ** 2 + \text{c2} * \text{cm}(7) ** 2 + \text{c3} * \text{cm}(8) ** 2$$

$$1 + 2 * \text{c4} * \text{cm}(6) * \text{cm}(7) + 2 * \text{c5} * \text{cm}(7) * \text{cm}(8) + 2 * \text{c6} * \text{cm}(8) * \text{cm}(6)$$

$$\text{invar5} = \text{cc1} * \text{cm}(6) ** 2 + \text{cc2} * \text{cm}(7) ** 2 + \text{cc3} * \text{cm}(8) ** 2$$

$$1 + 2 * \text{cc4} * \text{cm}(6) * \text{cm}(7) + 2 * \text{cc5} * \text{cm}(7) * \text{cm}(8) + 2 * \text{cc6} * \text{cm}(8) * \text{cm}(6)$$

$$\text{lambda\_f} = \text{sqrt}(\text{invar4})$$

c lambda\_f = sqrt(aa1\*aa1+aa2\*aa2+aa3\*aa3)

c lambda\_f: fiber stretch

$$\text{lnlambda\_f} = \text{log}(\text{lambda\_f})$$

$$\text{T\_fiber} = 3.0 * \text{cm}(4) * \text{lnlambda\_f}$$

c T\_fiber: fiber stress

```

Trr=T_fiber*sqrt(c3)
c  sqrt(c3) accounts for thickness change of the membrane element
c
c*****
c  the following implies that fibers are always in 1-2 plane
c*****

cons=aa1*aa1+aa2*aa2
m_aa1=aa1/sqrt(cons)
n_aa2=aa2/sqrt(cons)
m2=aa1*aa1/cons
n2=aa2*aa2/cons
cosin_theta=aa1/sqrt(cons)
c  PI=4.D0*DATAN(1.D0)
angle=acos(cosin_theta)*180.00000000/PI
c      "angle" is the fiber angle with respect to local direction 1
c
c*****
c  compute Cauchy stress
c*****
c
if (lambda_f .GT. 1.) then
sig(1)=Trr*m2
sig(2)=Trr*n2
sig(3)=0.0
sig(4)=m_aa1*n_aa2*Trr
sig(5)=0.0
sig(6)=0.0
else

```

```

c   assume zero compressive stiffness

sig(1)=0.0
sig(2)=0.0
sig(3)=0.0
sig(4)=0.0
sig(5)=0.0
sig(6)=0.0
endif

c*****

c   material model available for solids and shells
c*****

else

c   write(iotty,20) etype
c   write(iohsp,20) etype
c   write(iomsg,20) etype
c   call adios(2)
cerdat(1)=etype
call lsmsg(3,MSG_SOL+1151,ioall,ierdat,rerdat,cerdat,0)
endif

epsp=T_fiber

c*****

c   Noting fiber stress is T_fiber not Trr
c   fiber angle output is "angle" is with respect to local direction 1
c*****

c

c20 format(/
c 1 '*** Error element type ',a,' can not be',
c 2 '      run with the current material model.')
```

```
return
end
```

## Appendix B: Example LS-DYNA input file

The input file for uniaxial tensile deformations of a transversely isotropic solid with fibers in the loading direction is given below. Only one 8-node brick element is used.

```
*KEYWORD
```

```
$-----
```

```
$ Qian Li and Romesh Batra, Computational Mechanics Lab, Virginia Tech
```

```
$ All rights reserved
```

```
$-----
```

```
$
```

```
$ PRMR1 VAL1 PRMR2 VAL2 PRMR3 VAL3 PRMR4 VAL4
```

```
*PARAMETER
```

```
$ safety factor |
```

```
R sf 0.50
```

```
$# of hsv in d3plot | # of hsv in ASCII | dt for ASCII | dt for ascii |
```

```
I hsvd3p 18I hsvasc 18R dtd3p 1.0R dtAscii 1.0
```

```
$
```

```
*PARAMETER_EXPRESSION
```

```
R endtim 100.0
```

```
R maxdispl 0.1
```

```
$
```

```
*TITLE
```

```
Simple shear with fiber anlge 30 degree
```

```
*COMMENT
```

```
Units used: mass=kg , length=m , time=s
```

```
$
```

```

$ *****
$ ! UNITS TO USE IN THE INPUT FILE !
$ ! mass: kg _\ force: N !
$ ! length: m _ ) stress: Pa !
$ ! time: s / energy: J !
$ *****
$
$ * * * * *
$
$ -----
$ ! Material Definition !
$ -----
$
*PARAMETER_EXPRESSION
R cp1 100.0
R cm1 0.100
R poisson 0.499
$
$
R shear (&cp1+&cm1)
R bulk (&cp1+&cm1)*2.0*(1.0+&poisson)/(3.0*(1.0-2.0*&poisson))
*MAT_USER_DEFINED_MATERIAL_MODELS
$-----|-----|-----|-----|-----|-----|-----|-----|
$ MID RO MT LMC NHV IORTHO IBULK IG
1 1.00E+09 45 10 0 1 3 4
$-----|-----|-----|-----|-----|-----|-----|-----|
$ IVECT IFAIL ITERM IHYPER IEOS
0 0 0 1 0

```

```

$-----|-----|-----|-----|-----|-----|-----|-----|
$  AOPT  MACF  XP   YP   ZP   A1   A2   A3
    0.0   1    0    0    0    0    0    0
$-----|-----|-----|-----|-----|-----|-----|-----|
$  V1    V2    V3    D1    D2    D3    BETA  IEVTS
    0    0    0    0    0    0    0    0
$-----|-----|-----|-----|-----|-----|-----|-----|
$  C1    C2  BULK    G    VF    LAX    LAY    LAZ
$  P1    P2    P3    P4    P5    P6    P7    P8
1.000E+06 1.000E+06 5.000E+14 1.000E+09 0.30.866025400.50000000 0
$-----|-----|-----|-----|-----|-----|-----|-----|
$ gamma4  gamma5
$  P9    P10
2.000E+09 2.000E+09
$
$          !      Geometry and Mesh Definition      !
$          !-----!
*SECTION_SOLID_TITLE
$ SECID  ELFORM  AET
red. int.
    1    1    0
S/R int.
    2    2    0
full. int.
    3    3    0
CZM
    4    19    0
$

```

\*HOURGLASS\_TITLE

\$ HGID IHQ QM IBQ Q1 Q2 QB/VDC QW

hg6(0.20)

1 6 0.20

hg6(1.00)

2 6 1.00

hg5(0.10)

3 5 0.10

\$

\*PART

\$ PID SECID MID EOSID HGID

solid block

1 1 1 0 2

\$

\$ \* \* \* \* \*

\$ \* \* \* \* \*

\$

\$

\$ ! Nodes, Connectivity, Node- & Segment-Sets !

\$

\$

\*SET\_NODE\_LIST\_GENERATE\_TITLE

solid block

\$ SID

1

\$ B1BEG B1END

1 8

\*NODE

\$ NID	X	Y	Z
1	0.0	0.0	0.0
2	0.1	0.0	0.0
3	0.1	0.1	0.0
4	0.0	0.1	0.0
5	0.0	0.0	0.1
6	0.1	0.0	0.1
7	0.1	0.1	0.1
8	0.0	0.1	0.1

\*ELEMENT\_SOLID\_ORTHO

\$ EID	PID	N1	N2	N3	N4	N5	N6	N7	N8
1	1	1	2	3	4	5	6	7	8

\$-----|-----|-----|-----|-----|-----|-----|-----|

\$ BETA	A2	A3
0	0	0

\$-----|-----|-----|-----|-----|-----|-----|-----|

\$ D1	D2	D3
0	0	0

\*SET\_NODE\_LIST\_TITLE

bottom

\$ SID
2

\$ N1	N2	N3	N4	N5	N6	N7	N8
1	2	3	4				

\*SET\_NODE\_LIST\_TITLE

top

\$ SID
3

```
$  N1  N2  N3  N4  N5  N6  N7  N8
   5   6   7   8
```

```
*SET_NODE_LIST_TITLE
```

```
left
```

```
$  SID
```

```
4
```

```
$  N1  N2  N3  N4  N5  N6  N7  N8
```

```
1   2   6   5
```

```
*SET_NODE_LIST_TITLE
```

```
right
```

```
$  SID
```

```
5
```

```
$  N1  N2  N3  N4  N5  N6  N7  N8
```

```
4   3   7   8
```

```
*SET_NODE_LIST_TITLE
```

```
rear
```

```
$  SID
```

```
6
```

```
$  N1  N2  N3  N4  N5  N6  N7  N8
```

```
1   4   8   5
```

```
*SET_NODE_LIST_TITLE
```

```
front
```

```
$  SID
```

```
7
```

```
$  N1  N2  N3  N4  N5  N6  N7  N8
```

```
2   3   6   7
```

```
$
```

```
$                * * * * *
```

```

$
$
$      -----
$      !      Boundary Conditions      !
$      -----
$
$
$      *****
$      *** BOUNDARY CONDITIONS ***
$      *****
$
$
*BOUNDARY_SPC_SET_ID
$  ID  TITLE
    1  bottom
$  NSID  CID  DOFX  DOFY  DOFZ  DOFRX  DOFRY  DOFRZ
    2    0    0    1    1    0    0    0
*BOUNDARY_SPC_SET_ID
$  ID  TITLE
    2  top
$  NSID  CID  DOFX  DOFY  DOFZ  DOFRX  DOFRY  DOFRZ
    3    0    0    1    0    0    0    0
*BOUNDARY_SPC_SET_ID
$  ID  TITLE
    3  top
$  NSID  CID  DOFX  DOFY  DOFZ  DOFRX  DOFRY  DOFRZ
    4    0    1    0    0    0    0    0
*BOUNDARY_PRESCRIBED_MOTION_SET_ID
$  ID  TITLE
    2  x-displ
$  NSID  DOF  VAD  LCID  SF

```

5 1 2 1 1.0

\*DEFINE\_CURVE\_TITLE

displacement vs. time

\$ LCID SIDR SFA SFO

1 0&endtim &maxdispl

\$ Abcissa(time) Ordinate(dis)

0.000 0.000

1.000 1.000

10.000 10.000

\$ -----

\$ ! Controls !

\$ -----

\$

\$ \*\*\*\*\*

\$ \*\*\* TIME CONTROL KEYWORDS \*\*\*

\$ \*\*\*\*\*

\$

\*CONTROL\_TERMINATION

\$ ENDTIM ENDCYC DTMIN ENDNEG ENDMAS NOSOL

&endtim

\$

\*CONTROL\_TIMESTEP

\$ DTINIT TSSFAC ISDO TSLIMIT DT2MS LCTM ERODE MS1ST

0.0 &sf 99

\*DEFINE\_CURVE\_TITLE

time step control

\$ LCID SIDR SFA SFO OFFA OFFO DATTYP

99 0 1.0 1.0 0.0 0.0 0

```

$      Abcissa      Ordinate
      0.0          1.0E+20
&endtim          1.0E+20

$

$      *****
$      *** SOLUTION/MESH CONTROL KEYWORDS ***
$      *****
$

*CONTROL_SOLUTION
$  SOLN  NLQ  ISNaN  LCINT
      1

$

*CONTROL_SOLID
$  ESORT  FMATRIX  NIPTETS  SWLOCL  PSFAIL
      99

$ PSFAIL: Optional solid part set ID specifying which part ID's are checked for negative
volumes prior to element processing

*SET_PART_LIST_TITLE
psfail
$  SID  DA1  DA2  DA3  DA4
      99
$  PID1  PID2  PID3  PID4  PID5  PID6  PID7  PID8
      1

$      *****
$      *** ARTIFICIAL VISCOSITY ***
$      *****
$

*CONTROL_BULK_VISCOSITY
$  Q1  Q2  TYPE

```

```

1.5  0.06  1
$
$           * * * * *
$
$  -----
$  !      Data Output Settings      !
$  -----
$
$           *****
$           *** OUTPUT CONTROL ***
$           *****
$
*CONTROL_OUTPUT
$  NPOPT  NEECHO  NREFUP  IACCOP  OPIFS  IPNINT  IKEDIT  IFLUSH
    1
$  IPRTF  IERODE  TET10  MSGMAX  IPCURV  GMDT
    0
*CONTROL_ENERGY
$  HGEN  RWEN  SLNTEN  RYLEN
    2    2    2    2
*DATABASE_FORMAT
$  IFORM  IBINARY
    1
$
*PARAMETER_EXPRESSION
R  tfsafe 10.0*&endtim
*DEFINE_CURVE_TITLE
d3plot output

```

```

$  LCID  SIDR  SFA  SFO  OFFA  OFFO  DATTYP
    97    0   1.0   1.0   0.0   0.0   0
$  Abcissa(time)  Ordinate(Vel)
    0.0&dtd3p
&endtim          &dtd3p
&tfsafe          &dtd3p
*DEFINE_CURVE_TITLE
Ascii output
$  LCID  SIDR  SFA  SFO  OFFA  OFFO  DATTYP
    98    0   1.0   1.0   0.0   0.0   0
$  Abcissa(time)  Ordinate(Vel)
    0.0&dtAscii
&endtim          &dtAscii
&tfsafe          &dtAscii
$
$
$          *****
$          *** STATE PLOT OUTPUT ***
$          *****
$
*DATABASE_BINARY_D3PLOT
$ DT/CYCL LCDT/NR  BEAM  NPLTC  PSETID
    97    0    0    0
$ IOOPT
    1
*DATABASE_EXTENT_BINARY
$      shell  shell      shell  shell  shell  shell
$ NEIPH  NEIPS  MAXINT  STRFLG  SIGFLG  EPSFLG  RLTF LG  ENGFLG
&hsvd3p    0    0    1    0    0    0    0

```

\$ CMPFLG IEVERP

0 0

\*DATABASE\_BNDOUT

\$ DT BINARY LCUR IOOPT

98 1

\$

\$

\*DATABASE\_ELOUT

\$ DT BINARY LCUR IOOPT NEIPH

98 1&hsvasc

\*DATABASE\_HISTORY\_SOLID\_SET

\$ ID1 ID2 ID3 ID4 ID5 ID6 ID7 ID8

999

\*SET\_SOLID\_TITLE

elout

\$ SID

999

\$ K1 K2 K3 K4 K5 K6 K7 K8

1

\$

\*DATABASE\_NODOUT

\$ DT BINARY LCUR IOOPT

98 1

\*DATABASE\_HISTORY\_NODE\_SET

\$ ID1 ID2 ID3 ID4 ID5 ID6 ID7 ID8

999

\*SET\_NODE\_LIST\_TITLE

nodout

```
$  SID
    999
$  N1   N2   N3   N4   N5   N6   N7   N8
    1    2    3    4    5    6    7    8
$
$          *****
$          *** ENERGY DATA OUTPUT ***
$          *****
$
$
$
*DATABASE_MATSUM
$  DT  BINARY  LCUR  IOOPT
          98    1
*DATABASE_GLSTAT
$  DT  BINARY  LCUR  IOOPT
          98    1
*END
```

## References

1. Batra, R.C., *Rubber Covered Rolls - Non-Linear Elastic Problem*. Journal of Applied Mechanics-Transactions of the Asme, 1980. **47**(1): p. 82-86.
2. Bapat, C.N. and Batra, R.C., *Finite Plane-Strain Deformations of Nonlinear Viscoelastic Rubber-Covered Rolls*. International Journal for Numerical Methods in Engineering, 1984. **20**(10): p. 1911-1927.
3. Helnwein, P., Liu, C.H., Meschke, G., and Mang, H.A., *A New 3-D Finite Element Model for Fiber-Reinforced Rubber Composites—Application to Analysis of Automobile Tires*. Finite Element Analysis and Design, 1993. **14**: p. 1-16.
4. Meschke, G. and Helnwein, P., *Large-Strain 3d-Analysis of Fiber-Reinforced Composites Using Rebar Elements - Hyperelastic Formulations for Cords*. Computational Mechanics, 1994. **13**(4): p. 241-254.
5. Mang, H.A. and Meschke, G., *Nonlinear Finite-Element Analysis of Reinforced and Prestressed Concrete Structures*. Engineering Structures, 1991. **13**(2): p. 211-226.
6. ABAQUS, *ABAQUS Version 6.11 Documentation*. 2011.
7. Batra, R.C., Gopinath, G., and Zheng, J.Q., *Material parameters for pressure-dependent yielding of unidirectional fiber-reinforced polymeric composites*. Composites Part B-Engineering, 2012. **43**(6): p. 2594-2604.
8. Pipkin, A.C., *Stress Analysis for Fiber-Reinforced Materials*. Advances in Applied Mechanics, 1979. **19**.
9. Spencer, A.J.M., *Constitutive Theory of Strongly Anisotropic Solids*. Continuum Theory of the Mechanics of Fiber-Reinforced Composites, ed. Spencer A.J.M. 1984, Vienna: Springer.
10. Qiu, G.Y. and Pence, T.J., *Remarks on the behavior of simple directionally reinforced incompressible nonlinearly elastic solids*. Journal of Elasticity, 1997. **49**(1): p. 1-30.
11. Merodio, J. and Ogden, R.W., *Mechanical response of fiber-reinforced incompressible non-linearly elastic solids*. International Journal of Non-Linear Mechanics, 2005. **40**(2-3): p. 213-227.
12. Holzapfel, G.A., Gasser, T.C., and Ogden, R.W., *A new constitutive framework for arterial wall mechanics and a comparative study of material models*. Journal of Elasticity, 2000. **61**(1-3): p. 1-48.
13. Gasser, T.C., Ogden, R.W., and Holzapfel, G.A., *Hyperelastic modelling of arterial layers with distributed collagen fibre orientations*. Journal of the Royal Society Interface, 2006. **3**(6): p. 15-35.
14. deBotton, G., Hariton, I., and Socolsky, E.A., *Neo-Hookean fiber-reinforced composites in finite elasticity*. Journal of the Mechanics and Physics of Solids, 2006. **54**(3): p. 533-559.
15. Guo, Z.Y., Peng, X.Q., and Moran, B., *A composites-based hyperelastic constitutive model for soft tissue with application to the human annulus fibrosus*. Journal of the Mechanics and Physics of Solids, 2006. **54**(9): p. 1952-1971.
16. Weiss, J.A., Maker, B.N., and Govindjee, S., *Finite element implementation of incompressible, transversely isotropic hyperelasticity*. Computer Methods in Applied Mechanics and Engineering, 1996. **135**(1-2): p. 107-128.

17. Peng, X.Q., Guo, Z.Y., and Moran, B., *An anisotropic hyperelastic constitutive model with fiber-matrix shear interaction for the human annulus fibrosus*. Journal of Applied Mechanics-Transactions of the Asme, 2006. **73**(5): p. 815-824.
18. Ericksen, J.L. and Rivlin, R.S., *Large Elastic Deformations of Homogeneous Anisotropic Materials*. Journal of Rational Mechanics and Analysis, 1954. **3**(3): p. 281-301.
19. Batra, R.C., *Universal relations for transversely isotropic elastic materials*. Mathematics and Mechanics of Solids, 2002. **7**(4): p. 421-437.
20. Batra, R.C. and Liang, X.Q., *Finite dynamic deformations of smart structures*. Computational Mechanics, 1997. **20**(5): p. 427-438.
21. Love, B.M. and Batra, R.C., *Determination of effective thermomechanical parameters of a mixture of two elastothermoviscoplastic constituents*. International Journal of Plasticity, 2006. **22**(6): p. 1026-1061.
22. Bowen, R.M., *Theory of Mixtures*. Continuum Physics, ed. C. E.A. Vol. 3. 1976, New York: Academic Press.
23. Batra, R.C., *Elements of Continuum Mechanics*. 2006, Reston, VA: AIAA Publishers.
24. Mooney, M.A., *Theory of Large Elastic Deformations*. Journal of Applied Physics, 1940. **11**: p. 582-592.
25. Truesdell, C. and Noll, W., *Nonlinear Field Theories of Mechanics*. Vol. 3. 1965: Handbuch der Physik.
26. Corporation, L.S.T., *LS-DYNA R7.1 Keyword User's Manual, Appendix A*. 2014, Livermore, CA: LSTC.
27. Belytschko, T. and Bindeman, L.P., *Assumed Strain Stabilization of the 8 Node Hexahedral Element*. Computer Methods in Applied Mechanics and Engineering, 1993. **105**(2): p. 225-260.
28. Ericksen, J.L., *Deformations Possible in Every Isotropic Incompressible Perfectly Elastic Body*. Zeitschrift für angewandte Mathematik und Physik, 1954. **5**: p. 466-486.
29. Lai, W.M., Rubin, D., and Krempl, E., *Introduction to Continuum Mechanics, 4th ed.* 2010, Philadelphia: Elsevier.
30. Hughes, T.J.R., *The Finite Element Method: Linear Static and Dynamic Finite Element Analysis*. 2000, Mineola, NY: Dover Civil and Mechanical Engineering.

# Chapter 3: Strain Energy Density Function Quadratic in Components of Cauchy-Green Strain Tensor for Finite Deformations of Incompressible Transversely Isotropic Solids

Qian Li, David A. Dillard, Romesh C. Batra

Biomedical Engineering and Mechanics Department, Virginia Tech,

Blacksburg, VA, 24061, USA

## Abstract

We assume that a fiber-reinforced rubberlike material (FRRM) can be modeled as a homogeneous, transversely isotropic, incompressible and hyperelastic with the axis of transverse isotropy along the fiber. An explicit expression for the Cauchy stress tensor is derived by taking the stored energy function,  $W$ , to be a complete quadratic function of components of the Cauchy-Green strain tensor. Homogeneous deformations such as simple extension, simple shear, and biaxial loading are studied to delineate the mechanical behaviors of the FRRMs. Consistency with the infinitesimal theory requires terms linear in both the 4<sup>th</sup> and the 5<sup>th</sup> invariants,  $I_4$  and  $I_5$ , be included in the expression for  $W$ . A stability analysis of simple tensile/compressive deformations with the load along the fiber reveals the possibility of unequal lateral stretches triggered by the considering the  $(I_4 - 1)(I_1 - 3)$  term in  $W$ . Analytical solutions for inflation, extension and twist deformations caused by internal pressure, end torque, and axial force for a pressurized cylindrical laminate are derived using Ericksen's inverse method. Effects of fiber orientations on the mechanical deformations of a  $\pm\alpha$  angle-ply cylindrical tube are investigated. To numerically solve boundary-value problems, this material model is incorporated in the commercial software, LS-DYNA, as a user-defined subroutine. The implementation has been verified by ensuring that the computed solutions of a few boundary value problems agree well with either their analytical solutions or those available in the literature.

**Key words:** fiber-reinforced rubberlike material; transversely isotropic hyperelastic material; instabilities; finite deformations; combined twisting, extension and radial expansion of a cylinder

### 3.1 Introduction

Numerous phenomenological constitutive models for simulating the macroscopic response of structures composed of nonlinear and anisotropic hyperelastic materials have been proposed. For a hyperelastic material, there exists a stored or strain energy density function (per unit reference volume),  $W$ , of the deformation gradient,  $\mathbf{F}$ . For simplicity, we use rectangular Cartesian coordinates to describe the position of a material point in the undeformed ( $\mathbf{x}$ ), and the deformed ( $\mathbf{X}$ ) configurations. For a homogeneous material,  $W$  does not explicitly depend upon the material particle,  $\mathbf{X}$ . The requirement that  $W$  is invariant under rigid body motions superimposed upon the deformed configuration implies that  $W$  is a function of  $\mathbf{U}$  or  $\mathbf{C}$  where  $\mathbf{F} = \mathbf{R}\mathbf{U}$  is the polar decomposition of  $\mathbf{F}$  into an orthogonal matrix  $\mathbf{R}$  and a symmetric positive-definite matrix  $\mathbf{U}$ , and  $\mathbf{C} = \mathbf{U}^2$  is the right Cauchy-Green strain tensor.

For a general anisotropic hyperelastic material, there are no planes of symmetry and  $W$  is a function of the six components of  $\mathbf{C}$ . All six components of  $\mathbf{C}$  always determine the material response, however, they appear in specific forms when the material point exhibits material symmetry. For example, for an isotropic material,  $W$  must be invariant under all rotations of the reference configuration before it is loaded. This implies that  $W = W(\mathbf{C})$  be a function of the three invariants,  $I_1 = \text{tr } \mathbf{C}$ ,  $I_2 = \frac{1}{2}[(\text{tr } \mathbf{C})^2 - \text{tr}(\mathbf{C}^2)]$ ,  $I_3 = \det \mathbf{C}$ . A general requirement is that  $W > 0$  for every  $\mathbf{F} \neq \mathbf{R}$  that satisfies  $I_3 > 0$ . However, it is difficult to derive restrictions on  $W$  that satisfy this condition.

In terms of the components of  $\mathbf{C}$  with respect to a rectangular Cartesian coordinate system  $I_1 = C_{11} + C_{22} + C_{33}$ , and  $I_2 = C_{11}C_{22} + C_{11}C_{33} + C_{22}C_{33} - (C_{12})^2 - (C_{23})^2 - (C_{13})^2$ . We note that  $C_{ii}$  (no sum on  $i$ ) equals the square of the stretch of a line element parallel to the  $X_i$ -axis in the reference configuration. Thus  $I_1$  equals the sum of squares of stretches along the  $X_1$ -, the  $X_2$ - and the  $X_3$ -axes. The invariant  $I_3$  equals the product of the squares of these three stretches and hence is  $\geq 1$ .

It can be shown that for an incompressible material, for which admissible deformations are volume preserving and hence satisfy  $I_3 = 1$ ,  $I_1 \geq 3$ , and  $I_2 \geq 3$ , and the minimum values of  $I_1$  and  $I_2$  occur in the reference configuration. For an incompressible hyperelastic material, expressions for

stresses can be derived from  $W$  only to within a hydrostatic pressure that cannot be determined from  $\mathbf{F}$ , but is found as a part of the solution of the initial boundary value problem (IBVP).

Ericksen and Rivlin [3] showed that  $W$  for a transversely isotropic material is at most a function of five invariants of  $\mathbf{C}$  and the unit vector  $\mathbf{A}_0$  along the direction of transverse isotropy in the reference configuration (i.e.,  $I_1, I_2, I_3, I_4, I_5$ , where  $I_4 = \mathbf{A}_0 \cdot \mathbf{C} \mathbf{A}_0, I_5 = \mathbf{A}_0 \cdot \mathbf{C}^2 \mathbf{A}_0$ ), and obtained closed-form analytical solutions for a few BVPs. For a transversely isotropic

material, rotations about  $\mathbf{A}_0$  do not affect  $W$ , and material properties in every direction perpendicular to  $\mathbf{A}_0$  are the same. Rivlin [4] and Batra [5] independently derived universal relations for these materials that provide necessary conditions satisfied by deformations for the material being studied to be transversely isotropic.

In addition to  $I_1, I_2, I_3$  either  $I_4$  or  $I_5$  or both are commonly used to characterize transversely isotropic FRRMs. Murphy [6] pointed that both  $I_4$  and  $I_5$  should be considered if the shear modulus of the material for infinitesimal deformations in planes parallel to and normal to the fiber direction are to match with those found from the test data.

For incompressible FRRMs and inextensible fibers, Pipkin [7] has analytically solved several boundary value problems (BVP). The constraint of inextensibility of fibers implies that  $I_4 = 1$ , which is thus excluded from the expression for  $W$ , and the axial stress in the fiber cannot be found from  $\mathbf{F}$ .

A comprehensive review of constitutive relations for arteries is given by Holzapfel and Ogden [8].

The nonlinear elastic behavior of FRRMs is generally described by assuming  $W$  to be either a polynomial, or an exponential or a logarithmic function of the invariants. The mathematical expression and the number of invariants to be included in the expression for  $W$  is usually guided by the experimental data. For example, a strong stiffening effect of each layer observed at high pressures motivated researchers to use an exponential function of invariants for describing the strain energy stored in the collagen fibers. There is currently no single phenomenological

constitutive relation that can reasonably well predict the response of FRRMs under different loadings.

Structures made of FRRMs often involve multiple layers of material stacked to form laminates. Each layer may have a different fiber orientation and, in some cases, be composed of a different material. A two-layer,  $\pm\alpha$  angle ply tube is often seen in both engineering structures and biological tissues. For example, tire belts [9] as well as rubber hoses [10] reinforced with helically wound fibers, provide strength, stiffness, and flexibility for the structures. In [11], the media and the adventitia of an artery are modeled as thick-walled cylindrical tubes composed of two families of collagen fibers wound in a  $\pm\alpha$  angle configuration.

For plies of different fiber orientations bonded together, Spencer [12], among others, has shown that  $\mathbf{W}$  can be expressed as a function of several invariants of  $\mathbf{C}$  that involve the fiber direction in the reference configuration. Under the restriction of inextensible fibers, Spencer et al. [13] studied infinitesimal inflation and axial compression of a circular cylindrical tube reinforced with two families of  $\pm\alpha$  angle fibers.

Analytical solutions are desirable for characterizing the material response and designing structures. For isotropic rubberlike materials, Batra [14] studied the finite radial expansion and torsional deformations of cylindrical tubes under pressure and end torque loadings. Batra and Bahrami [15] studied finite axisymmetric radial deformations of a circular cylinder composed of an inhomogeneous Mooney–Rivlin material with the two material parameters varying continuously through the cylinder thickness either by a power law or an affine relation.

In Holzapfel et al. [16], an artery is modeled as a thick-walled cylindrical tube, representing a non-collagenous matrix reinforced by two layers, the media and the adventitia, each of which is composed of two families of collagen fibers wound in a helical configuration. For studying the response of an artery under combined axial extension, inflation, and torsion, each layer material is modeled as an orthotropic material. Hamdaoui et al. [17] analyzed combined finite extension, radial expansion, and torsion of a circular cylindrical tube made of a transversely isotropic material, and showed that the deformations are controllable only for certain directions of fibers,

namely, the radial direction and an arbitrary direction in planes locally normal to the radial direction.

For complex geometries of components made of FRRMs, it is very difficult, if not impossible, to find analytical solutions of IBVPs. Therefore, numerical methods, such as the finite element method (FEM), that can account for geometric irregularities, material heterogeneities, realistic boundary conditions and large deformations are used to analyze such problems. The FEM is a technique to numerically find an approximate solution of a given IBVP which is a mathematical representation of a physical problem. An IBVP is comprised of either ordinary or partial differential equations together with initial and boundary conditions. Several FE commercial software packages (e.g., ABAQUS, ANSYS, and LS-DYNA) are being routinely used in various industries. Many well developed material models such as linearly elastic and elastic-plastic are built into these codes, allowing engineers to predict deformations of structures made of these materials. However, reliable, thermodynamically consistent and experimentally validated material models for FRRMs suitable for analyzing finite deformations have not been implemented in these codes. The user-defined features in them allow users to add their own constitutive relations, and avoid the development of the complete software [18].

### 3.2 Material model for FRRM

We use rectangular Cartesian coordinate axes to describe deformations of the body, and denote positions of a material point in the stress-free reference and the current configurations, respectively, by  $(X_1, X_2, X_3)$  and  $(x_1, x_2, x_3)$ . Thus,  $\mathbf{u} = \mathbf{x} - \mathbf{X}$ , gives the displacement of a material point. For studying finite elastic deformations of an FRRM body, we model the material as transversely isotropic, hyperelastic and incompressible with the unit vector  $\mathbf{A}_0$  along the fiber in the reference configuration as the axis of transverse isotropy. Unless stated otherwise, the  $X_1$  – axis is assumed to be aligned along fibers, thus  $\mathbf{A}_0 = (1, 0, 0)$ .

As proved by Ericksen and Rivlin [3], the strain energy density function,  $W$ , for this material is a function of the four invariants,  $I_1, I_2, I_4$  and  $I_5$ , defined as

$$I_1 = \text{tr}(\mathbf{C}), I_2 = \left\{ [\text{tr}(\mathbf{C})]^2 - \text{tr}(\mathbf{C}^2) \right\} / 2, I_4 = \mathbf{A}_0 \cdot \mathbf{C} \mathbf{A}_0, I_5 = \mathbf{A}_0 \cdot \mathbf{C}^2 \mathbf{A}_0 \quad (3.1)$$

where  $\mathbf{C} = \mathbf{F}^T \mathbf{F}$  is the right Cauchy-Green tensor,  $\mathbf{F} = \text{Grad}(\mathbf{x})$  with gradients taken with respect to  $\mathbf{X}$  is the deformation gradient, and  $\mathbf{F}^T$  equals the transpose of  $\mathbf{F}$ . For incompressible materials, only isochoric deformations are admissible for which  $I_3 = \det[\mathbf{F}] = 1$

Finding the expression for  $W$  requires test data from numerous experiments, as should be clear from Rivlin's [19] and James et al.'s [20, 21] work for incompressible and isotropic materials for which  $W$  is a function of  $I_1$  and  $I_2$  only.

### 3.2.1 Expression for the strain energy density, $W$

Here we postulate the following expression for  $W$  that is quadratic in  $\mathbf{C}$ .

$$\begin{aligned} W = & h_1 (I_1 - 3) + h_{11} (I_1 - 3)^2 + h_2 (I_2 - 3) \\ & + h_4 (I_4 - 1) + h_{44} (I_4 - 1)^2 + h_5 (I_5 - 1) + h_{14} (I_1 - 3)(I_4 - 1) \end{aligned} \quad (3.2)$$

The seven material constants  $h_1, h_4, h_{11}, h_{44}, h_{14}, h_2,$  and  $h_5$  are to be determined from the test data. Equation (3.2) is a Taylor series expansion of  $W$  about the reference configuration similar to that used by James et al. [20, 21] for isotropic materials. For a Mooney-Rivlin material, only  $h_1$  and  $h_2$  are non-zero.

As pointed out by Ogden and Meridio [22] and Pence and Qiu [23], one can regard Eq. (3.2) as representing the strain energy density of an isotropic base matrix represented by the first three terms on its right-hand side, and the effect of fibers incorporated into the other four terms involving invariants  $I_4$  and  $I_5$ . The last term on the right-hand side of Eq. (3.2) represents the interaction between the matrix and the reinforcements.

The Cauchy stress tensor for the material described by Eq. (3.2) has the following expression [13]:

$$\begin{aligned} \boldsymbol{\sigma} = & -p\mathbf{I} + 2\mathbf{F} \frac{\partial W}{\partial \mathbf{C}} \mathbf{F}^T \\ = & -p\mathbf{I} + 2[h_1 + 2h_{11}(I_1 - 3) + h_{14}(I_4 - 1)]\mathbf{B} + 2h_2(I_1\mathbf{B} - \mathbf{B}^2) \\ & + 2[h_4 + 2h_{44}(I_4 - 1) + h_{14}(I_1 - 3)]\mathbf{a} \otimes \mathbf{a} + 2h_5(\mathbf{a} \otimes \mathbf{B}\mathbf{a} + \mathbf{B}\mathbf{a} \otimes \mathbf{a}) \end{aligned} \quad (3.3)$$

where  $\mathbf{I}$  is the identity matrix and  $p$  the hydrostatic pressure, not determined from  $\mathbf{F}$  but found by solving an IBVP that has normal tractions prescribed on a non-zero portion of the boundary. Furthermore,  $\mathbf{a} = \mathbf{F}\mathbf{A}_0$  is the vector into which the unit vector  $\mathbf{A}_0$  is deformed (or along a fiber in the current configuration),  $\mathbf{B} = \mathbf{F}\mathbf{F}^T$  is the left Cauchy-Green tensor, and  $\mathbf{a} \otimes \mathbf{b}$  denotes the tensor product between vectors  $\mathbf{a}$  and  $\mathbf{b}$  defined as  $(\mathbf{a} \otimes \mathbf{b})\mathbf{c} = (\mathbf{b} \cdot \mathbf{c})\mathbf{a}$ . Thus the magnitude of  $\mathbf{a}$  equals the fiber stretch and the angle,  $\theta$ , between vectors  $\mathbf{a}$  and  $\mathbf{A}_0$  given by

$$\cos(\theta) = \frac{(\mathbf{a} \cdot \mathbf{A}_0)}{|\mathbf{a}|} \quad (3.4)$$

equals the rotation of the fiber from its orientation in the reference configuration to that in the current configuration.

In the reference configuration,  $\mathbf{F} = \mathbf{B} = \mathbf{I}$ , and the expression (3.3) for the Cauchy stress tensor simplifies to

$$\boldsymbol{\sigma}|_0 = (-p|_0 + 2h_1 + 4h_2)\mathbf{I} + (2h_4 + 4h_5)\mathbf{A}_0 \otimes \mathbf{A}_0 \quad (3.5)$$

where  $p|_0$  is the hydrostatic pressure in the reference configuration. As mentioned above, we assume that the reference configuration is stress-free. Thus

$$2h_1 + 4h_2 = p|_0; h_4 + 2h_5 = 0 \quad (3.6)$$

That is, for the reference configuration to be stress-free, either both terms linear in  $(I_4 - I)$  and  $(I_5 - I)$  or none of these two terms should be included in the stored energy function. Eq. (3.6)<sub>2</sub> gives  $h_4 = -2h_5$ . We substitute  $h_4 = -2h_5$  into Eq. (3.2) and work with the modified constitutive relation henceforth.

### 3.2.2 Constitutive relation for infinitesimal deformations

A constitutive relation for a nonlinear elastic material must reduce to Hooke's law for infinitesimal deformations. We exploit this to identify some of the six material constants  $h_1, h_{11}, h_{44}, h_{14}, h_2,$

and  $h_5$ . The infinitesimal strain tensor  $\mathbf{e}$  is defined as  $\mathbf{e} = (\mathbf{H} + \mathbf{H}^T)/2$  where  $\mathbf{H} = \partial\mathbf{u}/\partial\mathbf{X}$  is the displacement gradient. For infinitesimal deformations, only first order terms in  $\mathbf{H}$  and  $\mathbf{e}$  are retained in the constitutive relation, and the incompressibility condition reduces to  $tr(\mathbf{e})=0$ . Thus, for fibers aligned along the  $X_1$ -axis,  $\mathbf{C}=\mathbf{B}=\mathbf{I}+2\mathbf{e}$ ,  $I_1=3+2tr(\mathbf{e})$ ,  $I_2=3+4tr(\mathbf{e})$ ,  $I_4=1+2e_{11}$ , and  $I_5 = 1+ 4e_{11}$ . Equation (3.3), in component form, can be rewritten as

$$\begin{aligned}
\sigma_{11} &= -p + 4(h_1 + h_2 + 2h_5 + h_{44})e_{11} \\
\sigma_{22} &= -p + 4(h_1 + h_2)e_{22} \\
\sigma_{33} &= -p + 4(h_1 + h_2)e_{33} \\
\sigma_{12} &= 4(h_1 + h_2 + h_5)e_{12} \\
\sigma_{13} &= 4(h_1 + h_2 + h_5)e_{13} \\
\sigma_{23} &= 4(h_1 + h_2)e_{23}
\end{aligned} \tag{3.7}$$

As pointed out by Spencer [12], Hooke's law for an incompressible transversely isotropic material has only 3 independent material elasticities. In terms of Young's modulus  $E_L(E_T)$  along (transverse to) the fibers, the shear modulus  $G_L(G_T)$  for shear deformations in the  $X_1X_2$ - ( $X_2X_3$ -) plane, the stress-strain relations (3.7) become

$$\begin{aligned}
\sigma_{11} &= -p + (E_L - G_T)e_{11} \\
\sigma_{22} &= -p + 2G_T e_{22} \\
\sigma_{33} &= -p + 2G_T e_{33} \\
\sigma_{12} &= 2G_L e_{12} \\
\sigma_{13} &= 2G_L e_{13} \\
\sigma_{23} &= 2G_T e_{23}
\end{aligned} \tag{3.8}$$

where

$$G_T = \frac{E_L E_T}{4E_L - E_T}. \tag{3.9}$$

For  $E_L/E_T \gg 1$ ,  $G_T = E_T/4$ . The comparison of Eqs. (3.4) and (3.5) gives

$$\begin{aligned}
2(h_1 + h_2) &= G_T \\
2(h_1 + h_2 + h_5) &= G_L \\
4(h_1 + h_2 + 2h_5 + 2h_{44}) &= E_L - G_T
\end{aligned} \tag{3.10}$$

For the strain energy density to be positive definite for non-trivial infinitesimal deformations, it is necessary and sufficient that  $E_L$ ,  $E_T$ ,  $G_L$  and  $G_T$  be positive. Thus  $(h_1 + h_2)$ ,  $(h_1 + h_2 + h_5)$  and  $(h_1 + h_2 + 2h_5 + 2h_{44})$  must be positive and  $E_L$  must be greater than  $E_T/4$ , since otherwise  $G_T$  will be negative. Equations (3.10) give

$$h_5 = (G_L - G_T)/2, \quad h_{44} = (E_L + G_T - 4G_L)/8. \tag{3.11}$$

Material parameters  $h_{11}$  and  $h_{14}$  do not appear in Eqs. (3.10), and hence their signs and orders of magnitude in comparison to that of  $E_L$ ,  $E_T$  and  $G_T$  cannot be determined by studying infinitesimal deformations.

### 3.2.3 Response of the matrix material

Noting that deformations of the matrix for which the strain energy density is given by the first three terms on the right-hand side of Eq. (3.3) have not been extensively studied in the literature. We first study its homogeneous and inhomogeneous deformations. For the matrix material,

$$W_m = h_1(I_1 - 3) + h_{11}(I_1 - 3)^2 + h_2(I_2 - 3) \tag{3.12}$$

$$\sigma_m = -p\mathbf{I} + 2[h_1 + 2h_{11}(I_1 - 3)]\mathbf{B} + 2h_2(I_1\mathbf{B} - \mathbf{B}^2) \tag{3.13}$$

James et al. [20, 21], amongst others, considered the strain energy density function (3.4), expanded  $W$  in terms of Taylor series and retained terms of different exponents of  $(I_1 - 3)$  and  $(I_2 - 3)$ . For one of the rubbers, they found the following values of the three material parameters for the strain energy density postulated by Eq. (3.12).

$$h_1 = 0.210 \text{ MPa}, \quad h_{11} = 0.057 \text{ kPa}, \quad h_2 = 7.8 \text{ kPa} \tag{3.14}$$

For infinitesimal deformations, the response of the *base matrix* material is identical to that of a Mooney-Rivlin material, and the shear modulus for infinitesimal deformations equals  $2(h_1 + h_2)$ .

We require that the strain energy density,  $W_m$ , is positive for all non-trivial admissible deformations. For  $h_{11} = 0$ , the constitutive relation (3.13) reduces to that for a Mooney-Rivlin material for which there is sufficient experimental evidence and theoretical reasoning that indicates that  $h_1$  and  $h_2$  be positive. Henceforth, we regard  $h_1$  and  $h_2$  as positive constants that ensure that the shear modulus for infinitesimal deformations is positive. Recalling that in an isochoric deformation,  $(I_1 - 3)$  and  $(I_2 - 3)$  are nonnegative, we postulate a deformation in which  $(I_2 - 3)$  is kept constant but  $(I_1 - 3)$  is varied as was done in the experiments of Rivlin [19] and James et al. [20, 21]. Then for  $h_{11} < 0$ ,  $W_m$  will become negative for some value of  $(I_1 - 3)$ . One possibility is to delimit the range of validity of Eq. (3.13) to deformations for which  $W_m$  is nonnegative by requiring

$$h_1(I_1 - 3) + h_2(I_2 - 3) > -h_{11}(I_1 - 3)^2 \quad (3.15)$$

The other is to assume that  $h_{11} \geq 0$  that ensures  $W_m \geq 0$  for all admissible deformations.

### 3.2.3.1 Coincidence of the principal axes of stress and strain

We rewrite Eq. (3.13) as

$$\boldsymbol{\sigma}_m = -p\mathbf{I} + 2[h_1 + 2h_{11}(I_1 - 3)]\mathbf{B} - 2h_2(\mathbf{B}^{-1}). \quad (3.16)$$

It then follows from Batra's theorem [24] that inequalities

$$[h_1 + 2h_{11}(I_1 - 3)] > 0, h_2 \geq 0 \quad (3.17)$$

imply that eigenvectors of  $\boldsymbol{\sigma}$  and  $\mathbf{B}$  coincide with each other. That is, inequalities (3.17) ensure that a principal axis of stress is also a principal axis of strain. These two inequalities are satisfied if the three material constants  $h_1$ ,  $h_2$  and  $h_{11}$  are positive. Truesdell and Noll [25] called inequalities (3.17) as empirical. We note that Baker-Ericksen's inequalities (i.e., greater principal stress occurs along the axis of the larger principal stretch) also imply that principal axes of stress and strain coincide with each other.

### 3.2.3.2 Simple uniaxial deformations

We consider the following static and homogeneous deformations produced by prescribing displacements along the  $X_1$  – axis at the ends of a cylindrical prismatic body with traction-free lateral surfaces.

$$x_1 = \lambda_1 X_1, x_2 = \lambda_2 X_2, x_3 = \lambda_3 X_3 \quad (3.18)$$

Here  $\lambda_1, \lambda_2$  and  $\lambda_3$  are stretches along the  $X_1$ , the  $X_2$ , and the  $X_3$  axes, respectively. The tensor  $\mathbf{B}$  for the deformation given by Eq. (3.18) is a diagonal matrix with  $B_{11} = \lambda_1^2$ ,  $B_{22} = \lambda_2^2$ , and  $B_{33} = \lambda_3^2$ . Thus the balance of linear momentum with zero body forces implies that the hydrostatic pressure  $p$  must be a constant. Boundary conditions of zero tractions on the lateral surfaces give expression (3.19) for  $p$  and Eq. (3.20) for finding  $\lambda_2$  in terms of  $\lambda_1$ .

$$p = 2h_1 \lambda_1^{-2} \lambda_2^{-2} + 4h_{11} \lambda_1^{-2} \lambda_2^{-2} (\lambda_1^2 + \lambda_2^2 + \lambda_1^{-2} \lambda_2^{-2} - 3) + 2h_2 (\lambda_1^{-2} + \lambda_2^{-2}) \quad (3.19)$$

$$\lambda_1^{-1} \lambda_2^{-2} (\lambda_2^4 - \lambda_1^{-2}) \left\{ h_1 + 2h_{11} \lambda_1^{-2} \lambda_2^{-2} \left[ 1 + \lambda_1^2 \lambda_2^2 (\lambda_1^2 + \lambda_2^2 - 3) \right] + h_2 \lambda_1^2 \right\} = 0 \quad (3.20)$$

Here we have not a priori assumed that  $\lambda_2 = \lambda_3$ . We note that Batra's theorem [24] gives that inequalities (3.17) guarantee  $\lambda_2 = \lambda_3$ .

For positive values of material constants  $h_1, h_2$  and  $h_{11}$ , the only solution of Eq. (3.20) is  $(\lambda_2^2 = \lambda_1^{-1})$  and then the incompressibility condition gives  $\lambda_2 = \lambda_3$ .

We consider the material with  $h_{11} > 0$ . Substituting  $\lambda_2 = \lambda_1^{-0.5}$  and for  $p$  from Eq. (3.19) into Eq. (3.13), and using  $\tilde{\mathbf{T}} = \sigma \mathbf{F}^{-T}$  for isochoric deformations, where  $\tilde{\mathbf{T}}$  is the first Piola-Kirchhoff stress tensor, we get expression (3.21) for the axial engineering stress or the present force per unit undeformed area in terms of the axial stretch  $\lambda_1$ .

$$\tilde{T}_{11} = 2\lambda_1^{-3} \left\{ \begin{array}{l} h_1 (\lambda_1^4 - \lambda_1) \\ + 2h_{11} (\lambda_1^3 - 1) [\lambda_1^3 + 2 - 3\lambda_1] \\ + h_2 (\lambda_1^3 - 1) \end{array} \right\} \quad (3.21)$$

We can thus write Eq. (3.21) as that used in the Mooney-Rivlin plot, i.e.,

$$\frac{\tilde{T}_{11}}{2(\lambda_1 - \lambda_1^{-2})} = \left\{ \begin{array}{l} h_1 + \\ 2h_{11} [(\lambda_1^2 + 2\lambda_1^{-1} - 3)] \\ + h_2 \lambda_1^{-1} \end{array} \right\} \quad (3.22)$$

As for a Mooney-Rivlin material, the plot of  $f = T_{11} / 2(\lambda_1 - \lambda_1^{-2})$  versus  $y = \lambda_1^{-1}$  determines the three constants,  $h_1, h_2$  and  $h_{11}$ , as follows. The value of  $f$  at  $y = 1$  equals  $h_1 + h_2$ ; the slope,  $df/dy$ , at  $y = 1$  equals  $h_2$ ; and the curvature,  $d^2f/dy^2$  at  $y = 1$  equals  $12h_{11}$ . In principle, one can find values of the three material parameters from the uniaxial test data. A possibility is to fit, by the least squares method, a quadratic polynomial in  $y$  to the  $f$  versus  $y$  test data near  $y = 1$ , and find values of the material parameters from this quadratic fit. *For the so found values of constants,  $h_1, h_2$  and  $h_{11}$ , if the computed and the experimental axial stress vs. the axial strain curves are not close to each other, then the material cannot be modeled by constitutive relation (3.12).* Alternatively, one can estimate values of  $h_1, h_2$  and  $h_{11}$  by using the entire experimental stress - strain curve and the least squares method in which case constitutive relation (3.12) will approximate the test curve.

For the test data of Sasso et al. [26], values of  $h_1, h_2$  and  $h_{11}$  found by the two methods are listed in Table 3.1. Values found by the two methods significantly differ from each other. For the values found from the Mooney-Rivlin plot of Figure 3.1, the predicted axial stress – axial stretch curve depicted in Figure 3.2 significantly differs from the experimental one suggesting that this material cannot be represented by the constitutive relation (3.21). However, with values of  $h_1, h_2$  and  $h_{11}$  found by using the least squares method, the predicted and the experimental curves are close to

each other as they should be. These values of the three material parameters may not approximate well the test data beyond that used in the least squares method. Whereas  $h_1$  is negative when found from the Mooney-Rivlin plot, it is positive when found by the least squares method. When additional data points were used in the Mooney-Rivlin plot,  $h_1$  still came out to be negative and the predicted and the experimental curves noticeably differed from each other. It is not clear if including data for compressive loading, not included in Sasso et al.'s paper [26] will improve upon the comparison.

Table 3.1. Material parameters found by the Mooney-Rivlin plot (denoted by \*) and the least squares fit to the experimental data

Source	Material	Values of material parameters		
		$h_1$ (MPa)	$h_2$ (MPa)	$h_{11}$ (MPa)
Sasso et al. [26]	Soft rubber	5.11E-01	1.46E-01	1.76E-03
		-9.9*	11.7*	5.73*

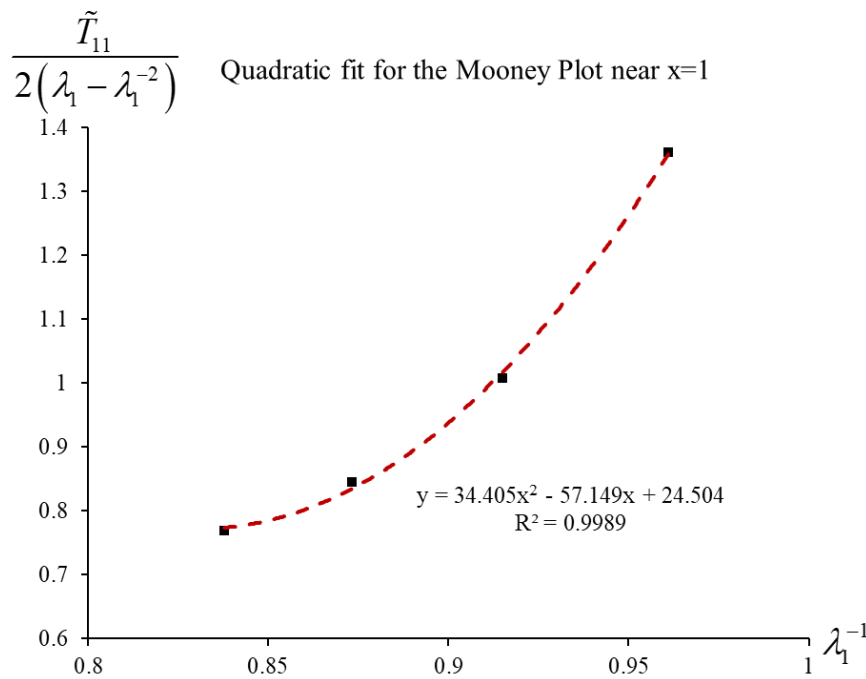


Figure 3.1. Mooney-Rivlin plot for the test data of Sasso et al. [26]

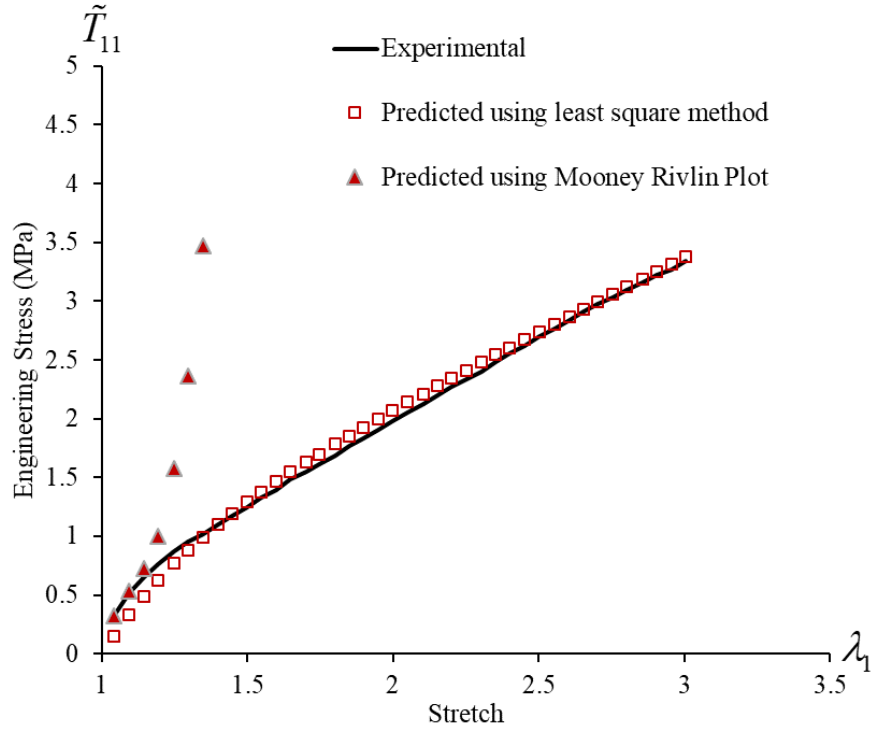


Figure 3.2. Comparison of predicted and experimental [26] engineering stress vs. axial stretch curves

Differentiation of expression (3.21) for  $\tilde{T}_{11}$  with respect to  $\lambda_1$  gives the tangent modulus of the uniaxial stress-stretch curve as

$$\frac{d\tilde{T}_{11}}{d\lambda_1} = (2 + 4\lambda_1^{-3})h_1 + 6\lambda_1^{-4}h_2 + 12(\lambda_1^2 - 1 + 2\lambda_1^{-4} - 2\lambda_1^{-3})h_{11} \quad (3.23)$$

The quantity  $(\lambda_1^2 - 1 + 2\lambda_1^{-4} - 2\lambda_1^{-3})$  has the minimum value 0 at  $\lambda_1 = 1$  and is always non-negative. Hence, for positive values of material constants  $h_1$ ,  $h_2$  and  $h_{11}$ , the tangent modulus is always positive, and the uniaxial stress-stretch response is stable. For  $\lambda_1 = 1$ ,

$$\frac{d\tilde{T}_{11}}{d\lambda_1} = 6(h_1 + h_2) \quad (3.24)$$

This relation confirms the known result that for an incompressible isotropic material, Young's modulus equals 3 times the shear modulus.

### 3.2.3.3 Kearsley's instability

We now study biaxial deformations of a square membrane of thickness  $h$  that is very small as compared to the in-plane dimensions. We assume that the membrane is stress-free in the reference configuration with the  $X_1$ - and the  $X_2$  – axes aligned along its edges. Following Kearsley [27], we assume that the membrane is loaded by equal and opposite dead loads on the edges and study its quasi-static deformations. Relations between the engineering stresses and the stretches  $\lambda_1$  and  $\lambda_2$ , respectively, along the  $X_1$ - and the  $X_2$  – axes are

$$\begin{aligned} \tilde{T}_{11} &= 2h_1\lambda_1^{-1}(\lambda_1^2 - \lambda_1^{-2}\lambda_2^{-2}) + 2h_2\lambda_1^{-1}(\lambda_1^2\lambda_2^2 - \lambda_1^{-2}) \\ &+ 4h_{11}\lambda_1^{-1}(\lambda_1^2 - \lambda_1^{-2}\lambda_2^{-2})(\lambda_1^2 + \lambda_2^2 + \lambda_1^{-2}\lambda_2^{-2} - 3) \\ \tilde{T}_{22} &= 2h_1\lambda_2^{-1}(\lambda_2^2 - \lambda_1^{-2}\lambda_2^{-2}) + 2h_2\lambda_2^{-1}(\lambda_1^2\lambda_2^2 - \lambda_2^{-2}) \\ &+ 4h_{11}\lambda_2^{-1}(\lambda_2^2 - \lambda_1^{-2}\lambda_2^{-2})(\lambda_1^2 + \lambda_2^2 + \lambda_1^{-2}\lambda_2^{-2} - 3) \end{aligned} \quad (3.25)$$

For equal dead loads applied on the edges,

$$\tilde{T}_{11} = \tilde{T}_{22} = F \quad (3.26)$$

Thus  $\lambda_1$  and  $\lambda_2$  must satisfy

$$(\lambda_1 - \lambda_2) \left\{ \begin{aligned} &1 + \frac{1}{\lambda_1^3\lambda_2^3} + \frac{h_2}{h_1} \frac{1}{\lambda_1^3\lambda_2^3} (\lambda_1^2 + \lambda_2^2 + \lambda_1\lambda_2 - \lambda_1^4\lambda_2^4) \\ &+ 2 \frac{h_{11}}{h_1} \frac{(1 + \lambda_1^3\lambda_2^3)}{\lambda_1^5\lambda_2^5} [1 + \lambda_1^2\lambda_2^2(\lambda_1^2 + \lambda_2^2 - 3)] \end{aligned} \right\} = 0 \quad (3.27)$$

We note that the term in  $\{ \}$  is symmetric in  $\lambda_1$  and  $\lambda_2$ . If values of material constants  $h_1$ ,  $h_2$  and  $h_{11}$  are such that the term in  $\{ \}$  is always non-zero, then the only solution of Eq. (3.27) is  $\lambda_1 = \lambda_2$ ; otherwise there are multiple solutions that depend upon values of  $h_2/h_1$  and  $h_{11}/h_1$ . Assuming  $h_{11}$

is non-negative, and taking  $h_2/h_1 = 0.1$  we plot in Figure 3.3 solutions of Eq. (3.27) for  $h_{11}/h_1 = 0.0, 0.005, 0.01, 0.03$ . For real and positive values of  $\lambda_1$  and  $\lambda_2$ , the term in  $\{ \}$  does not vanish for  $h_{11}/h_1 \geq 0.03$ . Thus for  $h_2/h_1 = 0.1$  and  $h_{11}/h_1 = 0.0, 0.005, 0.01$  there may be two solutions for the biaxially loaded membrane with equal dead loads.

In order to ascertain the stability of the solution, we find the free energy density,  $\Phi$ , given by

$$\Phi = W_m - F\lambda_1 - F\lambda_2 \quad (3.28)$$

For a given  $F$ , we use Eq. (3.27) to compute possible solutions of  $\lambda_1$  and  $\lambda_2$ , and plot them in Fig. 3.3. We use Eq. (3.28) to calculate the associated free energies, and have listed them in Table 3.2. For small dead loads, only the symmetric solution exists. As the load is increased, Eq. (3.27) admits both symmetric and non-symmetric solutions with the latter having the lower free energy than the former. Thus the membrane deformations suddenly switch from being one of equal stretches to that of unequal stretches, a phenomenon first analytically found by Kearsley [27] for a general incompressible and isotropic hyperelastic material, and subsequently verified experimentally by Batra et al. [28] for a Mooney-Rivlin rubber.

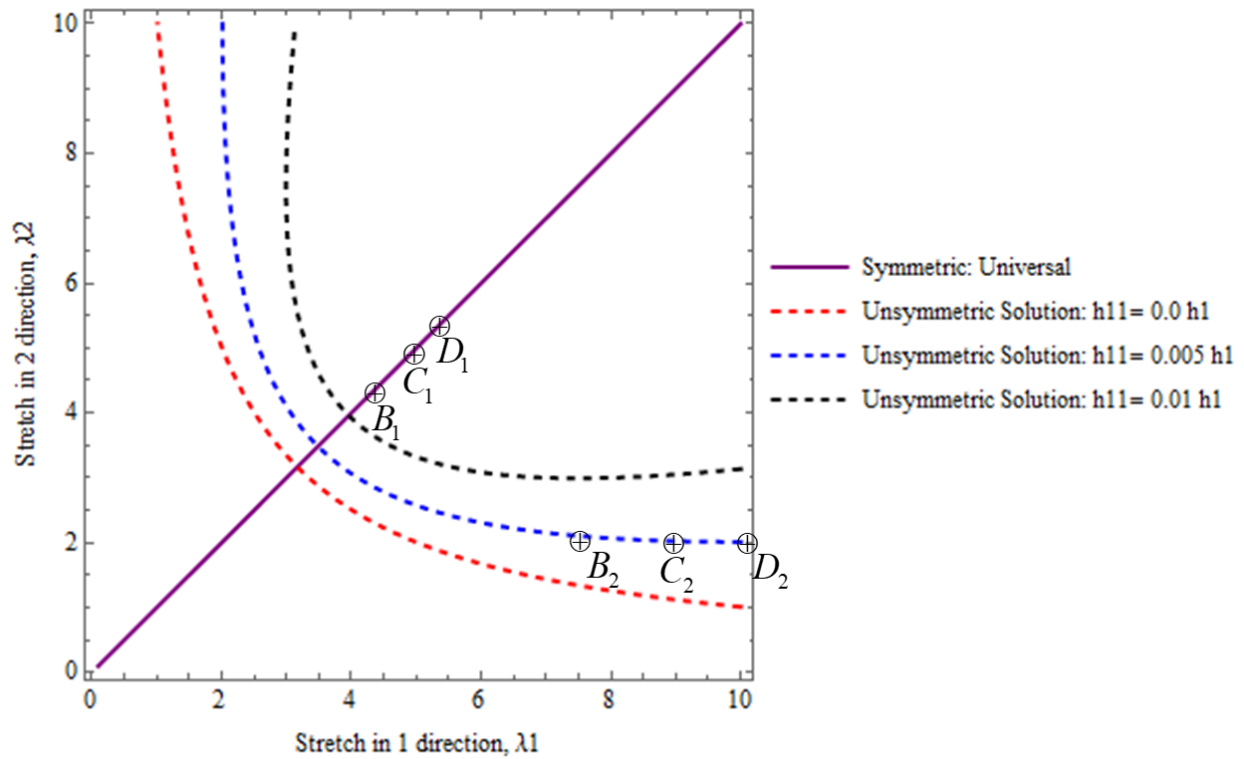


Figure 3.3. Stretches  $\lambda_1$  and  $\lambda_2$  for equal biaxial dead loading of a membrane represented by the material model (3.13) with  $h_2/h_1=0.1$  and  $h_{11}/h_1=0.0, 0.005, 0.01, 0.03$

Table 3.2. Stretch  $\lambda_2$  versus stretch  $\lambda_1$  for biaxially loaded membrane with equal dead loads. Free energies of solutions corresponding to points  $B_2$ ,  $C_2$  and  $D_2$  are less than those for  $B_1$ ,  $C_1$  and  $D_1$ , respectively.

F/h <sub>1</sub> =30	Stretches		Φ/h <sub>1</sub>
Point B <sub>1</sub>	λ <sub>1</sub>	4.46	-184.77
	λ <sub>2</sub>		
Point B <sub>2</sub>	λ <sub>1</sub>	7.45	-189.19
	λ <sub>2</sub>	2.11	
F/h <sub>1</sub> =40	Stretches		Φ/h <sub>1</sub>
Point C <sub>1</sub>	λ <sub>1</sub>	5.02	-279.75
	λ <sub>2</sub>		
Point C <sub>2</sub>	λ <sub>1</sub>	8.98	-292.25
	λ <sub>2</sub>	2.03	
F/h <sub>1</sub> =50	Stretches		Φ/h <sub>1</sub>
Point D <sub>1</sub>	λ <sub>1</sub>	5.47	-384.77
	λ <sub>2</sub>		
Point D <sub>2</sub>	λ <sub>1</sub>	10.2	-408.45
	λ <sub>2</sub>	2.01	

### 3.2.3.4 Simple shear deformations

We consider the following simple shear deformation

$$x_1 = X_1 + kX_2, x_2 = X_2, x_3 = X_3 \quad (3.29)$$

where  $k$  can be interpreted as the shear strain. This deformation is isochoric or volume preserving. Thus it is admissible in a body made of an incompressible material. It has been extensively studied for a general nonlinear elastic material, e.g., see Truesdell and Noll [25], and results reported below are a special case of those lucidly explained by Truesdell and Noll [25].

The deformation gradient, the left and the right Cauchy-Green tensors, and components of the deviatoric Cauchy stress tensor are functions of only  $k$ . The balance of linear momentum in the absence of gravity forces implies that the hydrostatic pressure must be a constant. Assuming that

surfaces  $x_3 = X_3 = \text{constant}$  are traction free, we have  $\sigma_{31} = \sigma_{32} = \sigma_{33} = 0$ , and the hydrostatic pressure  $p$  is given by

$$p = 2[h_1 + 2h_{11}k^2] + 2h_2(k^2 + 2) \quad (3.30)$$

We thus get the following expressions for the three non-zero components of the Cauchy stress tensor.

$$\begin{aligned} \sigma_{11} &= 2k^2h_1 + 4k^4h_{11} \\ \sigma_{22} &= -2k^2h_2 \\ \sigma_{12} &= 2kh_1 + 4k^3h_{11} + 2kh_2 \end{aligned} \quad (3.31)$$

These expressions imply that the consideration of the term  $h_{11}(I_1 - 3)^2$  in the stored energy expression (3.13) implies that the material exhibits strain-hardening/softening in simple shear deformations depending upon the sign of  $h_{11}$ . Furthermore, for this deformation,  $\tilde{T}_{12} = \sigma_{12}$ , and for  $h_{11} < 0$ , the material response will become unstable when

$$d\tilde{T}_{12}/dk = 0 \quad (3.32)$$

or equivalently,

$$k = \sqrt{h_1 + h_2} / (-4h_{11}) \quad (3.33)$$

For positive values of material constants  $h_1$ ,  $h_2$  and  $h_{11}$ , the response in simple shear is always stable.

There are the following two differences in the response of the material to infinitesimal and finite simple shearing deformations. First, the presence of the term  $k^3h_{11}$  in Eq. (3.31) makes the shear stress – shear strain relation nonlinear. Even for  $h_{11} = 0$ , different normal surface tractions are needed on the faces  $X_1 = \text{constant}$  and  $X_2 = \text{constant}$ ; this is usually referred to as the Poynting effect. Both these effects are well-known and are described in many books, e.g., see [25]. For infinitesimal deformations, no normal tractions act on the flat bounding surfaces, while for the finite deformations normal tractions  $\sigma_{11}$  and  $\sigma_{22}$  are needed to keep the bounding surfaces flat.

Note that  $\sigma_{11}$  and  $\sigma_{22}$  are not equal to each other in general, thereby implying that different normal surface tractions are needed on the faces  $X_1 = \text{constant}$  and  $X_2 = \text{constant}$  to maintain simple shearing deformations of the block.

### 3.2.4 Response of the fiber-reinforced rubberlike material (FRRM)

For simplicity, we assume that fibers are embedded in the  $X_1X_2$  – plane and make an angle  $\alpha$  with the  $X_1$  – axis in the stress-free reference configuration, as depicted in Figure 3.4. The unit vector,  $\mathbf{A}_0$ , along the fiber direction in the reference configuration, is expressed as  $\mathbf{A}_0 = (c, s, 0)$ , where  $c = \cos(\alpha)$  and  $s = \sin(\alpha)$ . Experimental results for FRRMs [29] suggest that  $G_L > G_T$ , thus we assume that  $h_5 = 0.5(G_L - G_T) > 0$ . Also, experimental results for soft tissues [29], rayon-rubber and steel-rubber composites [30] suggest that  $E_L \gg G_L$ . From Eq. (3.6),  $h_{44} = (E_L + G_T - 4G_L)/8$ . We assume  $h_{44}$  to be nonnegative.

Recalling that in an isochoric deformation,  $(I_1 - 3)$  is non-negative, but  $(I_4 - 1)$  can be either positive or negative, thus for  $h_{14} > 0$ ,  $W$  could become negative for some values of  $I_4 (< 1)$ , and for  $h_{14} < 0$ ,  $W$  will become negative for some values of  $I_4 (> 1)$ . We require that the strain energy density,  $W$ , is positive for all non-trivial deformations. Thus the material model represented by Eqs. (3.2) and (3.3) is valid for deformations and values of material parameters for which

$$h_{14}(I_1 - 3)(I_4 - 1) < -\left[ h_1(I_1 - 3) + h_{11}(I_1 - 3)^2 + h_2(I_2 - 3) + h_{44}(I_4 - 1)^2 + h_5(I_5 - 2h_4 + 1) \right] \quad (3.34)$$

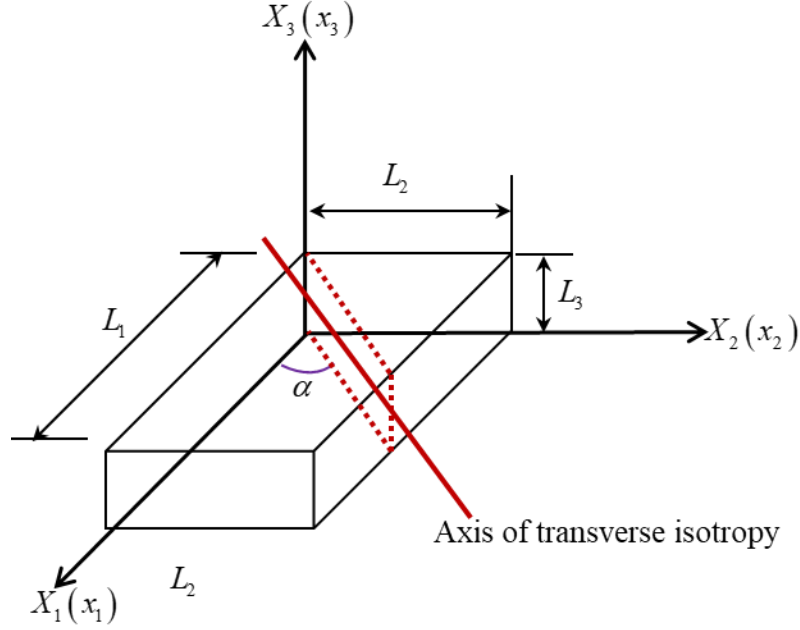


Figure 3.4. Schematic sketch of simple extension of a rectangular block made of an incompressible FRRM with fibers in the  $X_1X_3$ - plane inclined at angle  $\alpha$  to the  $X_1$ -axis.

### 3.2.4.1 Uniaxial homogeneous deformations

For the homogeneous deformations given by Eq. (3.18), we assume that surfaces  $X_3=0, L$  are traction-free. We recall that a homogeneous deformation can be produced in a homogeneous elastic body by applying only surface tractions. The strain invariants  $I_1, I_2, I_4$  and  $I_5$  have the following expressions:

$$\begin{aligned}
 I_1 &= \lambda_1^2 + \lambda_2^2 + \lambda_3^2 \\
 I_2 &= \lambda_1^2 \lambda_2^2 + \lambda_2^2 \lambda_3^2 + \lambda_3^2 \lambda_1^2 \\
 I_4 &= \lambda_1^2 c^2 + \lambda_2^2 s^2 \\
 I_5 &= \lambda_1^4 c^2 + \lambda_2^4 s^2
 \end{aligned} \tag{3.35}$$

Substituting from Eqs. (3.18) and (3.35) into the constitutive relation (3.3), and requiring that the surface  $x_3 = \text{constant}$  is traction free gives the following expressions for components of the Cauchy stress tensor and the hydrostatic pressure.

$$\begin{aligned}
\sigma_{11} &= 2h_1(\lambda_1^2 - \lambda_1^{-2}\lambda_2^{-2}) + 4h_5c^2\lambda_1^2(\lambda_1^2 - 1) + 4h_{11}(\lambda_1^2 - \lambda_1^{-2}\lambda_2^{-2})(\lambda_1^2 + \lambda_2^2 + \lambda_1^{-2}\lambda_2^{-2} - 3) \\
&+ 2h_2(\lambda_1^2\lambda_2^2 - \lambda_1^{-2}) + 4h_{44}c^2\lambda_1^2(\lambda_1^2c^2 + \lambda_2^2s^2 - 1) \\
&+ 2h_{14}\left[\lambda_1^{-2}\lambda_2^{-2} + \lambda_1^2\lambda_2^2 + \lambda_1^{-2}(2c^2\lambda_1^6 - s^2 - \lambda_1^4 - 3c^2\lambda_1^4)\right] \\
\sigma_{22} &= 2h_1(\lambda_2^2 - \lambda_1^{-2}\lambda_2^{-2}) + 4h_5s^2\lambda_2^2(\lambda_2^2 - 1) + 4h_{11}(\lambda_2^2 - \lambda_1^{-2}\lambda_2^{-2})(\lambda_1^2 + \lambda_2^2 + \lambda_1^{-2}\lambda_2^{-2} - 3) \\
&+ 2h_2(\lambda_1^2\lambda_2^2 - \lambda_2^{-2}) + 4h_{44}s^2\lambda_2^2(\lambda_1^2c^2 + \lambda_2^2s^2 - 1) \\
&+ 2h_{14}\lambda_1^{-2}\lambda_2^{-2}\left[1 + \lambda_1^4\lambda_2^4 + \lambda_1^2(2s^2\lambda_2^6 - c^2 - \lambda_2^4 - 3s^2\lambda_2^4)\right]
\end{aligned} \tag{3.36}$$

$$\sigma_{12} = 2cs\lambda_1\lambda_2\left[h_{44}(\lambda_1^2 + \lambda_2^2 + \lambda_1^{-2}\lambda_2^{-2} - 3) + 2h_{44}(\lambda_1^2c^2 + \lambda_2^2s^2 - 1) + h_5(\lambda_1^2 + \lambda_2^2 - 2)\right]$$

$$\sigma_{33} = \sigma_{13} = \sigma_{23} = \sigma_{31} = \sigma_{32} = 0$$

$$\begin{aligned}
p &= 2h_1\lambda_1^{-2}\lambda_2^{-2} + 4h_{11}\lambda_1^{-2}\lambda_2^{-2}(\lambda_1^2 + \lambda_2^2 + \lambda_1^{-2}\lambda_2^{-2} - 3) + 2h_2(\lambda_1^{-2} + \lambda_2^{-2}) \\
&+ 2h_{14}\lambda_1^{-2}\lambda_2^{-2}\left[\lambda_1^2c^2 + \lambda_2^2s^2 - 1\right]
\end{aligned} \tag{3.37}$$

where  $h_4 = -2h_5$  has been used.

For the simple tensile deformations, the non-zero components of the first Piola-Kirchhoff stress tensor, or the engineering stresses, are related to components of the Cauchy stress tensor as

$$\tilde{T}_{11} = \frac{\sigma_{11}}{\lambda_1}; \tilde{T}_{22} = \frac{\sigma_{22}}{\lambda_2}; \tilde{T}_{12} = \frac{\sigma_{12}}{\lambda_2}; \tilde{T}_{21} = \frac{\sigma_{12}}{\lambda_1} \tag{3.38}$$

Thus in order to produce the deformation (3.18) in the transversely isotropic body, one needs to apply non-equal tangential forces on the faces  $X_I = \text{constant}$  and  $X_2 = \text{constant}$ . The magnitudes of these forces depend upon the deformation and values of material parameters  $h_{14}$ ,  $h_{44}$ , and  $h_5$ .

*Fibers along the axial loading direction:*

For  $c=1$  and  $s=0$  in Eqs. (3.36), the equation for the stretch  $\lambda_2$  in terms of  $\lambda_1$  obtained by setting  $\tilde{T}_{22} = 0$  and the axial stress-axial stretch relation is:

$$\lambda_1^{-1} \lambda_2^{-2} (\lambda_2^4 - \lambda_1^{-2}) \left\{ h_1 + 2h_{11} [\lambda_1^{-2} \lambda_2^{-2} + \lambda_1^2 + \lambda_2^2 - 3] + h_2 \lambda_1^2 + h_{14} (\lambda_1^2 - 1) \right\} = 0 \quad (3.39)$$

$$\tilde{T}_{11} = 2\lambda_1^{-3} \left\{ \begin{array}{l} h_1 (\lambda_1^4 - \lambda_2^{-2}) + 2(h_5 + h_{44}) \lambda_1^4 (-1 + \lambda_1^2) \\ + 2h_{11} \lambda_1^{-2} \lambda_2^{-4} (\lambda_1^4 \lambda_2^2 - 1) [1 + \lambda_1^2 \lambda_2^2 (\lambda_1^2 + \lambda_2^2 - 3)] \\ + h_2 (\lambda_1^4 \lambda_2^2 - 1) \\ + h_{14} \lambda_2^{-2} \{ 1 + \lambda_2^2 \lambda_1^4 (2\lambda_1^2 + \lambda_2^2 - 4) \} \end{array} \right\} \quad (3.40)$$

Here we have not *a priori* assumed that stretches in the  $X_2$ - and the  $X_3$ -directions are equal. We note that the material constants  $h_5$  and  $h_{44}$  do not appear in Eq. (3.39), and the fiber-matrix interaction parameter  $h_{14}$  determines lateral stretches  $\lambda_2$  and  $\lambda_3$  in terms of the axial stretch  $\lambda_1$ .

*Solution*  $\lambda_3 = \lambda_2 = \lambda_1^{-1/2}$  of Eq. (3.39)

One solution of Eq. (3.39) is  $\lambda_2 = \lambda_1^{-1/2}$  and the incompressibility condition gives  $\lambda_3 = \lambda_2 = \lambda_1^{-1/2}$ ; we call it the symmetric solution. This solution is independent of the sign of  $h_{14}$ . Substituting  $\lambda_2 = \lambda_1^{-0.5}$  into Eq. (3.40), and differentiating it with respect to  $\lambda_1$ , we get

$$\begin{aligned} \frac{d\tilde{T}_{11}}{d\lambda_1} &= (2 + 4\lambda_1^{-3})h_1 + 6\lambda_1^{-4}h_2 + 12(\lambda_1^2 - 1 + 2\lambda_1^{-4} - 2\lambda_1^{-3})h_{11} \\ &+ 4(3\lambda_1^2 - 1)(h_{44} + h_5) + 4(-\lambda_1^{-3} - 2 + 3\lambda_1^2)h_{14} \end{aligned} \quad (3.41)$$

For positive values of  $h_2, h_1$  and  $h_{11}$ , the first three expressions on the right side of Eq. (3.41) are always positive. For positive values of  $(h_{44} + h_5)$ , the fourth term in Eq. (3.41) is always positive when  $\lambda_1 > 0.577$ . In the fifth term,  $(-\lambda_1^{-3} - 2 + 3\lambda_1^2)$  changes sign at  $\lambda_1 = 1$  from negative to positive.

For the material response to be stable, the tangent modulus of the stress-stretch curve should be positive. Thus, for stable material response,

$$\begin{aligned}
& (2 + 4\lambda_1^{-3})h_1 + 6\lambda_1^{-4}h_2 + 12(\lambda_1^2 - 1 + 2\lambda_1^{-4} - 2\lambda_1^{-3})h_{11} \\
& + 4(3\lambda_1^2 - 1)(h_{44} + h_5) + 4(-\lambda_1^{-3} - 2 + 3\lambda_1^2)h_{14} > 0
\end{aligned} \tag{3.42}$$

For a given deformation range (e.g.,  $0.8 \leq \lambda_1 \leq 3$ ), and values of material parameters for  $h_2, h_1, h_{11}, h_5$  and  $h_{44}$ , one can use Eqs. (3.42) and (3.34) to define the range of admissible values of  $h_{14}$ .

*Solution  $\lambda_3 \neq \lambda_2$  of Eq. (3.39)*

We now consider the possibility that the second bracket on the left hand side of Eq. (3.39) equals zero. That is,

$$2h_{11}(\lambda_1^2 + \lambda_2^2 + \lambda_1^{-2}\lambda_2^{-2} - 3) + h_1 + h_2\lambda_1^2 + h_{14}(\lambda_1^2 - 1) = 0 \tag{3.43}$$

For  $h_{14} \neq 0$ , Eqn. (3.43) can be solved for  $\lambda_2$  in terms of  $\lambda_1$  and the material moduli  $h_1, h_2, h_{11}$  and  $h_{14}$ , and then  $\lambda_3 = \lambda_1^{-1}\lambda_2^{-1}$ . This generally indicates  $\lambda_3 \neq \lambda_2$ , we call these unsymmetric solutions. Since  $\lambda_1^2 + \lambda_2^2 + \lambda_1^{-2}\lambda_2^{-2} \geq 3$  for isochoric deformations, for unsymmetric solutions to exist, we must have

$$\begin{aligned}
\lambda_1 &< \sqrt{\frac{h_{14} - h_1}{h_2 + h_{14}}} && \text{for } h_{14} > h_1 \\
\lambda_1 &> \sqrt{\frac{h_{14} - h_1}{h_2 + h_{14}}} && \text{for } h_{14} < -h_2
\end{aligned} \tag{3.44}$$

where we have assumed  $h_1 > 0, h_2 \geq 0$  and  $h_{11} \geq 0$ . We note that most of the previous studies (e.g. [16-17, 21- 23]) did not consider the terms involving  $h_{14}$  and  $h_{11}$ , and concluded  $\lambda_3 = \lambda_2 = \lambda_1^{-1/2}$  from Eq. (3.39).

*For the material with  $h_{11} = 0$  the second bracket on the left-hand side of Eq. (3.39) equals zero for*

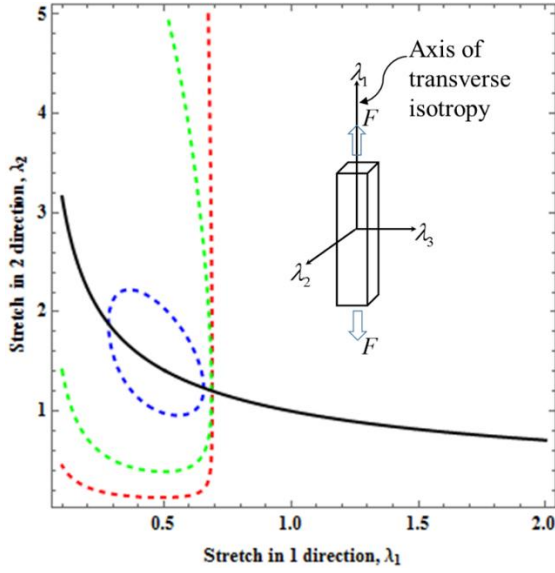
$$\lambda_1 = \sqrt{\frac{h_{14} - h_1}{h_2 + h_{14}}} \quad (3.45)$$

which is meaningful for either  $h_{14} > h_1$  or  $h_{14} < h_1$  and  $h_{14} < -h_2$ . For this material, we cannot find  $\lambda_2$  from the equilibrium equations and the boundary conditions, and there are no unsymmetric solutions.

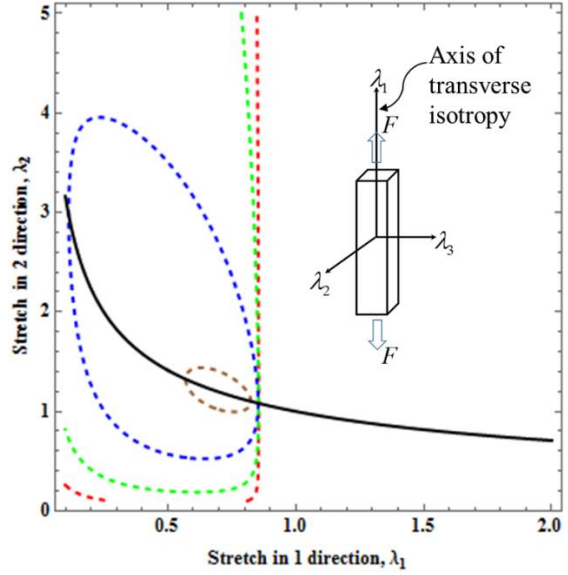
*Example of a material with unsymmetric stretches in lateral directions*

Inspired by the experimental data for muscles [29], we select  $G_L/G_T = 5$ ,  $E_L/G_T = 75$ , and set  $h_2/h_1 = 0.1$  resulting in  $h_5/h_1 = 4.4$ ,  $h_{44}/h_1 = 15.4$  according to Eqs. (3.10) and (3.11). For  $h_{14}/h_1 = 2, 4, 6, 8$ ;  $h_{11}/h_1 = 0.001, 0.01, 0.1, 1$ , and 10, we have plotted in Figure 3.5 the symmetric and the unsymmetric solutions, respectively, as solid and dashed curves. For a given value of  $h_{14}/h_1$ , values of  $h_{11}/h_1$  significantly influence the existence and the shapes of the resulting unsymmetric solutions. An increase in the value of  $h_{11}/h_1$  narrows regions enclosed by curves corresponding to unsymmetric solutions until they disappear for  $h_{11}/h_1 = 10$ . Moreover, at the “critical” points where bifurcation from a symmetric to an unsymmetric solution occurs,  $\lambda_1^c$  approaches 1.0 with an increase in  $h_{14}/h_1$ . For  $h_{14}/h_1 < 0$ , as depicted in Figure 3.6, the bifurcation occurs in the region of  $\lambda_1 > 1$ .

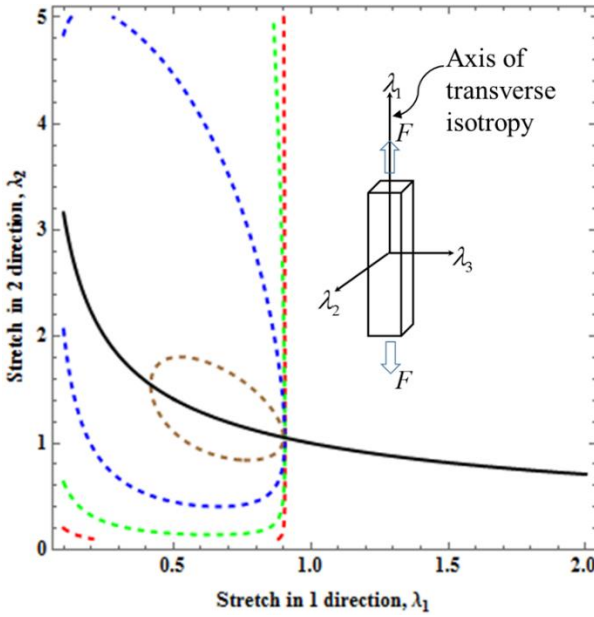
- Unsymmetric solution:  $h_{11} = 0.001 h_1$
- Unsymmetric solution:  $h_{11} = 0.01 h_1$
- Unsymmetric solution:  $h_{11} = 0.1 h_1$
- Unsymmetric solution:  $h_{11} = 1 h_1$
- Unsymmetric solution:  $h_{11} = 10 h_1$
- Symmetric solution: universal



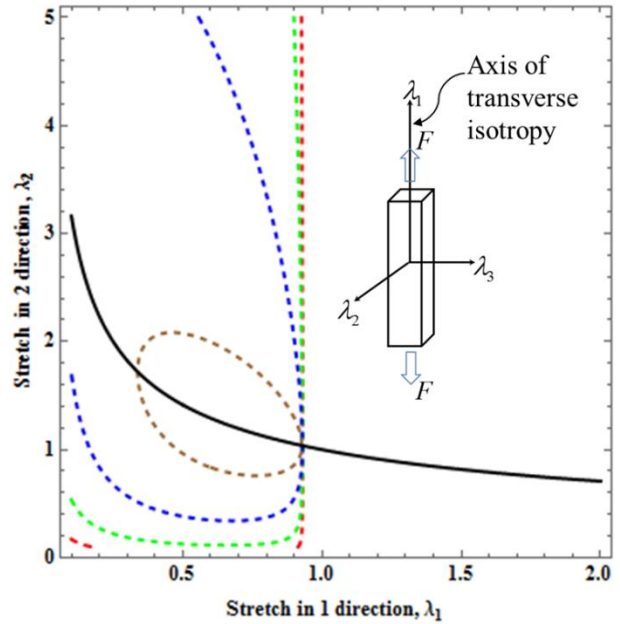
(a)  $h_{14}/h_1 = 2$



(b)  $h_{14}/h_1 = 4$



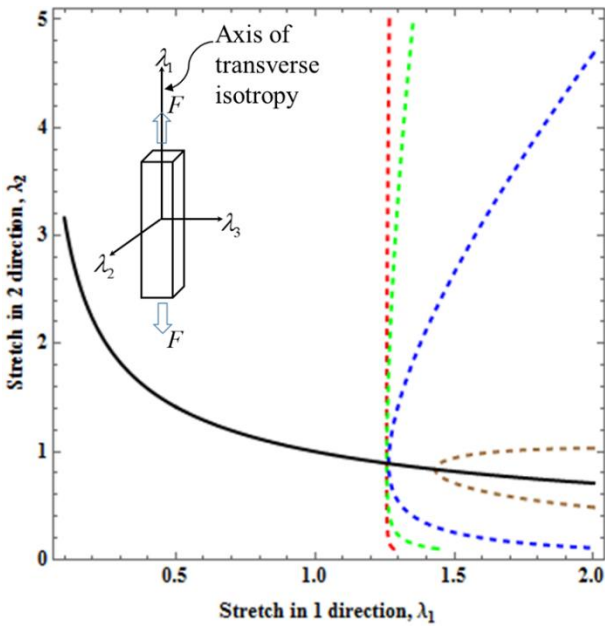
(c)  $h_{14}/h_1 = 6$



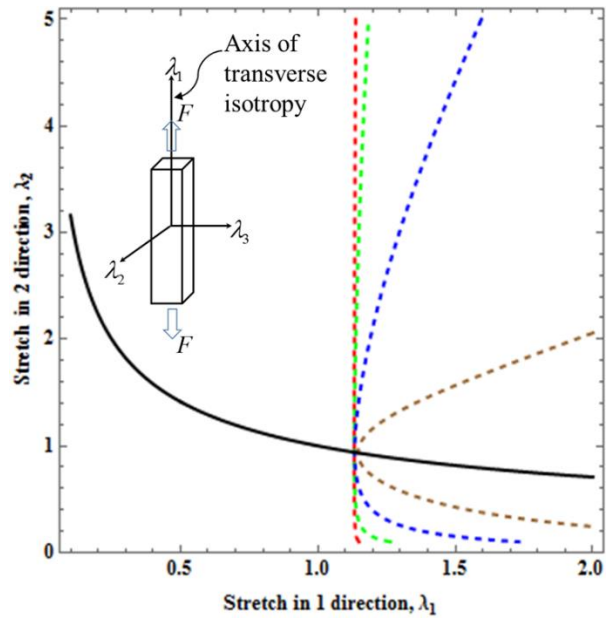
(d)  $h_{14}/h_1 = 8$

Figure 3.5. Plots of  $\lambda_2$  versus  $\lambda_1$  for symmetric and unsymmetrical solutions of Eq. (3.39);  $h_{11}/h_1 = 0.001, 0.01, 0.1, 1$ ; (a)  $h_{14}/h_1 = 2$  (b)  $h_{14}/h_1 = 4$  (c)  $h_{14}/h_1 = 6$  (d)  $h_{14}/h_1 = 8$

- - - Unsymmetric solution:  $h_{11} = 0.001 h_1$
- - - Unsymmetric solution:  $h_{11} = 0.01 h_1$
- - - Unsymmetric solution:  $h_{11} = 0.1 h_1$
- - - Unsymmetric solution:  $h_{11} = 1 h_1$
- - - Unsymmetric solution:  $h_{11} = 10 h_1$
- Symmetric solution: universal



(a)  $h_{14}/h_1 = -2$



(b)  $h_{14}/h_1 = -4$

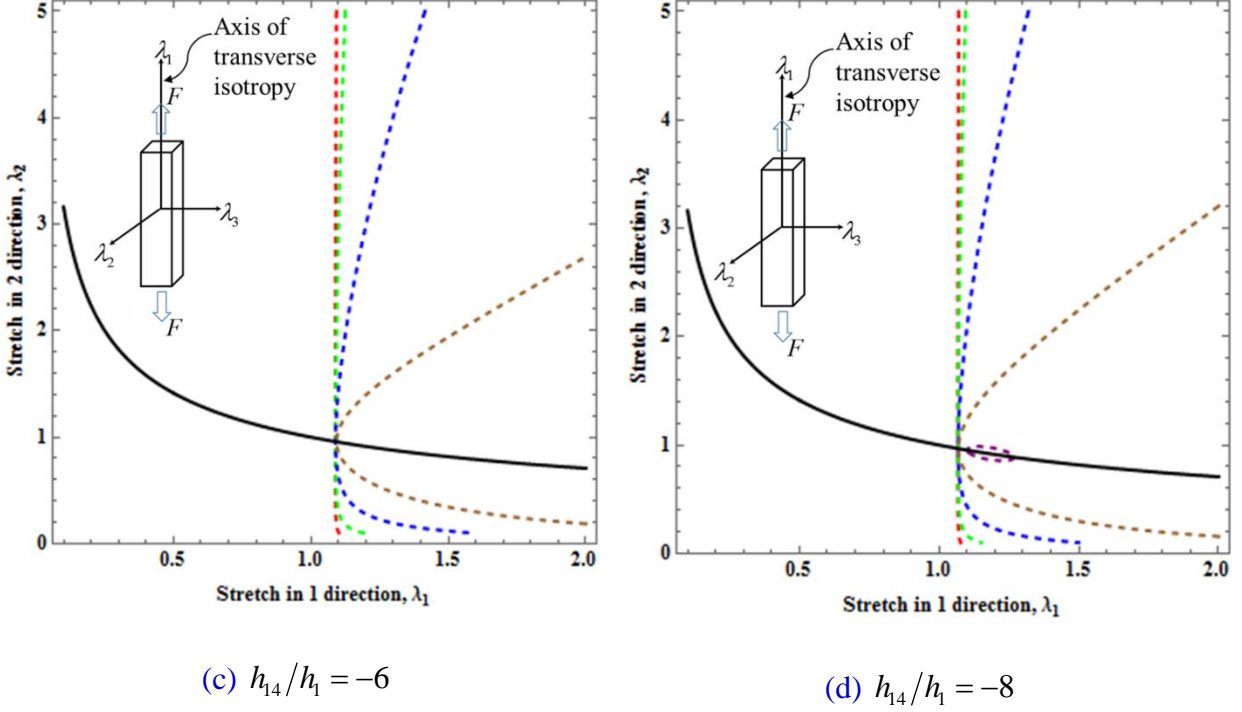
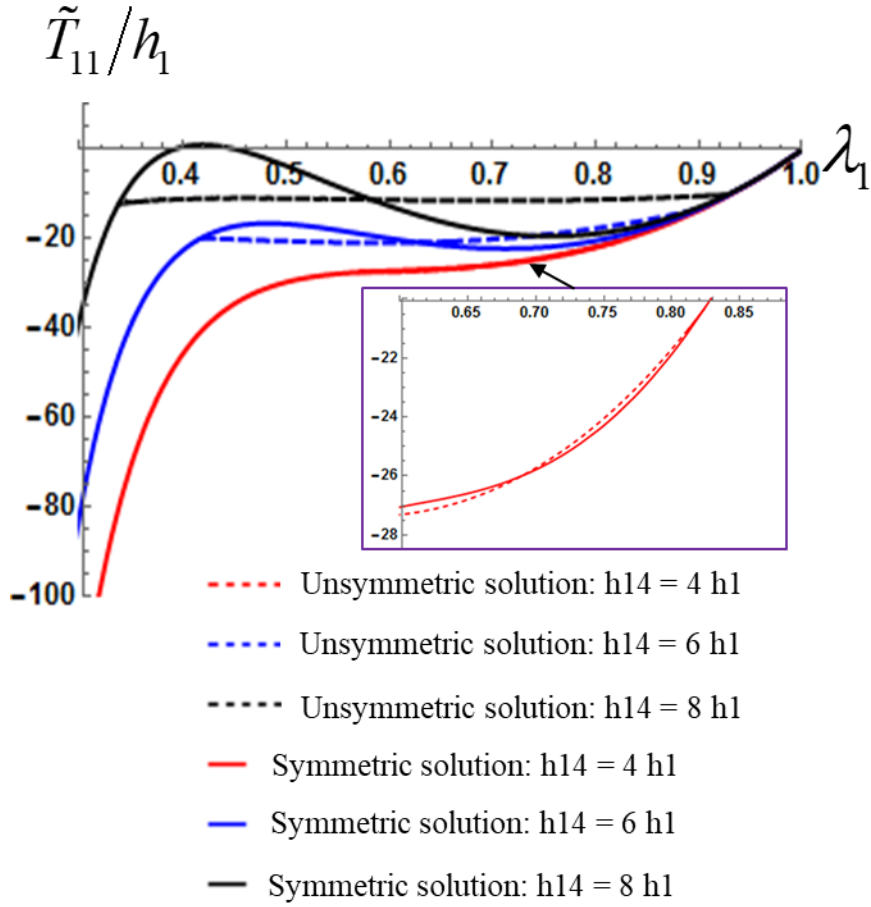


Figure 3.6. Plots of  $\lambda_2$  versus  $\lambda_1$  for symmetric and unsymmetrical solutions of Eq. (3.39);  $h_{11}/h_1 = 0.001, 0.01, 0.1, 1$ ; (a)  $h_{14}/h_1 = -2$  (b)  $h_{14}/h_1 = -4$  (c)  $h_{14}/h_1 = -6$  (d)  $h_{14}/h_1 = -8$

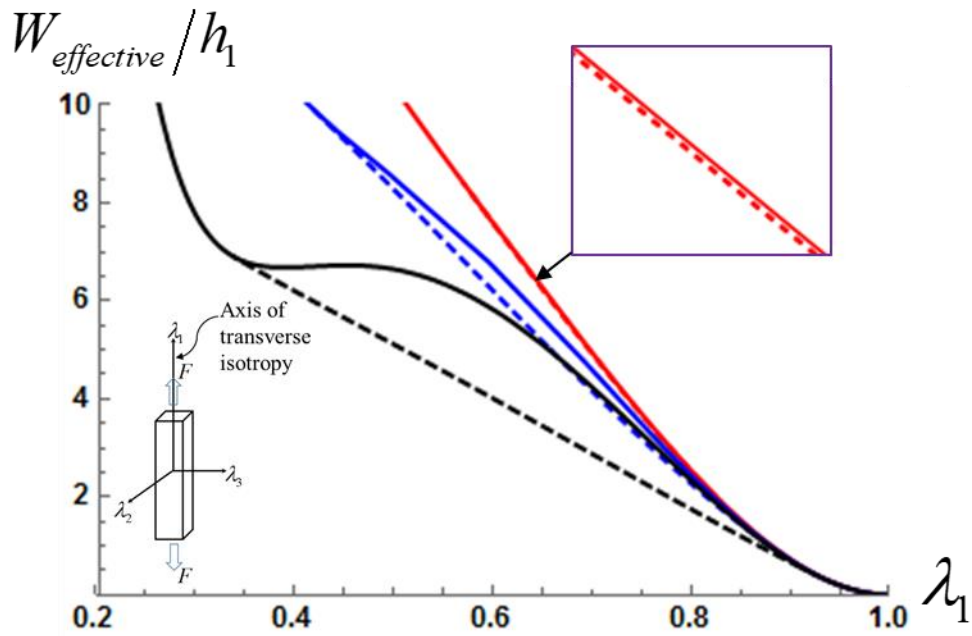
For studying the stability of the symmetric and the non-symmetrical solutions, we recall that for a displacement controlled test, the free energy equals the strain energy stored in the body. In Figure 3.7, the uniaxial stress-stretch relations and the free energy densities (or the total free energy since the deformations are isochoric) associated with the symmetric and the unsymmetric solutions are depicted by solid and dashed curves, respectively. For  $h_{14}/h_1 = 4, 6, 8$ , the non-symmetric solutions occur at  $\lambda_1^c = 0.83, 0.90, 0.93$ , respectively. From Eq. (3.43), it is found that for  $h_{14}/h_1 = 4$ , there is no loss of monotonicity in the stress-stretch relations for the symmetric solutions. However, for  $h_{14}/h_1 = 6$  (8), between  $\lambda_1 = 0.48$  (0.42) and  $\lambda_1 = 0.71$  (0.76), the tangent modulus of the axial stress – axial stretch curves for the symmetric solutions is less than zero, indicating the loss of monotonicity in the axial stress – axial stretch curve. That is, the magnitude of the axial engineering stress decreases with an increase in the compressive axial strain. We note that Qiu and Pence [23] also observed this non-monotonic axial stress-axial stretch curve, and Batra [32]

observed it for a homogeneous isotropic elastic material. It suggests that the bifurcation from symmetric into nonsymmetric solutions may occur much before the tangent modulus of the axial stress-axial stretch curve equals zero. Moreover, from the free energy plots, Figure 3.7 (b), we see that the unsymmetric solutions have lower free energies than the corresponding symmetric solutions, indicating that the unsymmetric deformations will be observable beyond the bifurcation points.

For  $h_{14}/h_1 = -4, -6, \text{ and } -8$ , the axial stress-axial stretch and the free energy density versus the axial stretch curves associated with the symmetric and the unsymmetrical solutions, displayed in Figure 3.8, indicate that the solutions, respectively, bifurcate at  $\lambda_1 = 1.15, 1.09, 1.07$ . Also, the free energy associated with the un-symmetric solution is lower than that with the symmetric solution. It is thus clear that values of  $h_{11}$  and  $h_{14}$  play critical roles in determining whether a solution bifurcates or not. We note that points where bifurcations occur satisfy  $(\lambda_1 - 1)h_{14}/h_1 < 0$ . The authors have not found experimental data reporting such instabilities in simple tensile/compressive deformations of transversely isotropic solids.

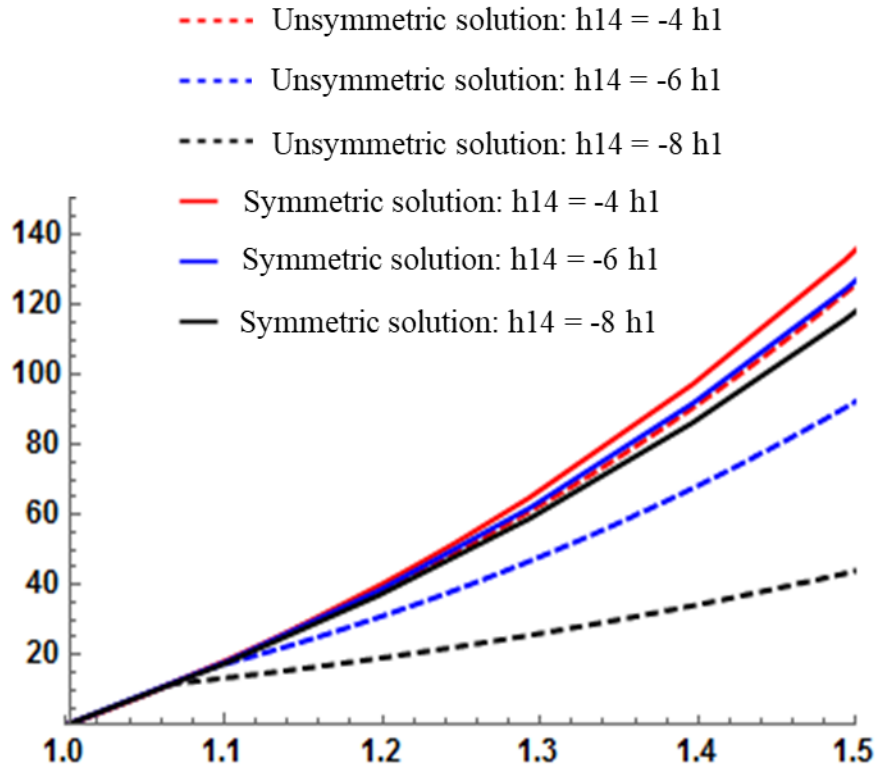


(a) normalized stress-stretch relations

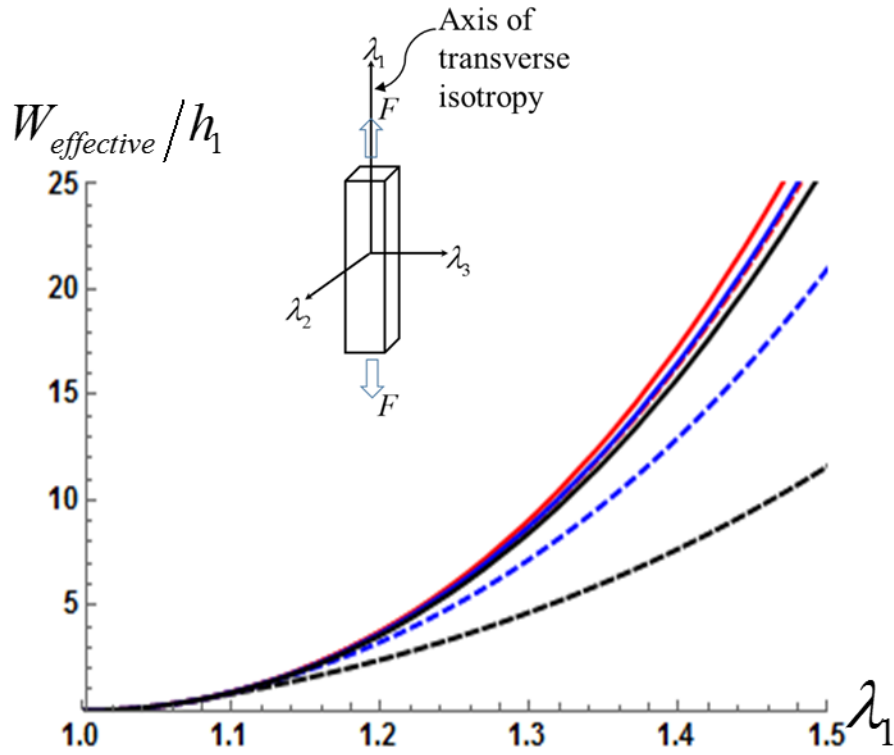


(b) normalized free energies (strain energies)

Figure 3.7. Uniaxial stress-stretch relations and free energy densities associated with “symmetric” and “unsymmetrical” solutions for  $h_{11}/h_1 = 1$ ;  $h_{14}/h_1 = 4, 6, 8$



(a) normalized stress-stretch relations



(b) normalized free energies (strain energies)

Figure 3.8. Uniaxial stress-stretch relations and free energy densities associated with “symmetric” and “unsymmetrical” solutions for  $h_{11}/h_1 = 1$ ;  $h_{14}/h_1 = -4, -6, -8$

#### 3.2.4.2 Simple shear deformations

For the simple shear deformation given by Eq. (3.29) and the surfaces  $x_3 = X_3 = \text{constant}$  kept traction-free, we get the following expressions for components of the Cauchy stress tensor and the hydrostatic pressure:

$$\begin{aligned}
\sigma_{11} &= 2k^2h_1 + 4k^4h_{11} + 4h_{44}(\cos\alpha + k\sin\alpha)^2 \left[ k^2(\sin\alpha)^2 + 2k\cos\alpha\sin\alpha \right] \\
&+ 2k^2h_{14} \left[ 2k^2(\sin\alpha)^2 + (\cos\alpha)^2 + 4k\cos\alpha\sin\alpha \right] \\
&+ 4kh_5(\cos\alpha + k\sin\alpha)(\sin\alpha + k\cos\alpha + k^2\sin\alpha) \\
\sigma_{22} &= -2k^2h_2 + 4h_{44}(\sin\alpha)^2 \left[ k^2(\sin\alpha)^2 + 2k\cos\alpha\sin\alpha \right]
\end{aligned} \tag{3.46}$$

$$\begin{aligned}
&+ 2k^2(\sin\alpha)^2 h_{14} + 4kh_5\sin\alpha(\cos\alpha + k\sin\alpha) \\
\sigma_{12} &= 2kh_1 + 4k^3h_{11} + 2kh_2 + 4h_{44}\sin\alpha(\cos\alpha + k\sin\alpha) \left[ k^2(\sin\alpha)^2 + 2k\cos\alpha\sin\alpha \right] \\
&2kh_{14} \left[ 2k^2(\sin\alpha)^2 + 3k\cos\alpha\sin\alpha \right] + 2kh_5 \left[ 2k^2(\sin\alpha)^2 + 3k\cos\alpha\sin\alpha + 1 \right]
\end{aligned}$$

$$p = 2 \left[ h_1 + 2h_{11}k^2 + h_{14} \left( k^2(\sin\alpha)^2 + k\sin 2\alpha \right) \right] + 2h_2(k^2 + 2) \tag{3.47}$$

The three stress components,  $\sigma_{11}$ ,  $\sigma_{22}$  and  $\sigma_{12}$ , are related as

$$\begin{aligned}
&\sigma_{11} - \sigma_{22} - k\sigma_{12} \\
&= 2k(\cos 2\alpha + \cos\alpha\sin\alpha k) \left[ 2h_{44}k(\sin\alpha)^2 + 4h_{44}\cos\alpha\sin\alpha + k(h_{14} + h_5) \right]
\end{aligned} \tag{3.48}$$

Thus material parameters  $h_{14}$ ,  $h_{44}$  and  $h_4$  that quantify effects of fiber reinforcements also influence the Poynting effect.

For  $\alpha=0^\circ$ , the third expression in Eq. (3.46) simplifies to

$$\sigma_{12} = G_L k + 2h_{11}k^3 \tag{3.49}$$

and for  $\alpha=90^\circ$  to

$$\sigma_{12} = G_L k + 4(h_{11} + h_{14} + h_{44} + h_5)k^3 \tag{3.50}$$

For FRRMs and soft biological tissues exhibiting strain hardening, one should require that

$$h_{11} > 0 \text{ and } h_{11} + h_{14} + h_{44} + h_5 > 0 \tag{3.51}$$

For simple shear in the  $X_1X_2$  – plane, fibers aligned along the  $X_1$ - axis and the  $X_2$ - axis affect the shear stress – shear strain curve as well as normal stresses on planes  $x_1 = \text{constant}$  and  $x_2 = \text{constant}$ .

During the simple shear deformation, fibers along the unit vector  $(\cos\alpha, \sin\alpha, 0)$  are rotated through the angle  $\alpha - \cos^{-1} \left[ (\cos\alpha + k \sin\alpha) / \sqrt{(1+k^2 \sin^2\alpha + 2k \sin\alpha \cos\alpha)} \right]$ . In particular, fibers oriented along the  $X_2$ - ( $X_1$ - ) axis in the reference configuration are rotated through the angle  $\frac{\pi}{2} - \cos^{-1} \left[ k / \sqrt{(1+k^2)} \right]$  (zero).

The slope of the  $\sigma_{12}$  versus  $k$  curve equals zero at

$$k = \frac{-3(h_{14} + h_5 + 2h_{44} \sin^2 \alpha) \cos \alpha \sin \alpha}{6(h_{11} + h_{14} \sin^2 \alpha + h_5 \sin^2 \alpha + h_{44} \sin^4 \alpha)} + \frac{0.25 \sqrt{144 \cos^2 \alpha \sin^2 \alpha (h_{14} + h_5 + 2h_{44} \sin^2 \alpha)^2 - 96(h_{11} + h_{14} \sin^2 \alpha + h_5 \sin^2 \alpha + h_{44} \sin^4 \alpha)(h_1 + h_2 + h_3 + 2h_{44} \sin^4 \alpha - 2h_{44} \sin^2 \alpha + 6h_{44} \cos^2 \alpha \sin^2 \alpha)}}{6(h_{11} + h_{14} \sin^2 \alpha + h_5 \sin^2 \alpha + h_{44} \sin^4 \alpha)}$$

and the material then may become unstable; e.g. see the text before Fig. 1 in [32].

### 3.2.4.3 Inflation, extension and twisting of a two-layer cylinder caused by internal pressure, end torque, and axial force

We use Ericksen's inverse method to analyze the combined inflation, twisting and extension of a hollow two-layer cylinder. Even though Ericksen gave this family of universal solutions for isotropic hyperelastic bodies, we explore if it also applies to transversely isotropic hyperelastic materials. The unit vectors along the fiber direction in the cylindrical coordinate system in the reference configuration are  $(0, \cos \alpha_1, \sin \alpha_1)$  for the inner layer, and  $(0, \cos \alpha_2, \sin \alpha_2)$  for the outer layer. In particular, for  $\pm \alpha_1$  angle-ply tubes  $\alpha_2 = -\alpha_1$ . Each layer of the composite cylinder is modeled using the above studied smeared/homogenized material model, Eq. (3.3).

Assume that the cylinder is long, the  $X_3$  - axis of the rectangular Cartesian coordinate axes coincides with the cylinder axis, and the applied internal pressure is independent of  $X_3$  and the angular position of a material point. Schematic sketches of the middle portion of the 2-layer

cylindrical tube are illustrated in Figure 3.9, where both rectangular and cylindrical coordinate axes are shown. We assume the following deformation field.

$$\begin{aligned}
 r &= \left( A^{(1)} + D^{(1)} R^2 \right)^{1/2}, \theta = \Theta + \frac{\tau^{(1)} Z}{D^{(1)}}, z = \frac{Z}{D^{(1)}} & r_1 \leq r \leq r_{mid} \\
 r &= \left( A^{(2)} + D^{(2)} R^2 \right)^{1/2}, \theta = \Theta + \frac{\tau^{(2)} Z}{D^{(2)}}, z = \frac{Z}{D^{(2)}} & r_{mid} \leq r \leq r_2
 \end{aligned} \tag{3.52}$$

where  $A$  is a non-zero constant,  $D$  represents the axial stretch of the tube,  $\tau$  represents the rotation per unit current axial length, and superscripts 1 and 2 correspond to the inner and the outer layers, respectively.  $R$ ,  $\Theta$ , and  $Z$  ( $r$ ,  $\theta$  and  $z$ ) are cylindrical coordinates of a material point in the reference (deformed) configuration. The cylinder bounded by surfaces  $R=R_1$  and  $R=R_2$  in the reference configuration is deformed into the cylinder bounded by surfaces  $r=r_1$  and  $r=r_2$  in the current configuration, as depicted in Figure 3.9. The deformed interface between the two plies is denoted by  $r=r_{mid}$ , corresponding to the undeformed interface  $R=R_{mid}$ .

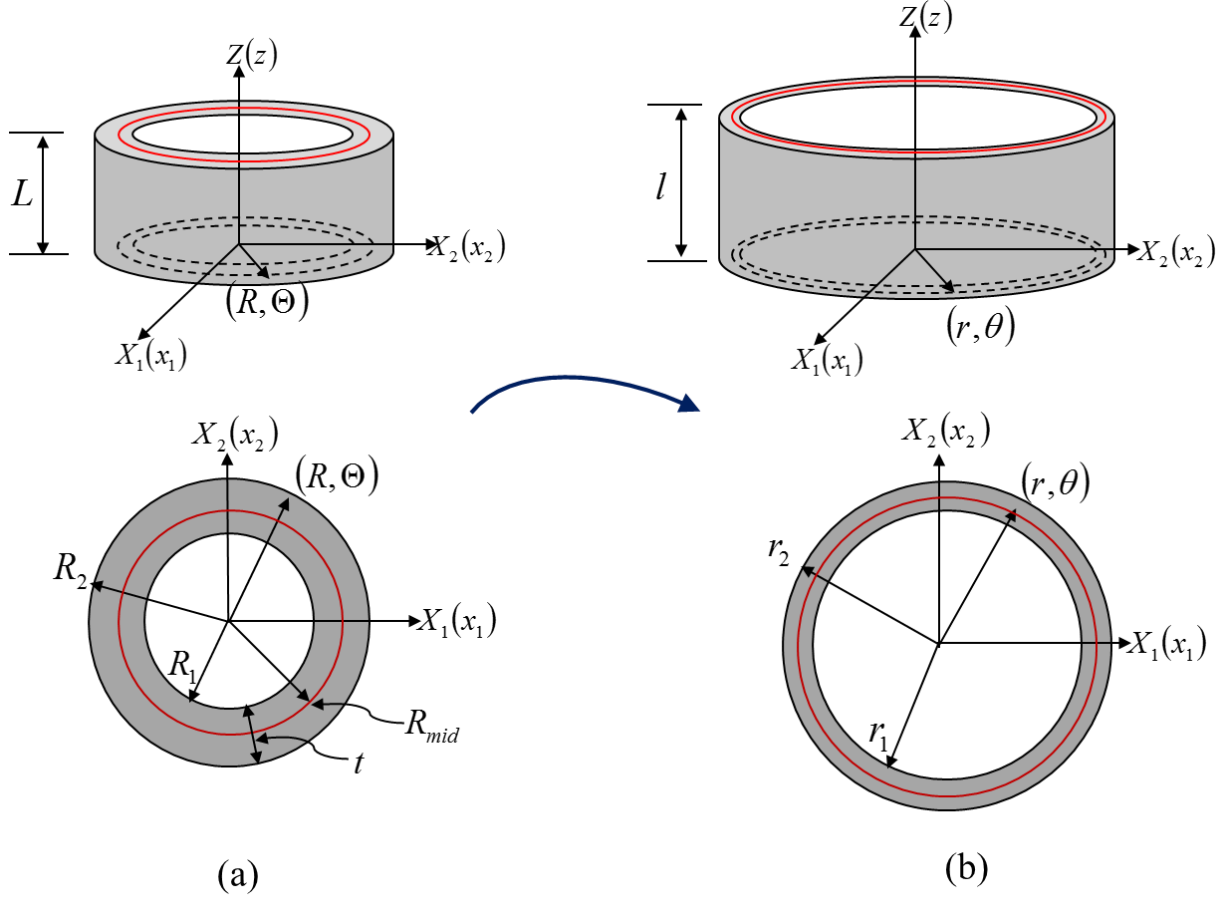


Figure 3.9. Schematic of deformations of the middle portion of a long cylindrical tube; (a) reference configuration, (b) deformed configuration

The two layers are assumed to be perfectly bonded to each other, which requires the following continuity conditions for displacements and surface tractions on the interface.

$$u_r^{(1)} = u_r^{(2)}, u_\theta^{(1)} = u_\theta^{(2)}, u_z^{(1)} = u_z^{(2)} \quad (3.53)$$

$$\sigma_{rr}^{(1)} = \sigma_{rr}^{(2)}, \sigma_{\theta r}^{(1)} = \sigma_{\theta r}^{(2)}, \sigma_{zr}^{(1)} = \sigma_{zr}^{(2)}$$

where  $u_r = r - R$ ,  $u_\theta = \theta - \Theta$  and  $u_z = z - Z$ . By enforcing Eq. (3.53), the following relations are obtained.

$$A^{(1)} = A^{(2)}, \tau^{(1)} = \tau^{(2)}, D^{(1)} = D^{(2)} \quad (3.54)$$

Thus Eq. (3.52) can be rewritten as

$$r = (A + DR^2)^{1/2}, \theta = \Theta + \frac{\tau Z}{D}, z = \frac{Z}{D} \quad \text{for } r_1 \leq r \leq r_2 \quad (3.55)$$

Physical components of the deformation gradient,  $\mathbf{F}$ , and of the left and the right Cauchy-Green tensors ( $\mathbf{B}$  and  $\mathbf{C}$ ) in cylindrical coordinates are:

$$\mathbf{F} = \begin{bmatrix} D \frac{R}{r} & 0 & 0 \\ 0 & \frac{R}{r} & \frac{r\tau}{D} \\ 0 & 0 & \frac{1}{D} \end{bmatrix}, \mathbf{B} = \begin{bmatrix} \frac{(DR)^2}{r^2} & 0 & 0 \\ 0 & \frac{r^2}{R^2} + \frac{(r\tau)^2}{(D)^2} & \frac{r\tau}{D} \\ 0 & \frac{r\tau}{D} & \frac{1}{(D)^2} \end{bmatrix}, \mathbf{C} = \begin{bmatrix} \frac{(DR)^2}{r^2} & 0 & 0 \\ 0 & \frac{r^2}{R^2} & \frac{r^2\tau}{DR} \\ 0 & \frac{r^2\tau}{DR} & \frac{1}{(D)^2} + \frac{(r\tau)^2}{(D)^2} \end{bmatrix} \quad (3.56)$$

The physical components of the Almansi-Hamel strain tensor in cylindrical coordinates are:

$$\varepsilon_{rr} = \frac{1}{2} \left[ 1 - \frac{r^2}{(DR)^2} \right], \varepsilon_{\theta\theta} = \frac{1}{2} \left[ 1 - \frac{(DR)^2}{r^2} \right], \varepsilon_{zz} = \frac{1}{2} \left[ 1 - (D)^2 - (r\tau)^2 \right], \varepsilon_{\theta z} = \frac{1}{2} \frac{R^2\tau}{r}, \varepsilon_{rz} = \varepsilon_{r\theta} = 0 \quad (3.57)$$

The strain invariants,  $I_1, I_4$  and  $I_5$ , for the inner layer,  $r_1 \leq r \leq r_{mid}$ , are:

$$\begin{aligned} I_1^{(1)} &= \left[ \frac{DR}{r} \right]^2 + \left[ \frac{\tau r + 1}{D} \right]^2 + \frac{r^2}{R^2} \\ I_4^{(1)} &= \left[ \frac{\sin \alpha_1}{D} \right]^2 + \left[ \frac{r}{DR} \right]^2 [D \cos \alpha_1 + R\tau \sin \alpha_1]^2 \\ I_5^{(1)} &= \frac{(\sin \alpha_1)^2}{[D]^4} + \frac{r^2}{[RD]^4} [D \cos \alpha_1 + R\tau \sin \alpha_1] \left[ 2R^3\tau \sin \alpha_1 + r^2 \left( (D)^2 + (R\tau)^2 \right) (D \cos \alpha_1 + R\tau \sin \alpha_1) \right] \end{aligned} \quad (3.58)$$

For the outer layer,  $r_{mid} \leq r \leq r_2$ ,  $I_1^{(2)}, I_4^{(2)}, I_5^{(2)}$  are obtained by replacing  $\alpha_1$  by  $\alpha_2$  in Eq. (3.58).

The boundary conditions corresponding to the tube subjected to an inflating pressure,  $P_{in}$ , on the inner face,  $r=r_1$ , null tractions on the outer surface,  $r=r_2$ , the resultant axial load,  $N_z$ , and the resultant torque,  $M_z$ , applied on the tube end faces are listed below.

$$\begin{aligned}
r = r_1 : \sigma_{rr} &= -P_{in}, \sigma_{\theta r} = \sigma_{zr} = 0 \\
r = r_2 : \sigma_{rr} &= \sigma_{\theta r} = \sigma_{zr} = 0 \\
z = 0, l : N_z &= \pm \int_{r_1}^{r_2} \int_0^{2\pi} \sigma_{zz} r dr d\theta, \\
N_r &= \pm \int_{r_1}^{r_2} \int_0^{2\pi} \sigma_{rz} r dr d\theta = 0, \\
N_\theta &= \pm \int_{r_1}^{r_2} \int_0^{2\pi} \sigma_{\theta z} r dr d\theta = 0, \\
M_z &= \pm \int_{r_1}^{r_2} \int_0^{2\pi} \sigma_{\theta z} r^2 dr d\theta
\end{aligned} \tag{3.59}$$

That is, at the end faces, the resultant forces and resultant moments, rather than pointwise tractions, are prescribed.

Substituting from (3.56) and (3.58) into (3.3), we get the following expressions for components of the Cauchy stress tensor:

For the inner layer ( $r_1 \leq r \leq r_{mid}$ ):

$$\begin{aligned}
\sigma_{rr}^{(1)} &= -p^{(1)} + 2\left[h_1 + 2h_{11}(I_1^{(1)} - 3) + h_{14}(I_4^{(1)} - 1)\right]\left(\frac{RD}{r}\right)^2 + 2h_2\left[D^2 + R^2\left(\tau^2 + \frac{1}{r^2}\right)\right] \\
\sigma_{\theta\theta}^{(1)} &= -p^{(1)} + 2\left[h_1 + 2h_{11}(I_1^{(1)} - 3) + h_{14}(I_4^{(1)} - 1)\right]r^2\left(\frac{\tau^2}{D^2} + \frac{1}{R^2}\right) + 2h_2\left[D^2 + R^2\tau^2 + \frac{r^2}{D^2R^2}\right] \\
&+ 2\left[h_4 + h_{14}(I_1^{(1)} - 3) + 2h_{44}(I_4^{(1)} - 1)\right]\left(\frac{r\tau \sin \alpha_1}{D} + \frac{r \cos \alpha_1}{R}\right)^2 \\
&+ 4h_5\frac{r^2}{D^4R^4}(D \cos \alpha_1 + R\tau \sin \alpha_1)\left[R^3\tau \sin \alpha_1 + r^2(D \cos \alpha_1 + R\tau \sin \alpha_1)(D^2 + R^2\tau^2)\right] \\
\sigma_{zz}^{(1)} &= -p^{(1)} + 2\left[h_1 + 2h_{11}(I_1^{(1)} - 3) + h_{14}(I_4^{(1)} - 1)\right]\frac{1}{D^2} + 2h_2\frac{1}{R^2r^2}\left[R^4 + \frac{r^4}{D^2}\right] \\
&+ 2\left[h_4 + h_{14}(I_1^{(1)} - 3) + 2h_{44}(I_4^{(1)} - 1)\right]\left(\frac{\sin \alpha_1}{D}\right)^2 \\
&+ 4h_5\frac{\sin \alpha_1}{D^4R}\left[r^2\tau D \cos \alpha_1 + R \sin \alpha_1(1 + r^2\tau^2)\right] \\
\sigma_{\theta z}^{(1)} &= 2\left[h_1 + 2h_{11}(I_1^{(1)} - 3) + h_{14}(I_4^{(1)} - 1)\right]\frac{r\tau}{D^2} + 2h_2\frac{R^2\tau}{r} \\
&+ 2\left[h_4 + h_{14}(I_1^{(1)} - 3) + 2h_{44}(I_4^{(1)} - 1)\right]\frac{r \sin \alpha_1}{D^2R}(D \cos \alpha_1 + R\tau \sin \alpha_1) \\
&+ 2h_5\frac{r}{D^4}\left[\tau(\sin \alpha_1)^2 + \frac{r^2 \sin \alpha_1}{R^3}(D \cos \alpha_1 + R\tau \sin \alpha_1)(D^2 + R^2\tau^2) + \right. \\
&\left. \frac{1}{R^2}(D \cos \alpha_1 + R\tau \sin \alpha_1)(Dr^2\tau \cos \alpha_1 + R \sin \alpha_1 + r^2\tau^2R \sin \alpha_1)\right] \\
\sigma_{rz}^{(1)} &= \sigma_{r\theta}^{(1)} = 0
\end{aligned} \tag{3.60}$$

The stress components,  $\sigma_{rr}^{(2)}$ ,  $\sigma_{\theta\theta}^{(2)}$ ,  $\sigma_{zz}^{(2)}$ ,  $\sigma_{r\theta}^{(2)}$ ,  $\sigma_{rz}^{(2)}$  and  $\sigma_{\theta z}^{(2)}$ , for the outer layer are similarly obtained.

For null body forces, equations expressing the balance of linear momentum in cylindrical coordinates are:

$$\begin{aligned}
\frac{\partial \sigma_{rr}}{\partial r} + \frac{1}{r} \frac{\partial \sigma_{r\theta}}{\partial \theta} + \frac{\partial \sigma_{rz}}{\partial z} + \frac{\sigma_{rr} - \sigma_{\theta\theta}}{r} &= 0 \\
\frac{\partial \sigma_{\theta r}}{\partial r} + \frac{1}{r} \frac{\partial \sigma_{\theta\theta}}{\partial \theta} + \frac{\partial \sigma_{\theta z}}{\partial z} + \frac{2\sigma_{\theta r}}{r} &= 0 \\
\frac{\partial \sigma_{zr}}{\partial r} + \frac{1}{r} \frac{\partial \sigma_{z\theta}}{\partial \theta} + \frac{\partial \sigma_{zz}}{\partial z} + \frac{\sigma_{zr}}{r} &= 0
\end{aligned} \tag{3.61}$$

Substitution for stress components from Eq. (3.60) into Eq. (3.61) gives  $\frac{\partial p^{(1)}}{\partial z} = 0$ ,  $\frac{\partial p^{(1)}}{\partial \theta} = 0$  for the inner layer ( $r_1 \leq r \leq r_{mid}$ ). Similarly, for the outer layer,  $\frac{\partial p^{(2)}}{\partial z} = 0$ ,  $\frac{\partial p^{(2)}}{\partial \theta} = 0$ . Thus the hydrostatic pressures  $p^{(1)}$  and  $p^{(2)}$  and hence all components of the stress tensor depend only upon the radial coordinate  $r$ . The only non-trivial equilibrium equation, the first equation in Eq. (3.61), reduces to

$$\frac{d\sigma_{rr}(r)}{dr} + \frac{\sigma_{rr} - \sigma_{\theta\theta}}{r} = 0 \quad (3.62)$$

From Eq. (3.60) it is found that two out of the three continuity equations (Eq. (3.53)) for surface tractions at the interface,  $r = r_{mid}$ , are trivially satisfied, and the remaining one to be satisfied is

$$\sigma_{rr}^{(1)} = \sigma_{rr}^{(2)} = \sigma_{rr}^{mid} \quad (3.63)$$

where the radial stress at the interface is denoted as  $\sigma_{rr}^{mid}$ .

Integration with respect to  $r$  of Eq. (3.62) from the interface to the outer surface gives

$$\sigma_{rr}^{(2)}(r) = \int_r^{r_2} \frac{\sigma_{rr}^{(2)} - \sigma_{\theta\theta}^{(2)}}{r} dr \quad (3.64)$$

where the boundary condition  $\sigma_{rr}(r_2) = 0$  has been used. Substituting expressions of  $\sigma_{rr}^{(2)}$  and  $\sigma_{\theta\theta}^{(2)}$  into Eq. (3.64), we get the expression for the hydrostatic pressure in the outer layer,  $p^{(2)}$ , as a function of deformation parameters ( $A$ ,  $D$  and  $\tau$ ), fiber angle ( $\alpha_2$ ) and radial coordinate ( $R$ ) as

$$p^{(2)} = 2 \left[ h_1 + 2h_{11} (I_1^{(2)} - 3) + h_{14} (I_4^{(2)} - 1) \right] \left( \frac{RD}{r} \right)^2 + 2h_2 \left[ D^2 + R^2 \left( \tau^2 + \frac{1}{r^2} \right) \right] - \int_r^{r_2} \frac{\sigma_{rr}^{(2)} - \sigma_{\theta\theta}^{(2)}}{r} dr \quad (3.65)$$

Thus expressions for stresses in the outer layer can be determined.

From Eq. (3.64), we get

$$\sigma_{rr}^{mid} = \int_{r_{mid}}^{r_2} \frac{\sigma_{rr}^{(2)} - \sigma_{\theta\theta}^{(2)}}{r} dr \quad (3.66)$$

Then the expression for the pressure ( $P_{in}$ ) acting on the inner surface of the tube, and radial stresses in the inner layer ( $\sigma_{rr}^{(1)}$ ) can be obtained by integrating Eq. (3.62) with respect to  $r$ .

$$P_{in} = \int_{r_1}^{r_{mid}} \frac{\sigma_{\theta\theta}^{(1)} - \sigma_{rr}^{(1)}}{r} dr - \sigma_{rr}^{mid} = \int_{r_1}^{r_{mid}} \frac{\sigma_{\theta\theta}^{(1)} - \sigma_{rr}^{(1)}}{r} dr + \int_{r_{mid}}^{r_2} \frac{\sigma_{\theta\theta}^{(2)} - \sigma_{rr}^{(2)}}{r} dr \quad (3.67)$$

$$\sigma_{rr}^{(1)}(r) = \sigma_{rr}^{mid} + \int_r^{r_{mid}} \frac{\sigma_{rr}^{(1)} - \sigma_{\theta\theta}^{(1)}}{r} dr = \int_{r_{mid}}^{r_2} \frac{\sigma_{rr}^{(2)} - \sigma_{\theta\theta}^{(2)}}{r} dr + \int_r^{r_{mid}} \frac{\sigma_{rr}^{(1)} - \sigma_{\theta\theta}^{(1)}}{r} dr \quad \text{for } r_1 \leq r \leq r_{mid} \quad (3.68)$$

Substituting for  $\sigma_{rr}^{(1)}$  and  $\sigma_{\theta\theta}^{(1)}$  from Eq. (3.60) into Eq. (3.68) gives

$$p^{(1)} = 2 \left[ h_1 + 2h_{11} (I_1^{(1)} - 3) + h_{14} (I_4^{(1)} - 1) \right] \left( \frac{RD}{r} \right)^2 + 2h_2 \left[ D^2 + R^2 \left( \tau^2 + \frac{1}{r^2} \right) \right] - \int_{r_{mid}}^{r_2} \frac{\sigma_{rr}^{(2)} - \sigma_{\theta\theta}^{(2)}}{r} dr - \int_r^{r_{mid}} \frac{\sigma_{rr}^{(1)} - \sigma_{\theta\theta}^{(1)}}{r} dr \quad (3.69)$$

The remaining stress components in the inner layer can then be calculated.

The expressions for the applied moment  $M_z$  and the axial load  $N_z$  exerted on the end faces are:

$$\begin{aligned} M_z &= \int_{r_1}^{r_{mid}} \int_0^{2\pi} \sigma_{\theta z}^{(1)} r^2 dr d\theta + \int_{r_{mid}}^{r_2} \int_0^{2\pi} \sigma_{\theta z}^{(2)} r^2 dr d\theta \\ &= 2\pi \int_{r_1}^{r_{mid}} \sigma_{\theta z}^{(1)} r^2 dr + 2\pi \int_{r_{mid}}^{r_2} \sigma_{\theta z}^{(2)} r^2 dr \end{aligned} \quad (3.70)$$

$$\begin{aligned} N_z &= \int_{r_1}^{r_{mid}} \int_0^{2\pi} \sigma_{zz}^{(1)} r dr d\theta + \int_{r_{mid}}^{r_2} \int_0^{2\pi} \sigma_{zz}^{(2)} r dr d\theta \\ &= 2\pi \int_{r_1}^{r_{mid}} \sigma_{zz}^{(1)} r dr + 2\pi \int_{r_{mid}}^{r_2} \sigma_{zz}^{(2)} r dr \end{aligned} \quad (3.71)$$

An equivalent expression for Eq. (3.71) can be given by adding and subtracting the radial stress. That is,

$$N_z = 2\pi \int_{r_1}^{r_{mid}} \left( \sigma_{zz}^{(1)} - \sigma_{rr}^{(1)} + \sigma_{\theta\theta}^{(1)} \right) r dr + 2\pi \int_{r_{mid}}^{r_2} \left( \sigma_{zz}^{(2)} - \sigma_{rr}^{(2)} + \sigma_{\theta\theta}^{(2)} \right) r dr \quad (3.72)$$

We integrate the right hand side by parts and use Eqs. (3.62) and (3.72) to get

$$N_z = \pi \int_{r_1}^{r_{mid}} \left( 2\sigma_{zz}^{(1)} - \sigma_{rr}^{(1)} - \sigma_{\theta\theta}^{(1)} \right) r dr + \pi \int_{r_{mid}}^{r_2} \left( 2\sigma_{zz}^{(2)} - \sigma_{rr}^{(2)} - \sigma_{\theta\theta}^{(2)} \right) r dr + P_{in} \pi r_1^2 \quad (3.73)$$

### 3.2.4.3.1 Comparison of present results with those of Ogden

By setting the thickness of one of the two layers equal to 0 or setting  $\alpha_1 = \alpha_2$ , one can the results of [17] for cylindrical tubes reinforced with a family of fibers. The strain energy density function used in [17] is

$$W_{effective} = \frac{\mu}{2} \left[ I_1 - 3 + \rho (I_4 - 1)^2 \right] \quad (3.74)$$

which is obtained from Eq. (3.2) by setting  $h_1 = \mu/2, h_{44} = \rho\mu/2, h_{11} = h_2 = h_4 = h_{44} = h_5 = h_{14} = 0$ , Following [17], the inner pressure, the applied torque, and the applied axial force are non-dimensionalized as

$$P_{in}^* = \frac{P_{in}}{\mu}, M_z^* = \frac{M_z}{\pi\mu R_1^3}, N_z^* = \frac{N_z - P_{in} \pi r_1^2}{\pi\mu R_1^2} \quad (3.75)$$

For  $\rho = 2, R_1=1$  m,  $R_2=2$  m,  $D = 1/1.2$  and  $\tau=0.4/R_1$ , we provide in Figure 3.10 numerical results for  $P_{in}^*, M_z^*$  and  $N_z^*$  versus  $r_1/R_1$  for a series of values of  $\alpha$ . The solid lines represent solutions computed using Eq. (3.67), Eq. (3.70), Eq. (3.73) and Eq. (3.75), and the symbols denote values found using Eq. (31), Eq. (35), Eq. (38) and Eq. (47) of [17]. The two set of results agree with each other within 0.0001%.

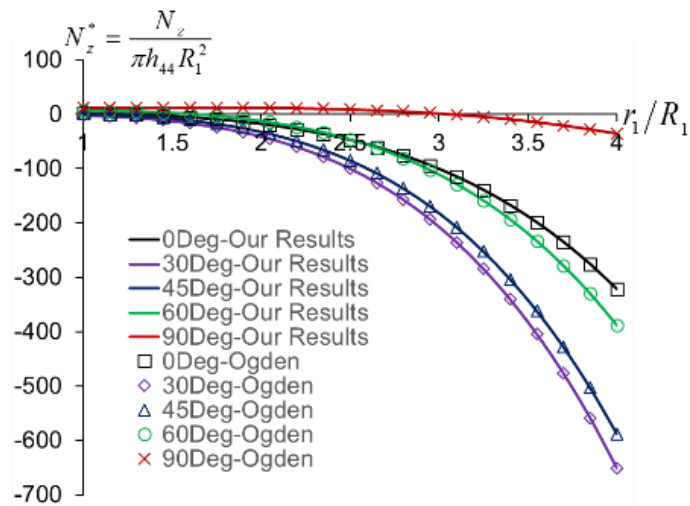
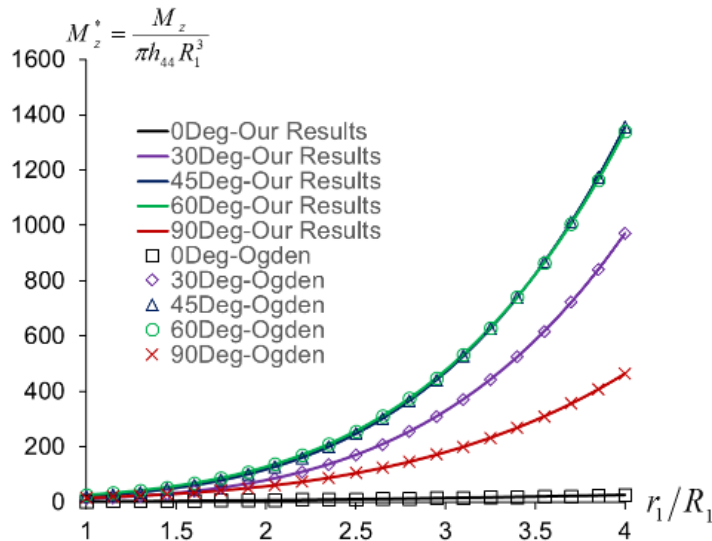
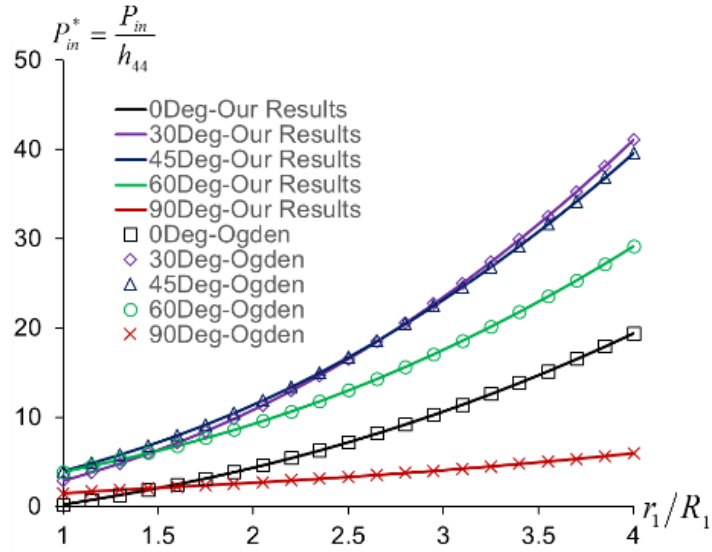


Figure 3.10. Plots of the dimensionless inner pressure, end moment and reduced axial load versus  $(r_1/R_1)$  for  $\alpha = 0^\circ, 30^\circ, 45^\circ, 60^\circ$  and  $90^\circ$  for Eq. (3.74)

Implicit relations among  $P_{in}, M_z, N_z^r$  and geometric parameters  $(R_1, t, R_{mid})$ , material parameters  $(\alpha, h_1, h_2, h_{11}, h_{14}, h_{44}, h_5)$  and deformation parameters can be written as follows.

$$\left\{ \frac{M_z}{\pi h_1 R_1^3}, \frac{N_z - P_{in} \pi r_1^2}{\pi \mu R_1^2}, \frac{P_{in}}{h_1} \right\} = f \left( \beta, \gamma, \alpha, \frac{h_{44}}{h_1}, \frac{h_{14}}{h_1}, \frac{h_{11}}{h_1}, \frac{h_2}{h_1}, \frac{h_5}{h_1}; \lambda_1 \right) \quad (3.76)$$

where  $\beta = \frac{t}{R_1}, \gamma = \frac{R_{mid} - R_1}{t}, \lambda_1 = \frac{r_1}{R_1}$ . Here  $\beta$  equals the ratio of total tube thickness  $t$  to the inner radius,  $\gamma$  the ratio of the inner layer thickness to the whole tube thickness, and  $\lambda_1$  equals the hoop stretch at the inner radius,  $r = r_1$ , defined as  $r_1/R_1$ . It is a challenge to find explicit forms of this function.

### 3.2.4.3.2 Effects of fiber orientations on M, N and P for plane strain radial expansion deformations

Because of time limitations, we have studied only plane strain radial expansion ( $A \neq 0 \text{ m}^2, D=1.0$  and  $\tau=0.0 \text{ rad/m}$ ) of a cylindrical tube made of a material with  $\frac{h_{14}}{h_1} = \frac{h_{11}}{h_1} = 0$ . We will study, in future, deformations for the combined loadings, a more general material, and different values of the fiber orientation angles  $\alpha_1$  and  $\alpha_2$ .

For simplicity, we adopted a reduced version of the material model Eq. (3.2),

$$W_{effective} = h_1 (I_1 - 3) + h_{44} (I_4 - 1)^2 + h_5 (I_5 - 2I_4 + 1) \quad (3.77)$$

where the assumption of the reference configuration being stress-free has been enforced ( $h_4 = -2h_5$ ). From Eqs. (3.10) we get

$$\begin{aligned}
h_1 &= \frac{1}{2} \frac{E_L E_T}{4E_L - E_T}; \\
h_5 &= \frac{1}{2} \left( G_L - \frac{E_L E_T}{4E_L - E_T} \right) \\
h_{44} &= \frac{1}{8} \left( E_L + \frac{E_L E_T}{4E_L - E_T} - 4G_L \right)
\end{aligned} \tag{3.78}$$

Then Eq. (3.76) can be written in an alternative form as

$$\left\{ \frac{M_z}{\pi h_1 R_1^3}, \frac{N_z - P_{in} \pi r_1^2}{\pi P_{in} R_1^2}, \frac{P_{in}}{h_1} \right\} = f \left( \beta, \gamma, \alpha, \frac{E_L}{G_T}, \frac{G_L}{G_T}; \lambda_1 \right) \tag{3.79}$$

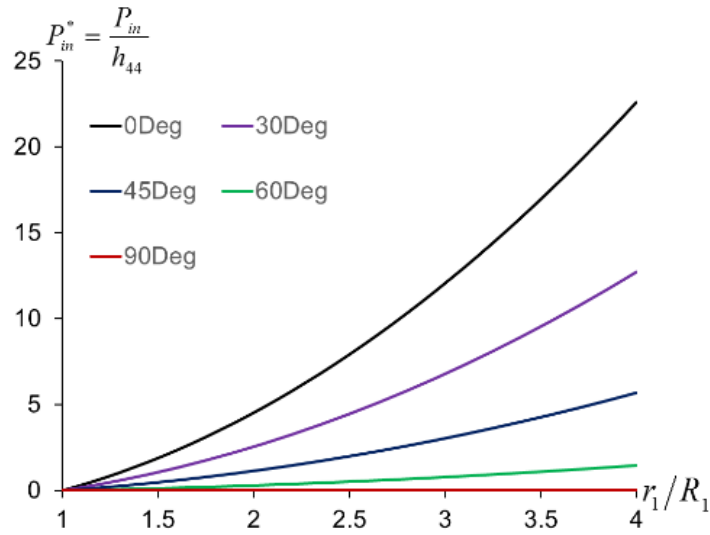
Parameters in Eq. (3.79) are summarized in Table 3.

Table 3.3 Values of parameters for the tube geometry and material constants

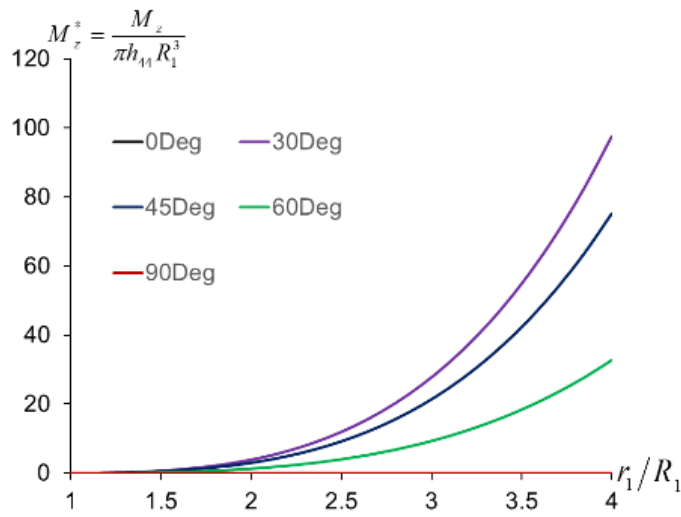
$R_I (m)$	$\beta$	$t (m)$	$r_I (m)$	$\gamma$	$R_{mid} (m)$
1.0	1.0	$= \beta R_I$	$\lambda_I R_I$	0.5	$= R_I + \gamma t$
$G_T$ (MPa)	$E_L / G_T$	$G_L / G_T$	$\lambda_I$	$D$ (axial stretch)	$\tau$ (torsional deformation)
2.0	varying parameter	varying parameter	varying parameter	1.0	0.0

Results for  $P_{in}$ ,  $M_z$  and  $N_z^r (= N_z - P_{in} \pi r_1^2)$  versus  $\lambda_I (= r_I / R_I)$  are plotted in Figure 3.11 for a series of values of  $\alpha$  with fixed values of  $R_I = 1m$ ,  $\beta = 1.0$ ,  $\gamma = 0.5$ ,  $E_L / E_T = 100$ , and  $G_L / G_T = 10$ . For each curve in Figure 3.11 (a), the qualitative behavior is the same, and for  $P_{in}$ ,  $M_z$  and  $N_z^r$  monotonically increase with an increase of  $r_I / R_I$ . Furthermore, for a given value of  $r_I / R_I$ , larger values of fiber angle  $\alpha$  are associated with smaller values of the pressure required. In Figure 3.11 (b), it is clear that the moment vanishes for  $\alpha = 0^\circ$  and  $90^\circ$ . Nonzero torques are needed at the end faces to maintain pure radial expansion for other fiber angles. As can be seen from Figure 3.11 (c), as the fiber angle  $\alpha$  decreases from  $\pi/2$  to 0, the reduced axial force changes from positive to negative as  $r_I / R_I$  increases. In addition, it is also interesting to see that at a fixed value of  $r_I / R_I$ ,

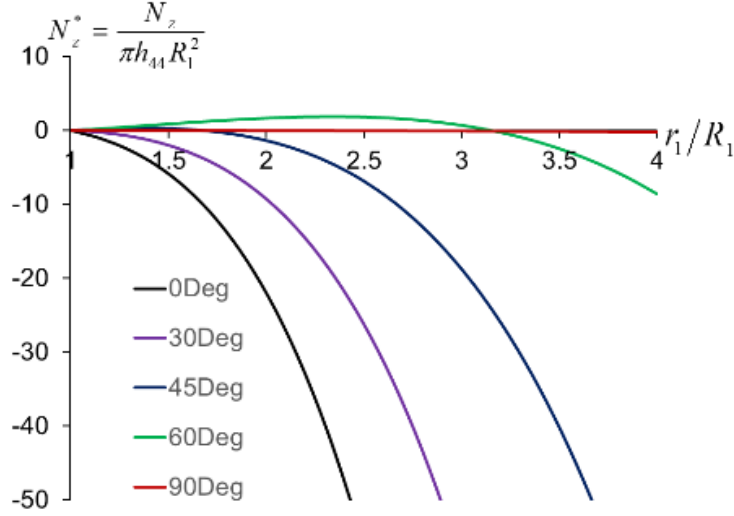
there is a special angle that corresponds with a change from compressive axial force to tensile axial force.



(a) Inner pressure



(b) End torque



(c) Reduced axial force

Figure 3.11. Plots of the dimensionless inner pressure, end moment and reduced axial load versus  $(r_1/R_1)$  for  $\alpha = 0^\circ, 30^\circ, 45^\circ, 60^\circ$  and  $90^\circ$  for Eq. (3.77)

For the material model given by Eq. (3.77), the dimensionless reduced axial force has the expression

$$\begin{aligned}
 N_z^* = & \\
 & c^2 \left( \frac{2E_L}{G_T} + 2 - \frac{8G_L}{G_T} \right) \left[ \frac{2c^2 R_1^2 (1 - 2\lambda_1^2 + \lambda_1^4)}{-r_1^2 + R_1^2 (-1 + \lambda_1^2)} - \frac{2c^2 R_1^2 (1 - 2\lambda_1^2 + \lambda_1^4)}{-r_2^2 + R_1^2 (-1 + \lambda_1^2)} \right. \\
 & \left. + 4(0.5c^2 - s^2)(\lambda^2 - 1) \log \left( \frac{r_1^2 + R_1^2 (1 - \lambda_1^2)}{r_2^2 + R_1^2 (1 - \lambda_1^2)} \right) \right] \\
 & + \frac{2(1 - 2\lambda_1^2 + \lambda_1^4)}{1 - \lambda_1^2} \left[ \log \left( \frac{r_1}{r_2} \right) + \frac{1}{2} \log \left( \frac{r_2^2 + R_1^2 (1 - \lambda_1^2)}{r_1^2 + R_1^2 (1 - \lambda_1^2)} \right) \right] \\
 & + \left( \frac{G_L}{G_T} - 1 \right) \left[ \frac{2c^2 R_1^2 (-1 + \lambda_1^2)^2}{-r_1^2 + R_1^2 (-1 + \lambda_1^2)} - \frac{2c^2 R_1^2 (-1 + \lambda_1^2)^2}{-r_2^2 + R_1^2 (-1 + \lambda_1^2)} \right. \\
 & \left. + 2c^2 (-1 + \lambda_1^2) \log \left( \frac{r_1^2 + R_1^2 (1 - \lambda_1^2)}{r_2^2 + R_1^2 (1 - \lambda_1^2)} \right) \right]
 \end{aligned} \tag{3.80}$$

For a neo-Hookean material,  $h_5 = h_{44} = 0$ , and Eq. (3.80) simplifies to

$$N_z^* = \frac{2(1-2\lambda_1^2 + \lambda_1^4)}{1-\lambda_1^2} \left[ \log\left(\frac{r_1}{r_2}\right) + \frac{1}{2} \log\left(\frac{r_2^2 + R_1^2(1-\lambda_1^2)}{r_1^2 + R_1^2(1-\lambda_1^2)}\right) \right] \quad (3.81)$$

For infinitesimal deformations,  $\lambda_1 = 1 + e_{11}$ , and Eq. (3.81) gives  $N_z^* = 0$ .

We define the fiber angle that decouples the axial load from the end torque and the inner pressure as the decoupling angle,  $\alpha^*$ . From Eq. (3.80) it is found that if  $G_L = G_T$ , the last term on its left hand vanishes, and the second term vanishes for infinitesimal deformations. Thus for infinitesimal radial expansion of the composite tube made of a material model with  $G_L = G_T$ ,

$$N_z^* = 4(0.5c^2 - s^2)c^2(\lambda^2 - 1) \left( \frac{2E_L}{G_T} - 6 \right) \log\left(\frac{r_1^2 + R_1^2(1-\lambda_1^2)}{r_2^2 + R_1^2(1-\lambda_1^2)}\right) \quad (3.82)$$

Two possible solutions for  $N_z^* = 0$ , are  $c = 0$  and  $0.5c^2 - s^2 = 0$ , resulting in  $\alpha^* = 90^\circ$  and  $35.26^\circ$ , respectively. Following [10],  $\alpha^* = 35.26$  is called the “magic” angle.

### 3.3 Implementation of the material model in LS-DYNA

We have implemented in the commercial FE software LS-DYNA the material model (3.3) as a user-defined subroutine. While analytically analyzing an IBVP, the homogenized material is assumed to be incompressible. However, during the numerical solution of the same IBVP, the material is taken to be nearly incompressible since the FE algorithms in LS-DYNA do not allow the assumption of perfect incompressibility. Here the following nearly incompressible form of the material model has been implemented in LS-DYNA.

$$W_{effective} = \frac{K}{2} \left( \frac{J^2 - 1}{2} - \ln J \right) + h_1(\bar{I}_1 - 3) + h_{11}(\bar{I}_1 - 3)^2 + h_2(\bar{I}_2 - 3) \quad (3.83)$$

$$+ h_4(\bar{I}_4 - 1) + h_{44}(\bar{I}_4 - 1)^2 + h_5(\bar{I}_5 - 1) + h_{14}(\bar{I}_1 - 3)(\bar{I}_4 - 1)$$

$$J\sigma = \frac{K}{2} (J^2 - 1)\mathbf{I} + 2[h_1 + 2h_{11}(\bar{I}_1 - 3) + h_{14}(\bar{I}_4 - 1)] \left( \bar{\mathbf{B}} - \frac{1}{3}\bar{I}_1\mathbf{I} \right) + 2h_2 \left( \bar{I}_1\bar{\mathbf{B}} - \bar{\mathbf{B}}^2 - \frac{2}{3}\bar{I}_2\mathbf{I} \right) \quad (3.84)$$

$$+ 2[h_4 + 2h_{44}(\bar{I}_4 - 1) + h_{14}(\bar{I}_1 - 3)] \left( \bar{\mathbf{a}} \otimes \bar{\mathbf{a}} - \frac{1}{3}\bar{I}_4\mathbf{I} \right) + 2h_5 \left( \bar{\mathbf{a}} \otimes \bar{\mathbf{B}} \bullet \bar{\mathbf{a}} + \bar{\mathbf{a}} \bullet \bar{\mathbf{B}} \otimes \bar{\mathbf{a}} - \frac{2}{3}\bar{I}_5\mathbf{I} \right)$$

where  $K$  is the bulk modulus that is assigned a value much larger than that of the other material parameters. For  $K \gg h_{44}$ , the solution of the IBVP for nearly incompressible materials is very close to that for incompressible materials. The source code and user's guide is given in Appendix C, and the input file for uniaxial tensile loading of a cube along the fiber direction is given in Appendix D. In order to verify the implementation of the subroutine, a few simple IBVPs, including simple extension, simple shear, and inflation and twisting deformations of a transversely isotropic cylindrical tube, have been analyzed and results compared with their analytical solutions.

For the composite tube problem analytically studied above, we set  $A=0.003 \text{ m}^2$ ,  $D=1.0$ ,  $\tau=5.0 \text{ rad/m}$  and  $\alpha_1=\alpha_2=\phi=30^\circ$ , and compare the computed Cauchy stresses and the Almansi-Hamel strains with the analytical ones. Values of material parameters and geometric dimensions are not critical for verifying the implementation of the subroutine. Thus results have been computed for a hollow cylinder with  $R_1 = 50 \text{ mm}$ ,  $R_2 = 100 \text{ mm}$ , and  $25 \text{ mm}$  thickness in the reference configuration,  $h_1=h_2=0.5 \text{ MPa}$ ,  $h_5=50 \text{ MPa}$ ,  $h_4=-2h_5$ ,  $h_{44}=50 \text{ MPa}$  and  $h_{11}=0.01 \text{ MPa}$ ,  $h_{14}=0.1 \text{ MPa}$ ,  $K = 1000h_{44}$ , and  $\alpha_1= \alpha_2= 30^\circ$ . With the outer surface ( $r=r_2$ ) traction free, we apply incremental displacements to the remaining surfaces as given by the analytical solution. Boundary conditions used are

$$\text{Surface } r = r_1: u_1 = r \cos \theta - R \cos \Theta, u_2 = r \sin \theta - R \sin \Theta, u_3 = 0$$

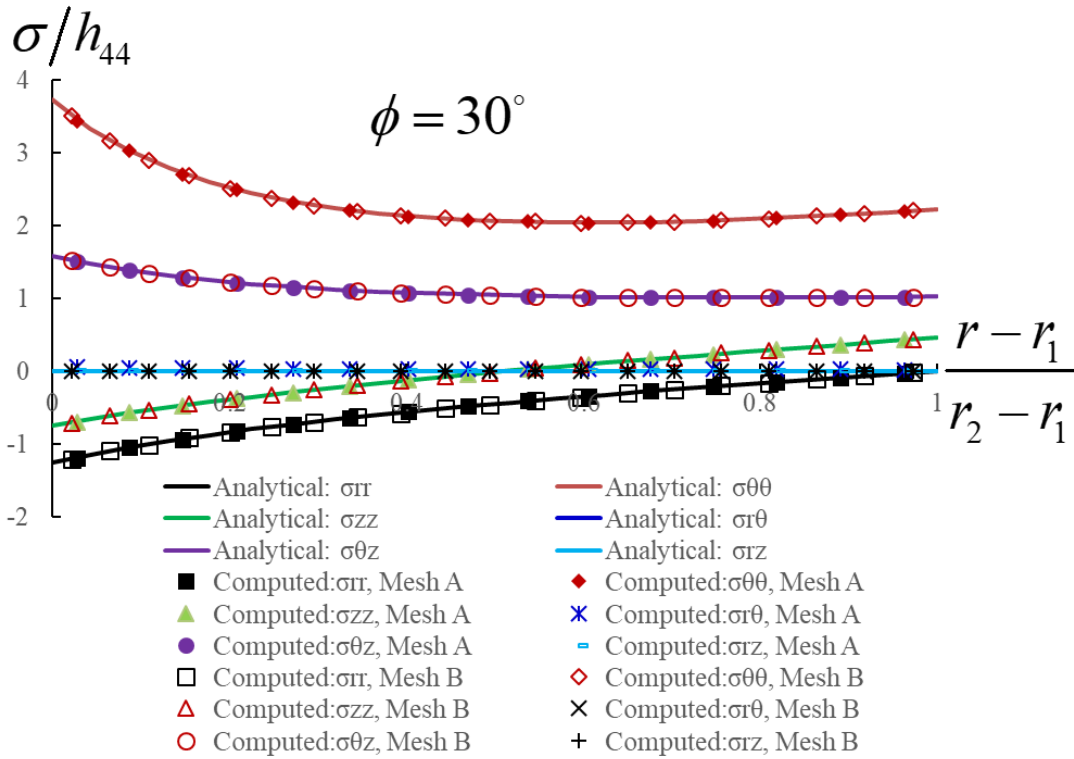
$$\text{Surface } r = r_2: \sigma_{rr} = \sigma_{r\theta} = \sigma_{rz} = 0$$

$$\text{Surface } z = 0: u_1 = r \cos \theta - R \cos \Theta, u_2 = r \sin \theta - R \sin \Theta, u_3 = 0$$

$$\text{Surface } z = l: u_1 = r \cos \theta - R \cos \Theta, u_2 = r \sin \theta - R \sin \Theta, u_3 = 0 \quad (3.85)$$

Eight-node brick elements, one integration point, and the Belytschko-Bindeman hourglass control algorithm [31] are used for all simulations. Static deformations have been simulated in LS-DYNA by artificially increasing the mass density to  $1e10 \text{ kg/m}^3$  for the FRRM, and employing two FE meshes A and B having  $15*60*5$  ( $r$ - $\theta$ - $z$ ) and  $20*80*5$  ( $r$ - $\theta$ - $z$ ) uniform elements. For  $\alpha_1 = \alpha_2 = \phi = 30^\circ$ , the computed Cauchy stresses normalized by  $h_{44}$  and the Almansi-Hamel strains from the two meshes are plotted versus the normalized radial locations in Figure 3.12 with the analytical

solutions indicated using solid lines. Both the stresses and the strains are output at the element centroids. Strains (stresses) from the FE meshes A and B differ from their analytical values by less than 0.5% (4.5%) and 0.1 % (3.1%), respectively. The computed kinetic and the hour glass mode energies equal, respectively, 0.0002% and 0.14% of the strain energy of the body. And the work done by the external forces differ from the strain energy of the body by 0.14%.



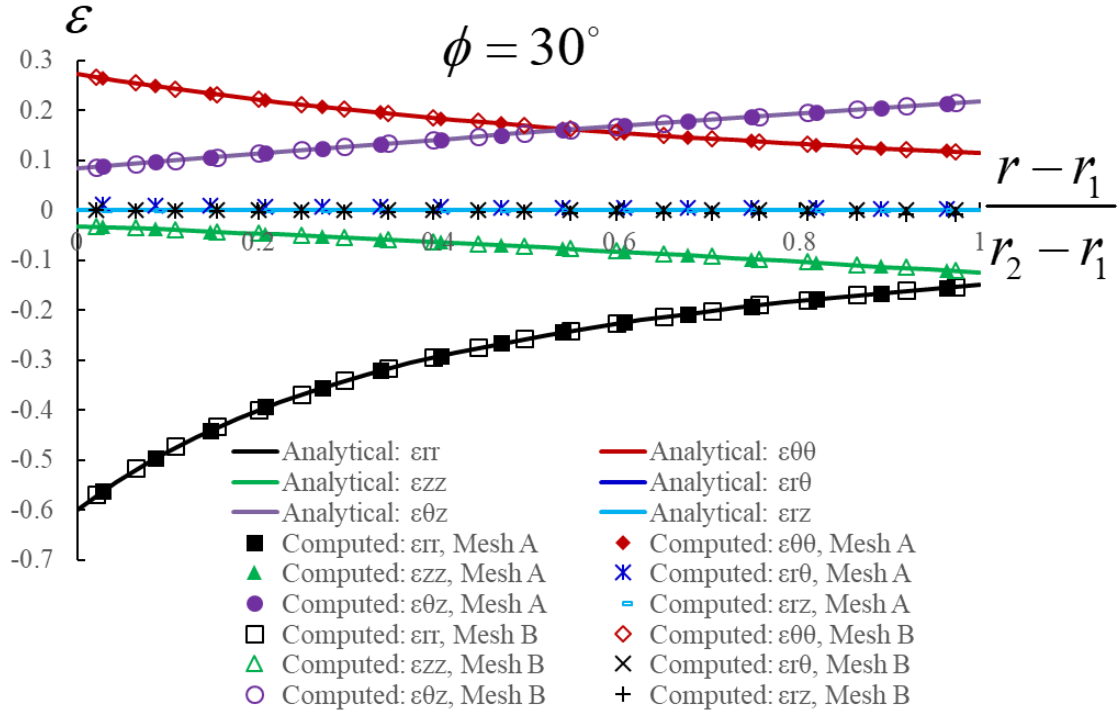


Figure 3.12. For  $\alpha_1 = \alpha_2 = \phi = 30^\circ$  the through-the-thickness variation of the Cauchy stresses and the Almansi-Hamel strains.

### 3.4 Conclusions

We have developed a material model for unidirectional fiber-reinforced rubberlike materials that assumes the homogenized material to be incompressible, transversely isotropic and hyperelastic, with the axis of transverse isotropy along the fiber direction. We assume that the stored energy is a polynomial function of the five invariants of the right Cauchy-Green tensor,  $\mathbf{C}$ , and the unit vector along the axis of transverse isotropy so that it is a complete quadratic function of  $\mathbf{C}$ . We have implemented this material model as a user-defined subroutine in the commercial finite element software, LS-DYNA, and verified its implementation by comparing the computed and the analytical solutions for radial expansion and twisting of a hollow cylinder.

For simple extension/compression of a prismatic body along the fiber direction, it is found that there may exist unequal lateral stretches for some values of the material parameters. The axial stretch corresponding to the bifurcation of the solution from equal lateral stretches to unequal ones

is lower than that at which the slope of the axial engineering stress versus the axial stretch becomes zero.

### Acknowledgements

The authors would like to acknowledge the support of the Biomedical Engineering and Mechanics Department at Virginia Tech.

### Appendix C: Source code for the user-defined material subroutines

```
subroutine umat45 (cm,eps,sig,epsp,hsv,dt1,capa,  
. etype,time,temp,failel,crv,cma,qmat,elsiz,idele)  
  
c  
c*****  
c| Livermore Software Technology Corporation (LSTC) |  
c| ----- |  
c| Copyright 1987-2008 Livermore Software Tech. Corp |  
c| All rights reserved |  
c*****  
c  
c*****  
c| This subroutine is developed by Qian Li and Romesh Batra |  
c| Computational Mechanics Laboratory, Virginia Tech |  
c| All rights reserved |  
c*****  
c  
c*****  
c|!!!!!!!!!!!!!!!!!!!!!!!!!!!!!!!!!!!!!!!!!!!!!!!!!!!!
```

c Change this file's name to "Li\_Batra-rebar.f" before use

c

c\*\*\*\*\*

c

c\*\*\*\*\*

c How to use the developed subroutine?

c 1. Bulid the new executables with the developed UMAT

c The required Object files can be downloaded from LS-DYNA website.

c Main program calls subroutine usrmat in dyn21.f,

c the developed material subroutine: "li\_batra-rebar.f" is called from there

c Use the "make" command for the Linux version to compile the code

c If compiling is successful, an executable will be created that you can use with your input file to run LS-DYNA.

c 2. To call the code in the LS-DYNA input file use this in keyword file:

c \*MAT\_USER\_DEFINED\_MATERIAL\_MODELS

c This defines the input for the user material interface

c Eaxample input deck is provided for the example of inflation of a 2-Ply cylindrical tube

c\*\*\*\*\*

c

c\*\*\*\*\*

c| Verison of LS-DYNA: smp d R7.0.0 |

c| Verison of ABAQUS: 6.13 |

c\*\*\*\*\*

c

c Transversely isotropic material (model 2)

- c  $W=h1(I1-3)+h2(I2-3)+h4(I4-1)+h5(I5-1)+h44(I4-1)^2$
- c  $+h11(I1-3)^2+h14(I1-3)(I4-1)$
- c
- c Variables
- c  $cm(1)=$ material constant  $h1$
- c  $cm(2)=$ material constant  $h2$
- c  $cm(3)=$ second material constant, here Bulk modulus  $K$
- c  $cm(4)=$ shear modulus  $G$
- c  $cm(5)=$ material constant  $h4$
- c  $cm(6)=$ material constant  $h5$
- c  $cm(7)=$ material constant  $h44$
- c  $cm(8)=$ material constant  $h11$
- c  $cm(9)=$ material constant  $h14$
- c  $cm(10)=$ components of the fiber direction wrt local  $x$
- c  $cm(11)=$ components of the fiber direction wrt local  $y$
- c  $cm(12)=$ components of the fiber direction wrt local  $z$
- c  $eps(1)=$ local  $x$  strain increment
- c  $eps(2)=$ local  $y$  strain increment
- c  $eps(3)=$ local  $z$  strain increment
- c  $eps(4)=$ local  $xy$  strain increment
- c  $eps(5)=$ local  $yz$  strain increment
- c  $eps(6)=$ local  $zx$  strain increment
- c  $sig(1)=$ local  $x$  stress
- c  $sig(2)=$ local  $y$  stress
- c  $sig(3)=$ local  $z$  stress

c sig(4)=local xy stress  
c sig(5)=local yz stress  
c sig(6)=local zx stress  
c  
c hsv(1)=1st history variable  
c hsv(2)=2nd history variable  
c .  
c .  
c .  
c .  
c hsv(9)=9th history variable  
c  
c dt1=current time step size  
c capa=reduction factor for transverse shear  
c etype:  
c eq."solid" for solid elements  
c eq."sld2d" for shell forms 13, 14, and 15 (2D solids)  
c eq."shl\_t" for shell forms 25, 26, and 27 (shells with thickness stretch)  
c eq."shell" for all other shell elements plus thick shell forms 1 and 2  
c eq."tshel" for thick shell forms 3 and 5  
c eq."hbeam" for beam element forms 1 and 11  
c eq."tbeam" for beam element form 3 (truss)  
c eq."dbeam" for beam element form 6 (discrete)  
c eq."beam " for all other beam elements  
c

```

c   time=current problem time.
c   temp=current temperature
c
c   cma=additional memory for material data defined by LMCA at
c   6th field of 2nd crad of *DATA_USER_DEFINED
c
c   All transformations into the element local system are
c   performed prior to entering this subroutine. Transformations
c   back to the global system are performed after exiting this
c   routine.
c
c   All history variables are initialized to zero in the input
c   phase. Initialization of history variables to nonzero values
c   may be done during the first call to this subroutine for each
c   element.
c
c   Energy calculations for the dyna3d energy balance are done
c   outside this subroutine.
c
include 'nlqparm'
include 'iounits.inc'
include 'bk06.inc'
character*5 etype
dimension cm(*),eps(*),sig(*),hsv(*),crv(lq1,2,*),cma(*),qmat(3,3)
logical fail1

```

```

real invar1,invar2,invar4,invar5,eps
1  ,b1,b2,b3,b4,b5,b6,bb1,bb2,bb3,bb4,bb5,bb6
2  ,c1,c2,c3,c4,c5,c6,cc1,cc2,cc3,cc4,cc5,cc6
4  ,aa1,aa2,aa3
5  ,aaaa1,aaaa2,aaaa3,aaaa4,aaaa5,aaaa6
6  ,baa1,baa2,baa3
7  ,aabaa1,aabaa2,aabaa3,aabaa4,aabaa5,aabaa6
9  ,detf,detfinv,T_vol
A  ,A01,A02,A03
B  ,detfp1,detfp2,Wstar1,Wstar2,Wstar4,Wstar5
c
if (ncycle.eq.1) then
  call usermsg('mat45')
endif
c
c
c
if (etype.eq.'solid'.or.etype.eq.'shl_t'.or.
1  etype.eq.'sld2d'.or.etype.eq.'tshel'.or.
2  etype.eq.'tet13') then
c*****
c  cm(10)=components of the fiber direction wrt local x
c  cm(11)=components of the fiber direction wrt local y
c  cm(12)=components of the fiber direction wrt local z
  PI=4.D0*DATAN(1.D0)

```

```

A01=cm(10)
A02=cm(11)
A03=cm(12)
if (ncycle.eq.0) then
  hsv(1)=1.0
  hsv(2)=0.0
  hsv(3)=0.0
  hsv(4)=0.0
  hsv(5)=1.0
  hsv(6)=0.0
  hsv(7)=0.0
  hsv(8)=0.0
  hsv(9)=1.0
endif
c
c  deformation gradient stored in hsv(1),...,hsv(9)
c
c  compute jacobian
c
  detf=hsv(1)*(hsv(5)*hsv(9)-hsv(6)*hsv(8))
1  -hsv(2)*(hsv(4)*hsv(9)-hsv(6)*hsv(7))
2  +hsv(3)*(hsv(4)*hsv(8)-hsv(5)*hsv(7))
c
c  compute left cauchy-green tensor
c

```

$$b1=hsv(1)*hsv(1)+hsv(4)*hsv(4)+hsv(7)*hsv(7)$$

$$b2=hsv(2)*hsv(2)+hsv(5)*hsv(5)+hsv(8)*hsv(8)$$

$$b3=hsv(3)*hsv(3)+hsv(6)*hsv(6)+hsv(9)*hsv(9)$$

$$b4=hsv(1)*hsv(2)+hsv(4)*hsv(5)+hsv(7)*hsv(8)$$

$$b5=hsv(2)*hsv(3)+hsv(5)*hsv(6)+hsv(8)*hsv(9)$$

$$b6=hsv(1)*hsv(3)+hsv(4)*hsv(6)+hsv(7)*hsv(9)$$

c

c compute square of left cauchy-green tensor FF\_T

c

$$bb1=b1*b1+b4*b4+b6*b6$$

$$bb2=b4*b4+b2*b2+b5*b5$$

$$bb3=b6*b6+b5*b5+b3*b3$$

$$bb4=b1*b4+b2*b4+b5*b6$$

$$bb5=b6*b4+b5*b2+b3*b5$$

$$bb6=b6*b1+b5*b4+b3*b6$$

c

c compute right cauchy-green tensor F\_TF

c

$$c1=hsv(1)*hsv(1)+hsv(2)*hsv(2)+hsv(3)*hsv(3)$$

$$c2=hsv(4)*hsv(4)+hsv(5)*hsv(5)+hsv(6)*hsv(6)$$

$$c3=hsv(7)*hsv(7)+hsv(8)*hsv(8)+hsv(9)*hsv(9)$$

$$c4=hsv(1)*hsv(4)+hsv(2)*hsv(5)+hsv(3)*hsv(6)$$

$$c5=hsv(4)*hsv(7)+hsv(5)*hsv(8)+hsv(6)*hsv(9)$$

$$c6=hsv(1)*hsv(7)+hsv(2)*hsv(8)+hsv(3)*hsv(9)$$

c

c compute square of right cauchy-green tensor F\_TF

c

$$cc1=c1*c1+c4*c4+c6*c6$$

$$cc2=c4*c4+c2*c2+c5*c5$$

$$cc3=c6*c6+c5*c5+c3*c3$$

$$cc4=c1*c4+c2*c4+c5*c6$$

$$cc5=c6*c4+c5*c2*c3*c5$$

$$cc6=c6*c1+c5*c4+c3*c6$$

c

c deformed fiber orientations aa,pp in current local configuration

c

$$aa1=hsv(1)*A01+hsv(4)*A02+hsv(7)*A03$$

$$aa2=hsv(2)*A01+hsv(5)*A02+hsv(8)*A03$$

$$aa3=hsv(3)*A01+hsv(6)*A02+hsv(9)*A03$$

c\*\*\*\*\*

c

c compute strain invariants invar1 (I1) invar2 (I2) invar4 (I4) invar5 (I5)

c

$$invar1=c1+c2+c3$$

$$invar2=0.5*(c1+c2+c3)**2-0.5*(cc1+cc2+cc3)$$

$$invar4=c1*A01**2+c2*A02**2+c3*A03**2$$

$$1 +2*c4*A01*A02+2*c5*A02*A03+2*c6*A03*A01$$

$$invar5=cc1*A01**2+cc2*A02**2+cc3*A03**2$$

$$1 +2*cc4*A01*A02+2*cc5*A02*A03+2*cc6*A03*A01$$

c

c\*\*\*\*\*

c

c compute aa tensor product aa

c

$$aaaa1=aa1*aa1$$

$$aaaa2=aa2*aa2$$

$$aaaa3=aa3*aa3$$

$$aaaa4=aa1*aa2$$

$$aaaa5=aa2*aa3$$

$$aaaa6=aa3*aa1$$

c

c compute b dot aa == baa

c

$$baa1=b1*aa1+b4*aa2+b6*aa3$$

$$baa2=b4*aa1+b2*aa2+b5*aa3$$

$$baa3=b6*aa1+b5*aa2+b3*aa3$$

c

c compute aa tensor product baa

c

$$aabaa1=aa1*baa1+baa1*aa1$$

$$aabaa2=aa2*baa2+baa2*aa2$$

$$aabaa3=aa3*baa3+baa3*aa3$$

$$aabaa4=aa1*baa2+baa1*aa2$$

$$aabaa5=aa2*baa3+baa2*aa3$$

$$aabaa6=aa3*baa1+baa3*aa1$$

```

c
c   compute cauchy stress
c
c   cm(1)=material constant h1
c   cm(2)=material constant h2
c   cm(3)=second material constant, here Bulk modulus K
c   cm(4)=shear modulus G
c   cm(5)=material constant h4
c   cm(6)=material constant h5
c   cm(7)=material constant h44
c   cm(8)=material constant h11
c   cm(9)=material constant h14
c   cm(10)=components of the fiber direction wrt local x
c   cm(11)=components of the fiber direction wrt local y
c   cm(12)=components of the fiber direction wrt local z
  detf=max(detf,1.e-8)
  detfinv=1./detf
  detfp1=detf**(-2./3.)
  detfp2=detf**(-4./3.)
  Wstar1=cm(1)+2.*cm(8)*(detfp1*invar1-3.)
2 +cm(9)*(detfp1*invar4-1.)
  Wstar2=cm(2)
  Wstar4=cm(5)+cm(9)*(detfp1*invar1-3.)
2 +2.*cm(7)*(detfp1*invar4-1.)
  Wstar5=cm(6)

```

c\*\*\*\*\*

c hydrostatic pressure T\_vol

c\*\*\*\*\*

$$T\_vol=cm(3)/2.*(detf-detfinv)$$

$$1 \quad -(2./3.)*Wstar1*invar1*detfp1*detfinv$$

$$2 \quad -(4./3.)*Wstar2*invar2*detfp2*detfinv$$

$$3 \quad -(2./3.)*Wstar4*invar4*detfp1*detfinv$$

$$5 \quad -(4./3.)*Wstar5*invar5*detfp2*detfinv$$

c\*\*\*\*\*

c

c Cauchy Stresses

c

c\*\*\*\*\*

$$sig(1)=T\_vol+detfinv*($$

$$1 \quad +2.*Wstar1*detfp1*b1$$

$$2 \quad +2.*Wstar2*detfp2*(invar1*b1-bb1)$$

$$3 \quad +2.*Wstar4*detfp1*aaaa1$$

$$4 \quad +2.*Wstar5*detfp2*aabaa1)$$

$$sig(2)=T\_vol+detfinv*($$

$$1 \quad +2.*Wstar1*detfp1*b2$$

$$2 \quad +2.*Wstar2*detfp2*(invar1*b2-bb2)$$

$$3 \quad +2.*Wstar4*detfp1*aaaa2$$

$$4 \quad +2.*Wstar5*detfp2*aabaa2)$$

$$sig(3)=T\_vol+detfinv*($$

$$1 \quad +2.*Wstar1*detfp1*b3$$

```

2 +2.*Wstar2*detfp2*(invar1*b3-bb3)
3 +2.*Wstar4*detfp1*aaaa3
4 +2.*Wstar5*detfp2*aabaa3)
sig(4)=detfinv*(
1 +2.*Wstar1*detfp1*b4
2 +2.*Wstar2*detfp2*(invar1*b4-bb4)
3 +2.*Wstar4*detfp1*aaaa4
4 +2.*Wstar5*detfp2*aabaa4)
sig(5)=detfinv*(
1 +2.*Wstar1*detfp1*b5
2 +2.*Wstar2*detfp2*(invar1*b5-bb5)
3 +2.*Wstar4*detfp1*aaaa5
4 +2.*Wstar5*detfp2*aabaa5)
sig(6)=detfinv*(
1 +2.*Wstar1*detfp1*b6
2 +2.*Wstar2*detfp2*(invar1*b6-bb6)
3 +2.*Wstar4*detfp1*aaaa6
4 +2.*Wstar5*detfp2*aabaa6)
c
c
else if (etype.eq.'shell') then
c
c compute remaining components of left cauchy-green tensor
c
10 epsp=detf

```

```

c
c  material model only available for solids and shells
c
  else
c  write(iotty,20) etype
c  write(iohsp,20) etype
c  write(iomsg,20) etype
c  call adios(2)
  cerdat(1)=etype
  call lsmsg(3,MSG_SOL+1151,ioall,ierdat,rerdat,cerdat,0)
  endif
  epsp=detf
c
c20  format(/
c  1 '*** Error element type ',a,' can not be',
c  2 '      run with the current material model.')
```

#### **Appendix D: Example LS-DYNA input file**

The input file for uniaxial tensile deformations of a transversely isotropic solid with loading in the fibers direction is given below. Only one 8-node brick element is used.

```

*KEYWORD
$
$  PRMR1  VAL1  PRMR2  VAL2  PRMR3  VAL3  PRMR4  VAL4
*PARAMETER
```

```

$ termination time | safety factor
R  endtim  100.0R   sf   0.50
$# of hsv in d3plot | # of hsv in ASCII | dt for ASCII | dt for ascii |
I  hsvd3p   0I  hsvasc   0R  dtd3p   1.0R  dtAscii   1.0
$

```

```
*TITLE
```

```
Simple tension with fiber 0 deg
```

```
*COMMENT
```

```
Units used: mass=kg , length=m , time=s
```

```

$
$          *****
$          !   UNITS TO USE IN THE INPUT FILE !
$          ! mass: kg  _\   force: N  !
$          ! length: m  _ )   stress: Pa  !
$          ! time: s   /   energy: J  !
$          *****
$
$
$          * * * * *
$
$          -----
$          !   Material Definition   !
$          -----
$

```

```
*MAT_USER_DEFINED_MATERIAL_MODELS
```

```
$-----|-----|-----|-----|-----|-----|-----|
```

```

$  MID    RO    MT    LMC    NHV  IORTHO  IBULK    IG
    1 1.00E+11  45    12    0    1    3    4

$-----|-----|-----|-----|-----|-----|-----|-----|
$  IVECT  IFAIL  ITERM  IHYPER  IEOS
    0    0    0    1    0

$-----|-----|-----|-----|-----|-----|-----|-----|
$  AOPT   MACF   XP    YP    ZP    A1    A2    A3
    0.0   1    0    0    0    0    0    0

$-----|-----|-----|-----|-----|-----|-----|-----|
$  V1     V2     V3     D1     D2     D3     BETA  IEVTS
    0     0     0     0     0     0     0     0

$-----|-----|-----|-----|-----|-----|-----|-----|
$  h1     h2     BULK   G      h4     h5     h44   h11
$  P1     P2     P3     P4     P5     P6     P7     P8
    1.000E+05 1.000E+05 5.000E+14 1.000E+09 -1.00E+08 5.000E+07 5.000E+07 0.01

$-----|-----|-----|-----|-----|-----|-----|-----|
$  h14    LAX    LAY    LAZ
$  P9     P10    P11    P12
    0.1   1.0   0.0   0.0

$-----|-----|-----|-----|-----|-----|-----|-----|
$
$          !      Geometry and Mesh Definition      !
$          -----
*SECTION_SOLID_TITLE
$ SECID  ELFORM  AET

```

red. int.

1 1 0

S/R int.

2 2 0

full. int.

3 3 0

CZM

4 19 0

\$

\*HOURLASS\_TITLE

\$ HGID IHQ QM IBQ Q1 Q2 QB/VDC QW

hg6(0.20)

1 6 0.20 1 0.25 0.01

\$

\*PART

\$ PID SECID MID EOSID HGID

solid block

1 1 1 0 1

\$

\$ \* \* \* \* \*

\$ \* \* \* \* \*

\$

\$ -----

\$ ! Nodes, Connectivity, Node- & Segment-Sets !

\$ -----

\$

\*SET\_NODE\_LIST\_GENERATE\_TITLE

solid block

\$ SID

1

\$ B1BEG B1END

1 8

\*NODE

\$ NID X Y Z

1 0.0 0.0 0.0

2 0.1 0.0 0.0

3 0.1 0.1 0.0

4 0.0 0.1 0.0

5 0.0 0.0 0.1

6 0.1 0.0 0.1

7 0.1 0.1 0.1

8 0.0 0.1 0.1

\*ELEMENT\_SOLID\_ORTHO

\$ EID PID N1 N2 N3 N4 N5 N6 N7 N8

1 1 1 2 3 4 5 6 7 8

\$-----|-----|-----|-----|-----|-----|-----|-----|

\$ BETA A2 A3

0 0 0

\$-----|-----|-----|-----|-----|-----|-----|-----|

\$ D1 D2 D3

0 0 0

\*SET\_NODE\_LIST\_TITLE

LINE1

\$ SID

2

\$ N1 N2 N3 N4 N5 N6 N7 N8

1 5

\*SET\_NODE\_LIST\_TITLE

LINE2

\$ SID

3

\$ N1 N2 N3 N4 N5 N6 N7 N8

1 4

\*SET\_NODE\_LIST\_TITLE

left

\$ SID

4

\$ N1 N2 N3 N4 N5 N6 N7 N8

1 2 6 5

\*SET\_NODE\_LIST\_TITLE

right

\$ SID

5

\$ N1 N2 N3 N4 N5 N6 N7 N8

4 3 7 8

\*SET\_NODE\_LIST\_TITLE

rear

\$ SID

6

\$ N1 N2 N3 N4 N5 N6 N7 N8

1 4 8 5

\*SET\_NODE\_LIST\_TITLE

front

\$ SID

7

\$ N1 N2 N3 N4 N5 N6 N7 N8

2 3 6 7

\$

\$

\* \* \* \* \*

\$

\$

-----

\$

! Boundary Conditions !

\$

-----

\$

\$

\*\*\*\*\*

\$

\*\*\* BOUNDARY CONDITIONS \*\*\*

\$

\*\*\*\*\*

\$

\*BOUNDARY\_SPC\_SET\_ID

\$ ID TITLE

```

1 x constr
$ NSID  CID  DOFX  DOFY  DOFZ  DOFRX  DOFRY  DOFRZ
   6    0    1    0    0    0    0    0
*BOUNDARY_SPC_SET_ID
$  ID  TITLE
   2  Y constr
$ NSID  CID  DOFX  DOFY  DOFZ  DOFRX  DOFRY  DOFRZ
   2    0    0    1    0    0    0    0
*BOUNDARY_SPC_SET_ID
$  ID  TITLE
   3  Z constr
$ NSID  CID  DOFX  DOFY  DOFZ  DOFRX  DOFRY  DOFRZ
   3    0    0    0    1    0    0    0
*BOUNDARY_PRESCRIBED_MOTION_SET_ID
$  ID  TITLE
   3  x-displ
$ NSID  DOF  VAD  LCID  SF
   7    1    2    1    1.0
*DEFINE_CURVE_TITLE
Displacement vs. time
$ LCID  SIDR  SFA  SFO
   1    0    10.0  10.0
$  Abcissa(time)  Ordinate(Dis)
   0.0000E+00      0
&endtim           0.050

```

```

$ -----
$      !           Controls           !
$      -----
$
$
$      *****
$      *** TIME CONTROL KEYWORDS ***
$      *****
$
$
*CONTROL_TERMINATION
$ ENDTIM  ENDCYC  DTMIN  ENDNEG  ENDMAS  NOSOL
&endtim
$
*CONTROL_TIMESTEP
$ DTINIT  TSSFAC  ISDO  TSLIMIT  DT2MS  LCTM  ERODE  MS1ST
    0.0  &sf                99
*DEFINE_CURVE_TITLE
time step control
$  LCID  SIDR  SFA  SFO  OFFA  OFFO  DATTYP
    99   0   1.0  1.0  0.0  0.0  0
$      Abcissa      Ordinate
          0.0      1.0E+20
&endtim          1.0E+20
$
$      *****
$      *** SOLUTION/MESH CONTROL KEYWORDS ***

```

\$ \*\*\*\*\*

\$

\*CONTROL\_SOLUTION

\$ SOLN NLQ ISNaN LCINT

1

\$

\*CONTROL\_SOLID

\$ ESORT FMATRX NIPTETS SWLOCL PSFAIL

99

\$ PSFAIL: Optional solid part set ID specifying which part ID's are checked for negative volumes prior to element processing

\*SET\_PART\_LIST\_TITLE

psfail

\$ SID DA1 DA2 DA3 DA4

99

\$ PID1 PID2 PID3 PID4 PID5 PID6 PID7 PID8

1

\$ \*\*\*\*\*

\$ \*\*\* ARTIFICIAL VISCOSITY \*\*\*

\$ \*\*\*\*\*

\$

\*CONTROL\_BULK\_VISCOSITY

\$ Q1 Q2 TYPE

1.5 0.06 1

\$

```

$           * * * * *
$
$           -----
$           !   Data Output Settings   !
$           -----
$
$           *****
$           *** OUTPUT CONTROL ***
$           *****
$
$
*CONTROL_OUTPUT
$ NPOPT  NEECHO  NREFUP  IACCOP  OPIFS  IPNINT  IKEDIT  IFLUSH
    1
$ IPRTF  IERODE  TET10  MSGMAX  IPCURV  GMDT
    0
*CONTROL_ENERGY
$  HGEN  RWEN  SLNTEN  RYLEN
    2    2    2    2
*DATABASE_FORMAT
$  IFORM  IBINARY
    1
$
*PARAMETER_EXPRESSION
R  tfsafe 10.0*&endtim
*DEFINE_CURVE_TITLE

```

d3plot output

```
$ LCID SIDR SFA SFO OFFA OFFO DATTYP
   97   0  1.0  1.0  0.0  0.0  0
```

```
$ Abcissa(time) Ordinate(Vel)
```

```
0.0&dtd3p
```

```
&endtim &dtd3p
```

```
&tfsafe &dtd3p
```

```
*DEFINE_CURVE_TITLE
```

Ascii output

```
$ LCID SIDR SFA SFO OFFA OFFO DATTYP
   98   0  1.0  1.0  0.0  0.0  0
```

```
$ Abcissa(time) Ordinate(Vel)
```

```
0.0&dtAscii
```

```
&endtim &dtAscii
```

```
&tfsafe &dtAscii
```

```
$
```

```
$ *****
```

```
$ *** STATE PLOT OUTPUT ***
```

```
$ *****
```

```
$
```

```
*DATABASE_BINARY_D3PLOT
```

```
$ DT/CYCL LCDT/NR BEAM NPLTC PSETID
   97   0   0   0
```

```
$ IOOPT
```

```
1
```

\*DATABASE\_EXTENT\_BINARY

\$ shell shell shell shell shell shell

\$ NEIPH NEIPS MAXINT STRFLG SIGFLG EPSFLG RLTF LG ENGFLG

&hsvd3p 0 0 1 0 0 0 0

\$ CMPFLG IEVERP

0 0

\*DATABASE\_BNDOUT

\$ DT BINARY LCUR IOOPT

98 1

\$

\$

\*DATABASE\_ELOUT

\$ DT BINARY LCUR IOOPT NEIPH

98 1&hsvasc

\*DATABASE\_HISTORY\_SOLID\_SET

\$ ID1 ID2 ID3 ID4 ID5 ID6 ID7 ID8

999

\*SET\_SOLID\_TITLE

elout

\$ SID

999

\$ K1 K2 K3 K4 K5 K6 K7 K8

1

\$

\*DATABASE\_NODOUT

```
$ DT BINARY LCUR IOOPT
      98 1
```

```
*DATABASE_HISTORY_NODE_SET
```

```
$ ID1 ID2 ID3 ID4 ID5 ID6 ID7 ID8
      999
```

```
*SET_NODE_LIST_TITLE
```

```
nodout
```

```
$ SID
      999
```

```
$ N1 N2 N3 N4 N5 N6 N7 N8
      1 2 3 4 5 6 7 8
```

```
$
```

```
$ *****
```

```
$ *** ENERGY DATA OUTPUT ***
```

```
$ *****
```

```
$
```

```
$
```

```
*DATABASE_MATSUM
```

```
$ DT BINARY LCUR IOOPT
      98 1
```

```
*DATABASE_GLSTAT
```

```
$ DT BINARY LCUR IOOPT
      98 1
```

```
*END
```

## References

1. Fung, Y.C., Fronek, K. and Patitucci, P., *Pseudoelasticity of Arteries and the Choice of Its Mathematical Expression*. American Journal of Physiology, 1979. **237**(5): p. H620-H631.
2. Chuong, C.J. and Fung, Y.C., *3-Dimensional Stress-Distribution in Arteries*. Journal of Biomechanical Engineering-Transactions of the Asme, 1983. **105**(3): p. 268-274.
3. Ericksen, J.L. and Rivlin, R.S., *Large Elastic Deformations of Homogeneous Anisotropic Materials*. Journal of Rational Mechanics and Analysis, 1954. **3**(3): p. 281-301.
4. Rivlin, R.S., *Universal relations for elastic materials*, Rendiconti di Matematica., 2000. **20**: p.35-55
5. Batra, R.C., *Universal Relations for Transversely Isotropic Elastic Materials*. Mathematics and Mechanics of Solids, 2002. **7**(4): p. 421-437.
6. Murphy, J.G., *Transversely Isotropic Biological, Soft Tissue Must Be Modelled Using Both Anisotropic Invariants*. European Journal of Mechanics a-Solids, 2013. **42**: p. 90-96.
7. Pipkin, A.C., *Stress Analysis for Fiber-Reinforced Materials*. Advances in Applied Mechanics, 1979. **19**.
8. Holzapfel, G.A. and Ogden, R.W., *Constitutive Modelling of Arteries*. Proceedings of the Royal Society a-Mathematical Physical and Engineering Sciences, 2010. **466**(2118): p. 1551-1596.
9. Gent, A.N. and Walter, J.D., *The Pneumatic Tire*. 2005.
10. Demirkoparan, H. and Pence, T.J., *Magic Angles for Fiber Reinforcement in Rubber-Elastic Tubes Subject to Pressure and Swelling*. International Journal of Non-Linear Mechanics, 2015. **68**: p. 87-95.
11. Gasser, T.C., Ogden, R.W. and Holzapfel, G.A., *Hyperelastic Modelling of Arterial Layers with Distributed Collagen Fibre Orientations*. J R Soc Interface, 2006. **3**(6): p. 15-35.
12. Spencer, A.J.M., *Constitutive Theory of Strongly Anisotropic Solids*. Continuum Theory of the Mechanics of Fiber-Reinforced Composites, ed. Spencer A.J.M. 1984, Vienna: Springer.
13. Spencer, A.J.M., Rogers, T.G. and Moss, R.L., *An Optimal Angle of Winding for Pressurized Fibre-Reinforced Cylinders* Mechanics Research Communications, 1974. **1**: p. 27-32.
14. Batra, R.C., *Elements of Continuum Mechanics*. 2006: AIAA Publishers.
15. Batra, R.C. and Bahrami, A., *Inflation and Eversion of Functionally Graded Non-Linear elastic Incompressible Circular Cylinders* International Journal of Non-Linear Mechanics, 2009. **44**: p. 311-323.
16. HOLZAPFEL, G.A., GASSER, T.C. and Ogden, R.W., *A New Constitutive Framework for Arterial Wall Mechanics and a Comparative Study of Material Models*. Journal of Elasticity, 2000. **61**: p. 1-48.
17. Hamdaoui, M.E., Merodio, J., Ogden, R.W. and Rodríguez, J., *Finite Elastic Deformations of Transversely Isotropic Circular Cylindrical Tubes*. International Journal of Solids and Structures, 2014. **51**(5): p. 1188-1196.
18. ABAQUS, *Abaqus Version 6.11 Documentation*. 2011.
19. Rivlin, R.S. and Saunders, D.W., *Large Elastic Deformations of Isotropic Materials .7. Experiments on the Deformation of Rubber*. Philosophical Transactions of the Royal

- Society of London Series a-Mathematical and Physical Sciences, 1951. **243**(865): p. 251-288.
20. James, A.G., Green, A. and Simpson, G.M., Strain Energy Functions of Rubber .1. Characterization of Gum Vulcanizates. *Journal of Applied Polymer Science*, 1975. **19**(7): p. 2033-2058.
  21. James, A.G. and Green, A., *Strain Energy Functions of Rubber .2. Characterization of Filled Vulcanizates*. *Journal of Applied Polymer Science*, 1975. **19**(8): p. 2319-2330.
  22. Merodio, J. and Ogden, R.W., *Mechanical Response of Fiber-Reinforced Incompressible Non-Linearly Elastic Solids*. *International Journal of Non-Linear Mechanics*, 2005. **40**(2-3): p. 213-227.
  23. Qiu, G.Y. and Pence, T.J., *Remarks on the Behavior of Simple Directionally Reinforced Incompressible Nonlinearly Elastic Solids*. *Journal of Elasticity*, 1997. **49**(1): p. 1-30.
  24. Batra, R.C., *A Theorem in the Theory of Incompressible Navier-Stokes-Fourier Fluids*. *Istituto Lombardo Accademia di Scienze e Lettere Rendiconti (A)*, 1973. **107**: p. 699-714.
  25. Truesdell, C. and Noll, W., *The Non-Linear Field Theories of Mechanics*. In: *Handbuch Der Physik*. Vol. 3. 1965: Springer Verlag.
  26. Sasso, M., Palmieri, G., Chiappini, G. and Amodio, D., *Characterization of Hyperelastic Rubber-Like Materials by Biaxial and Uniaxial Stretching Tests Based on Optical Methods*. *Polymer Testing*, 2008. **27**(8): p. 995-1004.
  27. Kearsley, E.A., *Asymmetric Stretching of a Symmetrically Loaded Elastic Sheet*. *International Journal of Solids and Structures*, 1986. **22**(2): p. 111-119.
  28. Batra, R.C., I. Mueller, and P. Strehlow, *Treloar's biaxial tests and Kearsley's bifurcation in rubber sheets*. *Mathematics and Mechanics of Solids*, 2005. **10**(6): p. 705-713.
  29. Morrow, D.A., Donahue, T.L.H., Odegard, G.M. and Kaufman, K.R., *Transversely Isotropic Tensile Material Properties of Skeletal Muscle Tissue*. *Journal of the Mechanical Behavior of Biomedical Materials*, 2010. **3**(1): p. 124-129.
  30. Clark, S.K., *Theory of the Elastic Net Applied to Cord-Rubber Composites*. *Rubber Chemistry and Technology*, 1983. **56**(2): p. 372-389.
  31. Belytschko, T. and Bindeman, L.P., *Assumed Strain Stabilization of the 8 Node Hexahedral Element*. *Computer Methods in Applied Mechanics and Engineering*, 1993. **105**(2): p. 225-260.
  32. R. C. Batra, *Comparison of Results from Four Linear Constitutive Relations in Isotropic Finite Elasticity*, *International Journal of Nonlinear Mechanics*, 2001. **36**: p. 421-432

## **Chapter 4: Experimental and Numerical Explorations of Transitions to Self-Similar Debonding in Steel and Aluminum T-peel Tests**

Qian Li<sup>1</sup>, Romesh C. Batra<sup>1</sup>, David A. Dillard<sup>1\*</sup>, and Ian Graham<sup>2</sup>

<sup>1</sup>Biomedical Engineering and Mechanics Department, Virginia Tech,

Blacksburg, VA, 24061, USA

<sup>2</sup>LORD Corporation,

Cary, NC, 27511-7923 USA

\*Corresponding author

(This manuscript is ready to be submitted for possible publication in a peer-reviewed journal)

### **Abstract**

The broad versatility of the T-peel test, widely used for characterizing adhesion across a plethora of adhesives, adherends, and geometries, results in a range of responses that may complicate meaningful interpretation. This research effort, involving several specific specimen types, was undertaken to investigate concerns that commonly used configurations may not always result in plateaus in the force-displacement response. We experimentally and numerically study debonding of T-peel specimens having 75 mm bond length and 0.81 mm thick adherends made of either 6061 aluminum (Al) or one of the three steels (G70 70U hot dip galvanized, E60 electrogalvanized (EGZ), 1010 cold-rolled steel) bonded with either LORD<sup>®</sup> 406 or Maxlok<sup>™</sup> acrylic adhesive. For the EGZ and the Al adherends, specimens with a bond length of 250 mm and adherend thickness of 1.60 mm are also examined. Effects of adherend materials and thicknesses, bond lengths, and adhesives on test results are examined using three metrics to interpret the T-peel bond performance. We find a limited correlation between the commonly used “T-peel strength” and the energy dissipated per unit debond area. For those two metrics, the relative performances of the CRS and the Al specimens are quite different. Quasi-static plane strain deformations of the test specimens are analyzed by the finite element method (FEM) and a cohesive zone model using the commercial software, ABAQUS, to help interpret the test data. Numerical results provided energies required to elastically and plastically deform the adherends, and help determine the transition from non-

self-similar to self-similar debonding. The FE simulations also facilitate determination of the fraction of the crosshead displacement at which the self-similar debonding occurs. Results reported herein should help engineers select appropriate specimen dimensions for extracting data for the adhesive performance.

**Keywords:** T-peel Test, Adherend Plastic Deformation, Self-similar Debonding, Finite Element Analysis, Adhesion Metrics

## 4.1 Introduction

The T-peel test, like some other peel tests, often involves large adherend deflections and strains. Compared to other adhesion test methods, the T-peel test is used when both adherends are sufficiently maleable to allow the unbonded portions to be bent perpendicular to the bonded portion of the joint for mounting in a universal test frame. Furthermore, since specimen fabrication is inexpensive and testing using realistic adherend thicknesses is easy, this method is frequently used in the automotive industry. Its widespread use, however, involves a large range of specimen configurations and resulting deformation modes that complicate the analysis and interpretation of the test data. The T-peel specimen deformations and test results strongly depend on the specific configuration and material properties, which influence the force required for debonding and the shape of the deformed specimen. Furthermore, it is recognized that many T-peel specimens require considerable energy to plastically deform the adherends. The fracture energy associated with the bond breaking is significantly less than the total work done by the applied load during the debonding process. Thus, without proper analysis and interpretation, typical results obtained from the T-peel tests, such as the “T-peel strength,” may only be useful for qualitatively comparing different bonds.

Kim et al. [1, 2] derived the moment-curvature relations for pure bending of elastic-plastic beams to calculate the plastic energy dissipated in the adherends, and used energy balance to relate the experimentally measured peel force to the specific fracture energy. They showed that the energy required for plastic deformations during peeling of thin ( $\sim 10 \mu\text{m}$  thick) Cu films could be two orders of magnitude higher than the fracture energy. Kinloch et al. [3] proposed an energy balance approach to estimate the fracture toughness of an adhesive for fixed-arm and T-peel tests. They

calculated the work done by moments acting on the peeling arms, and the rotation at the root and the maximum curvature of the adherend by assuming that the beam rested on an elastic foundation. Based on the theory work in [3, 4], they developed a freely available spreadsheet, ICPEEL, that assumes self-similar debonding, meaning that the forces, energies, and resulting shapes become independent of further propagation. Self-similar<sup>1</sup> debonding is a very useful construct for analytical models[5, 6], though determining if and when this idealization is achieved for numerical and experimental results can be ambiguous, as will be discussed later. Clearly, however, self-similar debonding is not achieved in all T-peel tests, where lower modulus and higher yield strength adherends, less tough adhesives, and shorter bond lengths can delay or prevent self-similar debonding for a given specimen configuration. In an effort to provide a framework for interpreting T-peel configurations and results, Dillard et al. [7-9] classified T-peel specimen configurations into four categories depending on whether or not debonding is self-similar and also whether adherend plasticity occurs. Using this convention, Category I applies where adherends deform elastically and self-similar debonding occurs; Category II corresponds to plastically deforming adherends and self-similar debonding being achieved; Category III configurations involve adherend plasticity but insufficient length to achieve self-similar debonding; and Category IV adherends remain elastic but self-similar debonding is not achieved.

Several analytical approaches [1-3, 10, 11] are available to extract the fracture energy from peel tests data involving adherends' plastic deformations. Here, we find it by using the finite element analysis (FEA) and the cohesive zone model (CZM) because the FEA requires fewer simplifying assumptions than analytical methods, e.g., see [12-17]. The FEA also permits examining the transition to self-similar debonding since it does not require *a priori* assumption of the steady state fracture propagation. Grant et al. [18] used the FEA to find the load needed to initiate failure in flush spew fillet T-peel joints with various geometric parameters using the maximum uniaxial stress as a failure criterion but without considering failure propagation. Yang et al. [12] and Alfano et al. [13] have employed the CZM to simulate fracture of 90 and 100 mm long T-peel specimens with, respectively, 30 (60) and 45 (55) mm bond (non-bonded pre-crack) lengths. Their computed

---

<sup>1</sup> Herein, self-similar is preferred over steady state to avoid possible temporal connotations, though steady-state is often used in the literature, including some cited herein. Such cases may use “steady-state” to reflect the cited author’s preference.

peel force versus crosshead displacement curves compared well with the experimental findings. They neither extracted the energy required to plastically deform the adherends nor observed self-similar debonding, possibly because of the short bond lengths employed.

Besides the CZM, other methods such as the node release [19] and the element deletion [20] have been employed to simulate crack initiation and propagation. Hadavinia et al. [19] modeled crack initiation in an adhesive layer by using a “critical plastic strain fracture criterion” in their FEA of elastic-plastic peel tests and crack propagation by the node release technique. Their computed adhesive fracture energy agreed well with that determined previously by analytical and direct-measurement methods in tests involving “steady-state” peeling.

The ASTM D1876 [21] standard defines “T-peel strength” as the average force per unit bond width needed to propagate the debond over 127 mm length after the initial peak, using at least 10 load readings taken at fixed increments of the crosshead displacement. The ISO11339 [22] recommends disregarding data from the first 25 mm and the last 25 mm of the debond length, and averaging the force for at least 100 mm of peeling by using the best fit horizontal straight line to the data. In order to reduce material required and test time, shorter specimens are commonly used. The 75 mm bond length is considerably less than that recommended by major standards organizations [21-23], but automotive companies regard it as being equivalent [24, 25] to the 250 mm bond length. An even shorter 25 mm bond length T-peel specimen, often referred to as a coach peel test, is also used for some adhesive, spot-weld, and weld-bond applications [20]. Among other issues, we explore the effect of the bond length on various bond strength metrics.

We have experimentally tested 25.4 mm wide symmetric T-peel specimens having 0.81 mm thick Al, and HDG, EGZ and CRS steel adherends bonded with 0.25 mm thick commercial acrylic either LORD<sup>®</sup> 406 or Maxlok<sup>™</sup> adhesives. A few tests were also conducted with 1.60 mm thick Al adherends. The failure of these specimens is found to belong to either category II or III or IV, as described above. The FEA with the CZM included in ABAQUS [26] is used to simulate debonding initiation and propagation by assuming that the bent adherends (the tabs bent for gripping) have negligible residual stress and strains. The computed permanently deformed shapes, and the reaction force versus the crosshead displacement curves are found to agree well with the corresponding experimental ones. The energies required for initiating fracture and plastically

deforming the adherends are ascertained from the FEA results. From the experimental and the numerical results, we deduce the following: (1) The elastic, self-similar debonding category I scenario was not observed for the systems studied herein, however, the other three debonding categories were observed. (2) The transition from non-self-similar debonding to self-similar debonding is signified by the occurrence of a “plateau” in the force-displacement curve. (3) For the HDG, the EGZ and the Al adherends, up to 88% of the total work done by the applied forces is used to plastically deform the adherend. (4) For the Al adherends, the FEA enabled determination of the ratio of the crosshead displacements during the non-self-similar and the self-similar debonding initiation to the total crosshead displacement that can help engineers select specimen dimensions for extracting meaningful data. (5) We find limited correlations between the T-peel strength and the energy released/dissipated per unit debond area.

## **4.2 Experimental results**

### ***4.2.1 Specimen description***

T-peel specimens, depicted in Figure 4.1, were prepared with 0.81 mm thick adherends of one of materials mentioned above. Several specimens with 1.60 mm thick Al adherends were also used. The adherend surfaces to be bonded were cleaned by wiping them with isopropyl alcohol, air-dried and then bonded with either LORD<sup>®</sup> 406 or Maxlok<sup>™</sup> acrylic adhesive dispensed from 4:1 volume ratio cartridges equipped with 21 element static mixers. A nominal bondline thickness of 250  $\mu$ m was maintained by glass beads embedded in the adhesives. The specimens were cured at room temperature for 4 days before testing. Subsequently, tabs were nominally bent to 90° angles for gripping; the radius of the bends was not always controlled, but was at least 2.4 mm. The bent tabs of the specimens were mounted in grips of an Instron testing machine and deformed at a crosshead displacement rate of 51 mm/min at room temperature. The peel force versus the crosshead displacement curves were recorded for six replicates for each joint configuration. However, only one Al specimen with 250 mm long bond length was tested.

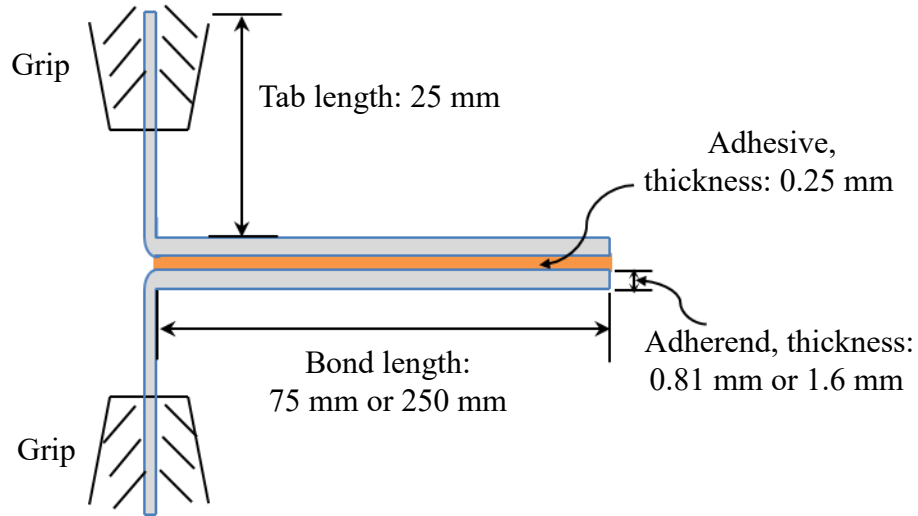


Figure 4.1. Geometric configuration of T-peel specimens (not to scale)

#### 4.2.2 Uniaxial tests on adherends

Flat specimens (250 mm long, 25.4 mm width, and 0.81 mm thickness) of the four adherend metals were tested in uniaxial tension at room temperature at a crosshead displacement rate of 5 mm/min, while recording the axial force ( $F_A$ ) and the corresponding axial engineering strain ( $\varepsilon_{eng}$ ) using an extensometer. The true axial strain,  $\varepsilon_{true} = \log(1 + \varepsilon_{eng})$ , versus the true axial stress,

$\sigma_{true} = \frac{F_A}{A_0}(1 + \varepsilon_{eng})$ , where  $A_0$  is the area of cross-section of the undeformed specimen, curves are

displayed in Figure 4.2. These evince that the three ductile materials, HDG, EGZ and Al, have similar work hardening profiles, and the CRS has a much higher yield strength than that of the other three materials but has very little ductility. Young's moduli in GPa and the yield strengths (0.25% offset) in MPa, determined by the least squares method, for the HDG, EGZ, Al, and CRS adherend stocks were found to be (210, 140), (210, 170), (69, 140) and (200, 290), respectively. Poisson's ratios for the four metals are assumed to be 0.3 since the lateral strains were not measured during the tests.

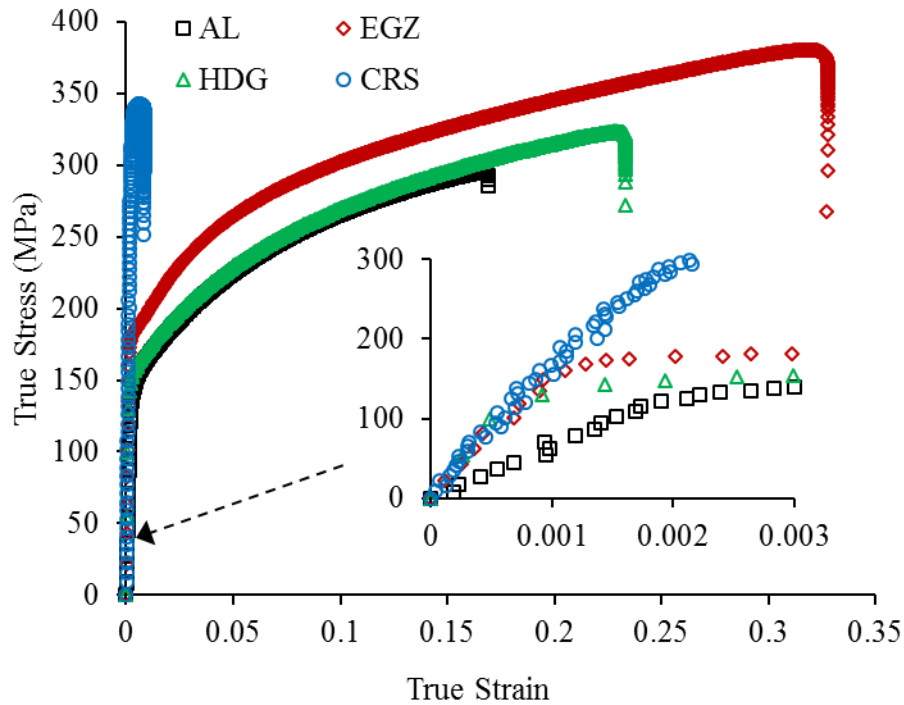


Figure 4.2. Experimental true axial stress-true axial strain curves for the four adherend materials.

### 4.2.3 Deformations of the adhesively bonded joints

#### 4.2.3.1 Deformed shapes and force-displacement curves

Figure 4.3 shows deformed shapes of the four adherends for bonds using each of the two adhesives. For both adhesives, visual inspection of failed surfaces suggested interfacial failures for the CRS adherends, and primarily cohesive failures for the other two steels. A mixture of cohesive and interfacial failures was observed for the Al adherends bonded with the LORD<sup>®</sup> 406 adhesive, while primarily cohesive failures were seen for the Al adherends bonded with the Maxlok<sup>™</sup> adhesive. The deformed shapes for the HDG and the EGZ adherends are similar to each other but differ significantly from those of the Al and the CRS adherends. The CRS adherends had very little, if any, plastic deformations, whereas the other three adherends experienced significant plastic deformations. Differences observed between final shapes for specimens bonded with the two adhesives suggested higher adhesion for the Maxlok<sup>™</sup> system.

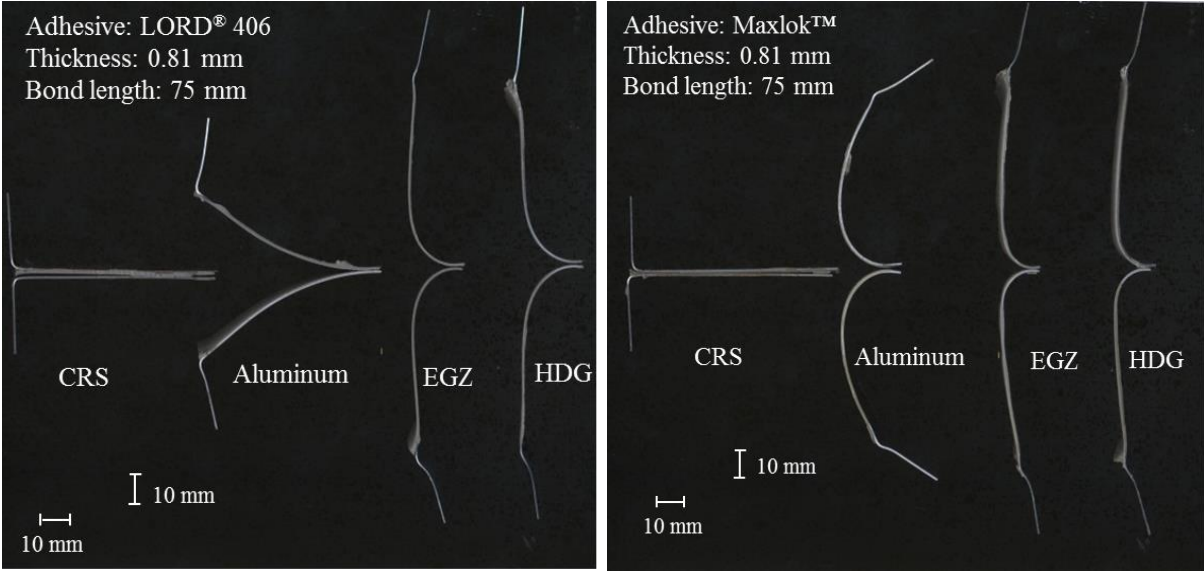
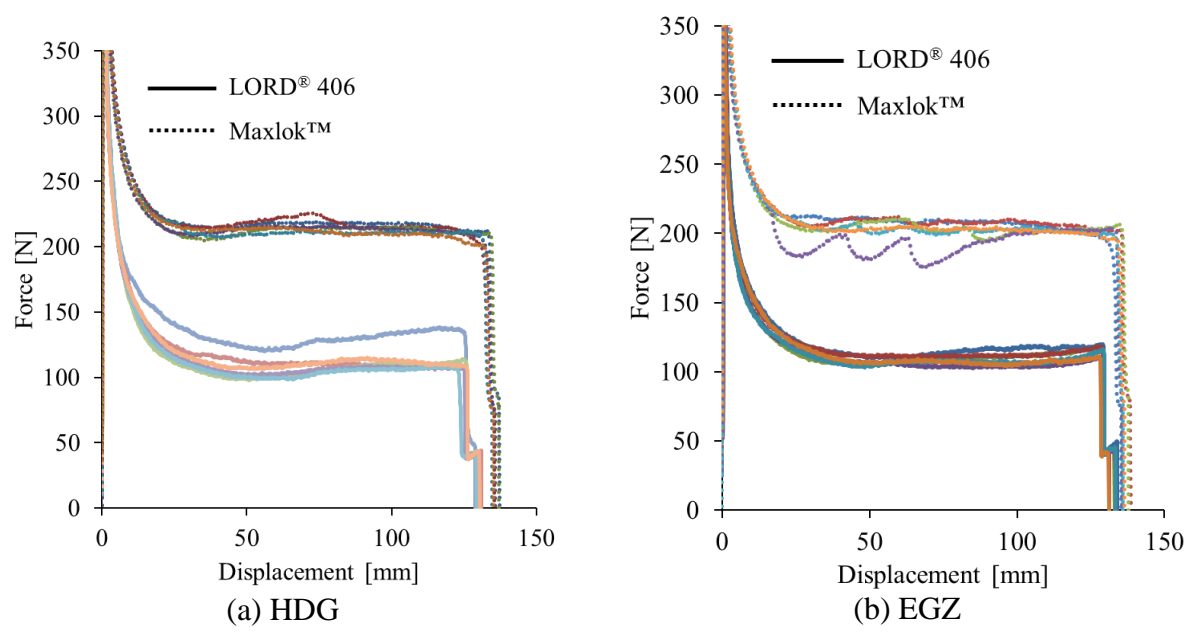


Figure 4.3. Representative images of the failed T-peel specimens for the two acrylic adhesives and the four adherend materials



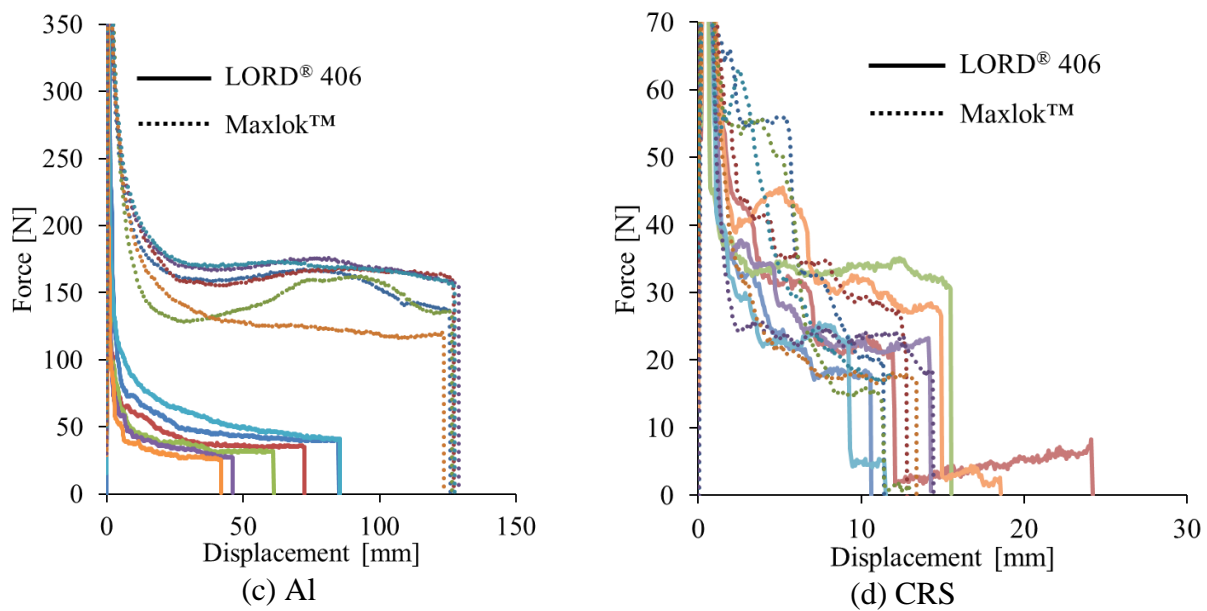


Figure 4.4. Axial force vs. the cross-head displacement curves (initial portion not shown) for six replicates of each specimen bonded with either LORD® 406 or Maxlok™ adhesive.

The plots in Figure 4.4 reveal significant differences in the responses of the eight systems tested. The peak forces associated with the debond initiation have been omitted from the plots to clearly show the portion associated with debond propagation. For the EGZ and HDG adherends, the axial force for a given crosshead displacement for systems with the Maxlok™ adhesive is nearly twice that obtained for the LORD® 406 adhesive. The difference was even more pronounced for the Al adherend specimens.

#### 4.2.3.2 Classification into different categories

The area under the force-displacement curve, i.e., the total work done by the applied force is nearly the same for the HDG and the EGZ adherends. However, it is considerably more than that for the Al and the CRS adherends. Since the adherends (except for the CRS) underwent significant plastic deformations, one cannot estimate the energy required for debonding from these areas. The larger areas for the Maxlok™ adhesive indicate that more energy is required to debond these specimens than those bonded with the LORD® 406 adhesive.

Self-similar debonding is a theoretical construct for analysis rather than an experimental criterion, though nonetheless useful to postulate its association with the occurrence of a “plateau” in the

force-displacement curve while recognizing the ambiguity of this criterion in light of the asymptotic approach. The force-displacement curves for the HDG and the EGZ specimens, with high Young's modulus and low yield strength, reach plateaus quickly after debond initiation, so fall in category II (self-similar and plastic deformation) for both adhesives. A similar conclusion can be drawn for the Al specimens bonded with the tougher Maxlok™ adhesive since plateaus appeared in five out of six force-displacement curves. The large force required for debonding induces considerable plastic bending that shortens the distance between the line of action of the applied load and the debond tip, and hastens transition to self-similar debonding, corresponding to category II. The situation is less clear for the Al specimens bonded using the LORD® 406 adhesive. There is considerable scatter in the “plateau” length, making it difficult to put them in either category II or III (failed surfaces for Al adherends bonded using the LORD® 406 adhesive are exhibited in Appendix E).

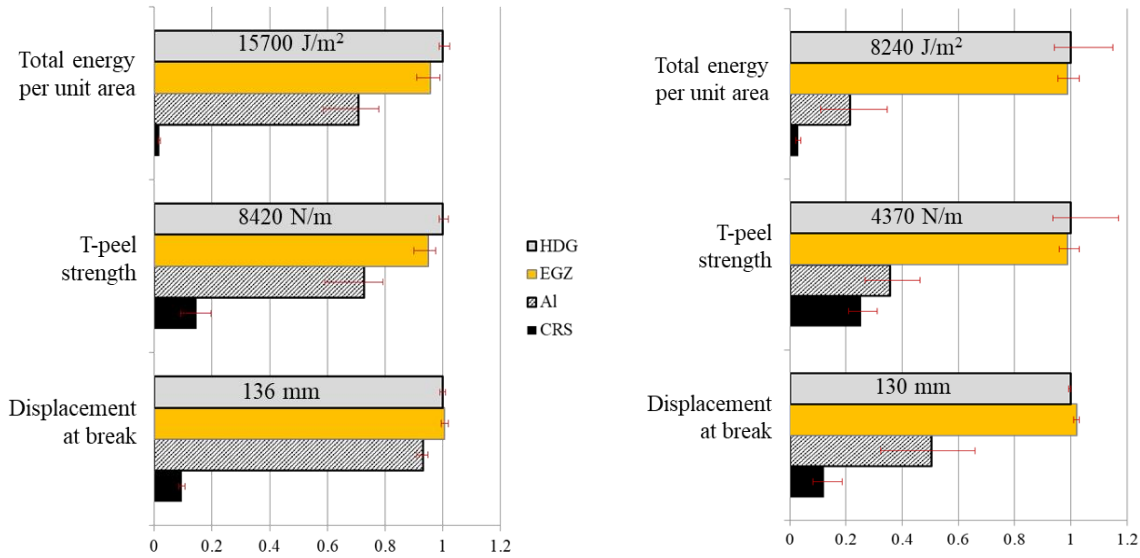
The peel force versus crosshead displacement curves for the CRS specimens almost never plateau, possibly due to the high yield strength of the adherend and the weak interfacial bond suggested by observed interfacial failures. Thus, they belong to category IV in which neither detectable plastic deformations nor self-similar debonding occurs. Debonding characterization from testing results is given in Table 4.1.

For the systems tested, we have exhibited in Figure 4.5 the crosshead displacement at break, the T-peel strength based on the force averaged over the plateau region (i.e., with the initial and the final regions omitted), and the total energy per unit debond area. This data has been normalized by the value of the corresponding quantity for the HDG specimens. For the EGZ and the HDG specimens exhibiting self-similar debonding, the displacement at break is close to the maximum distance traveled by the crosshead (twice the bond length of the specimen). The final displacement for the CRS and the Al specimens with the LORD® 406 adhesive is much less than twice the bond length. Since a plateau was not achieved for the CRS and the Al specimens with the LORD® 406 adhesive, the average force does not represent self-similar debonding. We note that the standards (e.g., see [21-23]) recommend using the same procedure to compute the peel strength irrespective of the occurrence of self-similar debonding. The total energy per unit debond area is based on the total area under the force-displacement curve.

Of particular interest is the difference between the T-peel strength and the energy per unit debond area. The T-peel strength does not depend upon the distance traveled by the crosshead or the work input into the specimen. In terms of these two metrics, the relative performance of the CRS (with both adhesives) and the Al specimens (with LORD<sup>®</sup> 406 adhesive) are quite different. For example, according to the peel strength criterion, the CRS specimens' performance equals, respectively, 25.4% and 14.6% of that of the HDG specimens for the Maxlok<sup>™</sup> and the LORD<sup>®</sup> 406 adhesives, but only 3.1% and 1.8% according to the total energy per unit debond area metric. Furthermore, for the Al specimens bonded with the LORD<sup>®</sup> 406 adhesive that fall into category III, the average total energy per unit debond area (the T-peel strength) is 22% (35%) of that of the HDG specimens. Although the use of the T-peel strength for these systems properly ranked them, this metric does not convey the much lower energy absorption capacity of the CRS specimens that might be relevant for arresting growing cracks in an actual adhesive bond application. It suggests that the commonly used T-peel strength does not provide quantitative information about the system performance in terms of the energy required for their failure that is more relevant for determining their ability to resist failures.

Table 4.1. Debonding characterization from testing results

<b>Adherend material</b>	<b>Adhesive material</b>	<b>Category</b>
HDG	Maxlok <sup>™</sup> (LORD <sup>®</sup> 406)	II (II)
EGZ	Maxlok <sup>™</sup> (LORD <sup>®</sup> 406)	II (II)
Al	Maxlok <sup>™</sup> (LORD <sup>®</sup> 406)	II (III)
CRS	Maxlok <sup>™</sup> (LORD <sup>®</sup> 406)	IV (IV)



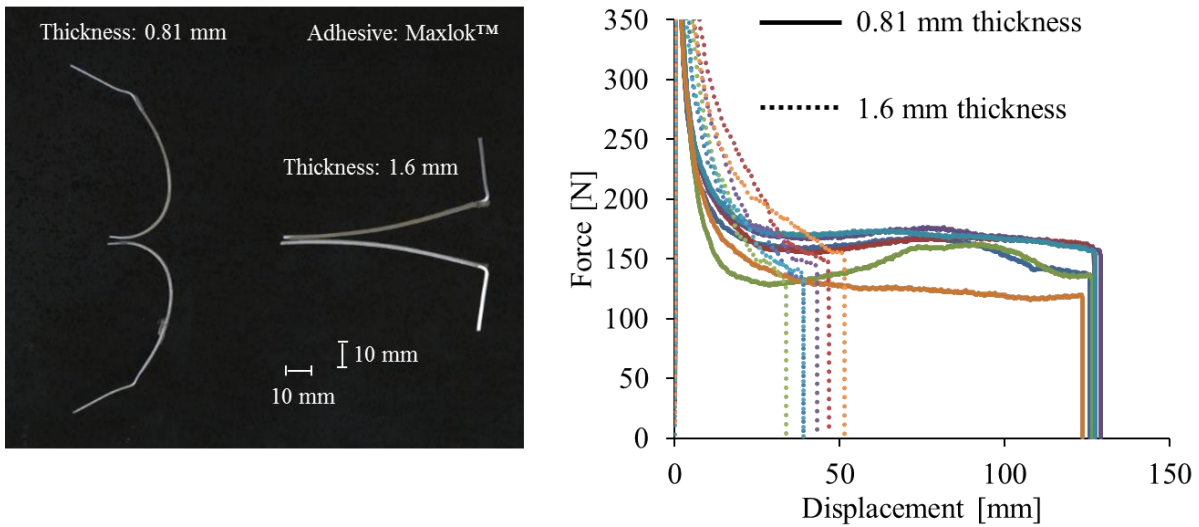
(a) Adhesive: Maxlok™

(b) Adhesive: LORD® 406

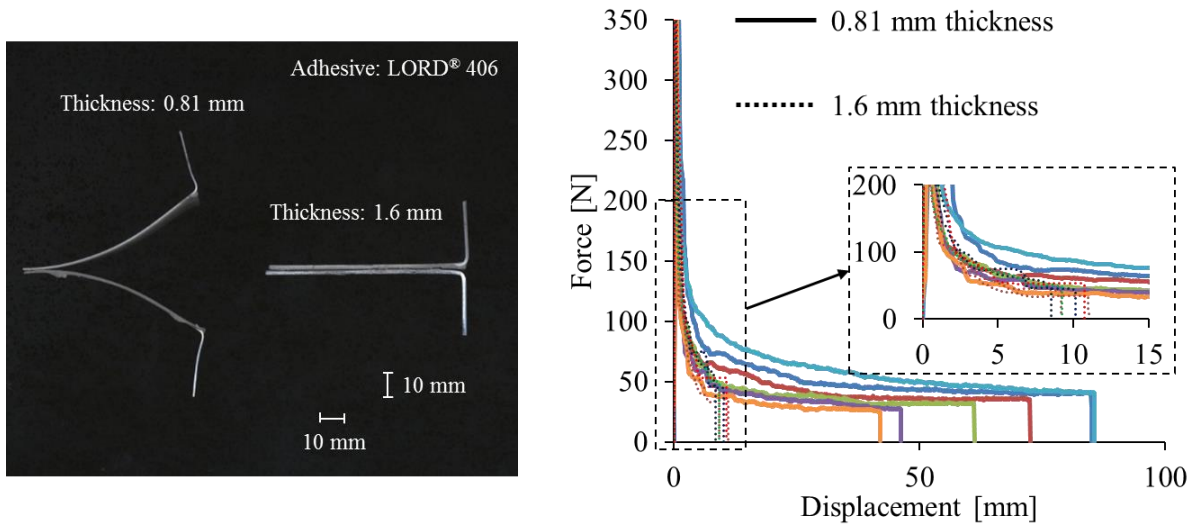
Figure 4.5. Three T-peel metrics normalized by their values for the HDG adherend for the two adhesives and the four adherends with 0.81 mm thickness.

#### 4.2.3.3 Effect of the adherend thickness

Figure 4.6 provides representative deformed shapes and the force-displacement curves for the 0.81 and the 1.60 mm thick Al adherends of 75 mm bond length and the two adhesives. Whereas for the Maxlok™ adhesive, the 0.81 mm thick specimens belong to category II, the 1.60 mm thick specimens are in category III since no plateau is evident in their force-displacement curves. However, for the LORD® 406 adhesive, as seen in Figure 4.6(b), the thin and the thick specimens belong, respectively, to categories III and IV. We note that the deformed thicker adherend has a larger curvature than the thinner one, and the two adherends have different fracture modes. For example, the 0.81 (1.60) mm thick adherends bonded with the Maxlok™ adhesive show pure cohesive (mixed cohesive and interfacial) failures. However, the failure patterns for the 0.81 (1.60) mm thick specimens bonded with the LORD® 406 adhesive were mixed cohesive and interfacial (pure interfacial). Different fracture energies associated with the fracture modes may shift their categories.



(a) Adhesive: Maxlok™



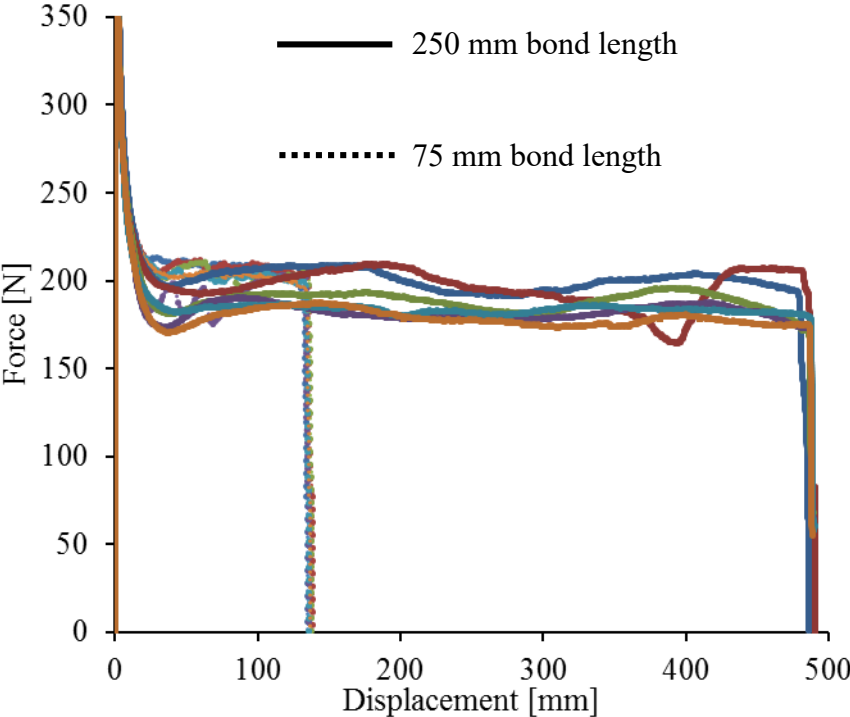
(b) Adhesive: LORD® 406

Figure 4.6. Effect of the Al adherend thickness on the deformed shapes (after failure) and the force-displacement curves. Bond length = 75 mm.

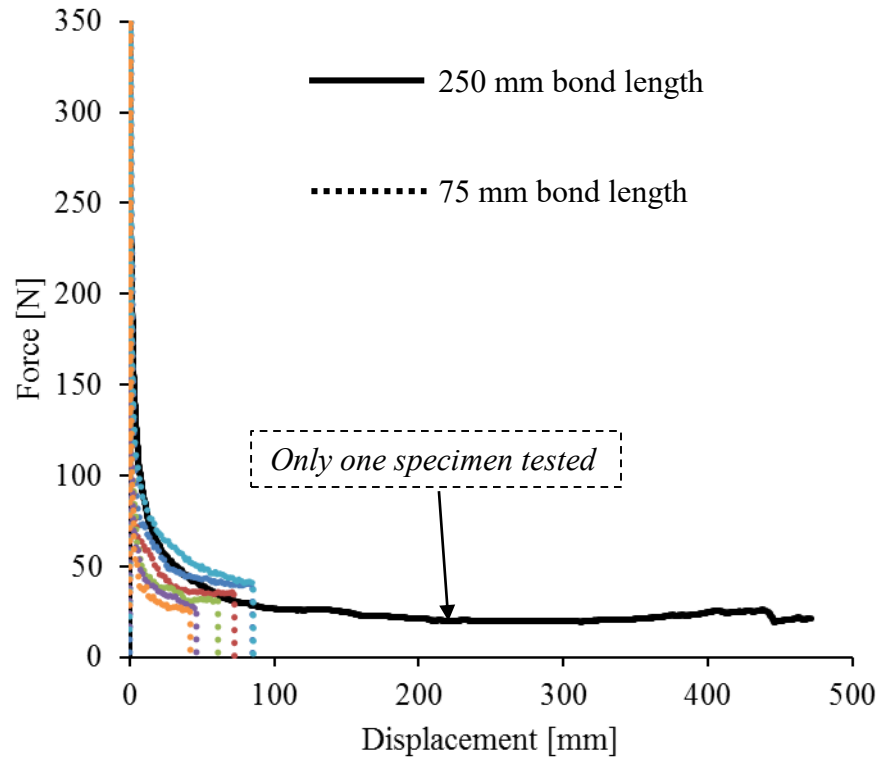
#### 4.2.3.3 Effect of the bond length

Figure 4.7(a) [7(b)] exhibits results for 0.81 mm thick EGZ [Al] adherends with 75 and 250 mm bond lengths. The EGZ specimens are bonded with the Maxlok™ adhesive while the Al specimens are bonded with the LORD® 406 adhesive. As expected, the plateau region is longer for the longer bond length specimens for both systems. The EGZ/Maxlok™ system specimens with 75 mm bond length have plateaus in their force-displacement curves, but the Al/LORD® 406 system do not

exhibit a clear plateau region. However, there is a clear plateau for both systems having 250 mm bond length. Thus, specimens with long bond lengths can help ensure self-similar debonding, but require more materials and test time (assuming a given crosshead rate), which has been driving the preference for short bond length configurations.



(a) Adherend: EGZ; Adhesive: Maxlok™; Thickness: 0.81 mm



(b) Adherend: Al; Adhesive: LORD® 406; Thickness: 0.81 mm

Figure 4.7. Force-displacement curves for the 0.81 mm thick Al adherends with 75 and 250 mm bond lengths.

## 4.3 Numerical simulations

### 4.3.1 Simulation details

The FEA coupled with a CZM available in ABAQUS is used to analyze plane strain quasi-static deformations of the system and the debond initiation and propagation as well as to help interpret the test results. The material properties, geometric dimensions, and boundary conditions used in the FEA are determined (unless otherwise noted) from the uniaxial tensile test data and the experimental configurations of the T-peel tests. The 90° bent adherends and the adhesives were assumed to be initially free of stress and strain. The adhesives were not tested, and are assumed to be isotropic and linearly elastic with estimated values of Young's modulus = 3 GPa and Poisson's ratio = 0.3. The adherend materials are assumed to be linearly elastic with their plastic deformations obeying the von Mises yield criterion and hardening determined from the

experimental axial stress versus axial strain curves exhibited in Figure 4.2. The plastic true axial strain, obtained by subtracting the true axial stress divided by Young's modulus from the true axial strain, and the corresponding true axial stress data, depicted in Figure 4.8, were input into ABAQUS. To ensure that the input stress-strain data is correctly used in ABAQUS, we simulated uniaxial deformations of the Al bar and found that the curve plotted from the ABAQUS output perfectly overlapped the experimental curve; these are not exhibited here.

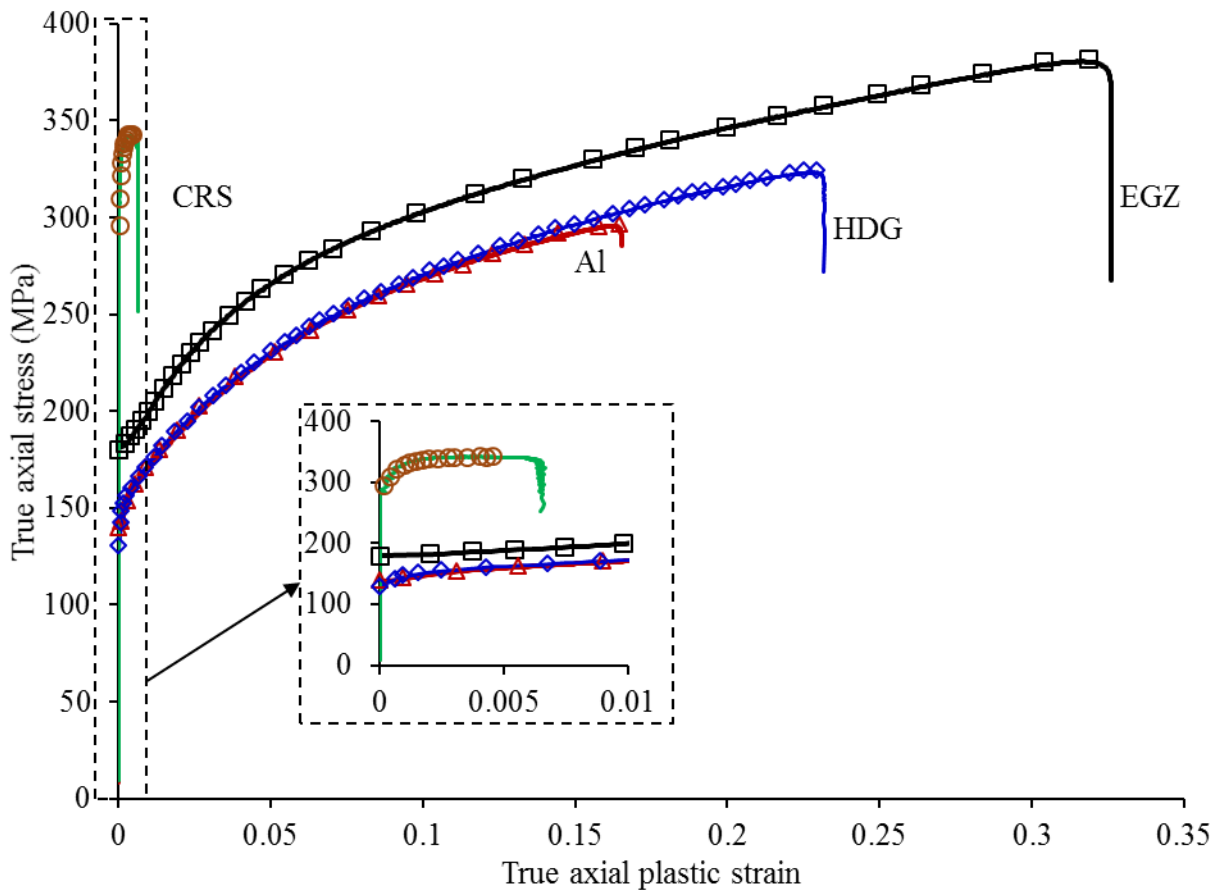


Figure 4.8. True axial stress-true axial plastic strain curves for the HDG, the EGZ, the Al and the CRS used in the FEAs. Solid curves are fits to the test data; symbols indicate data points input into ABAQUS

The crack is assumed to propagate either along the adhesive mid-surface or the adherend/adhesive interface. Thus the crack path is taken to be *a priori* known. We use the traction-relative displacement (usually called separation) relation shown in Figure 4.9 for the CZM (see Chapter 32.5 in ABAQUS documentation [26] for details), and study Mode-I failure under monotonically increasing loading of the specimen. When the tensile normal stress on a failure surface reaches the separation strength,  $T_{\max}$ , the interface strength is assumed to degrade and the traction-separation relation to follow path AB in Figure 4.9. When the separation at an interfacial point equals  $\delta_f$ , there is complete debonding at that point. The area of triangle OAB equals the critical energy release rate,  $G_{IC}$ , or the fracture energy for the interface. Values of the initial stiffness,  $K_e$ ,  $G_{IC}$  and  $T_{\max}$  characterizing the interface properties are input into the code.

The  $G_{IC}$  was found either from the test data on the debonding of a double cantilever beam (DCB) specimen having thicker adherends and adhesive, or estimated from analytical methods based on the energy balance (e.g., ICPEEL software based on [3, 4]). The fracture energy for the Maxlok™ adhesive so found for DCB testing with Al adherends exhibiting cohesive failure [27] was approximately 2 kJ/m<sup>2</sup>, and this value was also used for modeling cohesive failures for the EGZ, the HDG, and the Al adherends bonded using Maxlok™. Dillard et al. [9] used the software ICPEEL to find fracture energies of the EGZ, HDG, and Al T-peel specimens bonded with Maxlok™ that showed self-similar debonding. Given the force-displacement traces for the Al T-peel specimens, and the uniaxial tensile test data for the Al blanks, the predicted fracture energy from ICPEEL for Maxlok™ equaled 2.08 kJ/m<sup>2</sup> that agrees well with the 2 kJ/m<sup>2</sup> listed above. For the EGZ and the HDG T-peel specimens the ICPEEL software gave  $G_{IC}$  between 2.4 and 3 kJ/m<sup>2</sup>. Hadavinia et al. [19] have pointed out that for steel adherends undergoing large plastic deformations, the ICPEEL software over-predicts the fracture energy, possibly due to a large correction used for plastic deformations of the steel.

DCB tests were not conducted on specimens bonded with the LORD® 406 adhesive. The ICPEEL analysis of the T-peel test data for the 0.81 mm thick EGZ, HDG and Al specimens with 75 mm bond length and Al specimens with 250 mm bond length gave  $G_{IC} = 1.032 - 1.058$  kJ/m<sup>2</sup> for the EGZ and the HDG specimens, and 516 J/m<sup>2</sup> and 400 J/m<sup>2</sup>, respectively, for the 75 mm and the

250 mm bond length Al specimens. In the 75 mm bond length Al specimens, self-similar debonding was barely achieved before complete failure, making the applicability of the ICPEEL analysis uncertain.

There is no readily available method to find  $K_e$ . A rule of thumb is to set it equal to Young's modulus of the adhesive divided by its thickness, which equals 12 GPa/mm for the adhesives employed here. However, unless otherwise mentioned, we set  $K_e = 1$  TPa/mm. The value of  $T_{\max}$  is iteratively found by keeping  $G_{IC}$  and  $K_e$  fixed and increasing  $T_{\max}$  by 10 MPa till plateaus in the computed force-displacement curves for the EGZ adherends bonded with the Maxlok™ adhesive differed by less than 5% from the average of the six experimental values. This value of  $T_{\max} = 100$  MPa for the Maxlok™ adhesive was also used for the other three adherends. The same procedure is used for finding values of the CZM parameters for the LORD® 406 adhesive. (See Appendix F for effects of  $T_{\max}$  on the resulting force-displacement curves for one problem while  $G_{IC}$  and  $K_e$  are kept constants)

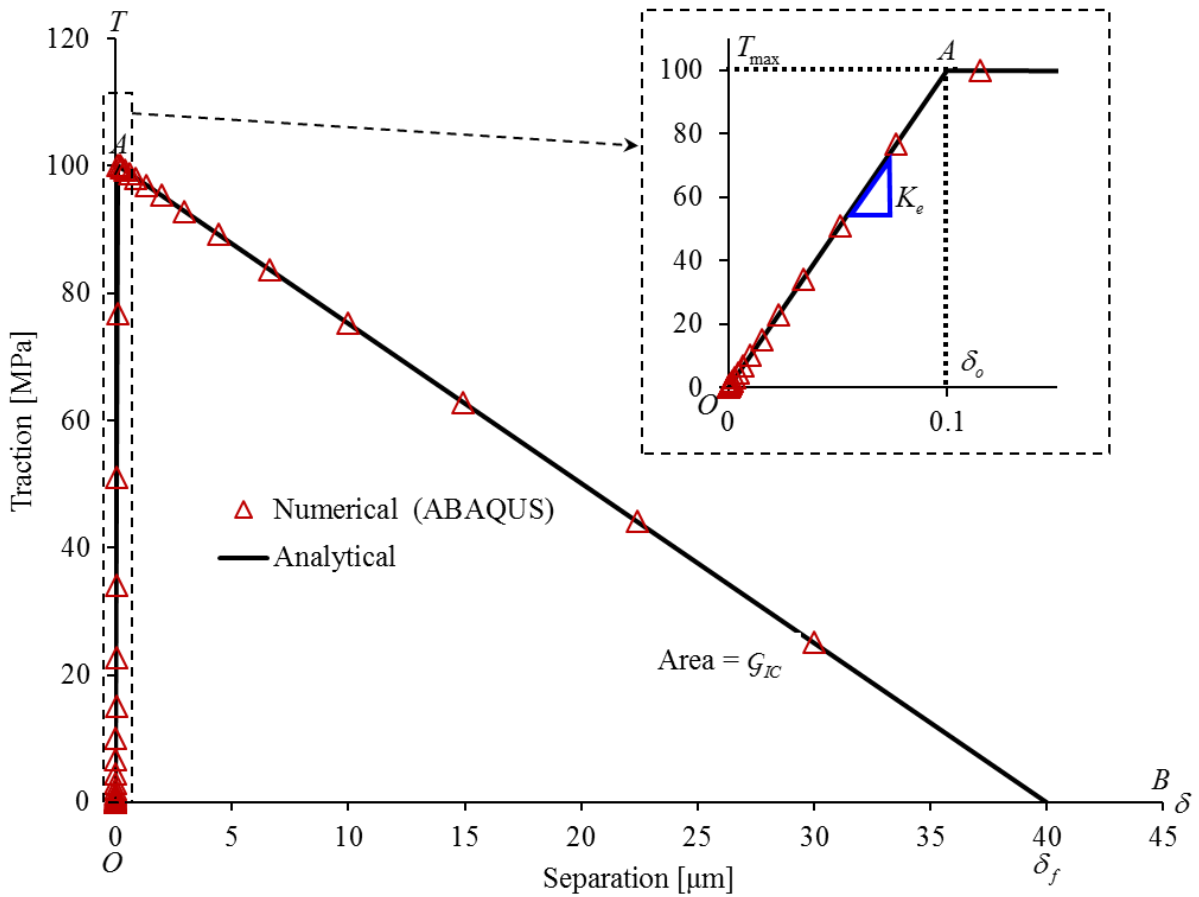


Figure 4.9. Mode-I traction-separation relation showing input to (solid lines) and output (triangles) from ABAQUS

$$G_{IC} = 2 \text{ kJ/m}^2, T_{\max} = 100 \text{ MPa}, K_e = 1 \text{ TPa/mm}$$

The adherends and the adhesive layer regions were discretized using 4-node quadrilateral elements (CPE4). Four-node COH2D4 elements of zero thickness were used for the cohesive/interfacial layer where debonding is assumed to occur. A FE mesh for a small region near the debond tip is shown in Figure 4.10 and element dimensions are listed below. The FE mesh is not fine enough to capture the singularity in deformations near corners A and B that are on the interface between two distinct materials, and where two faces of an FE with distinct boundary conditions meet. The assumption that the interfaces are perfectly bonded to each other and the adherend material is elastic-plastic should help mitigate the influence of singularities at points A and B on deformations near the debond tip.

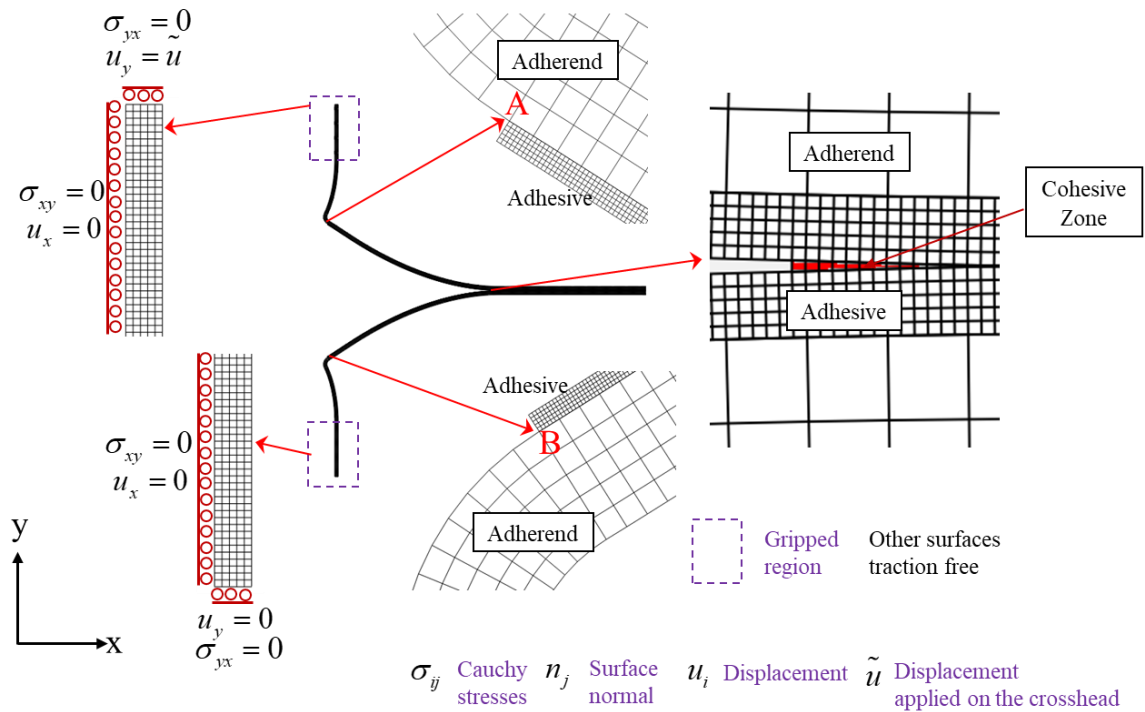


Figure 4.10. FE mesh in a small portion of T-peel specimen (during peeling).

On the adherend/adhesive interface, displacements of nodes on the adhesive and the adherend surfaces that are not common to the contacting surfaces are interpolated from displacements of nodes common to the two contacting surfaces.

In the FEA of the quasi-static problems, we considered several boundary condition settings in the gripped regions. One is as indicated in Figure 4.10, one-half of each tab length was assumed to be fixed in the horizontal direction on the left sides. Displacements in the vertical direction are constrained on the bottom side of the lower tab, and incremental vertical and null horizontal displacements prescribed on the top side of the upper tab. The other boundaries were taken to be traction-free. A more typical “gripped” boundary condition was also considered, where half of the lower tab length was assumed to be fixed in the horizontal and vertical directions on both right and left sides, while incremental vertical and null horizontal displacements prescribed on left and

right sides of the upper tab, and other boundary conditions were assumed to be traction-free. Due to the fact that the elongation in the gripped region is negligible comparing to the crosshead displacement, both settings give almost identical results for the force-displacement curves and final deformed shapes. We used the one depicted in Figure 4.10 for the simulations.

For the 0.81 mm thick Al adherends with 75 mm bond length, we computed the work done by the external force with the adherend, the adhesive and the cohesive layers, respectively, discretized by using the following two uniform FE meshes having elements of sizes (mm): (i)  $0.15 \times 0.15$ ,  $0.025 \times 0.025$ , and  $0.025$ , and (ii)  $0.075 \times 0.075$ ,  $0.0125 \times 0.0125$ , and  $0.0125$ . The 1.25% difference between the total work done ( $24.3 \text{ J/m}^2$  and  $24.6 \text{ J/m}^2$ ) for these two FE meshes was taken to imply that either one of the two meshes gives reasonably accurate results. The convergence of stresses/strains at critical points was not checked.

In the following subsections, the computed and the experimental results for the HDG specimens are not compared since they are similar to those for the EGZ specimens.

### **4.3.2 Maxlok™ adhesive**

#### *4.3.2.1 Comparison of computed and experimental force-displacement traces*

For the 75 mm bond length and 0.81 mm adherend thickness bonded with the Maxlok™ adhesive, and the cohesive failure along the adhesive mid-surface, the computed force-displacement curves for the EGZ and the Al specimens, exhibited in Figure 4.11, are close to the averaged experimental ones. For a few Al specimens cohesive debonding occurred in some regions and the adherend/adhesive interface debonded in other regions. However, this was not considered in numerical simulations.

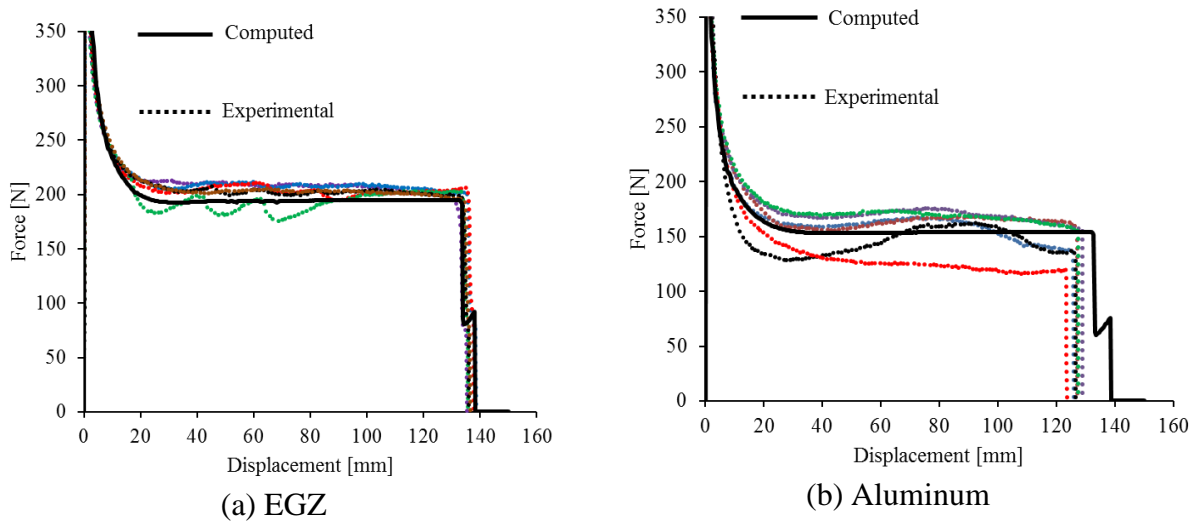


Figure 4.11. Comparison of the experimental and the computed force-displacement curves for the 0.81 mm thick EGZ and the Al specimens bonded with Maxlok™ and having 75 mm bond length

As illustrated in Figure 4.12, the numerical calculations qualitatively predict permanent deformation shapes of the adherends after separation that are quite similar to the experimentally observed patterns.

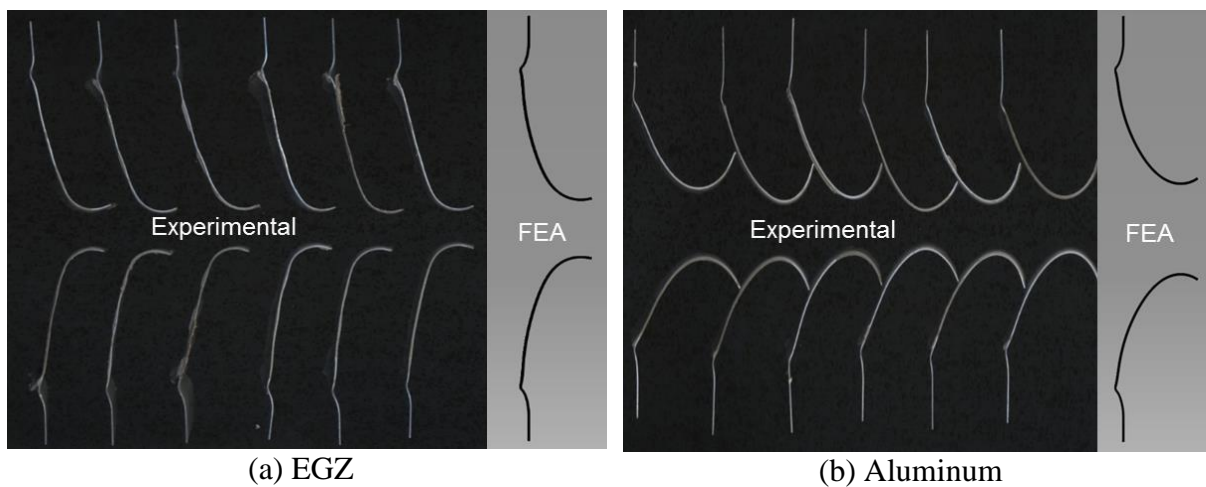
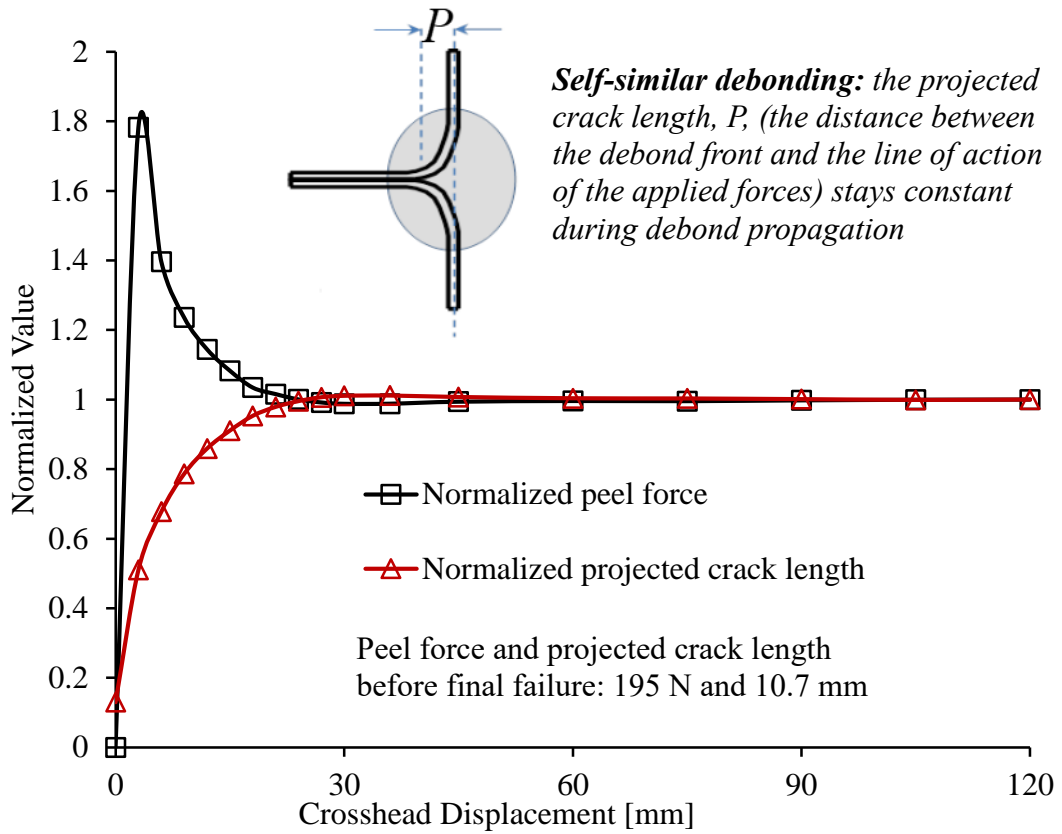


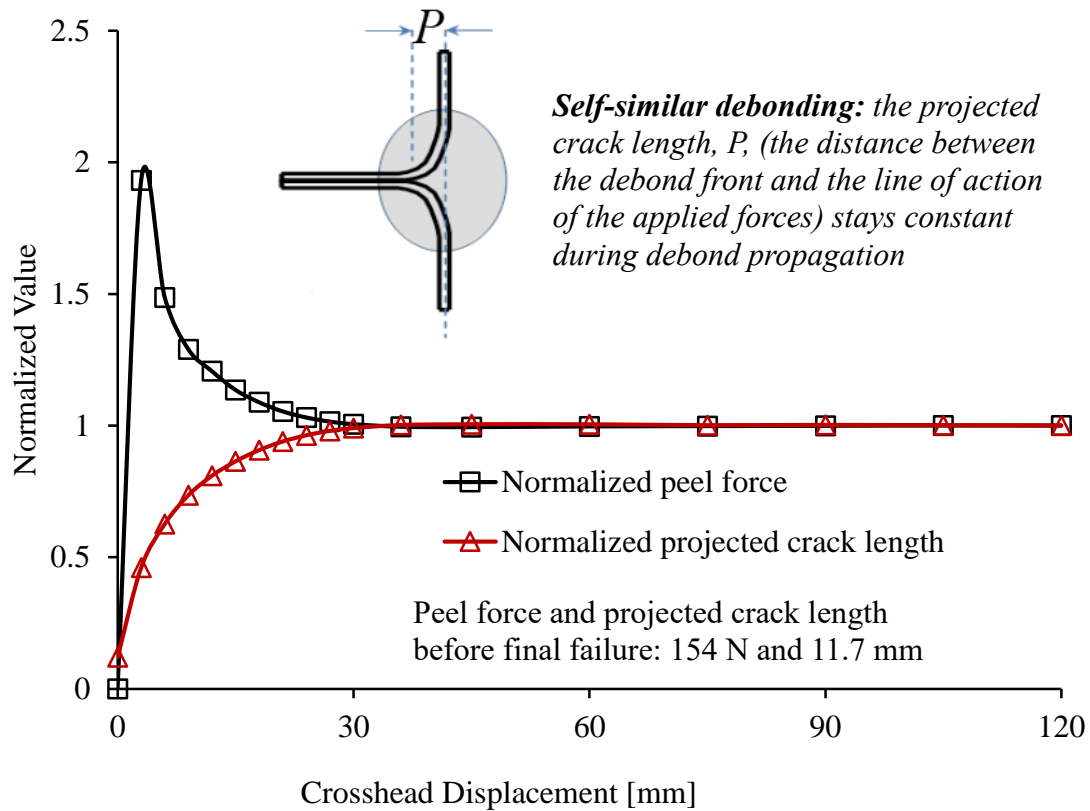
Figure 4.12. Qualitative comparison of the experimental and the computed deformed shapes for the 0.81 mm thick EGZ and the Al specimens bonded with Maxlok™ and having 75 mm bond length.

#### 4.3.2.2 Correlation between self-similar debonding and plateaus in force-displacement curves

Though reasonable to postulate that the onset of self-similar debonding should coincide with stabilization of the distance between the debond tip and the line of action of the applied loads and plateau in the load-deflection response, proving this equivalence is complicated by experimental variability and the asymptotic approach for each of these aspects. For the EGZ and the Al specimens, we have plotted in Figure 4.13 the computed peel force and the projected crack length normalized by the value before the final failure versus the crosshead displacement. The projected crack length (indicated as “ $P$ ” in this figure) is defined as the distance between the debond front and the line of action of the applied force. Non-self-similar behavior is associated with an increasing projected crack length as the debond propagates. From Figure 4.13, correlation between the occurrence of the plateaus in the “force-displacement” and the “projected crack length – displacement” curves is indicated. Even though the determination of the plateau is subjective, in this study we postulate its occurrence as an indicator of the self-similar debonding. A possible criterion for the plateau occurrence is the normalized force varying between 0.99 and 1.01 for at least 50% of the total crosshead displacement. Although such criterion is not applicable for experimental analysis, it can be used in numerical study for determining the occurrence of plateau. The averaged force in the plateau region can be used to calculate the “T-peel” strength. The region prior to the force plateauing can be considered as the non-self-similar debonding region.



(a) EGZ



(b) Aluminum

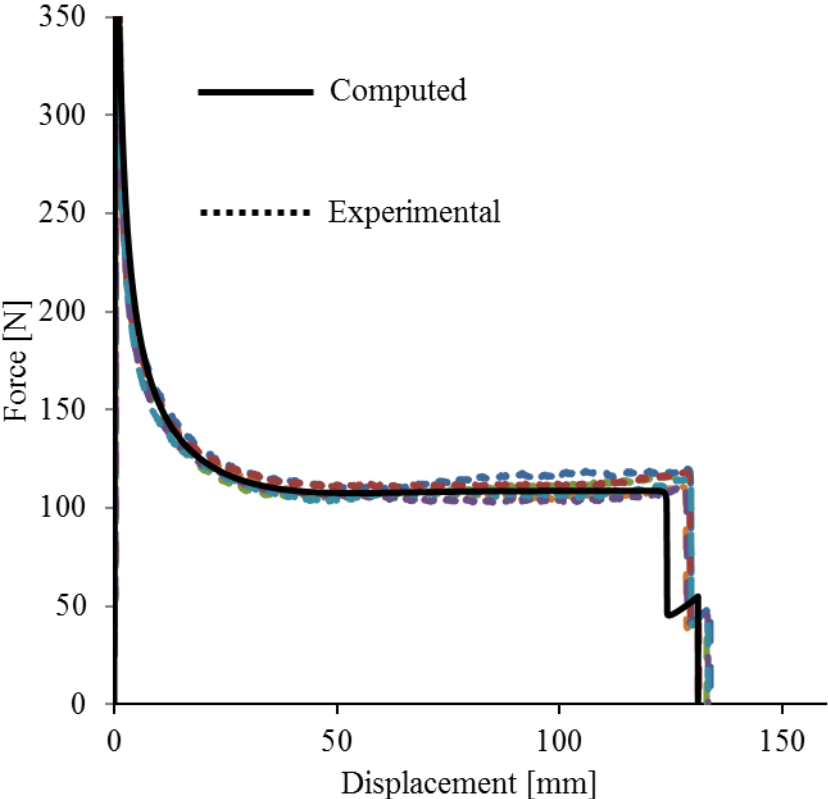
Figure 4.13. Peel force and projected crack length normalized by their plateau values versus the crosshead displacement for the EGZ and the Al specimens; Adhesive: Maxlok™; Bond length: 75 mm; Adherend thickness: 0.81 mm.

### 4.3.3 LORD® 406 adhesive

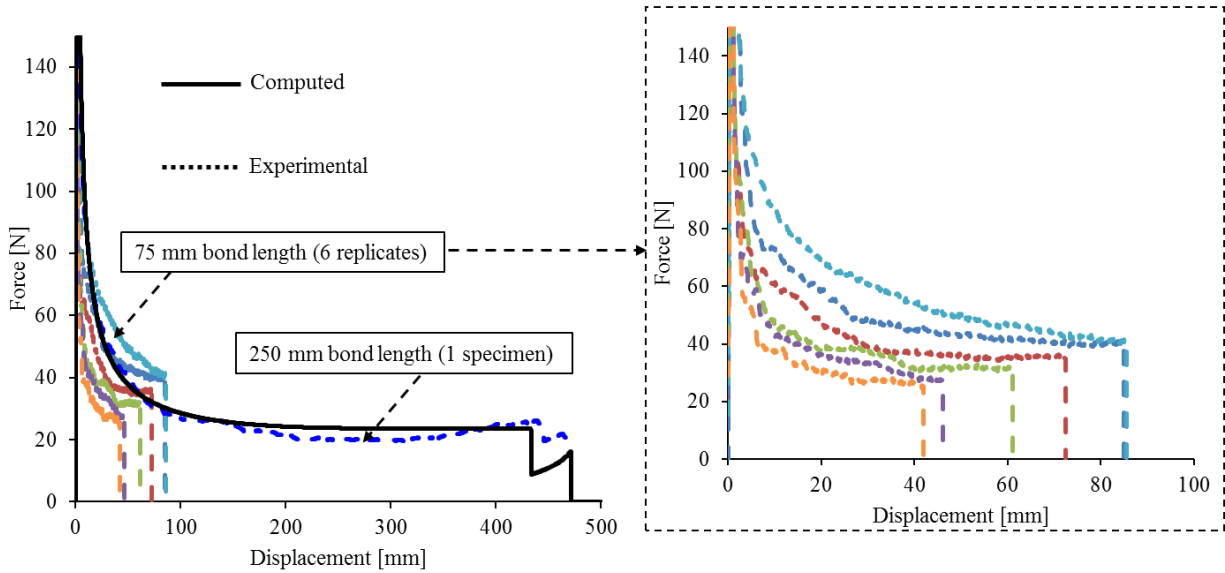
#### 4.3.3.1 Comparison of computed and experimental force-displacement traces

For  $K_e = 1$  TPa/mm,  $G_{IC} = 1$  kJ/m<sup>2</sup> and 0.4 kJ/m<sup>2</sup>, respectively, for the EGZ and the Al specimens  $T_{max} = 50$  MPa gave reasonable (within 5% difference) predictions for the force-displacement traces as demonstrated in Figure 4.14(a). Numerical results for the 250 mm long bond length Al specimens support the experimental observation that a longer bond length has self-similar debonding.

We notice that  $G_{IC} = 0.4 \text{ kJ/m}^2$  for bonds with the Al adherend is significantly less than  $1.032 - 1.058 \text{ kJ/m}^2$  for the HDG and the EGZ specimens possibly due to the Al specimens showing mixed cohesive and interfacial failures (failure modes of Al specimens bonded with LORD<sup>®</sup> 406 are discussed in Appendix E) and the other two adherends exhibiting cohesive failures. Typically, the fracture energy for a cohesive failure is greater than that for an interfacial failure [28].



(a) EGZ specimens, 75 mm bond length



(b) Al specimens, 75 and 250 mm bond length

Figure 4.14. Comparison of experimental and computed force-displacement traces for 0.81 mm thick specimens bonded with the LORD® 406 adhesive

#### 4.3.4 Debonding metrics from results of numerical simulations

Similar to the metrics from the test data given in Figure 4.5, we have listed in Table 4.2 their values from the computed results. Since No tests were conducted for CRS specimens to extract the actual fracture energy values, and one cannot employ the ICPEEL because of no plateau in the force-displacement curves, the metrics are not computed for CRS specimens here. However, a brief discussion with attempted numerical simulations for CRS specimens are given in Appendix G. In Table 4.2 the sum of the energy dissipated during plastic deformations, the strain energy of elastic deformations, and the energy dissipated during failure of the CZM layer differed from the work done by the reaction forces by at most 4.65 % (for Al adherends bonded with the LORD® 406 adhesive). Furthermore, the computed T-peel strengths agree with the experimental ones by less than 3.72% (for Al adherends bonded with the LORD® 406 adhesive). In addition, the computed work done by the reaction force (total energy) is within the range of the six experimental ones for each material system. We note that the T-peel strength and total energy per debond area for some specimens (e.g., Al adherends bonded with the LORD® 406 adhesive) shows relatively large

variations, potentially due to the mixed cohesive and interfacial failures in experiments (see Appendix E). The above comparisons indicate that the computed results are reasonably accurate.

Adherend	HDG		EGZ		Al	
	Mean	Standard deviation	Mean	Standard deviation	Mean	Standard deviation
Experimental T-peel strength [N/m]	8420	101	7990	210	6120	608
Experimental total energy/debond area [J/m <sup>2</sup> ]	15700	231	15000	385	11100	1040
Computed T-peel strength [N/m]	8140		7810		6160	
Computed total energy/debond area [J/m <sup>2</sup> ]	15400		14700		12000	
Computed fracture energy [J/m <sup>2</sup> ]	2000 ( $G_{IC} = 2 \text{ kJ/m}^2$ )		2054 ( $G_{IC} = 2 \text{ kJ/m}^2$ )		1970 ( $G_{IC} = 2 \text{ kJ/m}^2$ )	
Computed plastic energy/debond area [J/m <sup>2</sup> ]	12800		12000		9200	
Computed elastic energy/debond area [J/m <sup>2</sup> ]	377		454		689	

(a) Adhesive: Maxlok™

Substrate	HDG		EGZ		Al*	
	Mean	Standard deviation	Mean	Standard deviation	Mean	Standard deviation
Experimental T-peel strength [N/m]	4370	348	4320	113	1570	296
Experimental total energy/debond area [J/m <sup>2</sup> ]	8240	584	8140	209	1780	705
Computed T-peel strength [N/m]	4252		4450		1630	
Computed total energy/debond area [J/m <sup>2</sup> ]	7880		8130		2100	
Computed fracture energy [J/m <sup>2</sup> ]	981 ( $G_{IC} = 1 \text{ kJ/m}^2$ )		1010 ( $G_{IC} = 1 \text{ kJ/m}^2$ )		0.402 ( $G_{IC} = 0.4 \text{ kJ/m}^2$ )	
Computed plastic energy/debond area [J/m <sup>2</sup> ]	6410		6770		1360	
Computed elastic energy/debond area [J/m <sup>2</sup> ]	271		295		235	

(b) Adhesive: LORD® 406

Table 4.2. Energy metrics from the experimental and the computed results; bond length = 75 mm; thickness = 0.81 mm. Values of  $G_{IC}$  used in the CZM are listed in parentheses to gauge accuracy of the computed results. \*Partial cohesive and interfacial failures in experiments (see Appendix E)

Values listed in Table 4.2 imply that for the EGZ and the HDG (Al) specimens, only 12 – 14% (16 -19 %) of the total work done by the external forces is used to fracture the adhesive with the bulk used to plastically deform the adherends. These qualitatively agree with those of Kawashita

et al. [28] for the metal–epoxy laminates for which adherend’s plastic deformations consumed 75 % to 90 % of the total work done by external forces. They remarked that using the peel strength, that is related to the external work associated with peeling, is inadequate to describe the adhesive strength.

#### ***4.3.5 Adherend thickness and the bond length needed for the aluminum specimens to exhibit self-similar debonding***

In order to delineate the effect of the adherend thickness on the occurrence of self-similar debonding, we have displayed in Figure 4.15 the computed force-displacement traces for 0.4, 0.8, 1.2 and 1.6 mm thick Al specimens having 75 mm bond length, 0.25 mm adhesive thickness, and assuming cohesive failure on the adhesive mid-surface (assuming they are bonded with the Maxlok™ adhesive). Using the criterion (the plateau in force-displacement curve is assumed to occur when the normalized force varying between 0.99 and 1.01 for at least 50% of the total crosshead displacement) for self-similar debonding postulated in Section 3.2.2, it is clearly seen from results of Figure 4.15 that the non-self-similar debonding zone increases with an increase in the adherend thickness. The crosshead displacements can be divided into the non-self-similar and the self-similar debonding regions. For the four cases studied, the non-self-similar to the self-similar debonding regions (in mm) are (15, 128), (33, 100), (59, 60), (100, 0). That is, for the 0.4 mm thick adherend, the self-similar debonding initiates after the crosshead displacement equals 9.2 % of the total crosshead displacement indicating that a shorter bond length specimen can be used for the T-peel tests. However, a much longer specimen is needed for the 1.6 mm thick adherend since no self-similar debonding occurs for it. The information similar to that provided in Figure 4.15 can potentially be useful for engineers for selecting appropriate bond lengths to have self-similar debonding needed to define the peel strength.

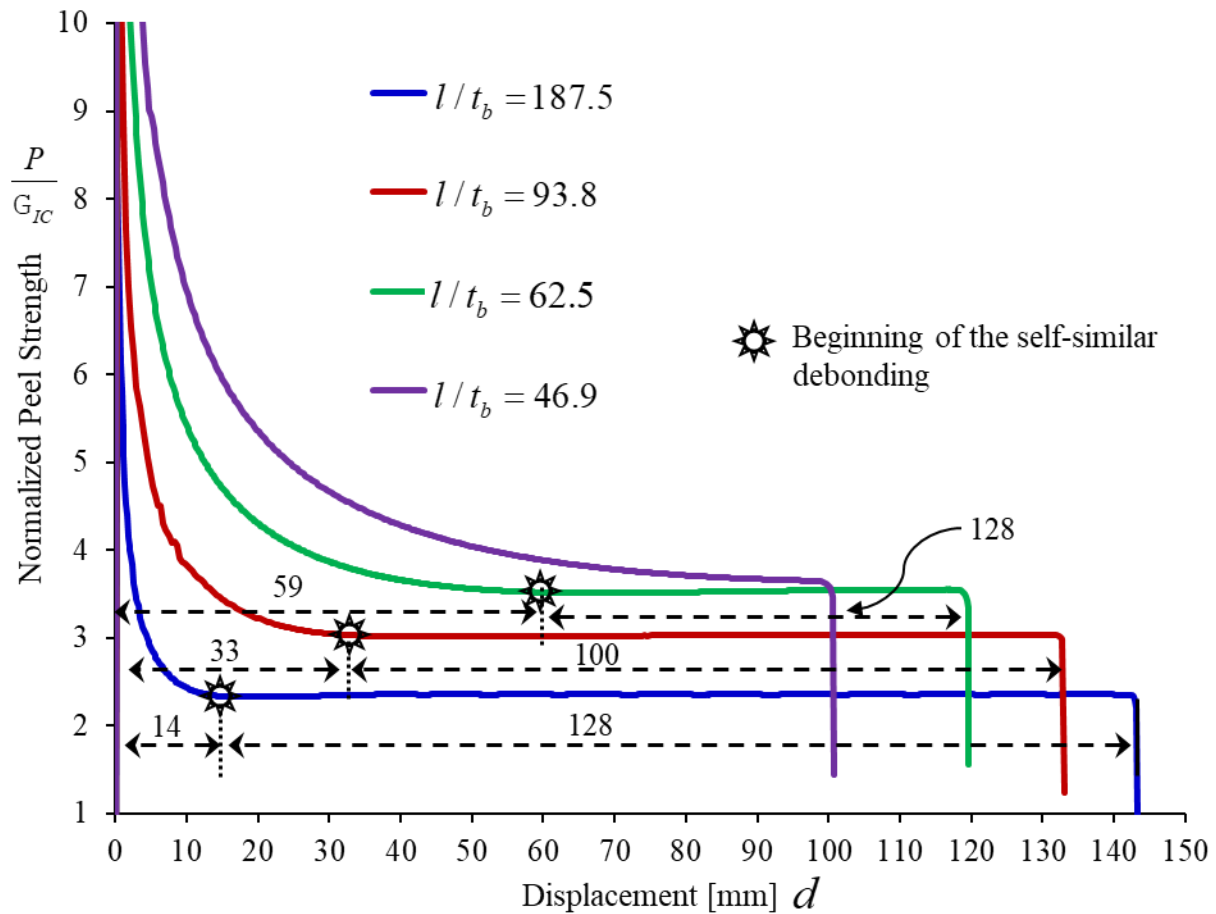


Figure 4.15. Normalized peel strength - displacement traces for the four Al specimens of different adherend thicknesses. ( $l = 75\text{mm}$ , bond length;  $t_b = 0.4, 0.8, 1.2$  and  $1.6$  mm, adherend thickness)

### 3.6 Discussion on the limitations of the numerical modeling in this work

Firstly, the mixed interfacial and cohesive fracture surfaces could not be modeled (e.g., see the failure surfaces for specimen 1 in Figure A-1) in the 2D plane strain simulations. Thus the FE simulations in this study are not designed for interpreting mixed mode failures. A detailed 3D model would be needed for capturing the detailed fracture surfaces, however, a trade-off between computational time and the modeling accuracy needs to be carefully considered, since each 2D simulation already cost around 5 hours for computation when one single CPU is used. Secondly, the peak forces in the force-displacement curves, which may depend strongly on details of the fillet and the initiation of debonding, has been used by some authors [18, 29] for characterizing initial break strength for T-peel joints, and are not studied here. In addition, brief results are given in

Figure 4.15 for demonstrating the effects of adherend thickness on the occurrence of self-similar debonding for Al specimens bonded with Maxlok™ system. One can similarly characterize the effect of other material and geometric parameters on the occurrence of self-similar debonding. However, a thorough parametric study might be needed to make the simulation results more useful to engineers. The realistic ranges of the material properties (adherend, adhesive, and interfaces), boundary conditions (half or full gripped), and geometric parameters: (adherend thickness, bond length, and adhesive thickness, etc.), are needed to be identified carefully. For example, from Figure 4.15, it is indicated that the thinner the adherend is, the sooner the specimen reaches self-similar debonding, and a shorter debond length is needed. However, very thin adherends not only raise the challenges for manufacturing devices, but also may result in tensile failures in the adherends. And design of experiments might also be needed to identify the possible coupling relations among those parameters. This would require a large amount of simulations, and will be addressed in a future work.

#### **4.4 Conclusions**

Depending upon whether or not plastic deformations occur and whether or not self-similar debonding is achieved during tests on T-peel specimens, they are divided into four categories [7, 8]. Using the test data on T-peel specimens with adherends of three steels and an aluminum alloy bonded with two acrylic adhesives, the category to which each configuration belongs is identified. Plane strain deformations of the specimens during their cohesive failure were also numerically analyzed by using the finite element method, the cohesive zone model, and taking the adherend materials to be linearly elastic and isotropically hardening during plastic deformations and the adhesives to be linearly elastic and isotropic. The key findings are: (1) The relative performances of different T-peel specimens depend upon the performance metric used. For specimens that do not reach self-similar debonding, the energy/debond area rather than the peel strength is an appropriate metric. (2) Short bond length T-peel specimens should be used only if self-similar debonding is achieved in tests. Otherwise, the relative performances of bonds will be affected by the metric used for characterizing them. (3) The correlation between the plateau in the computed peeling force and the constant projected crack length found from the numerical results suggests

using either one can be employed to characterize self-similar debonding. (4) Up to 88% of the total work done by the external force is used to plastically deform the ductile adherends. (5) For a fixed bond length and bond thickness using aluminum adherends, the self-similar debonding may totally disappear with an increase in the adherend thickness.

### **Acknowledgements**

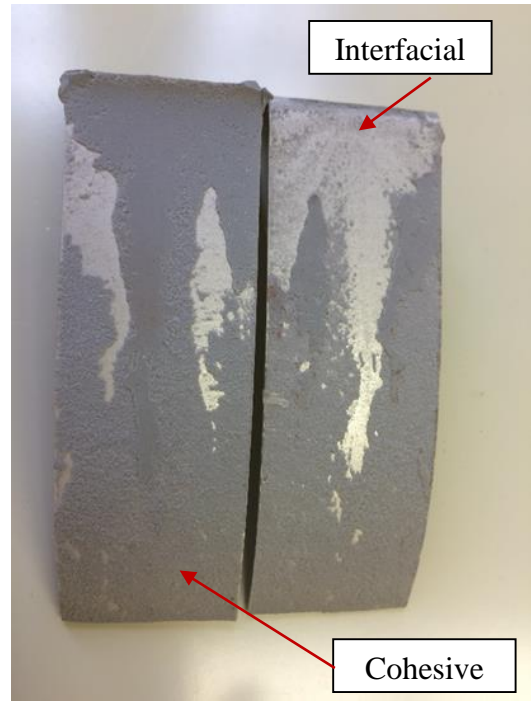
The authors would like to acknowledge the sponsorship of the National Science Foundation for this work (NSF/CMMI Award No. 0826143 to Virginia Polytechnic Institute and State University). The specimens were prepared by the LORD Corporation. The test results for Figure 4.6 were provided by the LORD Corporation. We also would like to acknowledge the support of the Biomedical Engineering and Mechanics Department as well as the interdisciplinary research environment fostered by the Macromolecules and Interfaces Institute at Virginia Tech.

### **Appendix E: Failure surfaces and failure modes of Al specimens bonded with LORD<sup>®</sup> 406**

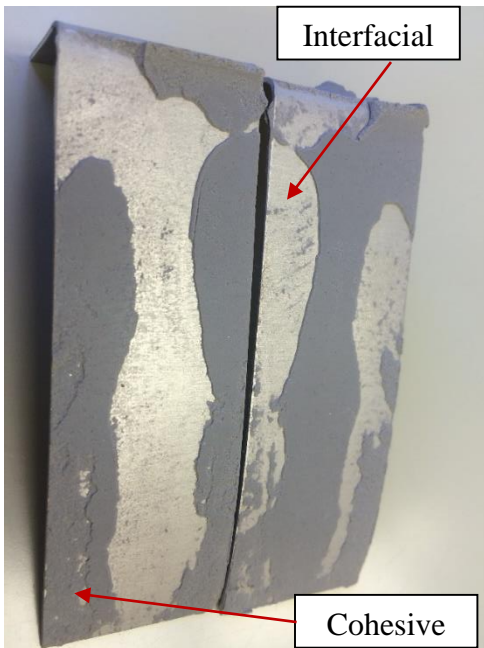
For the specimens bonded with Maxlok, the primary failure mode was cohesive, except for the CRS adherends. However, for specimens bonded with the LORD<sup>®</sup> 406 adhesive, the EGZ and the HDG adherends exhibited cohesive failures, and the CRS adherends again appeared to fail interfacially, but the Al specimens showed mixed failure modes with the ratio of the cohesive to the interfacial failure areas varying from one specimen to the other, as shown in Figure E-1 and E-2, along with approximate percentages of cohesive and interfacial failure, as estimated from visual inspection.



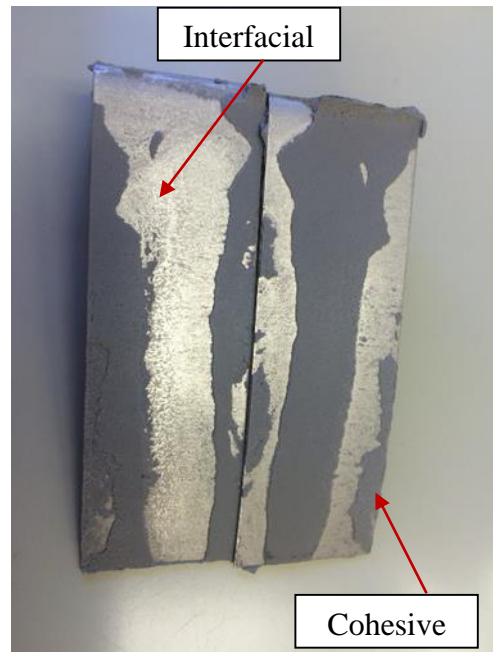
**Specimen 1:** 50 % cohesive + 50 %  
interfacial



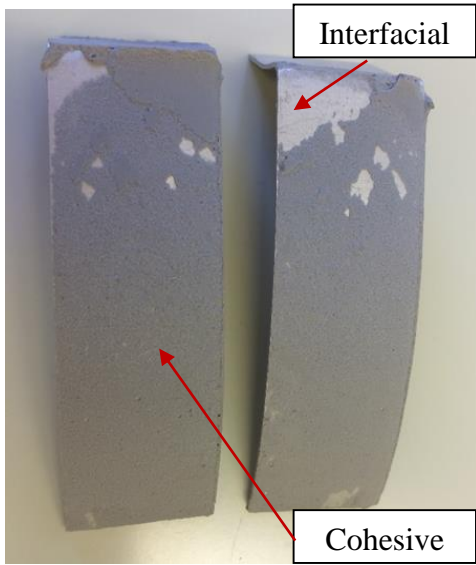
**Specimen 2:** 20 % cohesive + 80 %  
interfacial



**Specimen 3:** 10 % cohesive + 90 %  
interfacial



**Specimen 4:** 10 % cohesive + 90 %  
interfacial



**Specimen 5:** 90 % cohesive + 10 % interfacial

**Specimen 6:** 0 % cohesive + 100 % interfacial

Figure E-1. Failure surfaces of the six Al specimens bonded with LORD® 406.

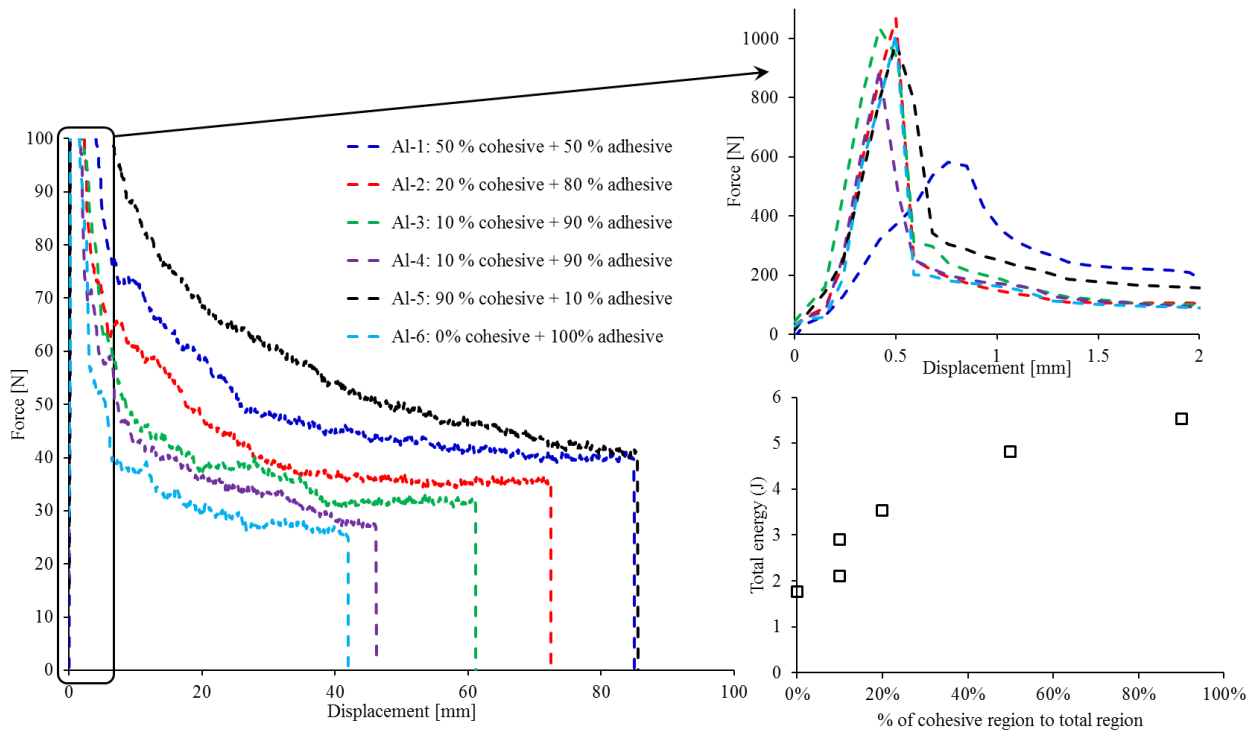


Figure E-2. Experimental force-displacement curves of the six replicates for Al specimens bonded with LORD® 406

By comparing the failure surfaces for six specimens with their respective force-displacement curve, it is concluded that cohesive failures appear to require more energy, as cohesive failures tend to result in larger loads, which induce larger curvatures and hence delay final failure (larger final displacement). Specimen 5 has the largest percentage of cohesive failure, and is associated with the largest final displacement and the area under the force-displacement curve (external energy required to pull the specimens apart). In contrast, specimen 6 has almost total interfacial failure, and has the smallest final displacement and the least area under the force-displacement curve. Specimens 3 and 4 have almost the same percentage of cohesive failure, but the trend is that specimen 4 remains mostly adhesive to the end, whereas specimen 3 has lots of cohesive failure late in the test, where extra bending results (see Figure E-3) in more displacement, leading to a larger final displacement at break. The peak forces for the six replicates varied considerably, possibly because of differences in the spew fillet, the adherend radius, and tab alignment.

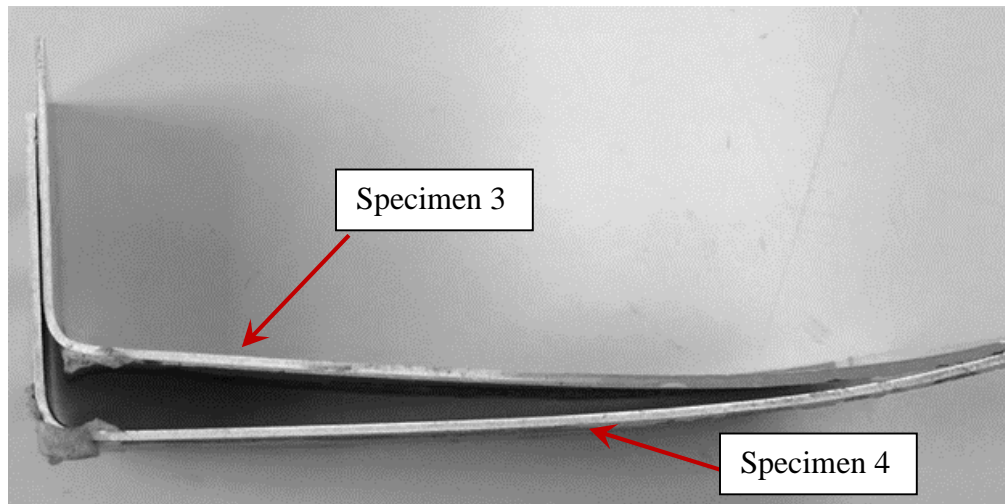


Figure E-3 Comparison of deformed Al specimens 3 and specimen 4 bonded with LORD® 406

A brief exploratory computational effort to see if different values of  $G_{IC}$  from 200 J/m<sup>2</sup> to 600 J/m<sup>2</sup> in the CZM can explain the change in failure modes has been carried out, as depicted by the solid lines in Figure E-4. Values of the initial stiffness ( $K_e = 1$  TPa/mm) and  $T_{max}$  (= 50 MPa) are kept fixed. With increase in  $G_{IC}$  from 200 J/m<sup>2</sup> to 600 J/m<sup>2</sup> for the cohesive failure, both the

computed reaction force and the final displacement at break increase. The force-displacement curve of specimen 6 in Figure E-1, which had almost 100% interfacial failure, is close to the one computed using  $G_{IC}$  between  $200 \text{ J/m}^2$  to  $250 \text{ J/m}^2$ . For specimen 5 with 90% of failure surfaces cohesive,  $G_{IC} = 500 \text{ J/m}^2$  gives a force-displacement curve close to the experimental one.

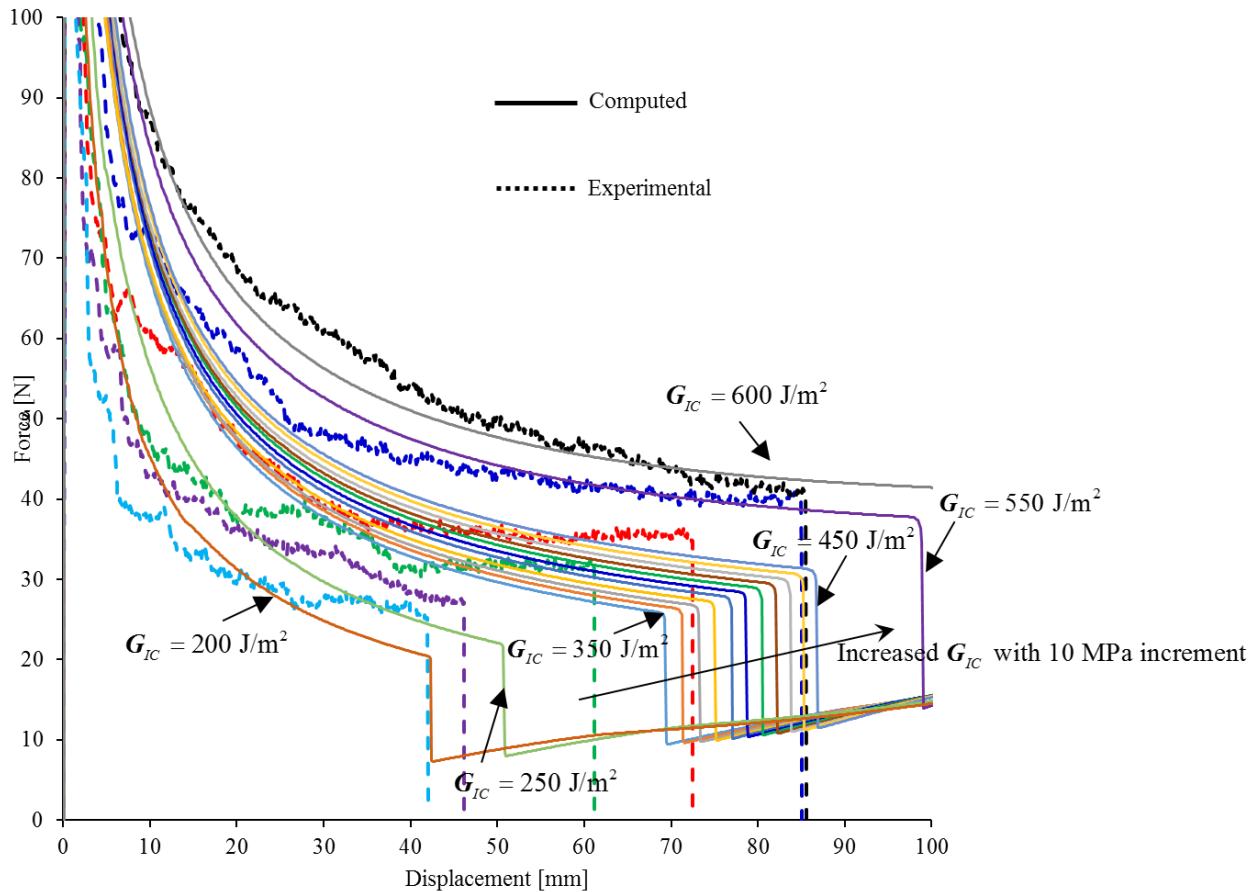


Figure E-4. Numerical force-displacement curves of the six replicates for Al specimens bonded with LORD<sup>®</sup> 406 and having bond length of 75 mm.  $K_e = 1 \text{ TPa/mm}$ ,  $T_{max} = 10 \text{ MPa}$ .  $G_{IC} = 200 \text{ J/m}^2 \sim 600 \text{ J/m}^2$

### Appendix F: Influence of the CZM parameter $T_{max}$ on numerical results

Plane strain deformations of the EGZ adherends bonded with the Maxlok<sup>™</sup> adhesive are analyzed for  $T_{max} = 10, 70, 80, 90, 100, 110$  and  $140 \text{ MPa}$ , and  $G_{IC} = 2 \text{ kJ/m}^2$ ,  $K_e = 1 \text{ TPa/mm}$ . From the

peeling force – crosshead displacement curves exhibited in Figure F-1, we find that the ultimate crosshead displacement and the plateau in the force decrease with a decrease in  $T_{\max}$ .

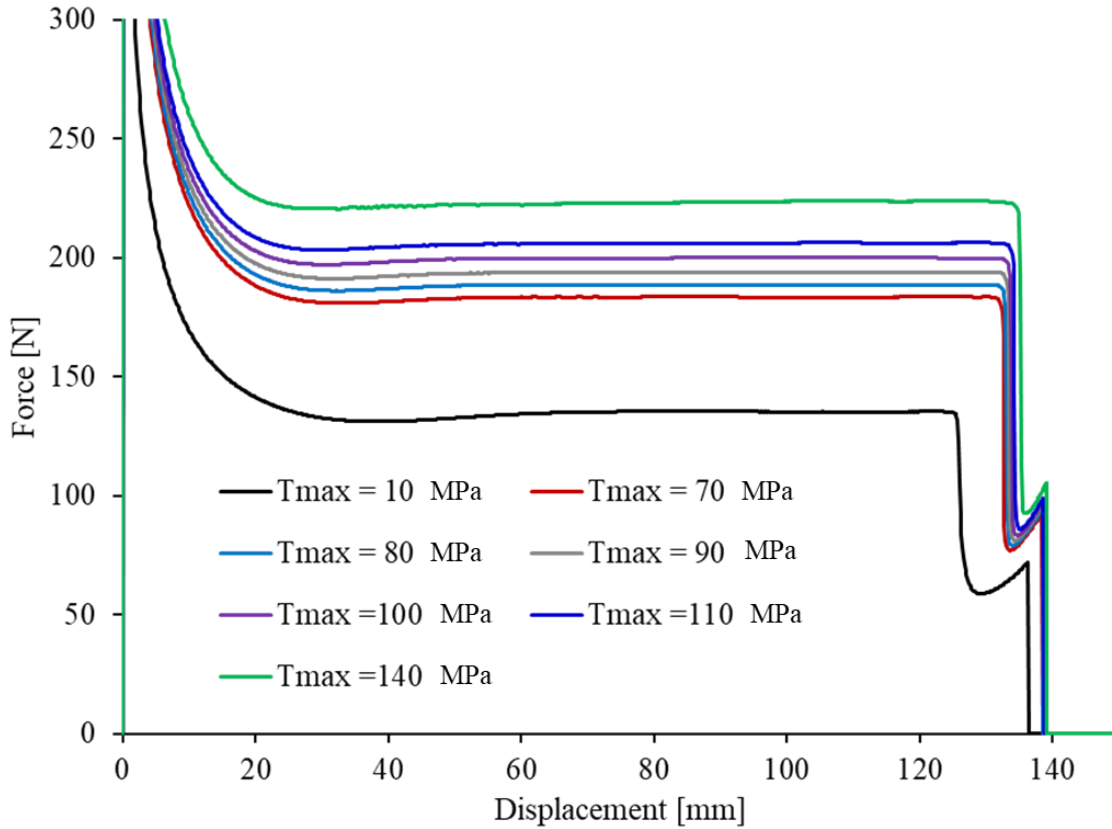


Figure F-1. Effect of  $T_{\max}$  value on the force - crosshead displacement curves for the EGZ specimens bonded with the Maxlok™ adhesive and having bond length of 75 mm.

### Appendix G: Remarks on CRS specimens

In Figure G-1 we have displayed the experimental and the simulation results using the following three arbitrarily chosen sets of values for the CZM parameters  $K_e = 1$  TPa/mm: (A)  $\mathcal{G}_{IC} = 2$  kJ/m<sup>2</sup>,  $T_{\max} = 100$  MPa; (B)  $\mathcal{G}_{IC} = 1$  kJ/m<sup>2</sup>,  $T_{\max} = 50$  MPa; (C)  $\mathcal{G}_{IC} = 0.4$  kJ/m<sup>2</sup>,  $T_{\max} = 50$  MPa. It is clear that none of the three computed force-displacement traces is close to the experimental ones. It seems to suggest that a much smaller value (e.g., 0.2 kJ/m<sup>2</sup>) of  $\mathcal{G}_{IC}$  should be chosen for simulating those CRS specimens. One simulation with  $K_e = 1$  TPa/mm,  $\mathcal{G}_{IC} = 0.2$  kJ/m<sup>2</sup>, and  $T_{\max} = 1$  MPa and with 250 mm bond length is given in Figure G-2. However, the computed force-displacement

curve barely plateaus, indicating that a longer bonded length is needed for the CRS specimens to reach self-similar debonding. One reason for CRS specimens need much longer bond length for self-similar debonding is that a small fracture energy value is used (e.g. here 200 J comparing to 2000J for HDG) in the simulations. When a larger value of fracture energy is used, such as Curve: Computed A or Computed B in Figure G-1, it can reach self-similar debonding even using the 75 mm bond length. Considering that the computational cost for running a simulation with 250 mm bond length is high (number of nodes: 170884, number of elements: 136448, time cost: 12 hours using 16 CPUs on a high performance cluster), we did not conduct additional parametric studies.

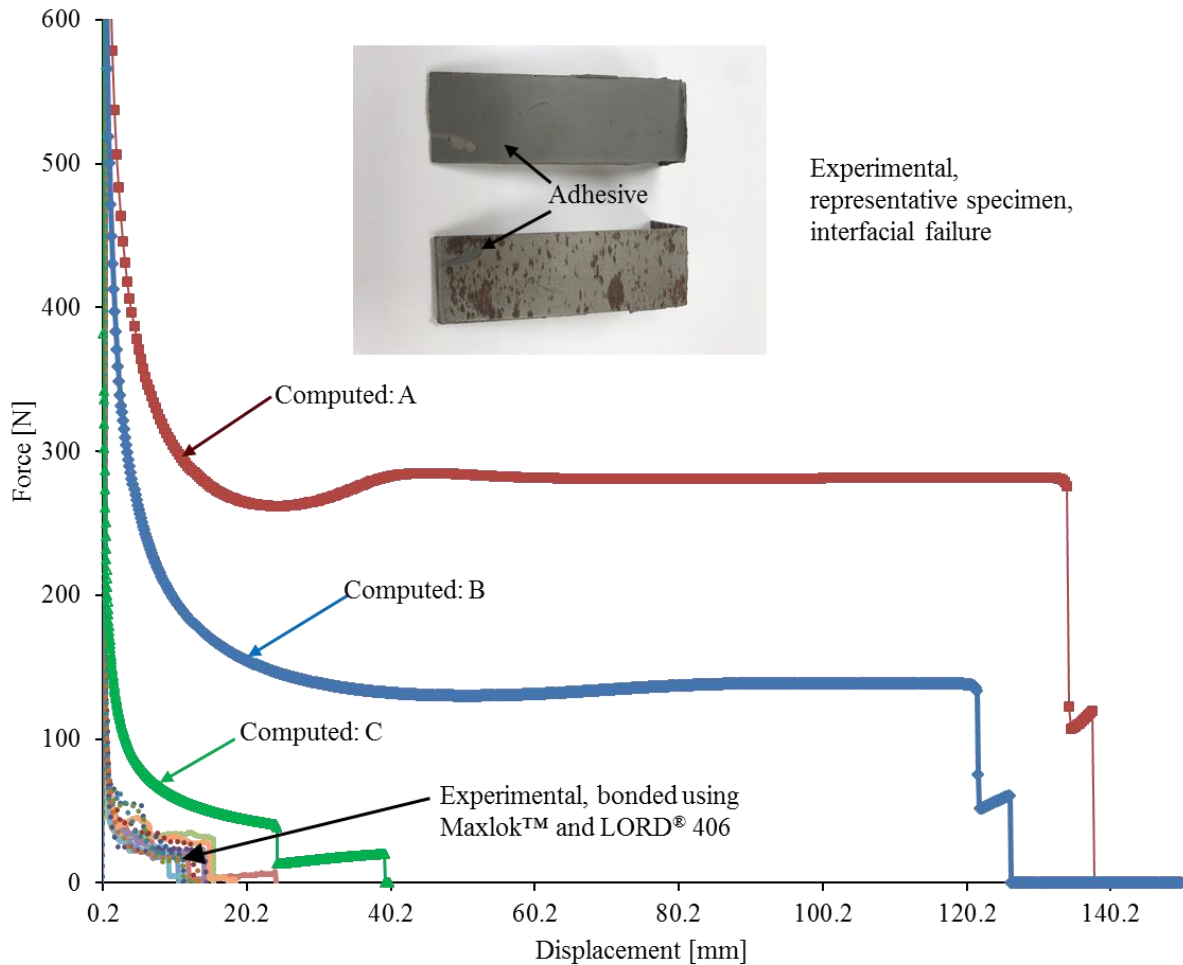


Figure G-1. Comparison of experimental and computed force-displacement curves for the CRS specimens using three sets of values of the CZM parameters. Pictures of the failed surfaces are included in the inset (oxide formation is present as photo taken long after testing).

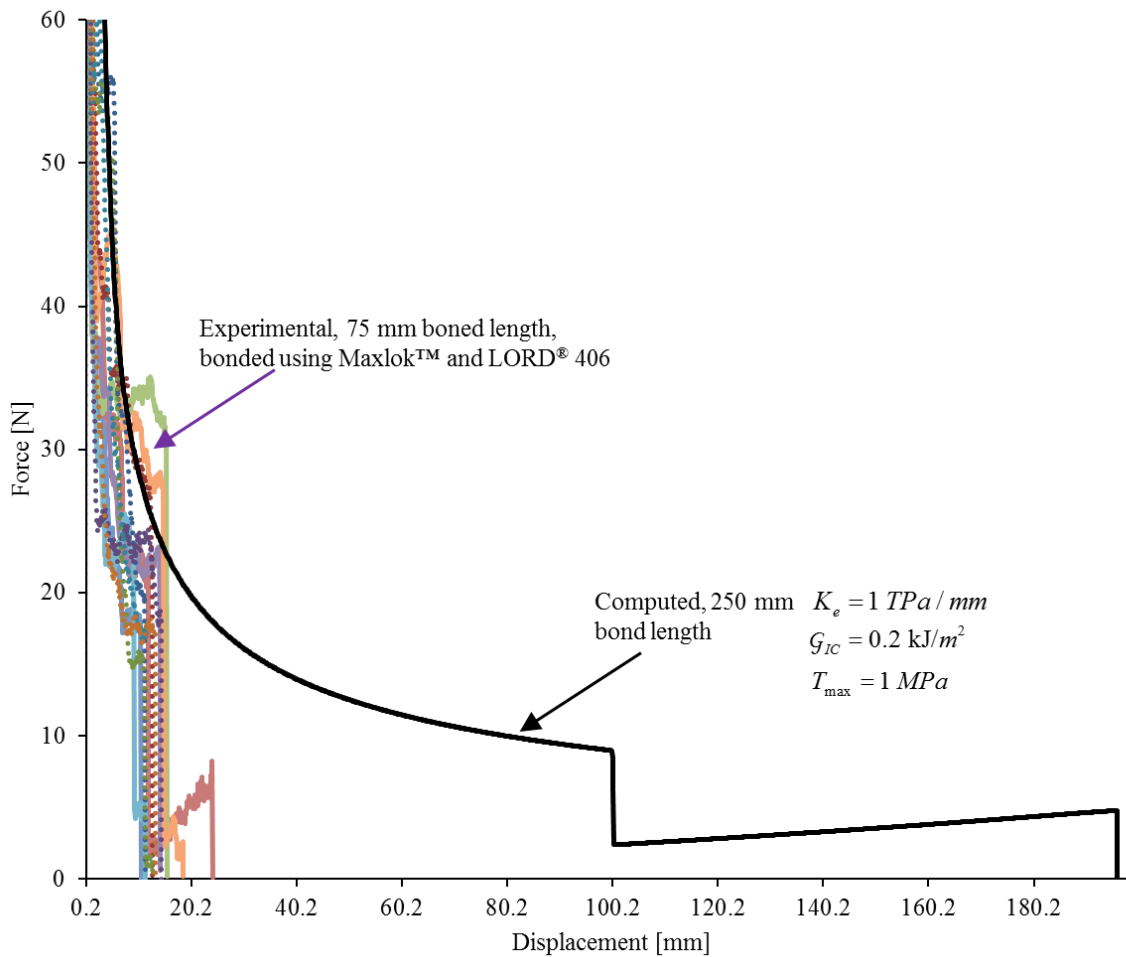


Figure G-2. Comparison of experimental force-displacement curves for 75 mm bond length CRS specimens with the computed force-displacement curves for 250 mm bond length CRS specimen using guessed CZM parameters.

## References

1. Kim, K.S. and Aravas, N., *Elastoplastic Analysis of the Peel Test*. International Journal of Solids and Structures, 1988. **24**(4): p. 417-435.
2. Kim, K.S. and Kim, J., *Elasto-Plastic Analysis of the Peel Test for Thin-Film Adhesion*. Journal of Engineering Materials and Technology-Transactions of the Asme, 1988. **110**(3): p. 266-273.
3. Kinloch, A.J., Lau, C.C. and Williams, J.G., *The Peeling of Flexible Laminates*. International Journal of Fracture, 1994. **66**(1): p. 45-70.
4. Georgiou, I., Hadavinia, H., Ivankovic, A., Kinloch, A.J., Tropsa, V. and Williams, J.G., *Cohesive Zone Models and the Plastically Deforming Peel Test*. Journal of Adhesion, 2003. **79**(3): p. 239-265.

5. Hutchinson, J.W. and Suo, Z., *Mixed-Mode Cracking in Layered Materials*. Advances in Applied Mechanics, Vol 29, 1992. **29**: p. 63-191.
6. Lindley, P.B., *Ozone Attack at a Rubber- Metal Bond*. J. Institution Rubber Industry 1971. **5**(6): p. 243-248.
7. Dillard, D.A., *The T-Peel Test*. Testing Adhesive Joints: Best Practices,, ed. al. L.F.M.d.S.e. 2012: Wiley-VCH: Weinheim.
8. Dillard, D.A., Li, Q., Batra, R.C. and Graham, I. *Interpreting T-Peel Test Results in Light of Four Different Specimen Configuration Categories*. in *36th Annual Meeting of the Adhesion Society*. 2013. Daytona Beach.
9. Dillard, D.A., Li, Q., Batra, R.C. and Graham, I., *The Four Categories of T-Peel Test Configurations and Their Interpretation as Fracture Specimens* Experimental Mechanics, In Review.
10. Moidu, A.K., Sinclair, A.N. and Spelt, J.K., *Analysis of the Peel Test - Prediction of Adherend Plastic Dissipation and Extraction of Fracture Energy in Metal-to-Metal Adhesive Joints*. Journal of Testing and Evaluation, 1995. **23**(4): p. 241-253.
11. Moidu, A.K., Sinclair, A.N. and Spelt, J.K., *On the Determination of Fracture Energy Using the Peel Test*. Journal of Testing and Evaluation, 1998. **26**(3): p. 247-254.
12. Yang, Q.D., Thouless, M.D. and Ward, S.M., *Numerical Simulations of Adhesively-Bonded Beams Failing with Extensive Plastic Deformation*. Journal of the Mechanics and Physics of Solids, 1999. **47**(6): p. 1337-1353.
13. Alfano, M., Furguele, F., Lubineau, G. and Paulino, G.H., *Simulation of Debonding in Al/Epoxy T-Peel Joints Using a Potential-Based Cohesive Zone Model*. Procedia Engineering, 2011. **10**: p. 1760-1765.
14. Needleman, A., *A Continuum Model for Void Nucleation by Inclusion Debonding*. Journal of Applied Mechanics-Transactions of the Asme, 1987. **54**(3): p. 525-531.
15. Tvergaard, V. and Hutchinson, J.W., *The Relation between Crack-Growth Resistance and Fracture Process Parameters in Elastic Plastic Solids*. Journal of the Mechanics and Physics of Solids, 1992. **40**(6): p. 1377-1397.
16. Wei, Y. and Hutchinson, J.W., *Interface Strength, Work of Adhesion and Plasticity in the Peel Test*. International Journal of Fracture, 1998. **93**(1-4): p. 315-333.
17. Needleman, A., *Numerical Modeling of Crack Growth under Dynamic Loading Conditions*. Computational Mechanics, 1997. **19**(6): p. 463-469.
18. Grant, L.D.R., Adams, R.D. and da Silva, L.F.M., *Experimental and Numerical Analysis of T-Peel Joints for the Automotive Industry*. Journal of Adhesion Science and Technology, 2009. **23**(2): p. 317-338.
19. Hadavinia, H., Kawashita, L., Kinloch, A.J., Moore, D.R. and Williams, J.G., *A Numerical Analysis of the Elastic-Plastic Peel Test*. Engineering Fracture Mechanics, 2006. **73**(16): p. 2324-2335.
20. Yang, X., Xia, Y., Zhou, Q., Wang, P.C. and Wang, K., *Modeling of High Strength Steel Joints Bonded with Toughened Adhesive for Vehicle Crash Simulations*. International Journal of Adhesion and Adhesives, 2012. **39**: p. 21-32.
21. ASTM-D1876, *Peel Resistance for Adhesives, T-Peel Test* American Society for Testing and Materials: West Conshohocken, PA.
22. ISO-11339, *T-Peel Test Flexible to Flexible Bonded Assemblies*.
23. BS-EN-1895:2001, *Adhesives for Paper and Board, Packaging and Disposable Sanitary Products. 180 Degrees. 'T' Peel Test for a Flexible-to-Flexible Assembly* 2001.

24. *Ms-Cd507: Structural Adhesive – Two Component – Room Temperature Cure – Metal Bonding Applications*. Chrysler.
25. *Wss-M2g410-A2: Aftermarket Adhesive, Weldable, Rivetable, Air Dry, Structural, Aluminum*. 2002, Ford Global Technologies.
26. ABAQUS, *ABAQUS Version 6.11 Documentation*. 2011.
27. Guan, Y.L., Tsai, C., Batra, R.C., Dillard, J.G., Ohanehi, D.C. and Dillard, D.A. *Crack Path Shifting Due to Mixed Mode Loading and Varied Surface Properties in Beam Like Adhesively Bonded Joints*. in *36th Annual Meeting of the Adhesion Society*. 2013. Daytona Beach, FL.
28. Kawashita, L.F., Moore, D.R. and Williams, J.G., *Comparison of Peel Tests for Metal-Polymer Laminates for Aerospace Applications*. *Journal of Adhesion*, 2005. **81**(6): p. 561-586.
29. Silva, d., L.F.M. and Adams, R.D., *The Strength of Adhesively Bonded T-Joints*. *International Journal of Adhesion and Adhesives*, 2002. **22**(4): p. 311-315.

## Chapter 5: Conclusions and Contributions

### 5.1 Fiber-reinforced rubberlike materials (FRRM)

#### 5.1.1 Major accomplishments:

Material modeling is a core problem for developing predictive techniques such as analytical and numerical methods to analyze engineering and biological systems. Numerous phenomenological constitutive relations have been proposed in the literature for the purpose of fitting experimental data for fiber-reinforced rubberlike materials. The nonlinear elastic behavior of FRRMs is generally described by assuming the strain energy density function,  $W$ , is a function of the strain invariants. The mathematical expression and the number of invariants to include in the expression for  $W$  are usually guided by knowledge of the materials and the experimental data. Polynomial forms are one of the popular forms used in the literature.

The major contributions in Chapter 2 are: (1) we presented a stored energy function in terms of the five invariants of the right Cauchy-Green strain tensor and account for a different response in tension and compression along the fiber direction. The constitutive relation accounts for both material and geometric nonlinearities and incorporates effects of the 5<sup>th</sup> strain invariant,  $I_5$ . It has been shown in the literature that in shear dominated deformations,  $I_5$  makes a significant contribution to the stress-strain curve. (2) Since material models considering the fifth invariant are generally not available in commercial FEA software, we have implemented the proposed constitutive relation, LS-DYNA as a user-defined material subroutine. (3) The analytical solutions for plane strain bending of a rectangle beam into a circular arc are derived using Ericksen's inverse approach, and are used to verify the implementation of the developed material subroutines.

The major contributions in Chapter 3 are: (1) An explicit expression for the Cauchy stress tensor is derived by taking the stored energy function,  $W$ , to be a complete quadratic function of the components of the Cauchy-Green strain tensor. Homogeneous deformations such as simple extension, simple shear, and biaxial loading are studied to delineate the mechanical behaviors of the FRRMs. Consistency with the infinitesimal theory requires terms linear in the 4<sup>th</sup> and the 5<sup>th</sup> invariants,  $I_4$  and  $I_5$ , be included in the expression for  $W$ . A stability analysis of the deformations reveals qualitative changes triggered by the consideration of quadratic terms in  $I_4$ . (2) Analytical

solutions for inflation, extension and twist deformations caused by internal pressure, end torque, and axial force for a pressurized cylindrical laminate are derived using Ericksen's inverse method. Effects of fiber orientations on the mechanical behaviors of a  $\pm\alpha$  angle-ply cylindrical tube are investigated using the derived analytical solutions. (3) The material model is also incorporated in the commercial software, LS-DYNA, as a user-defined subroutine. The implementation has been verified by ensuring that the computed solutions of a few boundary value problems agree well with either their analytical solutions or those available in the literature.

### ***5.1.2. Practical implications and future work***

(1) Our study on material modeling for FRRM provides insights/cautions for engineers and researchers using polynomial functions of invariants for hyperelastic material modeling. The stability analysis for several finite deformation states reveals that qualitative differences in the material responses are triggered by the second order terms. The bifurcation phenomenon for uniaxial deformations of FRRM presented in this dissertation has not been reported in the literature, but could serve as a guide for experiments seeking to demonstrate this behavior. Successful implementation of the model will require devising and conducting appropriate experiments to determine the material parameters required by the models, as well as validation of the predictive capabilities.

(2) We delivered softwares (user-defined subroutines) capable of analyzing large deformations of fiber-reinforced rubberlike materials having a different response in tension and compression along the fiber direction. One of the subroutines has been adopted by the commercial tire company, Bridgestone Americas, for modeling cord/rubber composites (e.g. tire belts, carcass etc.) in tires. The source codes developed and example input files have been included as appendices in Chapter 2 and Chapter 3.

(3) The derived analytical solutions for plane strain bending of a rectangle beam, inflation, twist and extension of fiber-reinforced cylindrical tubes can be used for early-stage design, and for verifying the implemented material subroutines for FRRMs. The remaining possible work includes studying some practical problems using the developed material subroutines. Those practical problems could not be studied using analytical methods but can be solved using the finite element

method with the developed material subroutines.

## **5.2 Adhesively bonded T-peel joints**

### ***5.2.1 Major accomplishments:***

In Chapter 4, we conducted both experimental and numerical analysis for several T-peel testing configurations. The major contributions can be summarized as follows:

(1) In the view of experimental results, the significant effects that properties such as adherend thickness, bond lengths, yield behavior, and adhesion levels have on the T-peel resulting configurations are assessed. This confirms the conceptual discussions given in the previous work [1-3].

(2) Several metrics were evaluated based on the experimental test results, and comparisons revealed some concerns with current practices, e.g., for specimens that do not reach self-similar state during debonding, the energy/debond area rather than the T-peel strength more realistically describes the adhesion's bonding ability.

(3) The finite element method with CZM model is employed to simulate the fracture process of the T-peel testing. The numerical model has been validated by comparing to experimental results. The partitioning of the computed total energy into different components based on the numerical model for several T-peel configurations (HDG, EGZ, and Al) indicates that most of the total energy is involved in deforming the adherend rather than fracturing the debond. The correlations between the computed force plateau and the constant projected crack length are presented from the FEA results. In addition, the effects of geometric parameters (e.g. adherend thickness) on the non-self-similar/self-similar ratio in the load-displacement curves have been studied numerically for one material system (aluminum/Maxlok<sup>TM</sup>).

### ***5.2.2 Practical implications and future work***

(1) Generally, the experimental study of different T-peel configurations and the evaluation of several metrics can serve as a caution for engineers using T-peel specimen for quantitatively evaluating adhesion. A qualitative comparison is possible; the quantitative comparison must be

used with caution. Short bond length T-peel specimens should be used only if self-similar debonding is achieved in tests. Otherwise, the relative performances of bonds will be affected by the metric used for characterizing them. The demonstrated success of predicting load-displacement traces, deformed shape, and by using CZM method in ABAQUS provides us with a framework to use in future assessment of T-peel configurations being addressed in this study. The transition between the non-self-similar and self-similar region in the load-displacement curves can be studied for various material and geometric parameters of interest. This can potentially provide insightful information for practitioners in selecting appropriate specimen dimensions for extracting meaningful data.

(2) The details of fillet and the initiation of debonding that strongly influence the initial breaking strength, are not often controlled when preparing the specimens. It is well known that for the short bond length specimens, the initial responses have a significant influence on the structure performance. Possible future work includes studying these details and their effects both numerically and experimentally. Moreover, in the discussion given in the dissertation, the bondline thickness has been kept constant. Another possible future work would be assessing the effects of the bondline thickness on the T-peel testing results.

## References

1. Dillard, D.A., *The T-Peel Test*. Testing Adhesive Joints: Best Practices,, ed. al. L.F.M.d.S.e. 2012: Wiley-VCH: Weinheim.
2. Dillard, D.A., Li, Q., Batra, R.C. and Graham, I. *Interpreting T-Peel Test Results in Light of Four Different Specimen Configuration Categories*. in *36th Annual Meeting of the Adhesion Society*. 2013. Daytona Beach.
3. Dillard, D.A., Li, Q., Batra, R.C. and Graham, I., *The Four Categories of T-Peel Test Configurations and Their Interpretation as Fracture Specimens* Experimental Mechanics, In Review.